THE DYNAMIC INTERPLAY BETWEEN MIOCENE TO POST-MIOCENE MAGMATISM, TECTONISM, AND GEOMORPHOLOGY IN NE OREGON

by

MATTHEW CONNOR MORRISS

A DISSERTATION

Presented to the Department of Earth Sciences
and the Graduate School of the University of Oregon
in partial fulfillment of the requirements
for the degree of
Doctor of Philosophy

September 2020

DISSERTATION APPROVAL PAGE

Student: Matthew Connor Morriss

Title: The Dynamic Interplay between Miocene to post-Miocene Magmatism, Tectonism and Geomorphology in NE Oregon

This dissertation has been accepted and approved in partial fulfillment of the requirements for the Doctor of Philosophy degree in the Department of Earth Sciences by:

Eugene Humphreys	Chair
Josh Roering	Core Member
Rebecca Dorsey	Core Member
Mark Fonstad	Institutional Representative
Eric Kirby	External Member
and	
Kate Mondloch	Interim Vice Provost and Dean of the Graduate School

Original approval signatures are on file with the University of Oregon Graduate School.

Degree awarded September 2020

DISSERTATION ABSTRACT

Matthew Connor Morriss

Doctor of Philosophy

Department of Earth Sciences

September 2020

Title: The Dynamic Interplay between Miocene to post-Miocene Magmatism, Tectonism and Geomorphology in NE Oregon

The Miocene to post-Miocene geologic history of Northeastern Oregon and West-Central Idaho is difficult to parse because this area has experienced several dramatic events. Within 35 km of each other, there are exposures of the Chief Joseph Dike Swarm (CJDS) the fed the youngest large igneous province (LIP) on Earth: the Columbia River Basalt Group (CRBG), and Hells Canyon — the deepest canyon in North America. Our understanding of these dikes and how they relate to the impingement of the Yellowstome plume and the movement of magma vertically in the crust during the eruption of this LIP are limited as most studies in the region have focused on the surface flows. Similarly, the age and origin story for Hells Canyon remain unknowns. This is despite a long history of research into the age and origin of the less deep Grand Canyon.

In the first chapter , I leverage a dataset of never before digitized maps of 4279 dikes within the CJDS to make key observations of the structure and mechanics of this swarm. I combine these data with field observations of cross-cutting relationships to constrain changes in the upper crustal stress field during the eruption of the CRBG and measure the amount of dilation accommodated by the upper crust due to diking.

The second and third chapters are focused on investigating Hells Canyon, namely I seek to answer the questions of "When did Hells Canyon Form?" and

"Why is it there?" The second chapter makes use of an elevation transect of low-temperature thermochronometers collected from the highest peaks above the canyon to the deepest points in the Canyon. These data reveal a long-lived story of cooling related to exotic terrane accretion and translation on the margin of North America. Forward modeling of our data reveals a potential cooling signature favoring canyon incision at ~ 4 Ma.

The third and final chapter discusses the landscape response to canyon incision. Close examination of tributaries streams reveals a pattern of knickpoints emblematic of a drainage divide which was incised through. The reaches above the knickpoints on these tributaries are an anachronism from the pre-capture time.

CURRICULUM VITAE

NAME OF AUTHOR: Matthew Connor Morriss

GRADUATE AND UNDERGRADUATE SCHOOLS ATTENDED:

University of Oregon, Eugene, OR, USA
North Carolina State University, Raleigh, NC, USA
Whitman College, Walla Walla, WA, USA

DEGREES AWARDED:

Doctor of Philosophy in Geological Sciences, 2020, University of Oregon
Masters of Science, 2015, North Carolina State University
Bachelor of Arts in Geology, 2013, Whitman College

AREAS OF SPECIAL INTEREST:

Tectonic Geomorphology
Western U.S. Tectonics
STEM education

PROFESSIONAL EXPERIENCE:

Physical Scientist, U.S. Geological Survey, 2020 – Present
NSF Intern, Utah Geological Survey, 2019–2020
Graduate Employee, University of Oregon, 2013–2019
Teaching Assistant, North Carolina State University, 2013–2015

GRANTS, AWARDS AND HONORS:

Committee of the Lewis and Clark Fund for Exploration and Field Research for Topographical Map Interpretation, American Philosophical Society, 2020.

INTERN PROGRAM, National Science Foundation: Coupling INSAR and Terrain Roughness to map Landslides, Utah Geological Survey, 2020.

INTERN PROGRAM, National Science Foundation: Automated Landslide Mapping, Utah Geological Survey, 2019.

Smith Warren Award, Department of Earth Sciences, University of Oregon, 2019.

Smith Warren Award, Department of Earth Sciences, University of Oregon, 2018.

Johnstone Geology Award, Department of Earth Sciences, University of Oregon, 2017.

Collaborative Research: An integrated mantle to surface study of the causes and consequences of high topography in the Northern US Cordillera, NSF EAR-1727046/1727139/1727451, 2017.

PUBLICATIONS:

Morriss M.C., Karlstrom, L., Nasholds, M., Wolff, J., (2020). The Chief Joseph Dike Swarm of the Columbia River Basalts, and the Legacy Dataset of William H. Taubeneck. *Geosphere*, 16(4): 1793–1817. doi: 10.1130/GES02173.1

Morriss, M.C., & Wegmann, K.,. (2017). Geomorphology of the Burnt River, eastern Oregon, USA: Topographic adjustments to tectonic and dynamic deformation. (2017) *Geomorphology*, 278: 43–59. doi: 10.1016/j.geomorph.2016.09.015

Leary, R., Decelles, P.G., Gehrels, G.E., & Morriss, M.C. (2014). Fluvial deposition during the transition from flexural to dynamic subsidence in the Cordilleran foreland basin: Ericson formation, western Wyoming. *Basin Research*, 27(4): 495-516. doi: 10.1111/bre.12085

ACKNOWLEDGEMENTS

A PhD is not only the sum of the work put in by a student; it is the collective effort of that student's support network. I haven't enough space to thank all of those who have contributed to me reaching this point in my graduate career, but I want to take a moment to say **Thank You** to the lovely friends, family, teachers, and fellow students who helped me achieve what at times felt impossible.

Before going on, I would like to thank my partner, Sarah Wolfe. Who shared me with this document for the past 5 years; who held me when I cried; who joined me in cursing the unforeseen roadblocks, and celebrated with me as I passed them. Thank you for so many things Sarah – I Love You.

I would next like to acknowledge the contribution of teachers. Who put so much effort in to developing our curiosity and knowledge base, but they often ask for so little in return. I owe much of who I am as a scientist to one inspiring teacher who challenged me to always ask: "is the observed relationship *correlative*, *causal*, or *coincidental*?" He supported me in an independent study during my Senior year of High School, helped to raise funds for long weekend High School field trips to West Texas, and hosted open observatory nights at the campus observatory. I think of him often when I start a new project or as I stare at the sky and in wonder of the universe we inhabit. I cannot thank him enough for all he has done for me and for so many others over the years. Thank you for so much Frank Mikan. My teacher, and my friend.

I would also like to thank: Freddy Jones & Johnny Wilson – without whom I never would have learned to love the Chihuahuan Desert. Bob Carson, who motivated me to pursue geology at Whitman College with a furvor and love for the subject I never knew I had. Karl Wegmann who above all else trusted me to get my

work done and provided support, both emotional and scientific at key points in my career.

My work would never have reached this point without the people I hold dear in my life, as a chosen family, of friends and acquaintances who fill my life with color and joy. To list them here would be inadequate. Just know that you all brighten my day everytime we talk; everytime we darken the others doorstep or stir up some dust on a run, every time we talk on the porch, over the phone, or through zoom, I am enriched beyond measure. You fill my life with endless joy and celebration – for that I am so grateful.

I would like to thank my parents. Who helped inspire in me the the curiosity to ask questions, to seek out the process behind mysteries, and above all to *wonder*. I am grateful to my sister Katherine, for teaching me that it is ok to be myself, and I am grateful to my sister Lauren to helping me to learn patience and appreciate the nostalgia of a good movie.

TO Gene, my advisor for five years, thank you for taking a risk on me: a geomorphologist joining a group of geodynamicists. I would also like to take my committee through my PhD: Ray Weldon, Leif Karlstrom, Eric Kirby, Josh Roering, Mark Fonstadt, and Becky Dorsey. Your feedback has been integral to the forward motion of my Research. And to my collaborators both on paper and off: Jim O'Connor, Lydia Staisch, Becky Flowers, Phil Shoettle-Greene, Brian Yanites, and Nate Mitchell.

For anyone I may have forgotten, my apologies but you are important as well! :)

TABLE OF CONTENTS

LIST OF FIGURES

Figure Page

Figure Page

LIST OF TABLES

Table Page

CHAPTER I

INTRODUCTION

Northeastern Oregon has been the focus of intense geologic events over the past ∼17 Ma. The voluminous Columbia River Basalt Group (CRBG) erupted from the Chief Joseph Dike Swarm (CJDS) exposed in the high Wallowa Mountains and deep canyons of the region (Taubeneck, 1970). From these dikes, ∼210,000 km^3 of basalt and basaltic andesite erupted between 16.9 and 6 Ma (Kasbohm & Schoene, 2018; S. P. Reidel, Camp, Tolan, & Martin, 2013). These flows inundated pre-existing topography and provide a canvas into which impressive modern geomorphology is carved (Bond, 1963; Lindgren, 1901). Through the CRBG flows the Snake River which carves a canyon 2.2 km deep; 500 m deeper than the Grand Canyon (Vallier, 1977; Vallier, Schmidt, & Lamaskin, 2016).

Within 35 kilometers, are the dikes which fed the youngest Large Igneous Province (LIP) on Earth, and the deepest canyon in North America (S. P. Reidel et al., 2013). The incredible exposure of the former makes it an ideal location to study the connection between the dikes at depth and the surface flows of a LIP. This connection is often poorly exposed (Mège & Korme, 2004; Svensen et al., 2009).LIPs are often the first surface expression of mantle plumes, which can be drivers of both volcanic and geodynamic processes (V. E. Camp & Hanan, 2008; Darold & Humphreys, 2013; Ernst & Buchan, 1997). The coincident occurrence of the CJDS, CRBG, and Hells Canyon implies large scale forcings within the crust and on the surface are at work in this compact region. Herein, I seek to understand and investigate these two phenomenon in distinct studies. Moreover, I want to gain insight into fundamental questions that remain unanswered about Hells Canyon, namely: When did it form? And what phenomena explains its formation?

Chapter II investigates the structure and mechanics of the Chief Joseph Dike Swarm exposed in the Wallowa Mountains and areas adjacent. This study was motivated and supported by a large map and notebook database collected by William H. Taubeneck over a nearly 50 year career. His unpublished maps and notebooks were the basis for our work. One-and-a-half years of digitizing >4000 dike segments, going through 50 scanned notebooks, three summer of field work, and four overall years of work produced a manuscript in publication in Geosphere. In this chapter, I combined Taubeneck's original observations with conclusions about the dynamics of the dike swarm and the eruption timescale of the Columbia River Basalts. Most notably, I was able to constrain how much dilation may have taken place in the upper crust during the very short time period of Grande Ronde basalt eruption. Crustal spreading rates may have approached plate velocity speeds during a short period of time. This publication was written with coauthors Leif Karlstrom, Morgan W. Nasholds, and John Wolff and is published in *Geosphere* in a paper titled "The Chief Joseph dike swarm of the Columbia River flood basalts, and the legacy data set of William H. Taubeneck."

Chapter **??** brings the time period for investigating the dynamics of NE Oregon to a younger time scale. In order to constrain the incision of the Snake River through Hells Canyon, I collected bedrock samples in a 2 km elevation profile on the Idaho side of the canyon. These samples were then processed to measure the U-Th/He in apatite and zircon. The intent of this investigation was to derive the rate of cooling through time for these samples using low-temperature thermochronology. I analyzed our results and provide greater constraint on the timing of exhumation in the late Cretaceous tied to terrane translation northward along the western margin or North America. Forward thermal modeling of these samples shows some promise of a younger incision history partially explaining the

results we observed. One main conclusion from this work is that the CRBG is offset by $\sim$ 1 km across the deepest portion of Hells Canyon. This indicates the presence of a long-wavelength fold across the region, the activity of which appears in neither our thermochronology nor modeling results. This work was conducted with co-authors Phil Schoettle-Green, Alison Duvall, Becky Flowers, and Becky Dorsey. This manuscript will shortly be submitted to *Earth and Planetary Science Letters*.

Chapter IV takes the ideas developed in Chapter III and delves more into the landscape response of the tributaries to the Snake River. This chapter starts with a hypothesis about what the landscape and specifically what the rivers should look like in response to a baselevel lowering event, wherein a large lake in southern Idaho – Lake Idaho – spilled over into a smaller tributary to the Columbia River in a proto-Hells Canyon. I hypothesize that this capture event would create a distinct baselevel lowering event preserved in the shape of knickpoints along tributary streams to the Snake River. To investigate this hypothesis, the longitudinal profiles of 97 tributaries were examined and knickpoints not proximal to faults or lithologic changes were identified on 54 of these tributaries. The pattern of knickpoints, with the highest elevation ones located mid-canyon, implicate a potential paleo-drainage divide between Lake Idaho and the Columbia River system. I further develop this hypothesis testing with a numerical model of the predicted pattern of incision from drainage capture and integration. I compared these model results to the projected relict profiles of each tributary. To further constrain the timing of capture, I investigated limestone caverns along the canyon, looking to date fluvial sediments stranded in caves high above the Snake River. Some of these results have yet to be returned from the Purdue Rare Isotope Measurement Laboratory, but these samples have great potential to provide rates of incision along Hells Canyon.

This work was aided and supported by my co-authors Dr. Brian Yanites, Nate Mitchell, and Dr. Lydia Staisch.

Together, these three chapters provide a time-integrated story of upper crustal dynamics (diking) and tectonic geomorphology (incision of Hells Canyon) in Northeastern Oregon. A region with such a diverse geologic history in such a short period of time is rare. I appreciated the opportunity to provide more insight into its dynamics and history.

CHAPTER II

THE CHIEF JOSEPH DIKE SWARM OF THE COLUMBIA RIVER FLOOD BASALTS, AND THE LEGACY DATASET OF WILLIAM H. TAUBENECK

From Morriss, M.C., Karlstrom, L., Nasholds, M.W.M., & Wolff, J.A. (2020). The Chief Joseph Dike Swarm of the Columbia River Flood Basalts, and the Legacy Dataset of William H. Taubeneck. *Geosphere*.

2.1 Summary

The Miocene Columbia River Basalt Group (CRBG) is the youngest and best studied continental flood basalt province on Earth. The 210,000 km^3 of basaltic lava flows in this province were fed by a series of dike swarms, the largest of which is the Chief Joseph Dike Swarm (CJDS) exposed in northeastern Oregon and southwestern Washington. We present and augment an extensive dataset of field observations, collected by Dr. William H. Taubeneck (1923–2016; Oregon State U., 1955-1983) which elucidates the structure of the CJDS in new detail.

The large-scale structure of the CJDS, represented by 4279 mapped segments mostly cropping out over an area of 100 x 350 km^2, is defined by regions of high dike density, up to ∼5 segments/km^2 with an average width of 8 m and lengths of ∼100-1000 m. The dikes in the CJDS are exposed across a range of paleo-depths, from visibly feeding surface flows to ∼2 km in depth at the time of intrusion. Based on extrapolation of outcrops, we estimate the volume of the CJDS dikes to be 2.5 x 10^2 – 6 x 10^4 km^3, or between 0.1% and 34% of the known volume of the magma represented by the surface flows fed by these dikes. A dominant NNW dike segment orientation characterizes the swarm. However, prominent sub-trends with consistent cross-cutting relations and clustering of dike segments suggest time-transgressive orientations that may correspond to magmatically driven

stress changes over the duration of swarm emplacement. Near-surface crustal dilation across the swarm is ∼0.5-2.7 km to the E-W and ∼0.2-1.3 km to the N-S across the 100 by 350 km region, resulting in strain across this region of 0.4–13.0% E-W and 0.04–0.3% N-S. Host-rock partial melt is rare in the CJDS, suggesting that only a small fraction of dikes were long-lived.

2.2 Introduction

Dikes represent the primary pathway between magma reservoirs at depth and the upper crust or eruptive centers at the surface. They are the most common mode of magma transport in nearly all volcanic provinces, from oceanic islands (e.g. Krumbholz et al., 2014) to arcs (e.g. Petford, Kerr, & Lister, 1993), and rifts (e.g. Passarelli, Rivalta, & Shuler, 2014). The largest dike swarms exposed on continents are commonly associated with Large Igneous Provinces (LIP). In this style of volcanism, the connection between dikes at depth and lava flows is often poorly exposed (Mège & Korme, 2004; Svensen et al., 2009). As a result, crustal magma transport pathways in these largest terrestrial volcanic systems remain poorly understood. Hence, it is difficult to connect theoretical models of magma flow and dike-related stress changes to observations. Such models are required to assess both the deep mantle origins (e.g. White and McKenzie, 1995) and the surface environmental impacts (e.g. Self, 2006) of these large events.

This study focuses on the dikes that fed the CRBG, the youngest flood basalt province on Earth. The CRBG covers an area of ∼210,000 km^2 with an estimated volume of ∼210,000 km^3 (2.1 S. P. Reidel et al., 2013). An estimated 99% was erupted between ∼17.2 and 15.9 Ma (Barry et al., 2013; Cahoon, Streck, Koppers, & Miggins, 2020; V. Camp, Reidel, Ross, Brown, & Self, 2017; Jarboe, Coe, Renne, Glen, & Mankinen, 2008; Kasbohm & Schoene, 2018; S. P. Reidel

& Tolan, 2013a). (Barry et al., 2013) The Grande Ronde Basalt (GRB), 71% of the CRBG by volume, erupted in $\leq$ 400,000 years (Kasbohm & Schoene, 2018). Because most published research has focused exclusively on the extrusive component of the CRBG (e.g. V. Camp, Reidel, et al., 2017; S. P. Reidel & Tolan, 2013a; D. A. Swanson, Wright, Hooper, & Bentley, 1979, and references therein), connecting surface flows to upper crustal storage and transport remains an outstanding challenge.

Petrologic mass balance provides one possible approach for estimating intrusive volumes, and because the GRB lavas are notable from other units of the CRBG for their evolved compositions, ranging up to 57% SiO2, we use this formation for illustration (Hooper, 2000; S. P. Reidel & Tolan, 2013a). The GRBs have been variously modeled as melts of foundering or recycled mafic crust (V. E. Camp & Hanan, 2008; Hoshi & Takahashi, 1999) or as residual liquids produced by differentiation at crustal depths from parents represented by Imnaha Basalt (Wolff & Ramos, 2013; Wolff, Ramos, Hart, Patterson, & Brandon, 2008). In the latter case, a significant addition of mass to the crust in the form of a volume of complementary gabbroic cumulates roughly equal to the GRB erupted volume (150,100 km^3, Kasbohm & Schoene, 2018) is implied. Detailed description of the mass balance calculation involved in this estimate is found in the Methods section.

This petrologically derived volume can then be compared to the estimated physical extent of intrusive CRBG volumes from mapped dikes encompassed by three named swarms: the Steens Mountain Dike Swarm (Steens Basalts), the Monument Dike Swarm (Picture Gorge Basalts), and the largest concentration of CRBG dikes: the Chief Joseph Dike Swarm (Imnaha; Grande Ronde, Wanapum, and Saddle Mountain Basalts; Figure 2.1; V. E. Camp & Ross, 2004; Fruchter & Baldwin, 1975; Taubeneck, 1970; Tolan et al., 1989). This swarm was first

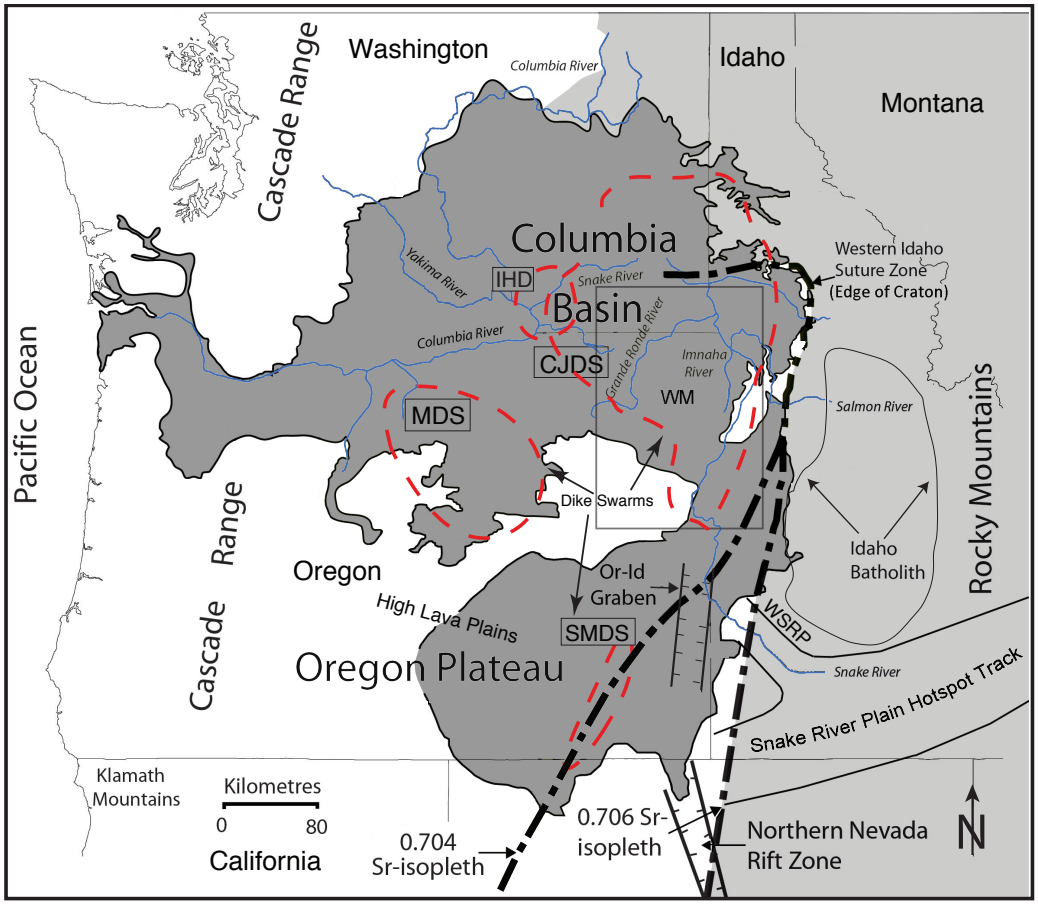

Figure 2.1. Major physiographic and geologic features associated with the Miocene Columbia River Basalts. Strontium isopleths demarcate the line between Precambrian lithosphere (light gray, to the east) and Paleozoic to Mesozoic accreted terranes (to the west; Pierce & Morgan, 2009). Darker gray coloration represents areas covered by CRBG. Thinner red dashed lines encircle the bulk of mapped dike swarms associated with this LIP: The Chief Joseph Dike Swarm (CJDS); Monument dike swarm (MDS); Steens Mountain Dike swarm (SMDS); and the Ice Harbor dike subswarm (IHD). The inset rectangle shows the approximate area of coverage for Figure 2. The Wallowa Mountains (WM) are a point of reference in many subsequent figures. (Modifed with permission from Camp et al., 2017). The western Snake River Plain is noted with WSRP.

recognized by Lindgren (1901) and described in detail by Taubeneck (1970). Dikes have been correlated to individual flows for some of the Wanapum and Saddle Mountain Basalts (S. P. Reidel, Camp, Martin, Tolan, & Wolff, 2016; S. P. Reidel et al., 2013). However, with a few exceptions (e.g. H. L. Petcovic & Dufek, 2005), physical correlations are more rare for the GRBs, in part because of the vast numbers of dikes and voluminous surface flows.

In this paper, we present an extensive CJDS dataset based on notes and field maps compiled by Dr. William H. Taubeneck (WHT). This dataset includes 4279 dike segments mapped at 1:24,000 scale across NE Oregon, SE Washington and west-central Idaho that define the structure of the CJDS in a regional context. The distributions of thickness, length, and orientation of dike segments help inform the following questions: What controls the orientation of dikes within the swarm? What are the implications for regional magmatic-tectonic relationships?

Our objectives are: (1) describe the structural, textural, and chemical dataset of WHT; (2) describe new observations to confirm and extend his measurements through field work, remote sensing, and re-analysis of geochemical samples; (3) quantify dike swarm morphology and geometry; (4) characterize sub-swarm size and systematic trends, and (5) measure dike widths and characterize host-rock and dike interactions at the outcrop-scale. We then make use of these observations to (1) assess relative emplacement timing and crustal dilation; (2) assess controls of regional stress vs local mechanical variability on dike emplacement; (3) detail potential perturbations to the local and regional strain field from dike emplacement, and (4) investigate potential geochemical variations present within the dike swarm.

2.3 Regional Geology

2.3.1 Pre-Miocene (< 23 Ma)

The CJDS stretches from the western Snake River Plain and northern Great Basin to the Columbia Basin. Most dikes are confined to an area approximately 100 km wide by 350 km long (Figure 2.1 and 2.2A; Plate 1 in M. Morriss, Karlstrom, Nasholds, and Wolff (2020)). The swarm traverses several lithospheric boundaries between Mesozoic accreted terranes and the margin of cratonic North America (Figure 2.1). These terranes docked with North America by the Jurassic and were later intruded by granitoids of the Wallowa and Elkhorn Mountains (2.2A Dorsey & LaMaskin, 2008; Schwartz et al., 2014). However, dikes intrude through rocks that range from Proterozoic to Miocene in age.

During the Eocene, four notable events took place in this region of eastern Oregon. First, the Siletzia oceanic plateau accreted to the Pacific Northwest (Irving, 1979; Snavely, MacLeod, & Wagner, 1968; Wells et al., 2014). Second, Eastern Oregon experienced a period of exhumation, exposing granitoid bodies at the surface (Michaels, Davenport, & Hole, 2017). This unroofing in eastern Oregon was concomitant with exhumation of rocks within the Idaho Batholith to shallow crustal levels (Figure 2.1 Fayon, Tikoff, Kahn, & Gaschnig, 2017; Giorgis, McClelland, Fayon, Singer, & Tikoff, 2008). Third, the 53-43 Ma Challis volcanics erupted just to the east (R. Gaschnig, Vervoort, Tikoff, & Lewis, 2016). Volcanism in eastern Oregon at this time period is linked with the dynamics of Farallon slab subduction (V. Camp, Reidel, et al., 2017; Liu & Stegman, 2011; Seligman, Bindeman, McClaughry, Stern, & Fisher, 2014). Fourth, the eruption of the calc-alkaline Clarno units and early bimodal John Day formation in central to eastern Oregon (McClaughry, Ferns, Streck, Patridge, & Gordon, 2009). Throughout this period of time, Oregon experienced south and westward increasing clockwise

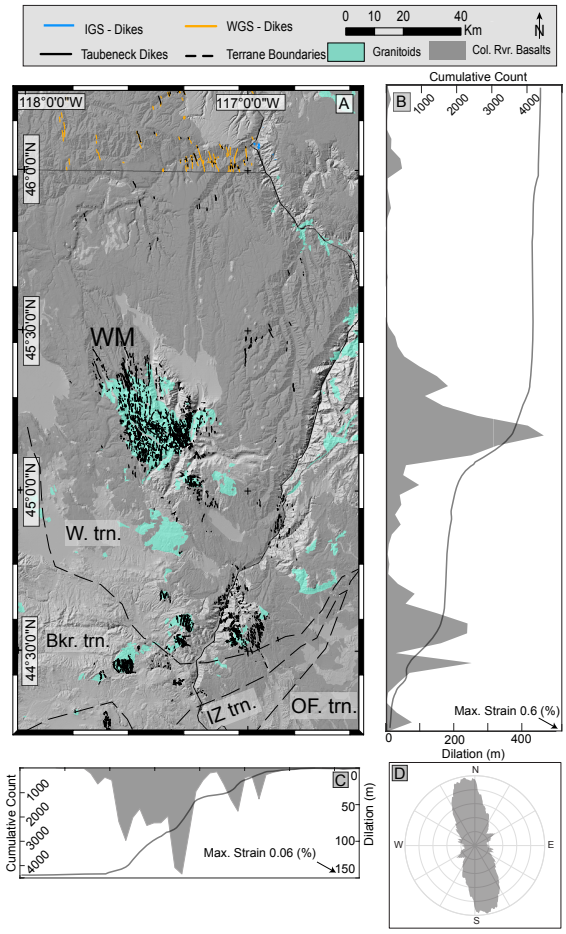

Figure 2.2. **A**. Current mapped extent of the Chief Joseph Dike Swarm, as mapped predominantly by William H. Taubeneck (n = 4279). Additional CRBG related dikes mapped by other sources are included. Dikes Mapped by the Idaho Geologic Survey, and Dikes Mapped by the Washington Geologic Survey (Blakely, Sherrod, Weaver, Wells, & Rohay, 2014; Lewis, Link, Stanford, & Long, 2012; Schuster, 2005). Major Mesozoic and Paleozoic terrane boundaries are within the dashed lines. The Wallowa terrane – W. trn.; Baker terrane – Bkr. Trn.; Izee terrane – IS trn.; Olds Ferry Terrane – OF. Trn. (Schwartz et al., 2014). Columbia River Basalt flows extracted the state geologic maps (Lewis et al., 2012; Schuster, 2005; Walker & MacLeod, 1991). **B.** The thin line is a cumulative count of dike segments across the dike swarm with increasing latitude. The opaque region is the calculation of minimum E-W dilation as a result of diking (see Methods section). Strain is calculated over a 350 km long region NS, and a 100 km wide region EW. **C.** The N-S minimum component of dilation. **D.** A moving average rose diagram of dike orientations (Munro & Blenkinsop, 2012).

rotation and intermittent volcanism to the west in the Cascades arc (V. Camp, Ross, Duncan, & Kimbrough, 2017; Wells et al., 2014)

2.3.2 Miocene Volcanism (17–6 Ma)

Volcanism in the Miocene began with the eruption of the Picture Gorge basalts at 17.23 ± 0.04 Ma (Cahoon et al., 2020), then by the Steens Basalts, starting around 16.9-16.6 Ma (Kasbohm & Schoene, 2018; Moore, Grunder, & Bohrson, 2018). There is also field and geochronologic evidence that after the eruption of the Steens Basalts a southward progression in mafic volcanism into the northern Nevada Rift began (Figure **??** V. E. Camp & Ross, 2004).

The first erupted unit of the CRBG mapped in NE Oregon is the Imnaha Basalt, erupting at ∼16.6 Ma contemporaneous with the last of the Steens eruptions to the south (Kasbohm & Schoene, 2018). This unit interfingers at its southernmost extent with the Steens Basalts (V. Camp, Reidel, et al., 2017; Hooper, Binger, & Lees, 2002). The Imnaha basalts have a volume of ∼11,000 km^3 (∼6% of total CRBG volume) and erupted from vents in eastern Oregon (V. E. Camp, 2013; Kasbohm & Schoene, 2018; S. P. Reidel & Tolan, 2013a; Taubeneck, 1970).

The next oldest sequence of flows associated with the CRBG is the Grande Ronde Basalt (GRB). The GRBs are grouped into four paleomagnetic polarities: R1, N1, R2, and N2, the last three of which erupted in ∼70,000 years, with the entire Grande Ronde erupting between ∼16.5 and ∼16.1 Ma (Kasbohm & Schoene, 2018). These flows make up 72% of the total volume of the CRBG (S. P. Reidel & Tolan, 2013a). Geochemically they are classified as mostly basaltic andesites with 52-57% silica versus 47-53% silica present in Imnaha basalts (Hooper, 2000). Radiogenic isotopes suggest potentially significant assimilation of Idaho Batholith

into the Grande Ronde basalts, a signal only weakly present in the Imnaha basalts (Wolff et al., 2008). The bulk of the dikes within the CJDS are likely associated with the GRBs (Taubeneck, 1970).

2.4 Methods

Our database includes nearly 53 years of data, digitized from the collection of William H. Taubeneck, augmented by our own data collection during 2016, 2017, and 2018. To contextualize the CJDS, we also synthesized data on other dike swarms associated with the CRBG. Those data are detailed in the Discussion section.

2.4.1 Dike Digitizing

William H Taubeneck Collection – Maps

WHT's original maps were scanned then processed through ESRI ArcMap by georeferencing each 1:24,000 USGS quadrangle onto which WHT had mapped dikes. We digitized each linear, non-linear, or curved feature marked on WHT's maps, creating a shapefile containing all potential mapped dikes. Dike orientation, length, X and Y coordinates for each dike midpoint, and midpoint elevation were then extracted from the 4279 dike segments across northeastern Oregon, southeastern Washington and west-central Idaho.

State geologic maps for Idaho, Oregon, and Washington were incorporated at this stage. The host rock was identified for each individual dike segment and recorded in the shapefile attribute table (Bond, Kauffman, Miller, & Venkatakrishnan, 1978; Huntting, Bennett, Livingston, & Moen, 1961; Walker & MacLeod, 1991). Host rock lithologies were simplified into several categories: metasedimentary units (slates and marbles); metavolcanic units (greenstones and

meta-rhyolites); granitoids (granite, tonalite, gabbro, and granodiorites); basalt (Miocene basalts or tholeiites); sedimentary (conglomerates, sandstones, and lake deposits), and andesite (andesite, and intermediate volcanic rocks).

We then cross checked each dike segment location using 1 m resolution U.S. Department of Agriculture National Agriculture Imagery Program (NAIP) aerial photography. This allowed us to remove duplicate segments; those segments that are clearly not dikes, or non-CRB dikes (older structures related to batholith intrusion in the Wallowa Mountains; Zak, Verner, Johnson, & Schwartz, 2012). These non-CRB dikes are often light colored in the field and are visible in some satellite images and aerial photography. The final dike dataset is available in the Digital Repository for M. Morriss et al. (2020) as an ArcGIS shapefile.

William H. Taubeneck — Notebooks

Notebooks contained in the WHT collection document field observations associated with the mapped dikes in our database. Measurements in the WHT notebooks include: strike (n = 1891 measurements), dip (n = 167), dike thickness (n = 3289), elevation when the observation was made (n = 3043), date of observation (June 23rd ,1953 - September 2nd, 2007), and approximate geographic location information (name of nearby peak or stream). WHT measurements of width likely represent a single locale along the length of a dike segment, so, at best, they should be treated as a "representative" width for the dike segment. WHT also included semi-quantitative descriptions of dike and host rock textures, such as vesicularity (n = 131), grain size (n = 194), inclusions (n = 117), weathering of dike (n = 37), partial melting of host rock (n = 120), and composition of dike (Grande Ronde v. Imnaha; D. A. Swanson et al., 1979). Each entry within the notebook that represented a dike was entered into an excel spreadsheet. We

quantified descriptions of dike vesicularity, inclusion density, and grain-size on a 1 to 5 rating scale for each dike. This is an interpretation of Taubeneck's notes. For example, dikes with a vesicularity of 1 contain no vesicles, while dikes with a rating of 5 correspond to "highly vesiculated" within Taubeneck's notes. This rating scheme was also applied to the presence of dike-marginal melted wall-rock, inclusions (e.g. xenoliths or other non-basalt lithologies), and dike grain size.

Inconsistencies in the data appear frequently. In particularly, location data was difficult to follow. Taubeneck rarely lists township and range or other identifying coordinates. The best geographical information provided was elevation and general named locations (e.g. east of Glacier Lake; west and southwest of Eagle Cap; on west side of Hurricane Creek). Taubeneck's system for locations on his maps (Loc. 1, 2, etc.) occasionally denoted multiple locations along a single dike, or one location for multiple dikes.

We have therefore been unable to clearly connect mapped dike segments directly with specific notebook entries. The digital database constructed from WHT's work is included as a series of files in the Digital Repository for M. Morriss et al. (2020). The supplementary files also contain a table with dike midpoints, host rock, bearing, and length (Table DR1 in M. Morriss et al. (2020)). Observations digitized from WHT's notebooks and our own original observations made at CJDS dikes are contained in Table DR2 of M. Morriss et al. (2020). Future work may provide a more robust link between these two datasets, and extend the scope of dike mapping.

2.4.2 Original Field Work

As part of an effort to check the accuracy of WHT maps to ensure any conclusions drawn from our database were robust, we have generated a new set

of data to compliment that of WHT. Our field observations and remote sensing aim to constrain relationships between fracture networks and dike orientation and the 3D geometry of dikes, both of which are poorly detailed in the WHT dataset. Although our preliminary observations do not cover the entire CJDS area, they confirm the accuracy of the WHT data and contribute to a cohesive picture of multiscale structure of the CJDS described in more detail below.

Targeted field work took place in the Wallowa Mountains and a few limited areas to the south during the summers of 2016, 2017, and 2018. We found that WHT maps are, for the most part, easily verified in the field, and some also in remote sensing imagery. We suspect that WHT documented only the largest dikes, as many examples of smaller dikes seen in the field are not included in the WHT materials. We view extending the mapping and characterization of dikes as a promising direction for future work. The nature of dike tips and differences in dike-host-rock interaction are not directly addressed by this work.

We measured 768 joints in granitoid host-rocks in the central Wallowas. Care was taken to measure joints greater than 10 m from any dike margin in an effort to avoid joints induced by dike emplacement (Hoek, 1991; Rubin, 1995). Dike width was measured with a measuring tape. Dike orientations were often difficult to measure on an outcrop scale due to the irregular nature of the dike host-rock contact. To better constrain dike strike and dip in the field, the orientation of cooling joints within the dike that were normal to the dike margin was measured. The poles to these joint measurements were plotted on a stereonet and a best-fitting plane fit through those points, using the Stereonet software (Cardozo & Allmendinger, 2013). This best-fitting plane provides a measure of dike orientation. This method was only applied to dikes that did not contain clear evidence of reintrusion (e.g. selvage zones; S. P. Reidel et al., 2013) and had margin-normal

columnar joints. The orientations of 40 dikes measured with this method are combined with noted strike-and-dip data from the WHT collection and orientations gathered through remote sensing.

2.4.3 Remote Sensing

Several remote sensing tools were used to provide data on dikes in areas that we did not visit, in addition to their use in verifying WHT mapped locations. We documented examples of: 1) cross-cutting relationships; 2) dike strike and dip; 3) whether or not a dike was visibly segmented (e.g., en echelon behavior; Hoek, 1991). Cross-cutting relationships between different dikes were observed in both Google Earth and 1 m resolution NAIP imagery.

Dike strike and dip were measured using 1 m horizontal resolution NAIP imagery in concert with Oregon Department of Gem and Mineral Resource LIDAR (where available) and the 10 m resolution National Elevation Dataset. A three (or more) point planar-fit was performed using the LayerTools extension to ArcGIS (Kneissl, Van Gasselt, Wendt, Gross, & Neukum, 2011). Dike segmentation was measured using Google Earth.

2.4.4 Structural Data Analysis

CJDS structures are scale-dependent. On the largest scales (>100 km), we compute statistics of the entire dike segment dataset and fit distributions of dike segment average widths and lengths to commonly applied distributions to assess the degree to which the CJDS is comparable to other dike swarms (Krumbholz et al., 2014). To calculate the dike density, we used the line-density tool in ArcGIS, with a kernel window of 5 km (Silverman, 1986). The dike line density measured in km of dike per square km can be converted into dike density, assuming an average

dike segment length (0.4 km). We calculated mean dike density by excluding areas with very low (0.1 km km^{-2}) to zero dike density, to isolate areas in which dike segments are exposed.

On smaller scales (1-100 km), we identify clusters of similarly-oriented dike segments (within 20° bins) through a nearest neighbor analysis, comparing nearest neighbor distances of segment midpoints to mean and maximum segment length derived from the whole dataset to demonstrate closeness of nearby segments 2.3. While not a true clustering analysis, this procedure effectively highlights sub-swarm patterning of dike segments as a function of orientation, which can be compared to dike density 2.4. At the smallest scale ($\leq$ segment length), we examine CJDS structures in outcrop.

2.4.5 Geochemical and Petrological Analysis

W.H. Taubeneck sent numerous dike samples to the GeoAnalytical Lab at Washington State University for major and trace element analysis by wavelength dispersive X-ray fluorescence (XRF). We powdered, refused, reanalyzed a number of original fused rock – Li tetraborate discs ("beads" hereafter) from the WSU bead archive on a ThermoARL Advant XP sequential XRF spectrometer using the methods of JD. Johnson, Hooper, and Conrey (1999) (see Table DR3, M. Morriss et al. (2020)).

Unfortunately, most of WHT's samples cannot be map-located, so we cannot explore relations between dike chemistry and physical characteristics such as geometry or orientation. Instead, we compare the chemical data to those of the CRBG as a whole, and assign samples to CRBG formations on a preliminary basis.

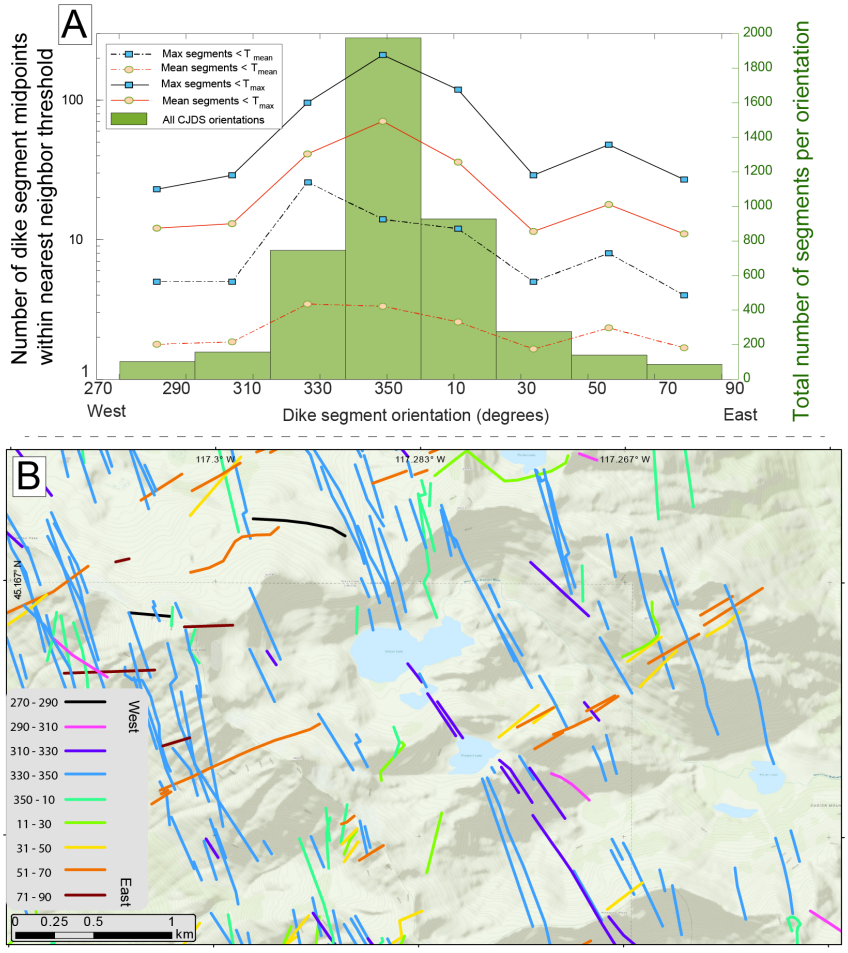

Figure 2.3. **A.** Results of nearest-neighbor spatial analysis of dike segment midpoints. Segments are binned in 20° increments then the number of nearby segment midpoints closer than either the mean dike length (0.4 km) or maximum dike length (4.3 km). Dashed lines refer to the average number of nearest neighbor distances closer than a particular threshold. **B.** Dikes in central Wallowa Mountains colored in 20° bins. This illustrates the predominance of many dike segments of similar orientations in close proximity to one another.

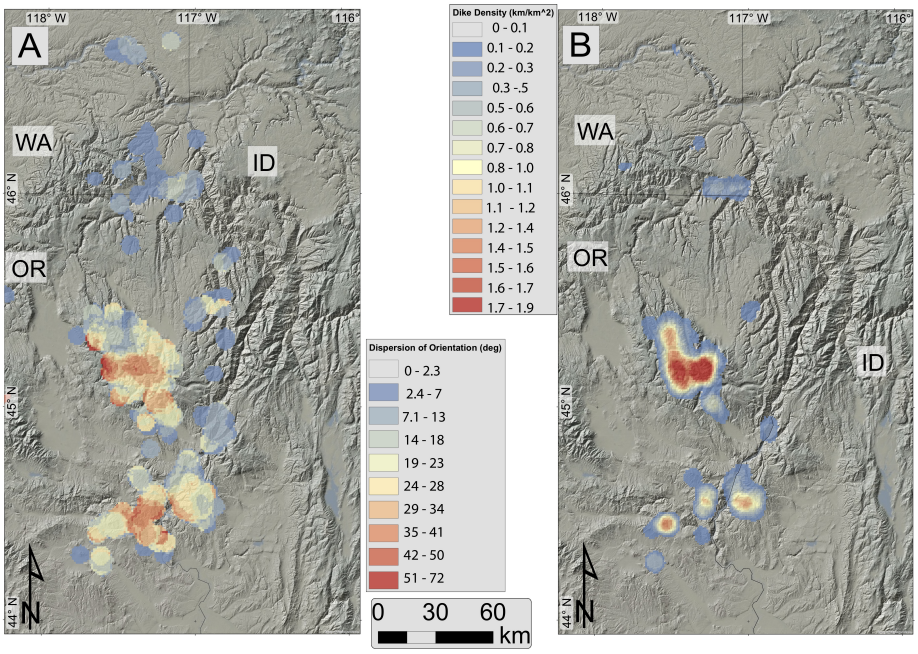

Figure 2.4. **A.** Dike dispersion (standard deviation) within 1 km radius bins across the CJDS. **B.** Dike line-density across the swarm measure in 5 km kernel, and corresponding dike density per square kilometer, assuming mean dike length of 0.4 km.

Mass Balance Calculations

The GRB lavas display remarkable homogeneity in some incompatible trace elements, in particular those that are least affected by the crustal contamination that accompanied crystallization-differentiation, such as Nb and Zr; relative 1 standard deviation variations are ∼10% (data of Wolff et al., 2008). Niobium is effectively incompatible in the crystallizing assemblage of Imnaha and GRB (plagioclase + pyroxene ± olivine) and is used as a fractionation monitor. It is also depleted in rocks of the Atlanta Peraluminous Suite of the Idaho batholith (R. M. Gaschnig, Vervoort, Lewis, & Tikoff, 2011) used by Wolff and Ramos (2013) as contaminants in their energy-constrained assimilation-fractional crystallization simulations (Bohrson & Spera, 2003) of the evolution from Imnaha to GRB compositions. Hence, fractionation can be tracked using Nb and assimilation is ignored.

The Imnaha lavas are themselves somewhat evolved at 4 – 7% MgO. Restoration of average parental Imnaha Basalt to 8% MgO, taken as the composition of basaltic liquid arriving in the crustal storage system from the mantle, using "reverse fractionation" gives a Nb content of 5.5 ppm. Reverse fractionation was done using MELTS (Ghiorso & Sack, 1995); average Imnaha Basalt composition was run at 10 °C below its liquidus at 1 GPa, f(O2) = QFM, and the resultant assemblage (Ca-cpx) added back into the liquid in 10% increments until 8% MgO was achieved at ∼22% Ca-cpx addition. At 0.5 GPa the MgO content of the pyroxene is little different but plagioclase joins it on the liquidus, hence the 1 GPa estimate is more conservative in that less crystal addition is needed to achieve 8% MgO so the calculated Nb in the starting magma is maximized. This minimizes the volume of cumulates calculated below.

2.5 Results

2.5.1 Structural Relations within the Chief Joseph Dike Swarm

Data on dike swarm structures are presented below at telescoping scales from the order of the entire dike swarm (10s-100s km) to single dike segment scale (1s-100s m).

2.5.2 Swarm Scale (10s - 100s km)

Length

Dikes mapped at 1:24,000 scale by WHT within the CJDS are often dismembered by valleys, buried by younger deposits (fluvial or glacial), or obscured by active hillslope processes. As a result, our dataset contains well constrained dike segments but not total dike lengths.

Individual dike segments within the CJDS range in length from 30 m to 4.3 km. The distribution of dike segment lengths is well approximated as a log-normal distribution (Figure 2.5B). The median length of a dike segment is 325 m. The log-normal mean and variance is 408 ± 8 m (RMSE of $1.3*10^{-6}$), consistent across host-rock type (Figure A.2). The median length for dikes hosted in granitoid rocks (n = 2291) is 363 m; for basalt 348 m (n = 1003); for metasedimentary rocks 243 m (n = 638), and for metavolcanic rocks 226 m (n = 346; Figure A.2). At the outcrop scale, there are some shorter dikes (<10 m in length), that branch off from a main dike. These probably are a small portion of the observed dikes within the swarm, but this is not quantified further here.

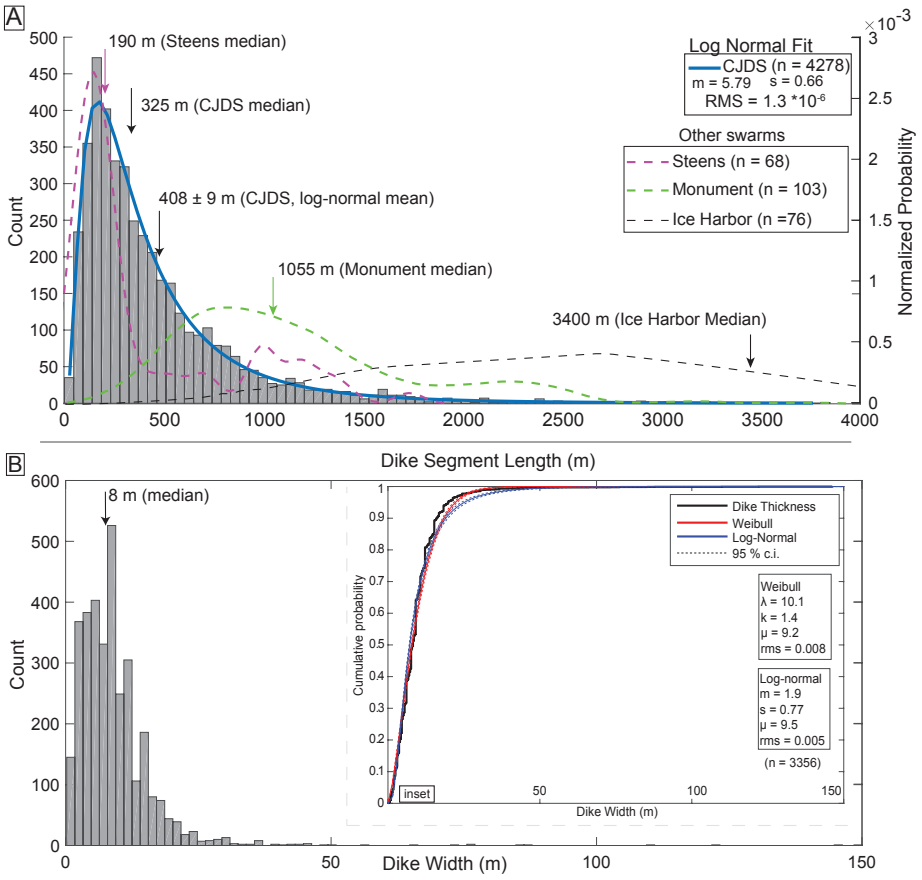

Figure 2.5. A. CJDS dike segment average dike width with median of 8 m. Inset shows cumulative distribution of dike width, with Weibull and Log-normal distribution fits. The log-normal distribution provides the best fit. The tail (25 m) suggests that both the Weibull and Log-normal distributions overestimate the probability of dikes of this width within the CJDS. The fitting parameters for these two distributions are included in the inset; κ is the shape parameter;λ is the scale parameter, and μ is the location parameter. m is the scale parameter; s is the standard deviation or shape parameter, and μ is the location parameter. RMS is the root-mean squared error **B.** CJDS dike segment length distribution. A log-normal fit provided the best fit for this distribution. The length distributions of the other swarms associated with the CRBG are also shown.

Width

Dike width, as measured in the field, may not correspond to the active width of the dike during emplacement, which depends on dynamic pressure of magma flow. Measured width is usually assumed to correspond with one intrusion event, although dikes exhibiting evidence of multiple injections (from either multiple columnar joint sets, or glassy internal contacts or selvage zones) are not uncommon within the CJDS (Taubeneck, 1970).

Widths vary somewhat along strike of many dike segments within the CJDS, and appear to be somewhat depth dependent. Such variation is seen in other dike swarms and is expected near the dike tip (Babiker & Gudmundsson, 2004; R. J. H. Jolly & Sanderson, 1995; Paquet, Dauteuil, Hallot, & Moreau, 2007). In Figure 2.5A, we plot all Taubeneck dike widths (see Appendix A). The median dike width across the CJDS is 8 m; comparable to other LIPs but much larger than typical dikes widths in other settings (Babiker & Gudmundsson, 2004; Krumbholz et al., 2014). The minimum dike width from WHT notebooks is 0.2 m, although we have observed thinner dikes that are not included in the WHT dataset. The maximum dike width from WHT is 146.3 m; however, no dike was observed during our field work approaching this size. The larger dikes are likely composite structures, recording multiple injections and selvage zones (S. P. Reidel & Tolan, 2013a; Taubeneck, 1970).

The distribution of dike widths has been proposed to inform processes associated with emplacement (i.e. 1. magmatic overpressure – Babiker and Gudmundsson (2004); 2. length of time for flow within the dike – Parfitt and Wilson (1994); 3. depth within the magmatic system – P. T. Delaney and Gartner (1997); Woods, Bokhove, de Boer, and Hill (2006); and 4. host rock rheology and elastic moduli – L. Karlstrom, Paterson, and Jellinek (2017); Krumbholz et

al. (2014)). A Weibull and a log-normal distribution both fit the swarm-scale distribution of dike widths well (Figure 2.5A inset). This has been found in other settings (P. T. Delaney & Gartner, 1997; R. J. H. Jolly & Sanderson, 1995; Krumbholz et al., 2014).

Dike Density and Orientation

The mean dike line density excluding the lowest values (<0.1) is 0.5 ± 0.37 km of dike per square km. This corresponds to a mean dike density of ∼ 1.2 ± 0.9 dikes per square km. Maxima in dike density occur in the Wallowa Mountains and several of the intrusions to the south, reaching 1.5 – 1.9 km of dike per square kilometer (Figure 2.4B). Assuming an average dike length of 0.4 km, this maximum dike density results in 5 dike segments per square kilometer. Dike density is also greatest in areas that also have the greatest variability in dike orientation (Figure 2.4A).

There are several identifiable trends in dike orientation across the CJDS. The dominant trend is NNW (median bearing of -352°; Figure 2.2D). This trend is generally consistent across all lithologies in which dikes are observed (Figure A.1). The median bearing for dikes in granitoids is 351°; metasedimentary rocks 355°; metavolcanic rocks 351°, and basalt 351° (Figure A.1). The dominance of this orientation makes it difficult to perceive other trends that appear visible in map-view (2.2A; Plate 1).

A moving average rose diagram with a 6° window size (Figure 2.2D) suggests smaller, yet still significant, trends within the dike swarm. This is confirmed by nearest neighbor analysis (Fig 2.3A), which reveals that segments at all orientations are commonly observed with similarly oriented segments nearby. Clusters of dike segments within the primary dike orientation (NNW) dominate:

on average, segments in within 10 degrees of N-S exhibit ∼70 nearby segment midpoints (maximum of 211) closer the CJDS maximum segment length of 4.3 km (2.3A). In contrast, dikes within 10 degrees of EW have on average 11 segments with midpoints this far away (maximum 27). Remarkably, this trend still holds when the nearest neighbor threshold is reduced to 0.4 km (the mean CJDS segment length), demonstrating that some areas of the CJDS exhibit extremely dense clusters of segments.

Figure 2.3B shows one such region in the central Wallowa Mountains, that exhibits dense and overlapping dike segment clusters of different orientations. Dikes are colored by their orientation broken into 20° angular bins. The observation that dike segments are often proximal to other segments with a similar orientation suggests that they may in some cases reflect a common deeper structure, broken up in map view by topography or covered by younger deposits.

Dip

Dike dips were collected from the WHT database (n = 112). These data were combined with original field measurements (n = 38) and remote sensing measurements (n = 172). There is a large range of dips. The lowest angle intrusion (sill) reported dips at 4° (from WHT). The steepest dikes are vertical (Figure 2.6). There is significant variance within dike dips but most are sub-vertical; the overall distribution of dips is negatively skewed with a median dip of 65° (Figure 2.6). Dikes also appear to dip at different orientations depending on the host rock. Those hosted by granitoid rocks appear steeper, with a median dip of 68° . Dikes hosted in metasedimentary rocks are less steeply dipping, with a median of 55°. Of the total dike dip measurements, data were available to classify 174 dikes as east-

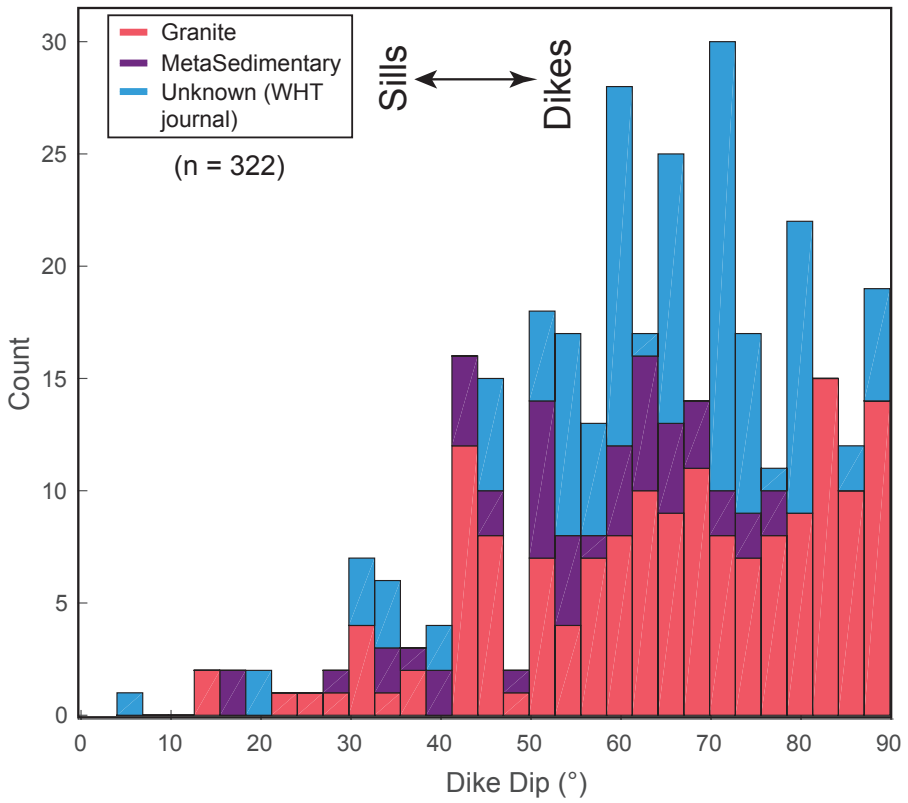

Figure 2.6. Dike dip subdivided by rock-type. Dike dips were measured by WHT; through remote sensing, and by fieldwork conducted as part of this study. Median values of dip are listed for metasedimentary hosted dikes (55°), granitoid hosted dikes (68°), and the overall median dip of dikes in the CJDS (65°). This plot highlights the paucity of sills present in the CJDS. Most intrusions measured as part of this study are high angle (>45°).

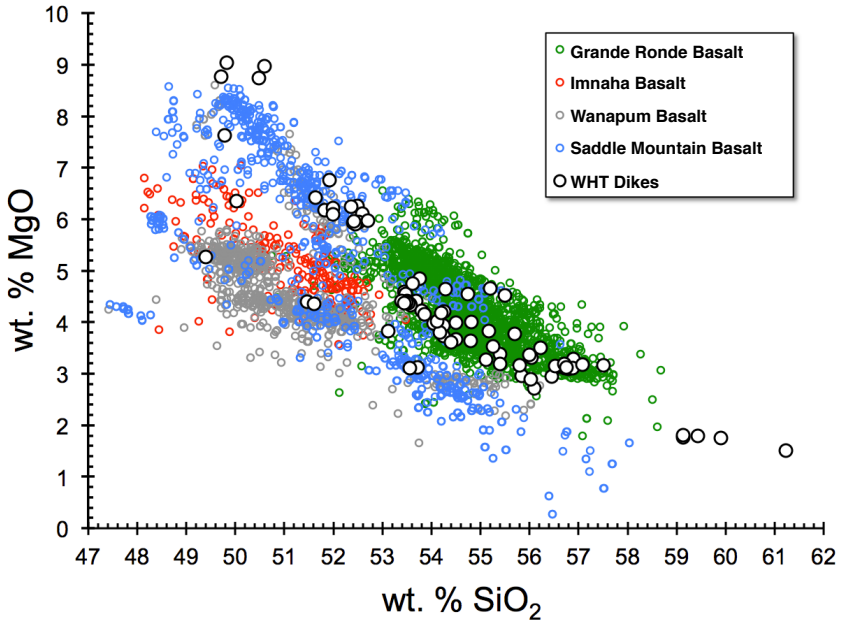

Figure 2.7. Geochemical distribution of weight percent SiO_2 vs weight percent MgO for all the formations within the CRBG associated with the CJDS. Closed white circles represent reanalyzed WHT samples collected from CJDS dikes. The majority of dike samples fall within the GRB and Saddle Mountain basalt fields; however, there are four dike samples with greater MgO content than any other known CRBG flows. Several other samples are higher in SiO_2 than any known CRBG flow. These discrepancies indicate potential for geochemical variability within the dikes that is not seen in the flows.

dipping, and 128 dikes as west-dipping. Only 17% of all intrusions measured within the CJDS (n = 322) have dip less than 45° (Figure 2.6).

Geochemistry

The WHT samples span beyond the distribution that generally defines the range of CRBG lavas (Figure 2.7), but most samples fall within that range, so in principle can be assigned to a unit using the chemical correlation approach of Hooper (2000). Of 93 samples total, most have affinities with Grande Ronde Basalt (Figure 2.7). There is some overlap between Grande Ronde and Imnaha Basalt in the 52 – 53% SiO_2 range (Wolff & Ramos, 2013; Wolff et al., 2008) with

current methods. Five andesites are more silicic than any known CRBG lava (59.1 – 61.2 % SiO_2), but have incompatible elements consistently elevated by ∼25% over typical Grande Ronde lavas (see Appendix A), hence could plausibly be related differentiates.

Of uncertain affinity is a group of four samples (WT28, -79, -847, -913) that are more magnesian (∼9% MgO) than any previously analyzed CRB samples with the exception of a few Steens Basalt flows (D. Johnson et al., 1999; Moore et al., 2018) and Monument dikes (Bailey, 1989). No lava that erupted from the CJDS with such high MgO contents has been found, although the basalt of Robinette Mountain (Eckler Mountain Member, Wanapum Basalt) is generally similar(see Appendix A and Hooper, 2000).

Geochemical Mass Balance

The average Nb content of the GRB is 11.4 ppm (data from Wolff et al., 2008), corresponding to 52% crystallization of a parental Imnaha Basalt. Using volume-weighted average compositions of each of the four magnetic polarity divisions of the GRB (S. P. Reidel & Tolan, 2013a) gives the same result. Without taking the volumetric contribution of crustal contamination into account, this yields a volume of gabbro added to the crust of ∼160,000 km^3. Wolff and Ramos (2013) estimate the recycled crustal contribution to the GRB at 9 – 59%, yielding net cumulate additions to the crust of 147,000 km^3 and 66,000 km^3 gabbro respectively, with a mean of 107,000 km^3. This volume has not been compared to estimates of the intrusive volume of the CRBG. Herein, we endeavor to do so.

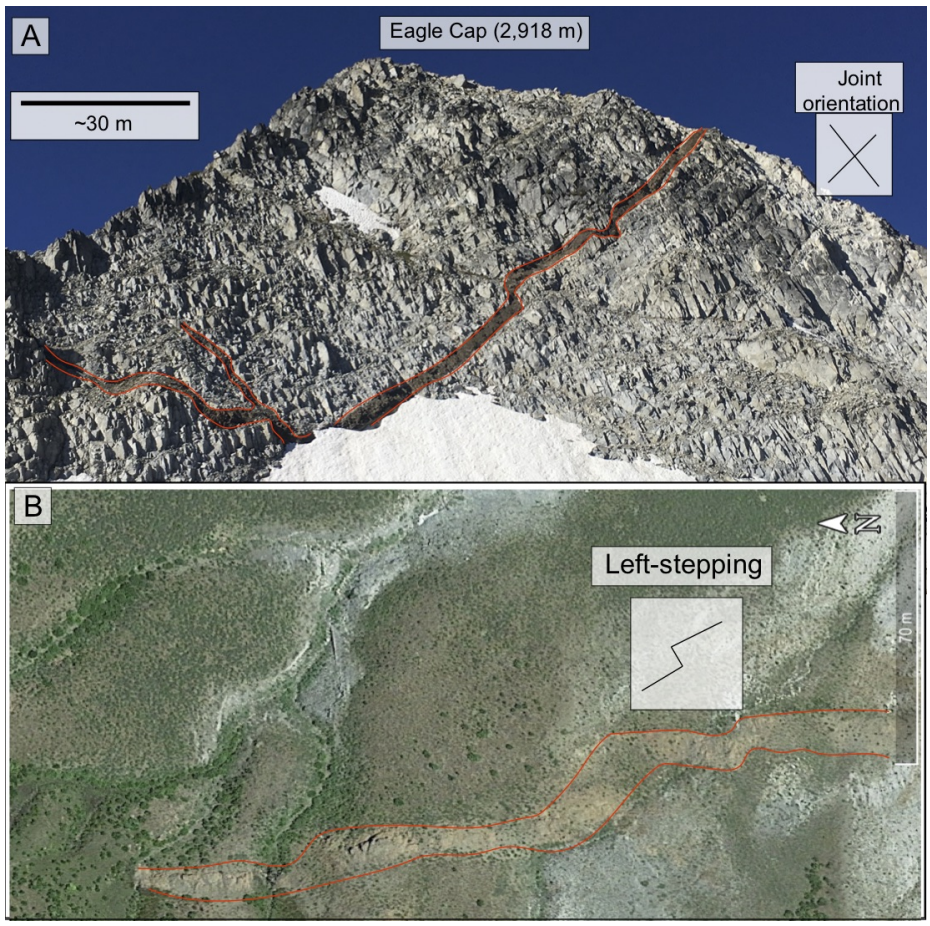

Figure 2.8. Dikes within the CJDS display non-planar geometry on an outcrop scale. **A.** The north face of Eagle Cap. **B.** is an example from Google Earth imagery of segmented dikes left-stepping along strike. Left and right steps were tabulated and did not show trends across the swarm (Figure A.3).

2.5.3 Sub-swarm Scale (1-10s km)

Segmentation and En Echelon Behavior

Dike segmentation has a variety of origins. It may occur during emplacement due to rotations of remote stresses along the dike propagation path, called en-echelon segmentation (Figure 2.8B; Pollard, Segall, & Delaney, 1982). Dikes may also exhibit branching or break-out structures that segment observed outcrops (Figure 2.8A Hoek, 1991). Inelastic deformation either syn- or post-emplacement may also segment dikes (Mathieu, van Wyk de Vries, Holohan, & Troll, 2008).

Dikes within the CJDS exhibit multiple apparent segmentation styles. There are many segments of dikes that are approximately linear over their entire length. However, a small percentage ($< 5\%$) of all dikes that we observed via satellite imagery contain segments that appear en echelon or "zig-zag" as classified by Hoek (1991), see our Figure 2.8B. There is no clear preference between left-stepping (n = 91) or right-stepping (n = 104) segments, over the dikes that we have analyzed (Figure A.3).

Dike Cross-Cutting Relations

A number of the CJDS dikes were continuously active for an extended period of time as they fed surface CRBG eruptions (perhaps several years e.g. L. Karlstrom, Murray, & Reiners, 2019; H. Petcovic & Grunder, 2003; H. L. Petcovic & Dufek, 2005; D. A. Swanson, Wright, & Helz, 1975; Thordarson & Self, 2003). Many other dikes were discontinuously active and reoccupied by multiple magma injection events, as seen by internal selvage zones or multiple internal chilled margins (S. P. Reidel et al., 2013; Taubeneck, 1970). We use cross-cutting relationships to document the relative progression of diking within the

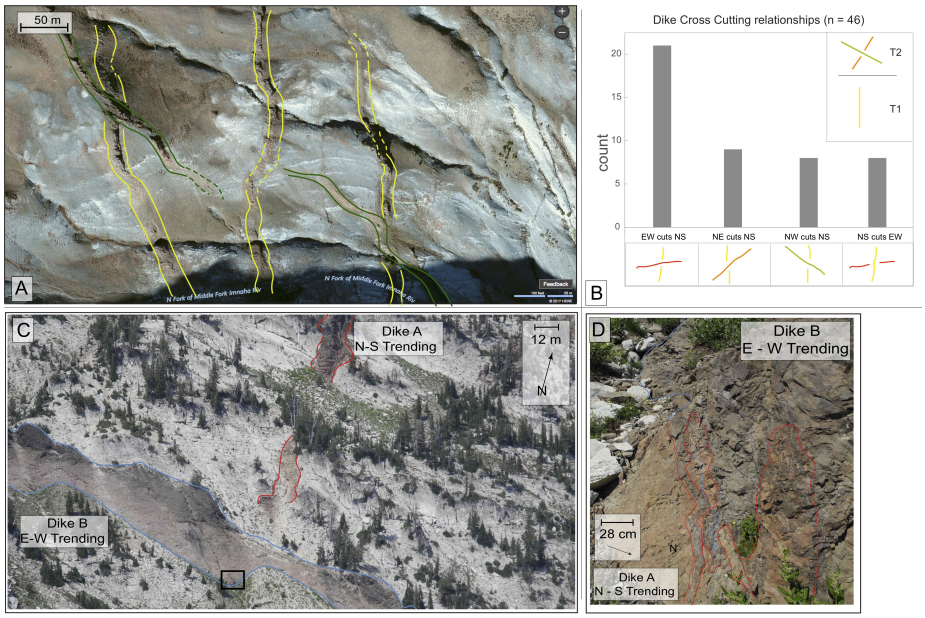

Figure 2.9. A. A NAIP image of cross-cutting dikes in the eastern Wallowa Mountains. **B.** Histogram of dike cross-cutting relationships. Relative timing of major trends is on the right. Time 1: intrusion of north-south oriented dikes. Time 2: either be the intrusion of the NE,NW, and some NS trending dikes. **C.** A field example of dike cross-cutting. The EW trending dike is lighter in color than the NNW trending dike. Small black box showing dike-dike contact is shown in panel D. **D.** Close up of cross-cutting outcrop, showing intrusion of an EW dike into a NS oriented dike.

CJDS. We measured 46 cross-cutting relationships between dikes exposed in the central Wallowa Mountains and Cornucopia region through a combination of field and remote-sensing observations to generate an aerially extensive dataset (Figure 2.9; Table 2.1). Observed cross-cutting relationships we observe suggest that the NNW oriented dike segments are the oldest. For the region analyzed, cross-cutting relations do not constrain the relative ages of subsequent diking, which may have been oriented NE-SW, NW-SE, E-W, or N-S.

Table 2.1. Mapped exposures of dikes crosscutting each other classified by type of cross-cutting relationship. We also note how observation was made.

Type	Latitude	Longitude	Type of Observation
EW cuts NS	45.198724°	-117.219498°	Satellite and Aerial Imagery
EW cuts NS	45.199344°	-117.218924°	Satellite and Aerial Imagery
EW cuts NS	45.046652°	-117.235198°	Satellite and Aerial Imagery
EW cuts NS	45.045741	-117.222663	Satellite and Aerial Imagery
EW cuts NS	45.033965	-117.226419	Satellite and Aerial Imagery
EW cuts NS	45.2020763	-117.31565	Field
EW cuts NS	45.177956	-117.291911	Field
EW cuts NS	45.141485	-117.291703	Satellite and Aerial Imagery
EW cuts NS	45.141564	-117.297258	Satellite and Aerial Imagery
EW Cuts NS	45.141271	-117.297795	Satellite and Aerial Imagery
EW Cuts NS	45.162112	-117.263631	Satellite and Aerial Imagery
EW cuts NS	45.138483	-117.232983	Satellite and Aerial Imagery
EW cuts NS	45.3138217	-117.235246	Satellite and Aerial Imagery
EW cuts NS	45.113094	-117.196305	Satellite and Aerial Imagery
EW cuts NS	45.092135	-117.292599	Satellite and Aerial Imagery
EW Cuts NS	45.125046	-117.459861	Satellite and Aerial Imagery
EW Cuts NS	45.137733	-117.236766	Satellite and Aerial Imagery
EW Cuts NS	45.13748	-117.235178	Satellite and Aerial Imagery
EW Cuts NS	45.082959	-117.374017	Satellite and Aerial Imagery
EW Cuts NS	45.084943	-117.285092	Satellite and Aerial Imagery
EW Cuts NS	44.485432	-117.555702	Satellite and Aerial Imagery
NE cuts NS	45.117789	-117.22161	Satellite and Aerial Imagery
NE cuts NS	44.596689	-117.253984	Satellite and Aerial Imagery
NE cuts NS	44.588061	-117.259345	Satellite and Aerial Imagery
NE cuts NS	44.460285	-117.541461	Satellite and Aerial Imagery
NE cuts NS	44.45582	-117.544316	Satellite and Aerial Imagery
NE cuts NS	45.192878	-117.3091	Field
NE cuts NS	45.158088	-117.359195	Satellite and Aerial Imagery
NE cuts NS	45.241053	-117.45375	Satellite and Aerial Imagery
NE cuts NS	45.115052	-117.334547	Satellite and Aerial Imagery
NW cuts NS	44.533469	-117.2957	Satellite and Aerial Imagery
NW cuts NS	45.162669	-117.38398	Satellite and Aerial Imagery
NW cuts NS	45.15047	-117.222432	Satellite and Aerial Imagery
NW cuts NS	45.152575	-117.225893	Satellite and Aerial Imagery
NW cuts NS	45.122223	-117.213815	Satellite and Aerial Imagery
NW cuts NS	45.092594	-117.289506	Satellite and Aerial Imagery
NW Cuts NE	45.144422	-117.250163	Satellite and Aerial Imagery
NW cuts NS	45.159611	-117.324663	Satellite and Aerial Imagery
NS cuts EW	45.177275	-117.515627	Satellite and Aerial Imagery
NS cuts EW	45.177275	-117.515627	Satellite and Aerial Imagery
NS cuts EW	45.155473	-117.210178	Satellite and Aerial Imagery
NS cuts EW	45.154747	-117.210433	Satellite and Aerial Imagery
NS cuts EW	45.117466	-117.307061	Satellite and Aerial Imagery
NS cuts EW	44.481539	-117.548842	Satellite and Aerial Imagery
NS cuts EW	44.476782	-117.539271	Satellite and Aerial Imagery
NS cuts EW	44.601113	-117.261489	Satellite and Aerial Imagery

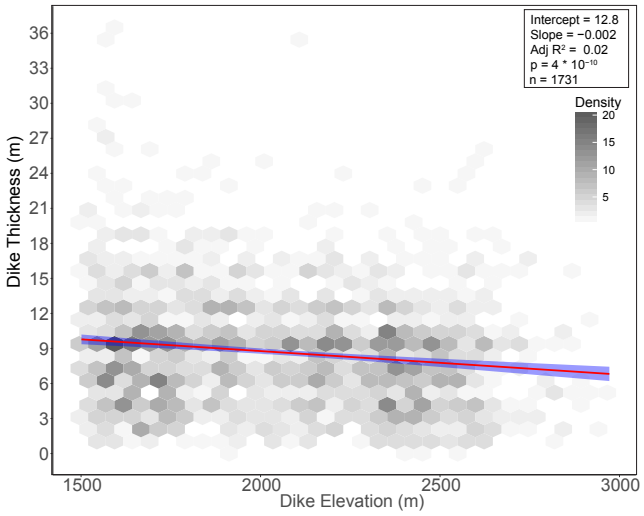

Figure 2.10. Density plot of dike width vs elevation, from 1731 WHT observations. The red line is a linear fitting model to that data and the blue envelope is the standard error to that model fit. The slope of the linear-fitting line is -0.002 with a y-intercept of 12.8. The adjusted R-squared calculated for this fit is 0.02, but the p-value for the fit still holds significance $4*10^{-10}$. This line shows that dikes thin toward higher elevations or shallower paleodepths

Width Variations

The WHT notebooks contain 3113 entries with dike elevation and dike thickness noted (see Appendix A). Of this dataset, 1731 measurements occur above 1500 m. The bulk of the topography in NE OR above 1500 m is exposed in the Wallowa Mountains, which are known to have uplifted post-CRBG and provide a depth-section through the magmatic plumbing system (Hales, Abt, Humphreys, & Roering, 2005; Schoettle-Greene & Duvall, 2016). There are Imnaha basalt flows atop ∼3000 m peaks with ∼1500 m of relief below these summits (Hales et al., 2005). So, while we cannot robustly identify the geographical location of WHT width measurements, we can test a relationship between dike elevation (as a proxy for paleodepth) and thickness in the Wallowas.

A linear regression through available data on dike elevation suggests that dikes thin toward shallower paleo-depths in the magmatic system (regression slope

of -0.002; Figure 2.10). The adjusted R-square reveals a poor fit between elevation and dike thickness (Adj. R2 = 0.02 explains only 2% of the variance in dike width; Zar, 2010). However, a P-value for this fit indicates the slope has significance (P-value = $4*10^{-10}$; Fisher, 1992; Zar, 2010).

2.5.4 Dike Scale (1s - 100s m)

Dike Interaction with Joints

Taubeneck (1970) hypothesized that dikes within the CJDS interact with and perhaps follow pre-existing host-rock joints. Dikes in other areas have been observed both to correlate with host rock joints (e.g. P. T. Delaney & Gartner, 1997; R. J. H. Jolly & Sanderson, 1995), or propagate without regard for host-rock joints (e.g. P. Delaney, Pollard, Ziony, & McKee, 1986). To further evaluate the importance of pre-existing fractures in the CJDS, the orientations of 251 joints were measured in the central Wallowa Mountains. Some dikes hosted within granitoid rocks appear to have some relationship with the pre-existing host-rock fractures on a <10-100 m scale (Figure 2.8A). Either the dikes are following and exploiting these pre-existing fractures (e.g. P. T. Delaney & Gartner, 1997), or the fractures are forming as a result of diking (P. Delaney et al., 1986).

These joint orientations are compared to the orientation of 185 dike segments exposed in the same area (Figure 2.11). There is an observed correlation between the 340° dike orientation and joints with a similar orientation, and the 60 – 80° oriented joints correspond with the 60° oriented dikes (Fig 2.11B). This observation is consistent with Taubeneck (1990), suggesting that some dikes interact with host-rock joints – at least locally.

As these joints were observed >10 m from dike margins, this indicates that dikes were not forming the joints but likely intruding pre-existing fractures. It

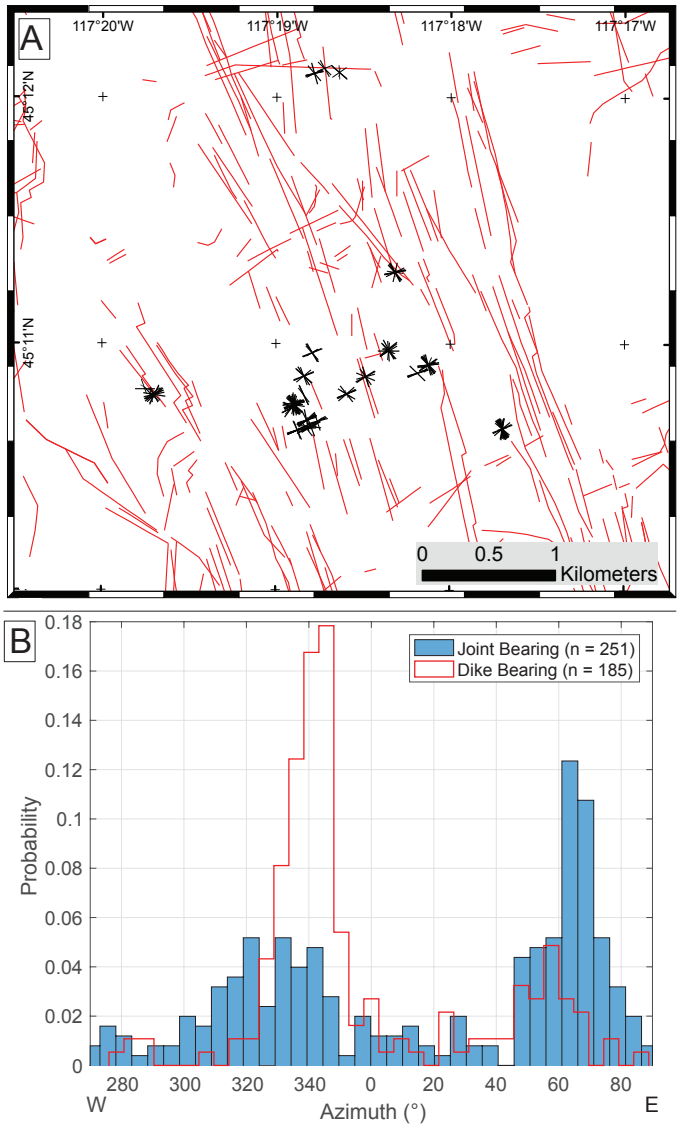

Figure 2.11. A. Joint measurement locations in the central Wallowa Mountains. Joints are small black lines oriented along the strike direction of the joint plane measured. Red lines represent dikes from the WHT database. **B.** A histogram of dike orientations (in red) and joint orientations (in blue) from the area shown in 1aA. Dike orientations correlate with joint orientations.

is rare to directly observe dike material intruding host rock joints in the CJDS (both in WHT notes and our observations). The dike exposed in the north face of Eagle Cap Peak appears to be an exception with a break-out segment that follows the orientation of host-rock fractures (Figure 2.8A). However, dikes that do not follow fractures also occasionally occur (Figure 2.11B), such as flame-like fracture sets suggestive of hydrofracture (see an example from the Cornucopia region of the Wallowas in Figure A.5). At a larger 1-10s of km scale, CJDS dike segments and segment clusters cut across fractures, host-rock changes, and even crustal boundaries between accreted terranes (Figure 2.2A) and still appear linear.

2.6 Discussion

The WHT database and adjoining data compiled here provide a detailed snapshot of the shallow CRBG plumbing system, a cross section through a massive continental dike swarm that is unique in preservation, and exposure. Here, we synthesize these data to generate a magma-tectonic framework for understanding the CJDS. In keeping with the structure of the Results section, we move progressively inward from province to outcrop scale. We first compare the CJDS to other mapped dikes within the CRBG, then discuss swarm-scale trends in segment geometry. We estimate the total intrusive volume of the CJDS and discuss implications for crustal magma reservoirs associated with the CRBG. Dike swarm structures are used to infer changes through time of the principal stresses in the shallow crust, regional dilation associated with dike emplacement, and possible swarm-scale dike thinning towards the surface. Finally, we connect segment geometry with simple models for magma flow to argue that most observed CJDS dikes were not feeders to surface flows.

2.6.1 Regional structure of the CJDS and magma-tectonic interaction

Other CRBG dike Swarms

While the CJDS is the largest dike swarm in both aerial extent and number of dike segments, three other CRBG swarms that have so far been identified throughout eastern OR, southeast WA, and west-central ID: the dikes which erupted the Steens basalts; the Monument dike sub-swarm which erupted the Picture Gorge Basalts, and the Ice Harbor dike sub-swarm which fed the Ice Harbor member of the Saddle Mountain Basalts (Blakely et al., 2014; V. Camp, Reidel, et al., 2017; Fruchter & Baldwin, 1975; Kasbohm & Schoene, 2018; S. P. Reidel et al., 2013). We have compiled a map of all known CRBG dikes here to contextualize the CJDS, and detail below where these data are sourced from (see Appendix A). We also created a simplified map of the dikes related to the CRBG, for use in plotting an accurate representation of dike locations,by removing excess vertices along dike segments and randomly down-sampling the population of dikes >1 km in length (see Plate 2 and 3 in M. Morriss et al. (2020)).

The Steens Basalt dikes are exposed on the eastern flank of Steens Mountain. We mapped 69 basaltic dikes using Google Earth Imagery. These dikes are highlighted in Plate 1 (M. Morriss et al., 2020)and are available as a shapefile in the Supplementary Material or M. Morriss et al. (2020). We also incorporated dikes from the Picture Gorge Basalts (Monument dike sub-swarm) exposed in central Oregon. These dikes were mapped originally by Brown and Thayer (1966) and Wallace and Calkins (1956), and then digitized by Cahoon et al. (2020). The Monument dikes are also available as a shapefile in the Supplementary Material, and plotted in Plate

The youngest set of dikes mapped as part of the CRBG magmatic event are those inferred to be from the Ice Harbor flows (8.8–8.5 Ma; Hutter, 1997; Mann

& Meyer, 1993; S. P. Reidel et al., 2013). There are some limited exposures of Ice Harbor dike sub-swarm in the Pasco Area (Figure 2.1; Plate 1 Hutter, 1997), but for the most part, these ∼130 dike segments were imaged using high-resolution aeromagnetic data (Plate 1 Blakely et al., 2014). We digitized the inferred dike positions and integrated this dataset into our collection of CRB related intrusions. These data are available in a shapefile within the Digital Repository for this document and visible in Plate 1. The Ice Harbor Dikes are the only features within this dataset that have an inferred position; all other dikes are constrained by outcroppings.

Length distributions of these other dike sub-swarms provide context for the CJDS. Steens dike segments have a median length of 189 m, with a maximum length of 1.7 km and a minimum length of 26 m. Monument dike segments have a median length of 1055 m, with a maximum length of 3.8 km and a minimum length of 260 m. Ice Harbor dike segments have a median length of ∼3400 m, with a maximum length of 22 km and a minimum length of 593 m (Figures 2.5B, A.4). That the Ice Harbor dikes are significantly longer may be explained by their observation geophysically. They have not been dissected by topography or obscured beneath younger deposits as is the case with the other dike segments in the CRBG. In fact, it might be appropriate to consider these dikes as a model for the "primary" CRBG dike segment length distribution before erosional dissection and sedimentary cover. We note that these dikes are from the Ice Harbor Member which is relatively small in volume compared to other CRBG formations (75 km^3 S. P. Reidel et al., 2013).

Our database across thousands of dike segments, transgressing different episodes of the CRBG event also allows for a regional assessment of dike orientation (Plate 1). The dike swarms that represent the oldest portions of this magmatic

event are the Steens (16.6–16.5 Ma), Monument (17.2–16.06 Ma), and perhaps some number of the NNW oriented dikes of the CJDS, which are cross-cut by many other dike orientations (Figure 2.9 Cahoon et al., 2020; Kasbohm & Schoene, 2018). Dikes of the Monument swarm are dominantly oriented NW-SE (330° ± 14°); Steens dikes are dominantly oriented NNE-SSW (10° ± 27°), and the oldest trend identified from our preliminary field work in the CJDS are the NNW oriented dikes (Figure 2.2; Plate 1 in M. Morriss et al. (2020)). The youngest dikes mapped in our database, those associated with the ∼8.5 Ma Ice Harbor flows are dominantly oriented NW (336° ± 12°). This is a notable ∼10-15° shift westward from the dominant trend of the CJDS, which is 352°.

Previous authors identified a radial orientation across these different dike swarms, invoking a rising plume head to explain dike orientation and dike distribution (V. E. Camp & Ross, 2004; Ernst & Buchan, 1997; Glen & Ponce, 2002). Such a model would require large scale lateral transport of magma through the dike swarm (e.g. Ernst & Baragar, 1992), or alternatively, migration of magmatism could be accomplished through lateral migration of localized magma chambers (e.g. V. E. Camp & Ross, 2004; Sleep, 2008). However, a lack of palinspastic reconstructions complicates the hypothesis of radial diking in the case of the CRBG dikes. Extension and rotation has taken place since the Miocene in northern Nevada and Southern Oregon (V. E. Camp, Pierce, & Morgan, 2015; McQuarrie & Wernicke, 2005). Tectonic deformation is less well constrained in the areas of NE OR and SE WA where most of the CJDS is exposed. Work conducted by McCaffrey, King, Payne, and Lancaster (2013) and Wells et al. (2014) place poles of rotation for post-Miocene extension and rotation in NE Oregon. This pole of rotation implies little tectonic extension has taken place in NE Oregon since the

Miocene; the lack of strong tectonic gradients in the region of the CJDS supports a magmatic stress dominated system.

Exposure Bias in the CJDS

Nearly 50 percent of all dikes exposed across the CJDS are hosted within granitoid bodies. Taubeneck (1970, 1997) suggests that dikes preferentially intruded this rock type. To test WHT's hypothesis, we examined the hypsometry of different rock-types across NE Oregon, comparing these elevations with the elevations of exposed dikes (Figure 2.12). The median dike elevation is ∼1900 m; the median elevation in NE Oregon is ∼1200 m (Figure 2.3B, 2.12A, and 2.12B). The two most common host rocks – basalt and granitoids (Figure 2.12C and 2.12D) – have median elevations of ∼1200 and ∼1750 m, respectively. The distribution of dikes below ∼1900 meters is constant with elevation; however, there is a notable increase in the occurrence of dikes above 1900 m. This elevation is closer to the elevation of the Pleistocene Equilibrium Line Altitude (ELA; ∼2000 m) than any other topographic and lithologic metric (Figure 2.12A Meyer, Fawcett, & Locke, 2004).

If dikes were focused toward granites, then one would expect to see a peak in dike occurrence at similar elevations areas dominated by granitoid rocks (1500 – 2250 m). However, dikes still occur with increasing probability at higher elevations (Figure 2.12A). We posit that more dikes are exposed at higher elevations due to glacial erosion, rather than due to a true increase in dike abundance in granitoids. A full comparison between dike elevation, hypsometry and all mapped host rock types is shown in Figure A.6. The exposure bias of dikes in higher elevation areas also suggests that there may be numerous unexposed dikes at lower elevations and similar paleo-depths.

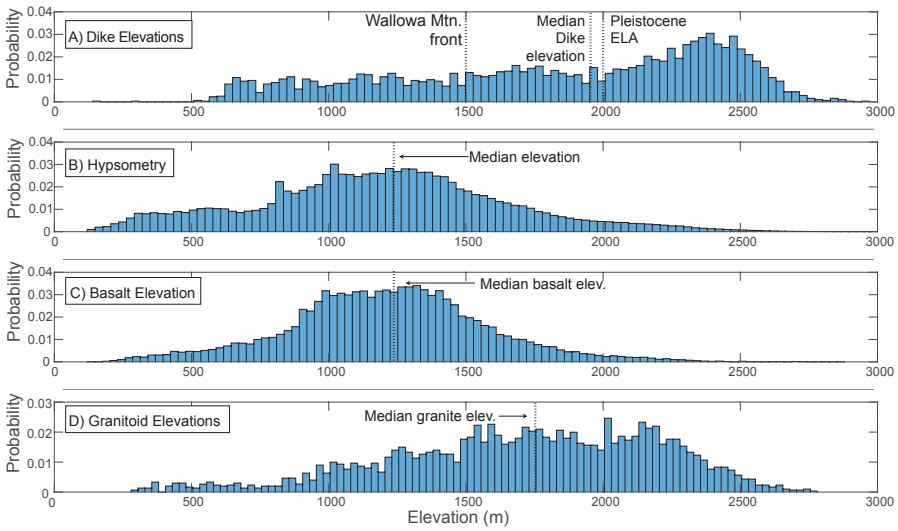

Figure 2.12. A. The elevation of dike segments within the CJDS from WHT notebooks. Significant topographic features are marked (i.e. Wallowa Mountain front or the Pleistocene equilibrium line altitude (ELA); Meyer et al., 2004). **B.** This figure shows the distribution of all elevations across the CJDS. The median elevation is ∼1200 m. There is noticeably less elevation (and thereby area) above ∼1500 m. **C.** This plot illustrates the hypsometry of the basalt covered landscape in NE Oregon. The median elevation of basalt in NE Oregon is ∼1200 m. **D.** Granitoid rocks are more dispersed throughout the landscape in NE Oregon; however, the median elevation for granitoids is still higher than that of basalt and the median elevation of topography in NE Oregon (∼ 1750 m).

Dike Segment Spatial Density

Taubeneck (1970) extrapolated a maximum number of dikes from the highest dike density within the Wallowas across the extent of the CJDS. He suggested that as many as 21,000 dike segments may exist across the region, with a potential upper limit of 30,000 segments. With a more complete database than was available in 1970, we can replicate this calculation. Within the main area of the CJDS (100 x 350 km), the greatest dike density measured within the Wallowas ($\sim$ 5 dike segments per km^2) yields $\sim$175,000 dike segments across this region, well beyond WHT's estimate (Figure 2.4B). Because the Wallowas represent $\sim$ 10% of the exposed area of the CJDS, this is likely a significant overestimate. However, extrapolating from the mean value of dike density ($\sim$1.2 $\pm$ 0.9 dikes per km^2) gives $\sim$42,000 dikes across the CJDS, which is also larger than WHT's estimate. Of course, because dikes are clustered, assuming homogeneous dike density across the swarm is an upper bound on the number of dike segments.

Regional Dilation Due to Diking

Dike intrusion represents unrecovered elastic strain normal to the propagation direction, with smaller contributions from thermal and mechanical erosion of wall rocks (Anderson, 1942; Fialko & Rubin, 1999; Hoek, 1991; Parfitt & Wilson, 1994). Integrated across a large dike swarm such as the CJDS, such opening implies significant dilation of the upper crust during emplacement of the CRBG.

The WHT dataset does not permit a direct association between mapped dike locations and thickness. However, the strongly peaked distribution of thicknesses across the CJDS from WHT notebooks suggests that a single representative thickness is a reasonable measure of dike opening (Figure 2.5). We

assume a median thickness value of 8 m and calculate dilation from mapped dike segments. For E-W and N-S directions, we extract the orthogonal component of mapped segments (treated as vectors) and average over bins (containing M segments per bin) in longitude and latitude according to

$$D_k\left(y_i\right) = \begin{cases} \frac{1}{y_{i+1}-y_i} \sum_{j=1}^{M} \mu(\overrightarrow{d_j} \bullet \overrightarrow{S_k}), & \text{if } M \geq 0 \\ 0, & \text{if } M = 0 \end{cases} \tag{2.1}$$

In equation 2.1, D_k is the component of dilation (in meters) oriented in the k = N-S, E-W direction for the ith bin of either longitude (for N-S dilation) or latitude (for E-W dilation). y_i is the start of the longitude and latitude bin, y_{i+1} is the end. We chose a bin width of 1.7 km in each case, and tested that the results are not highly sensitive to bin size. $\overrightarrow{d_j}$ is one of M total dike segments within each bin. It is scaled to a common origin, dotted into either N-S or E-W unit vectors $\overrightarrow{S_k}$, then multiplied by median dike thickness μ to obtain N-S or E-W dilation in meters.

This procedure results in a profile of average dilation that is plotted in Figure 2.2B and 2.2C. This is a lower bound for crustal dilation in the CJDS, for several reasons: 1) Surface exposures of many dikes are likely covered by CRBG lavas or post-Miocene sediments. 2) Dike segment spatial density likely increases with depth, and 3) many smaller dikes are not well documented in the WHT data.

In the observed pattern of dilation (Figure 2.2B and 2.2C), E-W extension peaks in the Wallowa Mountains (∼45.16° N, ∼117.30° W), the area of greatest dike exposure with ∼500 m of dilation. N-S dilation peaks in the same location with ∼150 m of dilation, reflecting the large dispersion in dike orientations here (Figure 2.4A). The envelope of dilation decreases substantially away from this central location.

Just like estimating the total number of dikes, we can estimate the near surface strain associated with the CJDS by scaling dilation over the 100 km E-W and 350 km N-S area over which much of the CJDS is exposed. Maximum strains associated with peaks in E-W and N-S dilation are ∼0.5% and ∼0.06 %. A maximum amount of strain can be calculated if the greatest dike density observed in the Wallowa Mountains (∼ 5 dike segments per km^2) is scaled to the 100 by 350 km area over which the CJDS is exposed. This calculation yields ∼13 % E-W oriented strain or 2.7 km of dilation, and ∼0.3 % N-S oriented strain or ∼1.3 km of dilation. To put this scale of dilation in perspective, John, Wallace, Ponce, Fleck, and Conrad (2000) calculated ∼1 km of extension due to diking across the contemporaneous northern-Nevada rift. Increased precision of dating suggests that three magnetostratigraphic divisions of the Grande Ronde basalts erupted in an increasingly short window of time ∼70,000 – 400,000 years (Kasbohm & Schoene, 2018). Given that a large fraction of the CJDS dikes are Grande Ronde in composition, such rapid emplacement indicates that the transient EW dilation rates represented by the strain calculated here are comparable to modern plate speeds (∼cm yr-1)!

Implications for Time Evolving Stress State

We examined dilation in cardinal directions (E-W and N-S) in Figure 2.2B and 2.2C. However, the dominant dilation direction is slightly rotated from E-W (Figure 2.2D). While the bulk of dike dilation appears consistent with other structures present in the intermountain west (i.e. the Northern Nevada Rift V. E. Camp et al., 2015; Colgan, 2013), CRBG-related crustal dilation oriented in other directions has not previously been studied (Figure 2.2D, 2.3 and 2.13; Colgan, 2013). Although the relative contribution of strain in these directions

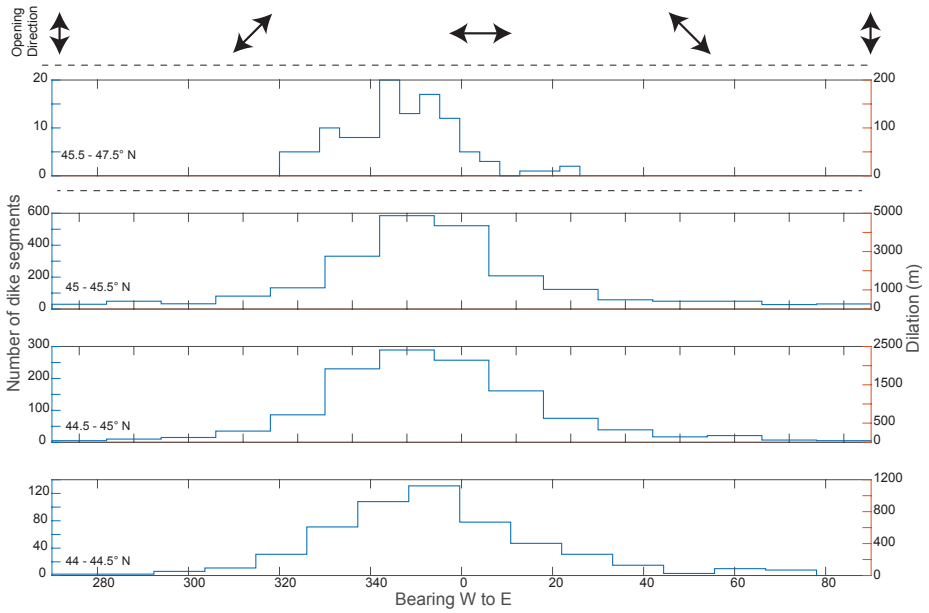

Figure 2.13. Dike dilation binned by bearing and latitude. Each subplot represents dikes binned initially by latitude (44–44.5°; 44.5–45°; 45–45.5°, and 45.5°–47.5° N), see Figure 2.2 for reference, with dilation as a function of orientation (compare with Figure 2.2B and 2.2C for the E-W and N-S components. The right scale is the magnitude of dilation assuming an average dike width of 8 m. The opening direction is provided for reference at the top, highlighting for example that a dike oriented due N-S is actually opening E-W. Dike count and total dilation calculation is sensitive to the range of latitudes chosen to limit each histogram, but this does not affect the overall shape of the distributions.

is small, it indicates that either 1) dikes are not responding purely to an ENE-WSW oriented minimum compressive stress direction, or 2) the stress field changed through time. It is also important to note here that our observations constrain the stresses within the upper ∼2 km of the crust. The stress field within the mid-crust and the orientation of deeper intrusions may be different (Corti et al., 2019; Isola, Mazzarini, Bonini, & Corti, 2014)

Mean dike orientation is often assumed to be a proxy for time-averaged stress field (Gudmundsson, 1995), although over-pressured dikes may not always follow background stresses (Pinel, Carrara, Maccaferri, Rivalta, & Corbi, 2017). We hypothesize that with intrusion of many NNW oriented dikes, dilating the crust

locally by as much as 2.7 km in as short as 70 - 400 ky, the initial regional stress field may have been wiped out or heavily modified, leaving the crust in either an isotropic or ortho-rhombic stress state (J. M. L. Miller, Nelson, Hitzman, Muccilli, & Hall, 2007; Reches, 1978, 1983). If we assume a background extension rate u over a length scale H, associated with far-field tectonic of magmatic forcing (e.g. plume or deep intrusion), the rate of intrusion (or strain) I over H that exactly balances background extension is ((e.g. Gudmundsson, 1990)

$$I = \frac{Eu}{\sigma_t H}. \tag{2.2}$$

In equation 2.2, σ_t is the tensile strength of the rocks, generally in the range of ∼1-10 MPa. With Young's Modulus E ∼30 GPa, if $H \sim$ 50-100 km to match the CJDS dimensions and $u \sim 1$ cm yr^{-1} to produce dilation of ∼1 km over ∼100 kyr, then $I \sim$ 102-104 yr^{-1} from equation 2.2. Dike intrusion at a higher rate, plausible given the larger number of segments in the high density regions of the CJDS, would transiently wipe out an extensional stress field as is suggested by clusters of dike segments with overlapping orientations (Figure 2.3A). Equation 2.2 balances extensional tectonic stresses with intrusion. If we estimate the extensional stress σ_{dike} associated with dike intrusion alone, simply scaling the stress associated with dike intrusion: $\sigma_{dike} \sim E * \epsilon_{dike}$ ∼3 MPa, where $\epsilon_{dike} \sim \frac{10m}{100km}\ 10^{-4}$ is the strain associated with a single dike. Given that the deviatoric stress in the upper crust ranges from 20-30 MPa (Stüwe, 2007), the intrusion of even 10-20 dikes in the absence of extension could alter regional principal stresses. The observation of a dominant early orientation for the CJDS segments, which is then cross cut by dike clusters with variable orientations (Figure 2.2D and 2.10), suggests that dikes intruded in a predominant NNW direction until reaching an isotropic (e.g.

Muirhead et al., 2014), or ortho-rhombic condition with unequal principal axes of stress (Reches, 1978).

If such a transition from tectonic to magmatically dominated stresses occurred, crustal magma transport could be increasingly affected by the CRBG-imposed magmatic reservoirs (e.g. L. Karlstrom, Dufek, & Manga, 2009; L. Karlstrom, Wright, & Bacon, 2015) as has been hypothesized by Wolff et al. (2008) for the CRBG, or stresses associated with surface loads from the lava pile (Burgess, Muirhead, & Bowring, 2017). Dikes in this scenario could be more easily affected locally by time and spatially varying magmatic stresses, but re-orient farther afield to a tectonic stress regime (Muller & Pollard, 1977). This would also support the observed dikes following joints in one stress condition and perhaps at another time cutting their own path regardless of joint orientation (Figure 2.11 P. Delaney et al., 1986). Such behavior might be used in the CJDS to map the spatial distribution of deep magma reservoirs if vertical versus horizontal flow can be established (Figure 2.4A; R. Jolly & Sanderson, 1997; Muller, 1986; Muller & Pollard, 1977). Moreover, the behavior of CRB dikes cutting their own path is consistent with observations made in the northern Nevada rift by Colgan (2013) and V. E. Camp et al. (2015) where diking is offset by $\sim 45°$ from the predominant Miocene extensional direction.

The high rates of deformation implicated by dike intrusion may be exacerbated by unique conditioning of the lower-crust above a mantle plume head. Much work has been done to discuss the potential movement of lower-crust and lithospheric mantle near a spreading mantle plume head in observational studies (e.g. V. E. Camp & Hanan, 2008; Darold & Humphreys, 2013) and modeling studies (e.g. Burov, Guillou-Frottier, D'Acremont, Le Pourhiet, & Cloetingh, 2007; Cloetingh, Burov, & Francois, 2013; Guillou-Frottier, Burov, Nehlig, & Wyns,

2007). If plume-head spreading resulted in lateral or vertical movement of the lithospheric mantle and lower-crust beneath the CJDS, then dike-induced dilation of the upper crust may not be directly communicated to the lower crust (Lustrino, 2005).

Dike-scale Observations and Emplacement Mechanics

Dikes are often idealized in the linear elastic fracture mechanics (LEFM) framework as pressurized, magma-filled, mode-I cracks (e.g. Rubin, 1995). In this model, dike width is controlled by a combination of factors including mechanical properties of host rocks, external far-field stress, and stresses associated with flowing magma within the dike (Rubin, 1995; Sneddon & Lowengrub, 1969). For an isolated dike, LEFM predicts that the maximum width w is

$$w = \frac{2P_o\,(1-v^2)\,L}{E}. \tag{2.3}$$

Here, v is the Poisson's ratio of the host rock, L is the length of the dike (perpendicular to width, and P_o is the magmatic overpressure (pressure in excess of lithostatic pressure) within the dike. Dike overpressure depends on a range of factors including magma buoyancy, magma reservoir pressure, and the differential background stress (Geshi, Kusumoto, & Gudmundsson, 2010; Gudmundsson, 1990).

Assuming that the median CJDS widths are representative of w in equation 2.3, we can estimate the horizontal lengths expected in the CJDS. Using a range of magmatic overpressures (P_o = 1-10 MPa), with E = 30 GPa, and v = 0.25 mean dike lengths range from L = 10-100 km. This is similar in magnitude to the largest remotely-sensed Ice Harbor dike length, but larger than the median CJDS segment lengths by a factor of $\sim$100. A LEFM scaling thus supports our hypothesis that Ice Harbor dike segments are more representative of dike length than CJDS segments.

Of course LEFM in its simplest form is likely not a complete description of LIP-scale dikes, and models that better account for multiple interacting hydraulic fractures (e.g. Bunger, Menand, Cruden, Zhang, & Halls, 2013) should be applied.

Dike Thickness Trends with Depth

The WHT data suggest a small but robust anticorrelation between dike width and paleodepth within the CJDS (Figure 2.10). There are three possible explanations for this trend: 1) Near the dike tip region, the fracture will narrow (Geshi et al., 2010). Therefore smaller widths at shallower depths could be an observation of long-wavelength tipward dike narrowing 2) Viscous pressure loss from a magma flowing away from a chamber within an elastic-walled dike results in thinning, although this does depend on the rate of viscous pressure drop and spatial distribution of stresses in the medium (Pinel et al., 2017; Woods et al., 2006). 3) Dike thinning is based on changes in buoyancy of the magma relative to the host rock. Where the density of the crust matches that of the magma in the propagating dike, the level of neutral buoyancy, the dike may either change direction and propagate laterally or stop propagating (perhaps temporarily) and form a magma reservoir (e.g. Sparks, Huppert, Turner, Sakuyama, & O'Hara, 1984). The dike will be thickest at its level of neutral buoyancy and thin toward the surface (Lister & Kerr, 1991; Townsend, Pollard, & Smith, 2017).

Dike Dip

One possible explanation for this apparent lack of sills within the CJDS is that a shallower paleodepth within the magmatic plumbing system is exposed than in other LIPs. In this case, future seismic work may detect sills or sill complexes at depth. Moreover, discontinuous bedded units in an extensional environment with

a horizontal minimum principal stress do not favor sill formation, which could also explain the difference between the CRBG and other provinces (Menand, Daniels, & Benghiat, 2010). The most regularly bedded rock type in the region are the flows of the CRBG; older host rocks in the CJDS area have undergone significant post-depositional deformation (Dorsey & LaMaskin, 2008; Stanley, Jr., McRoberts, & Whalen, 2008; J. D. White, White, Vallier, Stanley, & Ash, 1992; Zak et al., 2012, and references therein).

Implications for CRBG intrusion volume and total mantle flux

The extrusive component of the CRBG has been estimated as 210,000 km^3 (S. P. Reidel et al., 2013). With the WHT data, we can now estimate the intrusive volume of the CRBG contained within the CJDS. Estimates for the ratio between intrusive and extrusive (I:E ratio) rocks in magmatic provinces ranges from 1:1 up to 16:1 or more (Crisp, 1984; Shaw, 1980; Wadge, 1980; S. M. White, Crisp, & Spera, 2006). This estimate varies depending on tectonic setting and mantle melting regime, and could change over the duration of a magmatic system (Colón, Bindeman, & Gerya, 2018; L. Karlstrom et al., 2017).

The source depth of CJDS dikes is unknown, which complicates an accurate estimate of dike volumes. Geophysical evidence points to cumulate layers at the base of the crust in the CRBG (Catchings & Mooney, 1988; Davenport, Hole, Tikoff, Russo, & Harder, 2017), resulting in greater seismic velocities that are a common occurrence in flood basalt provinces worldwide (Ridley & Richards, 2010). The presence of large cumulate reservoirs is likely required for mantle-derived ultramafic melts to fractionate into basalts (L. Karlstrom & Richards, 2011). However, thermobarometry suggests CRBG magma crystallization throughout the crust rather than just at the Moho (Rodriguez & Sen, 2013). Moreover, significant

crustal assimilation is inferred for the GRB formation (Wolff et al., 2008). Depth distribution of magma reservoirs for the CRBG thus remains somewhat of an open question.

We therefore treat two magma reservoir depth scenarios – a Moho-level dike source at 30 km and a mid-crustal dike source at 15 km – to calculate the total volume of the CJDS from observed dike segment densities. If we simply sum the total length of mapped dikes in our dataset (∼2,000 km length) and assume a width of ∼10 m, we find a total intruded volume of ∼250-450 km^3. However incomplete exposure suggests this is a lower bound. If we instead take the mean mapped dike density (∼1 dike km^{-2}) as representative of the majority of the CJDS (defined by our 100 x 350 km rectangle), this results in ∼35,000 dike segments. With a representative length per segment of ∼1 km we get ∼5-10.5 x 10^3 km^3 intruded volume for the two depth scenarios. The highest estimate permitted by our data arises if we assume the maximum observed dike spatial density (∼5 dikes km^{-2}) is a representative crustal average. This results in 3-6 x 10^4 km^3 for the CJDS intruded volume.

The heterogenous nature of dike density throughout the swarm likely makes these estimates upper bounds to CJDS volume. Indeed, two orders of magnitude difference in volume estimates for the CJDS reflect our considerable uncertainty both in spatial density across the swarm that is not exposed, and to a lesser extent the unknown source depth. The range ∼2.5x10^2 – 6x10^4 km^3 represents 0.1-34% of the entire CRBG volume, the upper limits of which are surprisingly large given than we have neglected the presumably larger reservoir volumes that must have sourced the dikes. This volume of spatially distributed intrusive flux likely has a significant impact on crustal rheology (L. Karlstrom et al., 2017; Perry-houts & Karlstrom, 2019) and contributes non-negligible volumes to the overall

volatile budget and associated atmospheric impacts of the CRBG (B. A. Black & Manga, 2017; Self, 2006).. For example, if we assume 0.1-0.2 wt % primary SO_2 concentrations as inferred from melt inclusions in Grande Ronde near vent tephra (Davis, Wolff, Rowe, & Neill, 2017), this volume accounts for 1s-100s Gt SO_2 and is comparable to the largest CRGB flow units.

Our petrologic mass-balance calculations suggest a maximum of ∼160,000 km^3 of gabbro was added to the crust during the eruption of the Grande Ronde Basalts (similar to the extruded volume of the GRBs). This volume of basalt, if added to the entire region covered by the CJDS (100 x 350 km), would contribute 4.5 km to the thickness of the crust. If we assume that storage and crustal assimilation occurred in a more localized region, the resulting crustal thickening increases correspondingly (Wolff & Ramos, 2013; Wolff et al., 2008). Current seismically derived crustal thickness maps for this region does not support such significant thickening (Davenport et al., 2017). Combining geophysical mapping of crustal structure with the dike structural evidence for crustal dilation associated with dikes seems a promising direction for reconciling this apparent discrepancy. This may in turn help refine the crustal extent of the CJDS.

How many dikes within the CJDS are feeders of surface lava flows?

In shallower portions of the CJDS some dikes have been robustly linked to surface flows through geochemical correlation (e.g. S. P. Reidel et al., 2016; S. P. Reidel & Tolan, 2013a) In the central Wallowa Mountains, the deepest exposure of the CJDS, there are poor links between dikes and flows and very little published information on how long feeder dikes may have been active. citetKarlstrom2019, extending the petrographic study of H. Petcovic and Grunder (2003), used low temperature thermochronology and thermal modeling to show

two dikes within the CJDS have different thermal histories that imply variable flow durations. One ∼8 m wide dike within the Wallowa mountains in the CJDS was long lived (active flow duration perhaps as long as ∼10 years), whereas a similar dike to the south in the Cornucopia region actively transported magma for at most ∼2 years and likely less (L. Karlstrom et al., 2019). The WHT database allows us to coarsely extend these case studies, as only ∼3% of dikes in the database have some degree of partial melt at the dike margin that indicates long-lived transport. In fact, an inference based on simple flow models described below *requires* that most dikes were not feeders to the CRBG eruptions.

Viscous flow through a slot is a classic and widely used model for magma flow in dikes (e.g. Rubin, 1995; Rivalta et al., 2015). Volume flow rate in m^3s^{-1} Φ follows through a slot of length L and width w is

$$\Phi = -w^3 \frac{L}{3\mu} \frac{dP}{dz}. \tag{2.4}$$

where μ is magma dynamic viscosity, and $\frac{dP}{dz}$ is the gradient in non-hydrostatic pressure driving flow with z positive pointing up (Rivalta, Taisne, Bunger, & Katz, 2015). This model points to the importance of dike width on flux – while linear in other parameters, magma flux is proportional to the width of the dike cubed. What is the possible eruptive flux from a single CJDS dike from equation 2.4? We take representative parameters in the following illustration: With a median dike thickness of $w \sim 10$ m, a median dike length of $L \sim 500$ m, a viscosity of $\mu \sim 10$ Pas for basaltic magma, and assuming a driving pressure gradient due to buoyancy of $\sim$ -300 Pa m^{-1} , the predicted volumetric flux is 5 x 10^6 m^3 s^{-1}. The time to erupt the entire CRBG through this single dike is then ∼1.3 years. Given that there are ∼4000 dike segments within the CJDS, if

every dike was active within this scaling regime the entire CRBG could have been erupted in ∼3 hours!

To match estimates of CRBG from geochronology, ≤ 400,000 years for eruption of the GRB, most dikes of the CJDS cannot be feeders (Kasbohm & Schoene, 2018). Moreover, it is likely that flow was localized to smaller regions of those active feeders, on the order of 10s of m, not kilometers (e.g Wylie, Helfrich, Dade, Lister, & Salzig, 1999). Using the same parameters enumerated above yields active length $L = 0.5$ m to match a flux of $\Phi = 5000$ m^3 s^{-1} roughly equivalent to the estimated eruptive flux from the 1783-1784 Laki eruption in Iceland (Thordarson & Self, 2003). An active width less than the dike width is also physically unlikely, unless a fraction of the observed width actively transported magma. This change in width would have significant effects on the calculation above of the overall time period for CRB eruption. We view reconciling the observed geometry and extent of the CJDS with the observed erupted volume of the CRBG a major challenge for future work.

Host rock melting, dike textures, and vesicularity

The WHT dataset contains many qualitative descriptions of dike textures, inclusion density, grain size, and vesicularity, tabulated on a 1-5 semi-quantitative scale in Figure A.7 A.8. Although the lack of direct connection to spatial locations, geometry or direct compositional information precludes much general insight, it is clear that the CJDS is extremely diverse on a textural level. A direct comparison of dike interior textures to elevation data and width (the only spatial data available in the WHT notebooks) does not result in significant correlations.

WHT documented ∼3% of the total CJDS dikes as containing some host rock partial-melt. We further investigated whether there was a relationship between

any other variable in our database and thickness of the partially melted region suggests a correlation between dike thickness and partial melt thickness (Figure A.9). However, caution is required as we are not aware of what criteria WHT used to map partial melt. We do not attempt to compare with other studies of partial melt around the CRBG dikes (e.g. H. Petcovic & Grunder, 2003).

2.6.2 Outcrop-Scale

Dike-Joint Interactions

Previous authors have identified distinct times at which joints and dikes interact (e.g. P. Delaney et al., 1986). This interaction can be interpreted as reflecting the ratio between the confining tectonic stress and the magmatic overpressure in concert with the pre-existing fractures (e.g. P. Delaney et al., 1986; R. J. H. Jolly & Sanderson, 1995). Dike-joint interactions may also be superimposed on a larger overarching orientation (termed "zigzag" by Hoek, 1991). Dikes within the CJDS dike swarm appear to fit into this latter category. At the 1:24,000 map-scale dikes are linear features cutting across rock-type changes and even accreted terrane boundaries (Figure 2.2A). However at the outcrop scale, some dikes appear to correlate in orientation with joints measured in granitoids (Figure 2.11). This addresses the Taubeneck (1997) hypothesis, which posited that primary dike orientations were controlled by host-rock jointing. We instead interpret host rock joints as influencing magma transport in dikes at an outcrop scale (<10s m) only. Dike orientation at a map scale (1s-100s km) likely reflects regional tectonic or magmatic stresses at the time of emplacement (e.g. Corti et al., 2019).

2.7 Conclusions

The CJDS is the youngest and one of the best exposed magmatic plumbing systems of a Large Igneous Province on Earth. This study synthesizes the unpublished dike mapping and observations made by Dr. William H. Taubeneck (Oregon State University; 1923–2016). Over the timespan of his career, WHT mapped 4279 individual dike segments with detailed notebook entries that document thickness, host rock character, and qualitative textural observations. A database based on his work allows us to create the first holistic map of exposed dikes within the Chief Joseph Dike Swarm. We built on the WHT database by including dikes mapped by the Washington and Idaho Geologic Surveys (Figure 2.2A), supplemented by our own original observations and measurements. We also compiled the locations of all known mapped dikes related to the CRBG; those of the CJDS, Monument, and Steens swarms and the Ice Harbor dikes (Plate 1 in M. Morriss et al. (2020)).

The 1:24,000 scale map of dikes derived from the WHT database indicates that there are multiple and previously unrecognized systematic dike orientations within the CJDS (Figure 2.2D). The dominance of a single NNW trend (Figure 2.2D, 2.3A) suggests that throughout much of the active intrusive period the least compressive horizontal stress was oriented WSW-ENE. Other orientation trends within the swarm likely post-date the main trend based on cross-cutting relations. We hypothesize that these other trends may be the result of transient changes to a long-lived regional stress field initiated by CRBG intrusions.

On a sub-swarm scale, clusters of dike segments with similar orientations occur throughout the CJDS and point to a rich meso-scale structure of the swarm (Figure 2.3). Clustered segments reinforces the dominance of the NNW trend in orientations but overlapping clusters with different orientations also suggest

time-varying principal stresses. Clusters may reflect both dynamic dike-dike stress interactions as well as structural control of dike pathways by earlier structures.

On a dike segment scale, dikes of the CJDS often segment and exhibit ∼1 m undulations in strike and width. When examined on the outcrop scale (1s – 100s of m), dike segment orientations sometimes correlate with the orientation of joints within local granitoid rocks (Figure 2.11). However, we believe joints are a second order control on the form of dikes, behind regional scale tectonic and magmatic stresses, reflected in the dominant NNW dike trend (Figure 2.2D).

The number of dikes expressed regionally and the short time period involved has significant tectonic implications. We estimate a maximum observed dilation oriented E-W of 500 m with 150 m of dilation oriented N-S due to dike emplacement. If extrapolated regionally over areas where dikes are note well exposed, this increases to 2.7 km E-W, and 1.3 km N-S dilation from CJDS. This exceeds geologically observed amounts of strain in the proximal and largely concomitant Northern Nevada rift (John et al., 2000). CJDS intrusion thus seems capable of transiently overcoming regional tectonic extension, consistent with time-varying variations in dike orientation established through dike cross cutting relationships (Figure 2.9). Additionally, we calculate the upper bound volumes for the CJDS, ranging from $2.5\text{x}10^2$–$6\text{x}10^4$ km^3. This volume may contribute to part of the petrologically derived ∼160,000 km^3 of intrusions associated with the erupted portion of the GRB.

We find a possible swarm-scale narrowing of dike segments with increased elevation and hence shallower paleo-depth. This pattern is expressed over 1.5 km of paleodepth from the CRBG–granite contact exposed at ∼3000 m a.s.l. (Figure 2.10). This trend could arise from viscous losses in magmatic overpressure with

increasing distance from a deep magmatic reservoir; dike tipward thinning, or lateral dike propagation at a level of neutral buoyancy greater than ∼2 km depths.

The immensity of the CJDS dikes presents an intriguing challenge for CRBG eruption mechanics. The total volume of magma remaining in dikes implied by the observed CJDS is probably small compared to the erupted volume, but is large enough and spatially distributed enough to affect crustal evolution and volatile budgets for the CRBG. Flow rate calculations combined with the rarity of host-rock melting observations in the WHT dataset suggest that the vast majority (perhaps as high as 97%) of exposed dikes were not long lived transport structures and thus likely not feeders of surface flows.

A significant conclusion arises from the brief geochemical comparison of WHT dike samples with CRBG lavas: the dike swarm includes rocks that lie in non- or thinly-populated regions of lava compositional space and extend the range of known CRBG chemistry (Figure 2.7). This observation is consistent with only a subset of the mapped dikes feeding surface flows.

We view establishing the connection of the CJDS upwards to surface eruptions and downwards to magma storage zones, and evaluating the mechanical consequences of CJDS emplacement into the crust at all scales as promising directions for future work. The quiescence of the rocks today hides the frenetic pace at which magma intruded this region, which is unique amongst dike swarms on Earth in its scale of exposure and documentation, quality of exposure at a range of scales, and rich history of research. Apart from being an exquisite testament to a tenacious field geologist, we hope that the legacy dataset William H. Taubeneck in turn provides a baseline for future research.

2.8 Bridge

In Chapter II, I examined the structure and dynamic of the Chief Joseph Dike Swarm through northeastern Oregon. I looked in detail at how these dikes and others associated with the CRBG effected this region and what we can infer in terms of process, stress, and strain from their macro, meso, and outcrop scale patterns. I bring this work forward in time to focus in Chapter **??** on the cooling history of the deepest canyon in North America: Hells Canyon. This canyon is located just east of the Wallowa Mountains, and in this study, I hope to reveal more about the age of the canyon through a technique called Thermochronology.

This work was conducted in collaboration with Drs. Alison Duvall and Rebecca Flowers, at University of Washington and University of Colorado at Boulder – respectively. It also has major contributions from Philip Schoettle-Greene one of Dr. Duvall's PhD students. This work will be submitted for review shortly to the *Earth and Planetary Science Letters* Journal.

CHAPTER III

EXHUMATION IN NORTH AMERICA'S DEEPEST GORGE, HELLS CANYON, USA

3.1 Summary

Hells Canyon, carved deeply into the border of Oregon and Idaho by the Snake River, is North America's deepest river gorge. Despite its nearly 2.5 km depth, the age and origin of the canyon remain as unresolved problems. To address the questions of the timing and drivers of canyon formation, herein we present new structural observations and low-temperature thermochronology results from an elevation transect across the deepest section of the canyon. We constrain post-Miocene vertical movements across the canyon by constructing a surface of the base of Miocene Columbia River Basalt (CRB) at its contact with underlying basement rocks. This paleo-surface is warped in a long wavelength doubly-plunging antiform across Hells Canyon. The deepest portion of Hells Canyon is 9 km west of the axis of this elongate dome. To place new limits on the timing and mechanisms of canyon formation, we use apatite and zircon (U-Th)/He thermochronology from a 2-km-deep elevation transect. Apatite dates range from ∼70-80 Ma to 23.5 Ma along the transect. Zircon dates of 95 and 101 Ma show no vertical trend and overlap within sample uncertainties. Inverse thermal history modeling indicates rapid cooling of the sample suite in Late Cretaceous and early Cenozoic time, followed by deceleration in cooling rate. Building on our inverse modeling, we test explicit hypotheses about canyon formation with a coupled forward model using both Pecube and HeFTy. These results suggest a pulse of rapid fluvial incision that started at ∼4 Ma, likely due to drainage integration and capture of the Snake River.

3.2 Introduction

Deep canyons are some of the most visually stunning displays of fluvial geomorphology on Earth. The formation of these features (> 2 km in depth) is not well understood. Hypotheses range from by fluvial excavation of damaged rocks along fault zones (e.g. Robl, Hergarten, & Stüwe, 2008), localized tectonic strain (e.g. Salween, Mekong, and Yangtze rivers in China; Castelltort et al., 2012; Hallet & Molnar, 2001), regional uplift due to thrust faulting (e.g. Cotahuasi-Ocona Canyon in Peru; Schildgen, Hodges, Whipple, Reiners, & Pringle, 2007), or mantle-driven uplift (e.g. the Grand Canyon in the USA; K. E. Karlstrom et al., 2012). At the largest scale, canyons express a link between surface processes and geodynamics (e.g. Tsangpo gorge in Tibet; Zeitler et al., 2001). Hells Canyon, a 2200 m deep gorge on the border of northeastern Oregon and Idaho (Figures. 3.1, 3.2), is the deepest canyon in North America and yet it's genesis remains unresolved. Understanding how and when this canyon formed is integral to understanding the Neogene and Quaternary evolution of drainage basins in the region (Staisch, Blakely, Kelsey, Styron, & Sherrod, 2018; Staisch, O'Connor, Holm-Denoma, Lasher, & Alexander, 2019). In addition, new information on the region's fluvial history may provide data to aid biologists in understanding the timing of species migration and molecular diversification of regional aquatic organisms (e.g. Smith, Unmack, Markle, Chow, & Dowling, 2017; Spruell, Hemmingsen, Howell, Kanda, & Allendorf, 2003). The timing of incision is particularly important as Hells Canyon provides a key biological connection between the northern Rocky Mountains and Pacific Northwest (Smith et al., 2017). Literature establishing constraints on the timing of canyon formation are described below. Hells Canyon must be younger than the 16.7-16.0 Ma Columbia River Basalts, which blanket the region and are deeply incised through by the Snake River (Figure 3.1A; S. P. Reidel et al.,

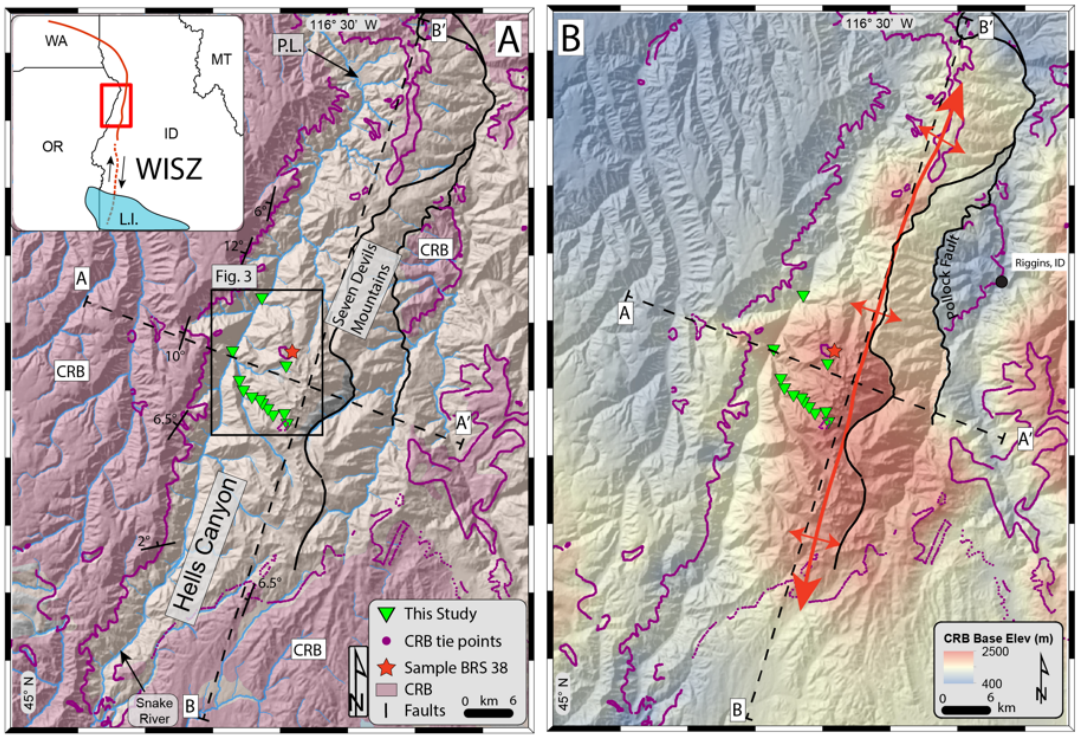

Figure 3.1. A. Topography from 10 m resolution elevation data in the Hells Canyon region with thermochronology and geochemical sample locations shown. Elevation data from the USGS 3D Elevation Program (Arundel et al., 2015). P.L. is Pittsburgh landing. Tan color highlights pre-CRB bedrock units, purple are CRB flows. Mapped CRB-Basement contact points used in construction of paleo-surface are marked in purple. The inset map shows the location of the main figure and the approximate location for the Western Idaho Shear Zone (WISZ) and the areal extent of Lake Idaho (L.I.; S. H. Wood & Clemens, 2002). **B.** Map of base-CRB paleosurface constructed using ArcMap spline with barriers tool. Major faults from Idaho state geologic maps (1:750,000 scale, respectively) are also shown as black lines (Kauffman et al., 2014; Lewis et al., 2012; Walker & MacLeod, 1991). A-A' and B-B' are locations of 5 km wide swath profiles of topography and CRB-basement contact elevation shown in Figure 3.2. The red line shows the approximate trace of the doubly-plunging antiform represented by this paleosurface and discussed in the text.

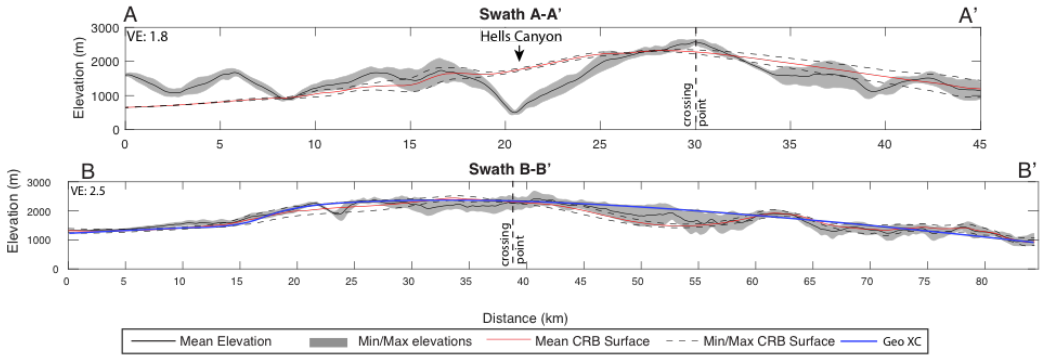

Figure 3.2. A-A'. Five km wide topographic swath profile showing mean, minimum, and maximum elevations across the deepest section of Hells Canyon - coincident with the elevation transect. The red line is the mean topographic swath profile across the CRB-Basement surface, showing an 550 m vertical offset across Hells Canyon. **B-B'.** This swath profile shows the arcuate shape of the Seven Devil Mountains and that the Columbia River Basalts drape that topography. The crossing point line is where the two swath profiles cross one another. The thin purple line marks how the surface would be drawn in a geologic cross-section constrained only by outcrop locations along the central line of the swath would appear. The synform between km 45-60 in the interpolated surface is in error given the geologic constraints of erosional remnants in the high Seven Devils Mountains.

2013). Canyon formation may also be concurrent with Pliocene draining of the terminal Lake Idaho, which deposited sediment in the western Snake River Plain from ∼11 Ma to as young as ∼4 Ma (Figure 3.1, Inset; S. H. Wood & Clemens, 2002). Fossil fish indicate possible fluvial connections between sedimentary basins in southern Idaho and Washington by ∼3.8 Ma (Smith, Morgan, & Gustafson, 2002; Smith et al., 2017; Van Tassell, Ferns, McConnell, & Smith, 2001; Wheeler & Cook, 1954). Detrital zircons derived from Idaho found in the Miocene to Pliocene Ringold Formation in central Washington suggest that a fluvial connection between southern Idaho and Washington state was established after 3.48 ± 0.11 Ma (Staisch et al., 2017, 2019). A single apatite (U-Th)/He (AHe) sample from pre-CRB bedrock in the northern portion of the canyon indicates rapid cooling consistent with canyon carving at 3.4 ± 0.6 Ma (Kahn, Fayon, & Tikoff, 2020). A minimum canyon age of 1.6 ± 0.1 Ma comes from dated basalt flows that overlie the Tuana

and Tenmile gravels (Othberg, 1994). These units prograde across the basin formerly occupied by Lake Idaho without interbedded fluvial facies, indicating the lake had drained by this time (Othberg, 1994).

In this paper, we reconstruct a CRB-basement contact in the Hells Canyon are to constrain post-Miocene deformation, use geochemical analysis to fingerprint CRB flows east of the canyon, and provide an elevation transect of low-temperature thermochronology data from Hells Canyon (Figure 3.1B and 3.2A). We incorporate our new thermochronology data into an inverse model, and then use forward thermal-history forward models to test explicit hypotheses for canyon formation. We conclude by interpreting these results in the context of regional erosion and canyon incision.

3.3 Geologic Background

Hells Canyon is carved through a region with a complex geologic history, ranging from oceanic subduction, terrane-continental collision, lateral translation, plutonic intrusion, and flood basalt exmplacement. To fully describe the geologic history of the region is beyond the realm of this paper, (see Dorsey & LaMaskin, 2007; Vallier, 1995; Vallier et al., 2016; Zak et al., 2012, for more comprehensive reviews). Below, we present the geologic history most relevant to Hells Canyon and the geologic units sampled as part of this study.

Most of the geologic formations exposed in Hells Canyon are part of the Mesozoic Seven Devils group, comprising metavolcanic, sedimentary, and plutonic rocks of the larger Wallowa terrane — an accreted intra-oceanic island arc complex (Kurz, Schmitz, Northrup, & Vallier, 2017; Vallier, 1977). The Wallowa terrane was accreted to North America by ca. 160 Ma (early-Late Jurassic; Dickinson, 1979; Dorsey & LaMaskin, 2007, 2008; LaMaskin et al., 2015; Schwartz et al., 2014; Snee,

Lund, Sutter, Balcer, & Evans, 1995; Zak et al., 2012). The accretionary boundary was reactivated as the dextral, transpressive Western Idaho Shear Zone, which was active from about 105 to 90 Ma (WISZ, Figure 3.1A; Giorgis et al., 2008; Manduca, Kuntz, & Silver, 1993; Tikoff, Kelso, Manduca, Markley, & Gillaspy, 2001). The youngest plutonic body in Hells Canyon is found along Little Granite Creek (Figure 3.3), which intruded at 115.3 ± 2.5 Ma (K-Ar; Vallier, 1995). This phase of plutonism likely represents the initiation of subduction along the western margin of N.A., outboard of the previously accreted terranes (Getty et al., 1993; K. Johnson, Schwartz, Wooden, O'Driscoll, & Jeffcoat, 2011; LaMaskin et al., 2015; Vallier, 1995; Zak et al., 2012).

The Cenozoic geologic history of NE Oregon is poorly recorded because the region was being eroded by rivers draining west during much of the Cenozoic time (Allen, 1991). These rivers drained the Sevier hinterland to the east and incised across the landscape, transporting cobble to boulder sized clasts of Proterozoic Quartzite and Eocene Challis rocks (Allen, 1991; Reiners, 2005). These deposits are now preserved underneath the oldest flows of the Miocene CRB as inverted topography in the Wallowa Mountains and at bottom of paleochannels filled with basalt in Hells Canyon and the Seven Devil Mountains (Allen, 1991; Vallier et al., 2016).

The earliest CRBs near Hells Canyon are the Imnaha Basalts, which erupted near the Oregon-Idaho border at ∼16.6 Ma (Hooper et al., 2002; Kasbohm & Schoene, 2018). The basaltic lavas flowed over an irregular landscape, filling 600-1200 m deep W-oriented paleochannels ∼40 km north of Hells Canyon in Idaho and Washington (Bond, 1963; Holden & Hooper, 1976). The Imnaha basalts were followed by the main pulse of CRB volcanism, the Grande Ronde basalts, which erupted from ∼16.5 – 16.1 Ma (Kasbohm & Schoene, 2018). This voluminous unit

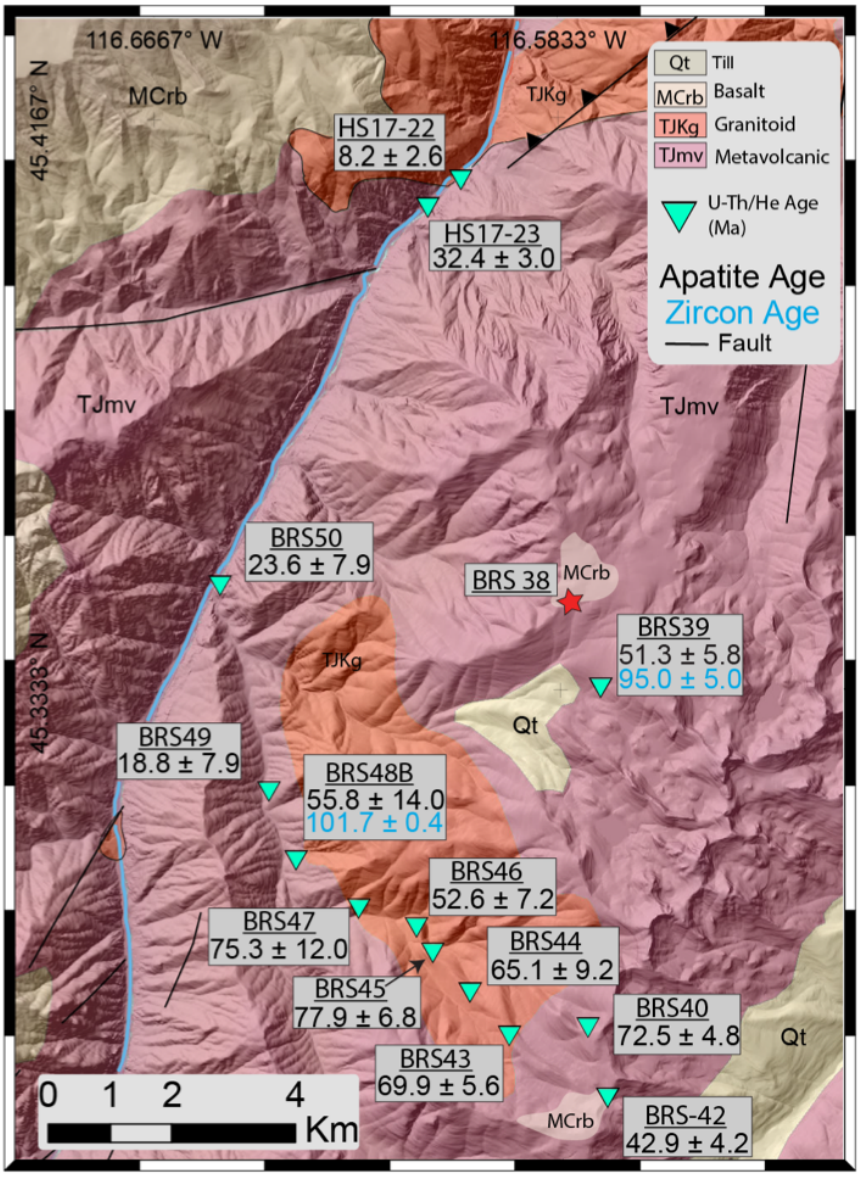

Figure 3.3. Hillshade overlain by Hells Canyon geology modified from Lewis et al. (2012) and Walker and MacLeod (1991). Green triangles show sample locations and apatite (U-Th)/He and zircon (U-Th)/He dates. Sample BRS 38 is the basalt sample collected for XRF analysis. N.B. Mesozoic granitoid in northern and southern portion of the image is not offset across the canyon.

makes up ∼72% of the 210,000 km^3 volume of the CRB (S. P. Reidel & Tolan, 2013a). Much of the remaining pre-CRB topography was inundated by these flows (V. Camp, Reidel, et al., 2017). The exact form of pre-CRB topography in Hells Canyon is poorly constrained, partly because the geologic maps across the CRB-basement contact has not be examined in detail.

Post-16 Ma tectonism in the region can be determined by measuring stratigraphic displacement of CRB flows. In the Hells Canyon region, proprietary reports conducted by the Idaho Power Company in the early 1990s describe faults at the south end of Hells Canyon that offset CRB flows by ∼600 m (Zollweg & Wood, 1993). Twenty kilometers east and south of Hells Canyon, along the Salmon River, faults displace CRB flows down-to-the-east by ∼300 m vertically (Zollweg & Wood, 1993). In the Seven Devils Mountains, combined normal-sense displacement on the Heavens Gate fault (a low-angle normal fault, reactivating an older thrust fault) and the steeper Pollock Fault offsets CRB down-to-the-east by ca. 1.5 km (Figure 3.1B; Hamilton, 1963; Kauffman et al., 2014). Many of these faults are Mesozoic thrust faults that have been reactivated with normal sense of motion (Kauffman et al., 2014; Tikoff et al., 2001). The age of these faults is constrained by the observation that the largest normal-displacement (up to ∼1.5 km) offset the ca. 16-Ma CRB. Kahn et al. (2020), building on a suggestion of Gray and Oldow (2005), proposed that a previously unmapped down-to-the-west normal fault is in Hells Canyon in the northern portion of Hells Canyon. According to this model, the inferred normal fault in the canyon is proposed to offset CRB flows E-W across the canyon. Below, we present data to test this hypothesis.

3.3.1 Previous Thermochronology Studies

There is a long history of thermochronometric studies in the Hells Canyon region. High-temperature thermochronometers, described below, record cooling related to terrane accretion and translation. Hornblende and biotite $^{40}Ar/^{39}Ar$ dates from samples in the suture zone east of Hells Canyon suggest that post-accretion cooling through temperatures of ∼550 and ∼350 °C respectively took place by ∼130 Ma (Snee et al., 1995; Tikoff et al., 2001; Vallier, 1995). Biotite $^{40}Ar/^{39}Ar$ dates from the WISZ, which is superimposed on the suture zone, indicate cooling below ∼350 °C by 85-70 Ma (Giorgis et al., 2008). The oldest thermochronology results in Hells Canyon proper are hornblende $^{40}Ar/^{39}Ar$ dates for rocks of the Seven Devils group, which record rapid cooling below ∼550 °C between 244 and 226 Ma (Snee et al., 1995). These ages pre-date suturing of the Wallowa Terrane to North America (Giorgis et al., 2008; Snee et al., 1995) and coincide with Triassic arc volcanism of the Wild Sheep Creek Formation (Vallier, 1977; D. White & Vallier, 1994). Potassium-Argon dating constrains the age on the youngest pluton within Hells Canyon as 115.3 ± 2.5 Ma (K-Ar; Vallier, 1995). This indicates rocks in the deepest portion of the canyon cooled through ∼550 °C and 350 °C for K-Ar in hornblende and biotite, respectively (Figure 3.1; Reiners & Brandon, 2006; Vallier, 1995).

Previous studies of lower-temperature thermochronometers constrain upper crustal cooling across region. Zircon (U-Th)/He (ZHe) dates of ∼80 Ma record cooling below ∼150 °C and indicate that transpression on the WISZ drove exhumation of the Little Goose Creek complex, exposed ∼50 km SE of Hells Canyon, to shallow crustal levels (Figure 3.1 inset A; Fayon et al., 2017; Giorgis et al., 2008). Apatite fission track dates which record cooling below ∼120 ° C, reveal a punctuated period of faster cooling in the Eocene in the same region (Giorgis

et al., 2008; Reiners, 2005). Regional AHe data from the Wallowa Mountains, 30 km west of Hells Canyon, record cooling from Late Cretaceous to Miocene (Kahn et al., 2020; Schoettle-Greene & Duvall, 2016). These dates record both post-crystallization cooling (∼85-95 Ma; Kahn et al., 2020) and partial or full resetting by proximal CRB dikes (e.g. L. Karlstrom et al., 2019).

The lower temperature AHe thermochronometer has been little applied in Hells Canyon in prior work. A sparse AHe dataset that includes samples at the southern end and in the northern portion of the canyon contains a single 3.4 ± 0.6 Ma AHe date from Pittsburgh Landing (Figure 3.1A; Kahn et al., 2020). The authors explain this anomalously young date collected 10 m below 17-16 Ma CRB flows as the result of burial and reheating above the partial retention zone for apatite, likely during the Miocene emplacement of the CRB (Kahn et al., 2020). This young cooling date was interpreted by Kahn et al. (2020) as a constraint on the incision of Hells Canyon.

3.4 Methods

The methods employed in this study are aimed at constraining the late Cenozoic evolution of Hells Canyon. To better understand and test the potential for CRB flow offset across Hells Canyon, we construct a paleosurface of the CRB-basement contact. To confirm that basalt flows preserved as erosional remnants in the Seven Devils Mountains east of hells Canyon are part of the regionally extensive CRB sequence, as mapped by (Kauffman et al., 2014), a sample of basalt from 2300 m a.s.l. was analyzed for major element chemistry (Figures 3.1, 3.3). We also evaluated the timing of canyon incision using low-temperature AHe and ZHe thermochronometric systems. We progressively built on our data by incorporating inverse and then forward modeling to test canyon formation hypotheses.

3.4.1 Paleosurface Reconstruction

We map the base of CRB, at the contact Imnaha and Grande Ronde basalts and underlying pre-Miocene (Figure 3.1B). This is motivated by observations of isolated erosional remnants of CRB flows at high elevations in the Seven Devils Mountains east of Hells Canyon (Figure **??** D. A. Swanson et al., 1979), which indicate deep incision and close to 2 km of post-CRB local erosional relief. This information was extracted from digital state geologic maps of Washington (1:500,000 scale), Idaho (1:750,000 scale), and Oregon (1:100,000 scale), as well as georeferenced USGS reconnaissance level geologic maps (1:100,000 scale; Bond et al., 1978; Kauffman et al., 2014; Lewis et al., 2012; Schuster, 2005; D. Swanson et al., 1980; Walker & MacLeod, 1991). Elevations of this contact were extracted from the 10 m 3DEP dataset (Arundel et al., 2015). Using point elevations along the contact as a datum, a surface was fit to these points using the spline with barriers tool in ESRI's ArcMap. The spline tool produces a minimum curvature surface satisfying the spatial constraints of input data. The resulting spline surface is interpreted as a map of pre-CRB topography deformed by post-CRB tectonics (Figure 3.1B).

Additional structural constraints on the CRB orientations were made with strike-and-dip measurements. These measurements are made using a combination of 1 m horizontal resolution NAIP imagery in concert with the 10 m resolution National Elevation Dataset. A three (or more) point planar-fit is performed using the LayerTools extension to ArcGIS (Kneissl et al., 2011).

3.4.2 Geochemistry

Discriminating between the two major early eruptive events in the CRB, Imnaha and Grande Ronde, is important not only for the timing of flow

emplacement, but also because the early Imnaha flows inundated pre-existing topography and the Grande Ronde Basalts blanketed the landscape (Bond, 1963; Tolan et al., 1989). Flow identity can therefore provide a measure the magnitude of post-CRB erosion, and our results can be compared with the geologic mapping of flows on the west side of the canyon by D. A. Swanson et al. (1979). The two units are readily distinguishable as the Imnaha flows are true basalts while the Grande Ronde flows are basaltic andesites (Hooper, Kleck, Knowles, Reidel, & Thiessen, 1984; S. P. Reidel & Tolan, 2013a).

We used wavelength x-ray fluorescence (XRF) to measure major and trace elements in sample BRS 38 collected in the Seven Devils Mountains (Figure 3.1). This sample was collected from a previously unmapped small erosional remnant of horizontal basalt (∼30-40 m thick) preserved at ∼2,320 m in the Seven Devils Mountains, 1900 m above the Snake River. This sample was analyzed for major and trace element geochemistry at the Franklin and Marshall College X-Ray Laboratory. For more details on the XRF process and sample preparation see the Appendix. XRF results were interpreted with standard bi-variate plots of major element compositions to compare with established fields of geochemical variation for different units within the CRB. Three plots were chosen as diagnostic of the main CRB units that this basalt sample is likely to represent: a total alkali silica plot; TiO_2 v SiO_2; and TiO_2 v MgO (V. Camp, Reidel, et al., 2017; Hooper, 2000).

3.4.3 (U-Th/He) Thermochronology

We use low-temperature thermochronology to assess the formation history of Hells Canyon. The AHe and ZHe systems record cooling through temperatures of ∼110-50 °C and ∼200-<50 °C respectively, depending on radiation damage accumulation (Farley, 2000; R. M. Flowers, Ketcham, Shuster, & Farley, 2009;

Guenthner, Reiners, Ketcham, Nasdala, & Giester, 2013; Reiners, 2005). AHe and ZHe are widely used to decipher cooling related to faulting (e.g. Stockli, Dumitru, Mcwilliams, & Farley, 2003) or canyon creation via fluvial incision (e.g. R. Flowers & Farley, 2012; Schildgen et al., 2007). Given the 2 km depth of Hells Canyon, cooling related to canyon carving may be detectable with AHe. The ZHe systems may provide an additional constraint on cooling of the region over the pre-canyon formation interval.

Fourteen bedrock samples were collected by raft and by foot along the edge of Hells Canyon in a ca. 2 km elevation transect in the Seven Devil Mountains during the summers of 2014 and 2017 (Figures 3.1,3.3). Care was taken to collect samples of granitoid bedrock that did not show any hydrothermal alteration and were >100 m from Columbia River Basalt dikes (see L. Karlstrom et al., 2019, for complexity of dike-related rock reheating). We also removed the outer 10 cm of rock when collecting samples to avoid potential thermal perturbations from wildfires (S. Mitchell & Reiners, 2003). Samples were collected every 200 to 300 m up a steep elevation transect, covering 2 km of vertical elevation in ∼10 km of distance (Figures 3.1. 3.3). Seven of our samples were collected from the ∼115 ± 2.5 Ma pluton (Figure 3.3) mapped by citetVallier1995. Seven other samples were collected in the Triassic Wild Sheep Creek formation, composed of metamorphosed basalt, basaltic andesite, and andesite with some volcaniclastic units (Figure 3.3 Vallier, 1977). Apatite and zircon mineral separation and analytical methods are summarized in the Appendix.

3.4.4 Inverse Thermal History Modeling

To incorporate the radiation damage accumulation and annealing models for apatite and zircon (RDAAM and ZRDAAM R. M. Flowers et al., 2009;

Guenthner et al., 2013, respectively) into our data interpretation, we modeled the AHe and ZHe data using QTQt (QTQt64R5.7.0k, Gallagher, 2012). The software performs a Bayesian inversion of thermochronology dates to find the most likely time-temperature (tT) paths for each sample while taking into account the paleodepth separation of the sample suite (Gallagher, 2012). The code allows for inclusion of multiple constraints or prior information from regional geology or other thermochronology, and uses a Markov Chain Monte Carlo (MCMC) algorithm to explore parameter space and identify an expected thermal history within 95% credible intervals to match sample dates (Gallagher, 2012). This model is a weighted mean model, where weights are derived from the posterior probability. All samples were included in this inverse model except for 3, for which there were concerns about partial resetting from CRB flows and hydrothermal fluids. Model runs incorporated prior information from K-Ar on the cooling of the sampled pluton; a range of values for the geothermal gradient; the mean annual temperature for the shallowest sample, and a modern environmental lapse rate. Full model parameters, constraints, and run time iterations are outlined in the Appendix.

3.4.5 Coupled Forward Modeling

QTQt provides a weighted average inverted thermal history; however, QTQt is limited to 2-D modeling. This software does not have the ability to directly test for different thermal histories given variable 3-D landscapes. To this end, we built on our QTQt modeling and setup a coupled forward thermal modeling experiment using the software Pecube (Braun, 2003) and HeFTy (Ketcham, 2005) to test explicit canyon formation hypotheses. Pecube is a 3-D thermo-kinematic model that can be provided with a real or synthetic landscape that develops into the modern landscape over a specified duration. Pecube solves the heat-transport

equations during landscape evolution, which can then can be used to predict tT paths for any sample location within the model framework (Braun et al., 2012). HeFTy is a frequentist based software that explores parameter space with a Monte Carlo algorithm and supports both inverse and forward modeling (Ketcham, 2005). HeFTy uses the existing ZRDAAM and RDAAM kinetic models for He diffusion in zircon and apatite, respectively, but Pecube does not.

We tested three different distinct scenarios for the formation of Hells Canyon: (1) An "Old Canyon" scenario in which exhumation across the canyon has continued at a constant pace since slowing from rapid exhumation at 60 Ma. In this scenario, cooling in the Hells Canyon region occurred slowly with no faulting. This model setup has Hells Canyon as an emergent feature through the Cenozoic, perhaps partially formed before the region was inundated by CRB flows (Bond, 1963). (2) A "Young Canyon" scenario, in which slow exhumation since 60 Ma is perturbed at ∼4 Ma by the carving of a canyon below the CRB-basement unconformity. The timing of incision is chosen based on the ∼3.4 Ma AHe cooling age from Kahn (2018) and the time when Lake Idaho began lowering in elevation (S. H. Wood & Clemens, 2002). In this model, the canyon is formed entirely by Pliocene to present fluvial incision. (3) A "Faulted Canyon" scenario, in which slow exhumation since 60 Ma is perturbed by movement along a fault at ca. 10 Ma. This timing was chosen because it corresponds to the beginning of sedimentation in Lake Idaho. Sediment accumulation started in the western Snake River Plain with the activation of normal faults in that region (Figure 3.1; S. H. Wood & Clemens, 2002) and when Salmon River, to the east, experienced a pulse of incision perhaps tied to base level fall and faulting (Larimer, Yanites, Phillips, & Mittelstaedt, 2018).

In each modeling scenario, we impose a slowing of exhumation rate from 90 to 60 Ma followed by still slower exhumation from 60 Ma until either: the present (model 1); 4 Ma (model 2), or 10 Ma (model 3). We experimented with pre-60 Ma exhumation rate conditions of 0.15, 0.18, and 0.2 mm yr^{-1}. Post-60 Ma, these rates slow to 0.025 mm yr^{-1}. These models used 3 different reasonable geothermal gradients of 20, 25 and 30 °C km^{-1}. For all of our models, we use the Pecube default environmental parameters for thermal conductivity and heat capacity.

To evaluate the importance of radiation damage on our modeled thermal histories, we couple Pecube with HeFTy. We first developed the Pecube models described above, and then exported the tT path results from these models. These tT paths were imported into HeFTy and forward modeled to include effects of radiation damage (Ketcham, 2005). This approach to forward modeling ensures the current state of knowledge regarding radiation damage and helium kinetics are incorporated into our results. A coupled modeling approach may be important because radiation damage affects the retentivity of helium in apatite, and because the RDAAM and ZRDAAM models are important for correct interpretation of samples which cooled slowly or which spent significant time near the retention temperature for helium, both of which could apply in our forward models.

The misfit between our coupled forward model results and the observed thermochronology dates was assessed using a modified chi-squared statistic:

$$\chi^2 = \left(\frac{t_o - t_m}{\sigma_o} \right)^2 \tag{3.1}$$

Where t_m is predicted model age for a particular sample and t_0 and σ_o are observed sample age and uncertainty, respectively. This modified chi-squared test was first developed and used for thermochronology by Thiede and Ehlers (2013), subsequently used by Adams et al. (2015) and Michel, Ehlers, Glotzbach, Adams,

and Stübner (2018). This equation provides an intuitive distance between the observed sample age, age uncertainty, and modeled age. An array of χ^2 calculated for a single model run can be summarized with $\chi^2_{reduced}$.

$$\chi^2_{\text{reduced}} = \frac{1}{n-2} \sum \left(\frac{t_o - t_m}{\sigma_o} \right)^2 \tag{3.2}$$

In this equation, n is the number of samples included in a particular model run.

3.5 Results

3.5.1 Paleosurface Reconstruction

Elevations of the derived paleosurface (base of CRB) vary from ∼900 m to 1700 m on the west side of the canyon, up to ∼2400 m east of the canyon in the Seven Devils Mountains (Fig 3.1b). Mapping of the reconstructed paleosurface (Figure 3.1B), a representative E-W Swath profile (Figure 3.2A), and an oblique 3D satellite imagery (Fig 3.4). All reveal a ca. 60-km long doubly plunging antiform whose axis is traced along the ∼N trending range crest of the Seven Devils Mountains. Structural relief across this antiform is ∼1500 m based on the change in elevation of the base-CRB surface from the west to the crest of the Seven Devils Mountains (Figure 3.2A). A north-south swath along the Seven Devil Mountains shows that the elevation of the CRB-basement surface generally tracks topography, with the base-CRB contact in places projecting slightly above and below the modern surface between small erosional remnants (Figure 3.2B). The similarity between topography and the CRB contact illustrated by section B-B', Figure 3.2B indicates that the crest of the Seven Devils Mountains has not undergone significant post-CRB faulting, though large normal down-to-the-east

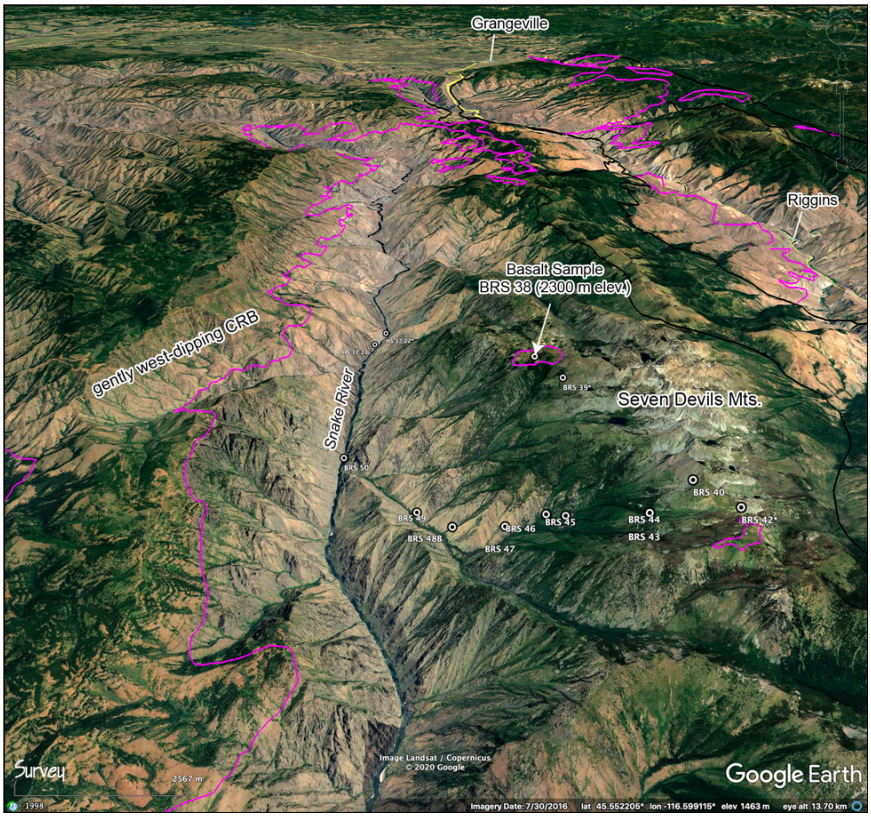

Figure 3.4. Oblique view looking north along the Snake River in Hells Canyon, showing samples collected for thermochronologic and geochemical analysis. Ca. 1900 m of erosional relief isolates flat-lying remnants of CRB perched on the axis of a doubly-plunging antiform in the Seven Devils Mountains (sample BRS 38) from the Snake River channel at 414 m elevation. The base of CRB (magenta line) projects west across Hells Canyon to gently west-dipping flows on the west side of Hells Canyon.

normal faults are observed to cut and offset the CRB in the eastern Seven Devils Mountains (Figure 3.1 Kauffman et al., 2014).

3.5.2 Basalt Geochemistry

A plot of total alkali v silica (Figure 3.5) shows that the composition of sample BRS 38 overlaps that with geochemical domain of the Imnaha unit of the CRB (see also Table B.1). Other plots (TiO_2 v SiO_2; TiO_2 v MgO) confirm correlation of this sample to the ∼16.6 Ma Imnaha unit (Figures B.1; B.2).

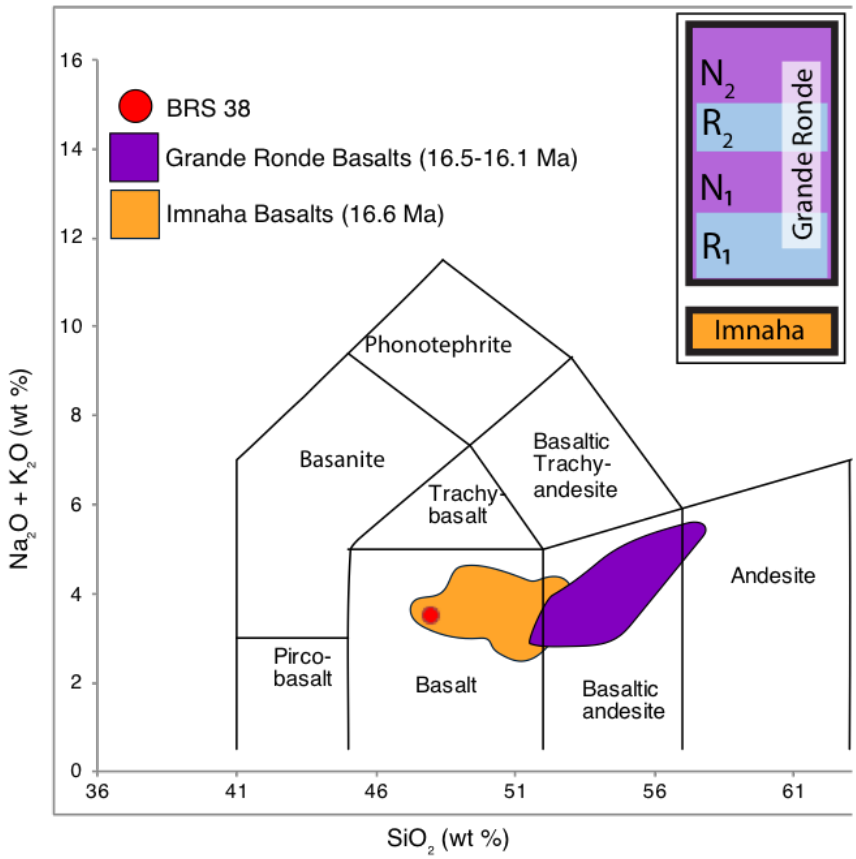

Figure 3.5. Total akali silica bivariate plot. Fields for Imnaha and Grande Ronde basalts are derived from V. Camp, Reidel, et al. (2017). Sample BRS-38, collected on the east side of Hells Canyon at 2319 m plots well within the known range for timing of Imnaha flows. Inset. Chronostratigraphy for the Imnaha and Grande Ronde basalts (Kasbohm & Schoene, 2018). The Grande Ronde basalts are mapped by their paleomagnetic polarity, reversed or normal (S. Reidel, 1982).

Without detailed geologic mapping on the Idaho side of hells Canyon to match the work done on the Oregon side, these results provide an additional constraint on our map of the CRB-basement contact (D. A. Swanson et al., 1979). Moreover, the presence of Imnaha basalt at 2319 m elevation provides evidence for significant uplift and erosion below the base of the CRB in the Seven Devils Mountains east of Hells Canyon (see below).

3.5.3 (U-Th/He) Thermochronology

The depth below the reconstructed CRB-basement contact was calculated for each sample to provide an estimate of Miocene sample paleodepth. The shallowest samples in the transect reflect early Cenozoic to late Mesozoic cooling dates (∼70–80 Ma; Figures 3.3, 3.6). The mid-depth transect dates range between 40-60 Ma, and dates in the bottom of the canyon (∼1.3 km deep) range between 8-32 Ma, significantly younger than those dates returned from the top of the transect. Mean AHe dates are plotted against their paleodepth to assess changes in the pattern and rate of cooling through the Cenozoic (Figure 3.6; Table B.2 and B.3). This plot also allows for anomalous sample dates to be identified. Apatite dates from two shallow samples, BRS 39 (51.3 ± 5.8 Ma) and BRS 42 (42.9 ± 4.2 Ma) are excluded from modeling due to concerns about partial resetting of these apatites by the presence of CRB flows visible within ∼40 m horizontal distance of our sample site (Figures 3.3 and 3.6). One low elevation sample, HS17-22 (8.2 Ma), also is excluded from modeling because field observations indicate hydrothermal alteration of the granitic host rock, and the AHe date is anomalously young relative to samples of comparable and deeper depth. Reheating by hot fluids may have caused partial resetting of this sample.

ZHe dates from BRS 39 and BRS 48B at the bottom and top of the transect overlap within uncertainty at 95.0 ± 5.0 and 101.7 ± 0.4 Ma. These two dates are close to the approximate crystallization age for the sampled pluton (115.3 ± 3 Ma K-R on Hornblende; Vallier, 1995), which cooled over ∼14 Myr to the ∼200 °C closure temperature for ZHe system (Guenthner et al., 2013; Murray, Braun, & Reiners, 2018; Reiners & Brandon, 2006). Our data also indicate a relationship between apatite grain age and effective Uranium, (BRS-48 and 50; Figures B.3 and

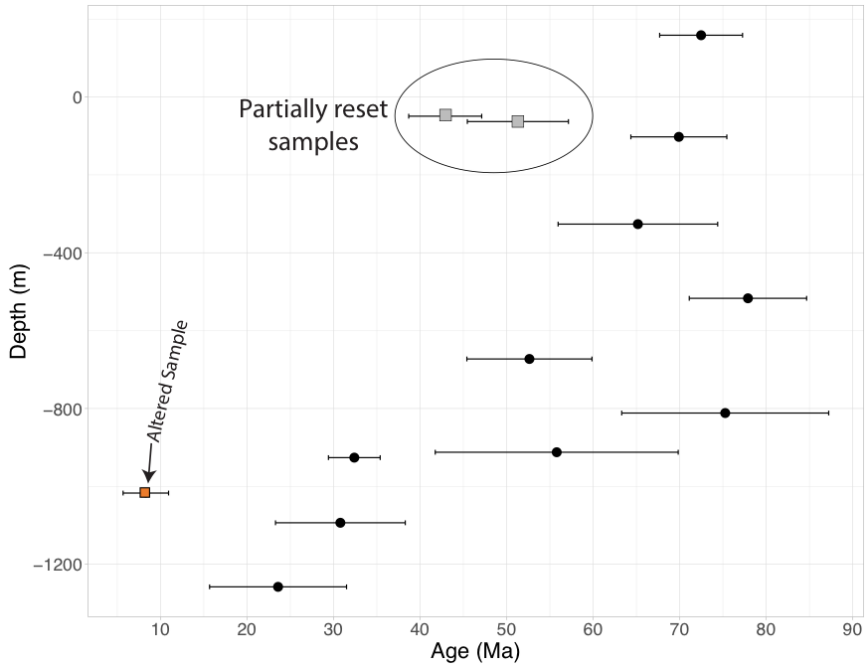

Figure 3.6. Apatite Helium cooling dates vs. paleo-depth. Plotted uncertainties are the 1-σ uncertainty of sample grain dates. The steeper trend for late Cretaceous age samples indicates initially rapid cooling from ∼80 to 65 Ma, followed by less rapid cooling after ∼60 Ma. Two samples (BRS39 and 42) are excluded from subsequent modeling due to likely partial resetting by heat from emplacement of proximal CRB flows, not similar depth for both samples. Sample HS17-22 near the bottom of the profile is excluded from modeling due to potential for hydrothermal resetting evidenced by alteration products and anomalous age with respect to depth.

??), emblematic of radiation damage for the deeper samples (R. M. Flowers et al., 2009).

3.5.4 Thermal History Modeling

Inverse model results show the fastest rates of cooling, ∼40 °C Myr^{-1}, took place between 110 and 105 Ma (Figure 3.7A), shortly after pluton emplacement. Cooling slowed rapidly to ∼15 °C Myr^{-1} between 105 and 100 Ma. Less rapid cooling continued from 95 Ma until 55 Ma at a rate of ∼2.5 °C Ma^{-1}. After this, there is little to no detectable cooling (Figure 3.7A) until 10-5 Ma. This pattern of cooling is broadly in line with results observed from our mean-age versus depth profile (Figure 3.6). QTQt model accuracy was evaluated by direct comparison between sample mean date and model produced date (Figure 3.7B). The MCMC exploration of parameter space is further evaluated through the stability of the posterior chain that is discussed in more detail in the Appendix and Figure B.5. Inverse modeling also places a constraint on the geothermal gradient experienced by the sample sequence. The average geotherm from 110 to ∼10 Ma is ∼18 °C km^{-1}.

3.6 Discussion

Thermochronology results from our elevation transect provide key insights into the long-term history of erosion and cooling in the Hells Canyon region. These data reveal evidence for late Cretaceous rapid cooling ∼75-65 Ma, followed by Cenozoic slow, monotonic cooling ∼60-25 Ma (Figure 3.6). Inverse modeling reveals a similar history (Figure 3.7A). Below, we use these results and incorporate our coupled forward models to test explicit hypotheses about canyon formation.

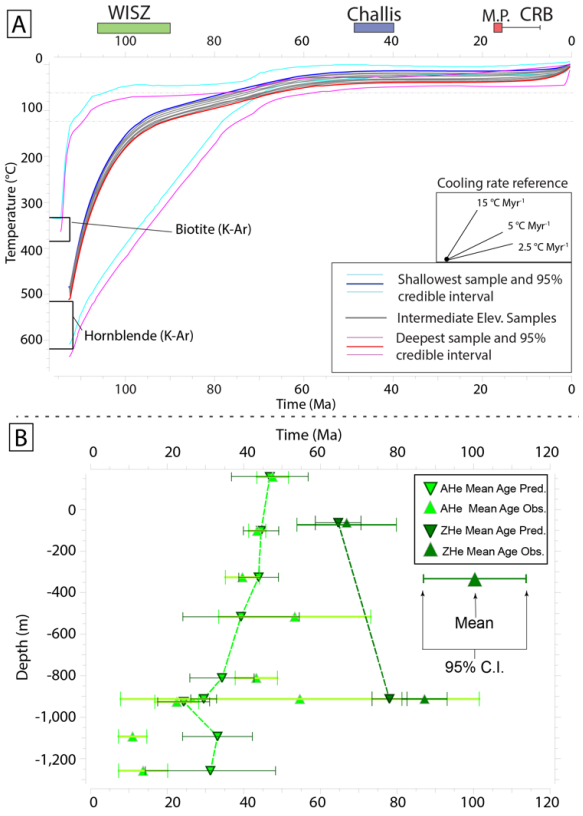

Figure 3.7. A. QTQt inversion results for vertical transect and the time periods for major tectonic and volcanic events in the region. Samples move through tT space collectively to generate a combined history for the elevation transect. The credible interval (C.I.) shows the 95% probability of a tT path falling within those bounds. The two boxes are prior knowledge in the inverse modeling regarding pluton crystallization from K-Ar (Vallier, 1995). Our samples show rapid cooling ($\sim$40 °C Myr^{-1}) immediately following the $\sim$115 Ma crystallization age of the sampled pluton. Cooling slowed between 90 and 60 Ma to $\sim$2.5 °C Ma^{-1}, followed by little to no cooling in the Cenozoic. Modeling shows no thermal perturbation associated with either the Challis volcanism ($\sim$50-40 Ma) or the main pulse (M.P.; 16.7-16.0 Ma) of the Columbia River Basalts. However, below $\sim$50 °C, the model is plotting non-unique solutions. Three reference lines are included to as means to help visualize cooling rates. **B.** Summary of mean QTQt predictions and observations. Right-side up triangles are the analyzed mean thermochronometric ages for both ZHe (dark green) and AHe (light green). Upside-down triangles are the mean ages and uncertainties predicted by the QTQt inverse model run. Model efficacy is judged by how closely the modeled ages to closely replicate the measured ages. This model estimates a mean geotherm of up to 23 °C km^{-1} at 100 Ma and shows significant cooling after 60 Ma (Figure B.6).

3.6.1 Structural Deformatin in Hells Canyon

Systematic changes in elevation of the base-CRB surface reveal an elongate dome, or doubly plunging antiform, with a N to NNE-trending axis that follows the crest of the Seven Devils Mountains (Figure 3.1B). CRB flows are preserved as discontinuous patches and erosional remnants in the Seven Devils Mountains at elevation up to ca. 2300 m (Figure 3.1A), providing an important constraint on late Cenozoic crustal deformation and exhumation. The Imnaha flows are found at ∼2250 m on the east side of Hells Canyon, whereas the younger R1 unit of the Grande Ronde Basalts are at ∼1700 m on the west side. The simplest explanation for this is long-wavelength folding and potentially up to 300 m of erosion and removal of the younger, overlying CRB units (Figures 3.2A and 3.4). However, it is possible that a local Imnaha feeder dike fed the flow found in the Seven Devils. The single dike that has been mapped in the Seven Devils is oriented to the NE; an orientation determined through cross-cutting relationships to be later in the Imnaha-Grande Ronde eruption sequence (M. Morriss et al., 2020). Thus, we suggest that this dike likely did not feed the flows we sampled in the Seven Devils and the long wavelength fold hypothesis is favored.

Observed broad warping of the CRB post-dates the main initial pulse of CRB volcanism (16.6-16.1 Ma; Kasbohm & Schoene, 2018). A broad, doubly-plunging antiform cored by basement rocks in the Seven Devils Mountains is revealed by mapping of the reconstructed base-CRB paleosurface (Figures 3.1B, 3.2B, 3.4). Previous workers have proposed a different structural model across the canyon: a large down-to-the-west normal fault which the Snake River follows through the canyon (Gray & Oldow, 2005; Kahn et al., 2020; Wheeler & Cook, 1954), without fully evaluating this structural evidence for such a structure. Published geologic data in Hells Canyon refute this hypothesis and show that a

large-offset normal fault is not present in the canyon, In particular, granitoid bodies and Mesozoic unit contacts correlate across the channel in several locations (Vallier, 1974). Moreover, the isopach map used to construct flow thicknesses by Kahn et al. (2020) does not include key evidence from erosional remnants of the CRB flows high in the Seven Devils Mountains, directly east of the deepest portion of the canyon. The basalt exposures project across the canyon at a gentle westward dip of 3-4° and correlate to west-dipping CRB flows on the west side of the canyon, with no indication of a structural discontinuity or fault offset in the canyon (Figure 3.2A). These new observations show that a long-wavelength doubly-plunging antiform in the Seven Devils Mountains satisfies all the available geologic data and explains the annular pattern of the CRB-basement paleo-surface surrounding the Sevne Devils Mountains (Figure 3.1A).

Post-CRB folding and growth of the doubly-plunging basement cored antiform in the Seven Devils Mountains appears to be related to slip on low- and high-angle normal faults east of the range crest that reactivate older Mesozoic thrust faults (e.g. Gray, Isakson, Schwartz, & Vervoort, 2020; Kauffman et al., 2014). Similar structures to the south and east record orogenic collapse of a formerly convergent orogen (Gray et al., 2020; Tikoff et al., 2001). Extension in Hells Canyon and areas to the east may be driven by clockwise rotation of the Pacific Northwest away from Idaho and stable North America (e.g. Kahn et al., 2020; McCaffrey et al., 2013; Wells et al., 2014). We discuss below how our thermochronology data and models may shed some light on the timing and scope of this folding and fluvial erosion in Hells Canyon.

3.6.2 Timing and Drivers of Hells Canyon Incision

We consider the low-temperature thermochronology data to address the age and incisional history of Hells canyon. The initial cooling signal detected by the ZHe samples in our elevation transect is best explained by post-crystallization cooling. Combined with the existing K-Ar dating, we infer that the pluton cooled at a rate of ∼25 °C Myr^{-1} from between 115.3 Ma to ca. 95 Ma (Figure 3.7A). The next phase of cooling detected by the AHe dates and indicated in inverse thermal models was a period of slow cooling at ∼4.5 °C Ma^{-1} to ∼2.5 °C Ma^{-1} from ∼95-60 Ma, after cessation of activity along the WISZ (Giorgis et al., 2008).

The modeled rate of cooling continues to slow into the Cenozoic (Figure 3.7A). The Eocene period is coincident with deposition of quartzite- and volcanic-clast gravels near the uppermost samples in our profile, indicating these samples were at or near the surface soon after activity in the Challis volcanic field (∼51-43 Ma; R. M. Gaschnig, Vervoort, Lewis, & McClelland, 2010; Reiners, 2005). The 95% credible interval from QTQt on our shallowest sample (Figure 3.7) accommodates this constraint. Slower exhumation during the mid-to-late Cenozoic time period is consistent with the presence of extensive, low-relief surfaces throughout central and western Idaho that probably developed during this time (Larimer et al., 2018; Umpleby, 1912). Much of central Idaho shares the slow Cenozoic cooling history recorded in our samples (Fayon et al., 2017; Kahn et al., 2020). The next large scale tectonic and volcanic event to take place locally is the eruption of the CRB, starting at 16.6 Ma (Kasbohm & Schoene, 2018). Our inverse modeling shows no thermal perturbation associated with this event (Figure 3.7; Kasbohm & Schoene, 2018; S. P. Reidel et al., 2013). Importantly, two samples collected from less than 40 m below the base-CRB surface were excluded from thermal modeling because they appear to have been partially reset by heat related

to CRB emplacement (Figure 3.6) This suggests that reheating of basement was below the detectable threshold for AHe (∼60 °C) for rocks at greater depths.

After 16 Ma, CRB flows in the mid-canyon reach were broadly folded, and pre-CRB basement was incised to a depth of ∼1200 m below the base of the CRB in the deepest part of the canyon (Figure 3.2A). With a geothermal gradient of ∼20 °C km^{-1}, a paleo-depth of ∼2.5 km would be needed to expose rocks with young, reset dates related to canyon carving. Indeed, our inversion results show no change in cooling rate after ∼55 Ma (Figure 3.7). By 16 Ma, all samples are projected to have cooled below the ∼50 °C threshold for detectability with AHe. tT paths for our samples during the Miocene are unperturbed by any rate change in cooling (Figure 3.7). Moreover, the current best estimates on the age of fluvial incision through Hells Canyon suggest linkage between southern Idaho and the Columbia River was established between ∼4 and 1.6 Ma (Othberg, 1994; Staisch et al., 2017). Incision-driven cooling would therefore occur after sampled apatites cooled below the detectable threshold for AHe. Inverted tT paths display constant cooling rate over the past ∼5 Myr (Figure 3.7A). These results indicate that our samples do not record cooling related to either post-CRB folding and related fluvial incision of Hells Canyon. However, we can still build on the QTQt inversion results. We develop a set of numerical experiments below to test if faulting or river incision could still influence the observed distribution of sample dates even if neither of these geologic events are directly detectable through a formal inversion scheme.

We employ a coupled forward modeling approach combining HeFTy and Pecube to explicitly test three different hypotheses for canyon formation and exhumation (1) Old Canyon model in which Hells Canyon developed since 60 Ma (Figure 3.8A); (2) Young Canyon model with canyon formation taking place at 4 Ma (Figure 3.8B); and (2) a Faulted Canyon scenario in which slow cooling

Model Type	Uplift Rate Pre-60 (Ma) (mm yr^{-1})	Uplift Rate Post-60 (ma) (mm yr^{-1})	Geotherm (°C km^{-1})	Pecube χ^2-reduced	Average	HeFTy χ^2-reduced	Average	% Difference
Old Canyon	0.15	0.025	20	23.27		27.54		
Old Canyon	0.15	0.025	25	12.25		16.59		
Old Canyon	0.15	0.025	30	8.53		12.32		
Old Canyon	0.18	0.025	20	22.05		25.28		
Old Canyon	0.18	0.025	25	11.91		15.57		
Old Canyon	0.18	0.025	30	8.49		12.05		
Old Canyon	0.2	0.025	20	26.75		32.39		
Old Canyon	0.2	0.025	25	13.54		19.37		
Old Canyon	0.2	0.025	30	8.94	15.08	13.45	19.40	25%
Young Canyon	0.15	0.025	20	9.29		18.63		
Young Canyon	0.15	0.025	25	8.55		16.25		
Young Canyon	0.15	0.025	30	17.78		21.62		
Young Canyon	0.18	0.025	20	8.95		17.25		
Young Canyon	0.18	0.025	25	8.64		16.06		
Young Canyon	0.18	0.025	30	17.98		21.82		
Young Canyon	0.2	0.025	20	8.83		16.61		
Young Canyon	0.2	0.025	25	8.72		15.98		
Young Canyon	0.2	0.025	30	18.09	11.87	21.99	18.47	43%
Faulted Canyon	0.15	0.025	20	12.13		27.16		
Faulted Canyon	0.15	0.025	25	10.94		19.36		
Faulted Canyon	0.15	0.025	30	18.25		20.59		
Faulted Canyon	0.18	0.025	20	9.65		22.55		
Faulted Canyon	0.18	0.025	25	10.11		17.33		
Faulted Canyon	0.18	0.025	30	18.12		20.38		
Faulted Canyon	0.2	0.025	20	8.87		20.48		
Faulted Canyon	0.2	0.025	25	9.98		16.70		
Faulted Canyon	0.2	0.025	30	18.20	12.92	20.47	20.56	46%

Table 3.1. Forward modeling results from just Pecube and the coupled Pecube-Hefty method. The average percent difference between the two model outputs is significant, nearly 50%.

is interrupted by faulting at 10 Ma (Figure 3.8C). These models excluded grain BRS49a, which created unstable results when evaluated with the $\chi^2_{reduced}$ statistic. The coupled model also allows us to evaluate the difference in modeling results there is by including RDAAM and ZRDAAM in a forward model. We calculate the average difference in the $\chi^2_{reduced}$ statistic (equation 3.2) between Pecube models and those run with the Pecube-HeFTy approach. The range in $\chi^2_{reduced}$ (Table 3.1) between the Pecube models with radiation damage taken into account and those without radiation damage varies from 25% to as much as 46% difference in $\chi^2_{reduced}$ (Table 3.1). Thus, we find that accounting for the effects of radiation damage are important.

The best performing model scenario using the coupled Pecube-HeFTy method is the one in which canyon carving started at 4 Ma (Table 3.1). The single best performing model is the Old Canyon model with a geotherm of 30 °C km^{-1}

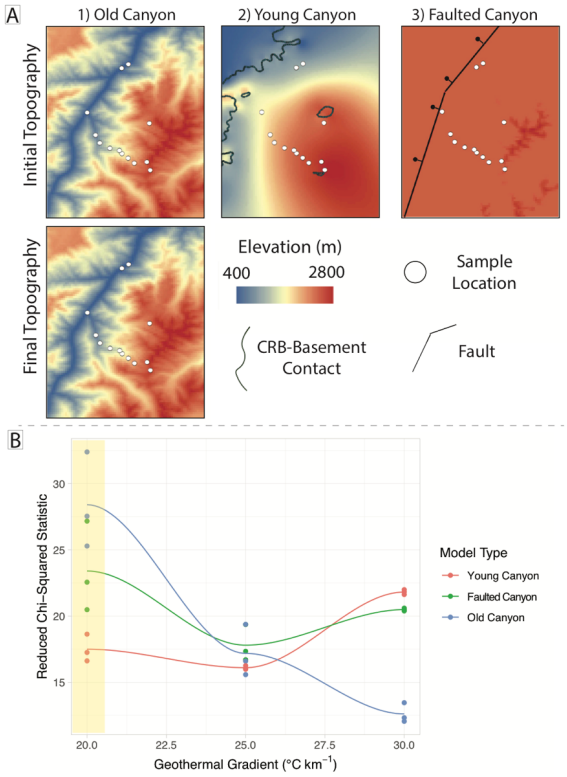

Figure 3.8. (A). The three scenarios evaluated through our Pecube forward models. The top row is the initial topography, and the bottom figure is the final topography for each Pecube Model. 1) Hells Canyon is an old feature, exhuming steadily since 60 Ma. 2) The CRB surface is undissected until 4 Ma, when Hells Canyon starts incising to its present morphology. 3) The flat CRB surface is present and undissected until a fault in Hells Canyon is initiated at 10 Ma, offsetting the CRB surface and incising Hells Canyon. **(B)** Model results from Pecube, with geothermal gradient plotted against the $\chi^2_{reduced}$ statistic. Each point is the summary of 9 individual samples. The colors correspond to the three model types discussed above. The colored lines are a LOESS smoothing, applied for the sake of visualizing the trends in each model run. Although the best performing result is the Old Canyon model with a geothermal gradient of 30 °C km^{-1}, QTQt modeling (Figure B.6) indicates a thermal gradient of ∼20 °C (yellow shading). Thus the Young Canyon model is favored by this analysis.

(Table 3.1; Figure 3.8). In our coupled model results, the poorest performing suite of simulations, on average, is the Faulted Canyon model (Table 3.1). To properly interpret these results we need to incorporate another constraint from our QTQt inversions to make an informed decision on which forward model best fits our data. Inverse model results predict that our samples experienced an average geothermal gradient of ∼18 °C km^{-1} for the past 110 Ma (Figure B.6). This limits our focus to the forward models with a 20 °C km^{-1} geotherm. The suite of models with the lowest $\chi^2_{reduced}$ statistic under this geothermal gradient is the 4 Ma Young Carving scenario (Figure 3.8B). This age for the canyon is consistent with surrounding geologic evidence discussed above.

With ∼1700 m of structural relief across the fold combined with potentially 300 m of Grande Ronde R1 strata eroded from the fold crest and at most 1300 m of fluvial incision, there has not been enough total incision in Hells Canyon to produce a cooling signature in the AHe system. However, the forward modeling suggests that the thermal structure of the canyon has been influenced by rapid incision since ∼4 Ma.

3.7 Conclusions

Mapping of the reconstructed base-CRB paleosurface reveals a ca. 60-km long doubly plunging antiform with ∼1700 m of structural relief and a N-trending axis that follows the crest of the Seven Devils Mountains We document incision of up to ∼1.3 km in Hells Canyon that as occurred in the past ca. 4 Myr. Apatite and zircon U-Th/He thermochronology results do not reflect the influence of canyon carving because the depth of young river incision is shallower than the partial retention zone for the AHe system. The data do record a history of rapid cooling related to Cretaceous pluton emplacement and tectonic activity in the Western

Idaho Shear Zone. Inverse thermal modeling indicates that this region experienced very slow exhumation during most of Cenozoic time. Further hypothesis testing with a coupled Pecube-HeFTy forward model supports a history of slow Cenozoic erosion until the start of rapid incision at ∼4 Ma.

3.8 Bridge

In Chapter **??**, I tested hypotheses linked to the creation of Hells Canyon. I used low-temperature thermochronology to investigate how old the canyon could be and test whether or not an observed normal fault could be at play in the Canyon's creation. This Chapter discussed the crustal scale cooling effects of canyon creation and linked faulting with subsequent fluvial incision. The landscape response to incision was not discussed in great detail. This was left to to Chapter IV.

In this chapter, I worked with Drs. Lydia Staisch, Brian Yanites and Nate Mitchell at the USGG and Indiana University – respectively, to examine the landscape response to the capture of Lake Idaho. I specifically looked for transient signals in the form of knickpoints that could record incision tied to the Snake River.

CHAPTER IV

DRAINAGE INTEGRATION AND CANYON INCISION: A HELLS CANYON STORY

4.1 Summary

The largest landscapes on Earth (e.g. the highest mountains or deepest canyons) often provide a window into processes at work beneath the surface. Quantitative analysis of these landscapes provides a better understanding of the rates at which our planet changes. Despite recent advances in methods and more remote sensing data, dramatic landscapes in the interior Pacific Northwest remain unstudied or understudied. Hells Canyon, the deepest canyon in North America, is one such landscape. Its exact age is unknown and the processes that drove the Snake River to incise ∼2.2 km below the crest of the Seven Devil Mountains remain the subject of debate. In this study, I seek to provide the first quantitative geomorphological study of the Snake River through Hells Canyon.

The general consensus in the geologic literature is that the canyon's incision relates to the capture of Lake Idaho, an intermittently terminal lake which developed in the western Snake River Plain from ∼10 – ∼3 Ma. To test this hypothesis, we examined 97 tributary streams for knickpoints which would indicate a transient signal responding the capture of Lake Idaho. We also incorporate a series of linked 1-D stream power based models to measure the expected landscape response to the capture and integration of such a large drainage area. We identified a distinct knickpoint signal through Hells Canyon. We hypothesize this transient signal was created as the result Lake Idaho overtopping its damming sill and incising. The large increase in drainage area created the knickpoints we observe on tributary basins; this result is supported by our 1-D modeling results. Projections of relict fluvial reaches upstream of the knickpoints indicates that, at maximum,

the Snake River has incised ∼1 km since this capture event. Cosmogenic burial data from caves have yet to be returned from the analyzing laboratory, but we intend to leverage these data to further evaluate the age of Hells Canyon. Our results indicate that Hells Canyon is a dynamic and rapidly evolving landscape that continues to respond to regional scale drainage reorganization and integration.

4.2 Introduction

The deepest canyons in the world are often loci for study by geomorphologists hoping to understand processes from fluvial geomorphology to geodynamics. Any region of large and stunning changes in topography could indicate multiple processes are at work (e.g. geodynamics coupled with erosion). The processes that contribute to the formation of the world's deep canyons can range from: rapid uplift in geologically fast paced regions of the world where the surface of the Earth is deformed by 10s of mm yr^{-1} (e.g. the Ganges, Indus, Cotahuasi-Ocona, and Tsang-Po gorges; Finnegan et al., 2008; Schildgen et al., 2007), to river capture and integration (e.g. the Yellow and Yangtze rivers in China Harkins, Kirby, Heimsath, Robinson, & Reiser, 2007; Rohrmann, Schwanghart, & Kirby, 2018).

For over a century, the bulk of geomorphic inquiry into deep canyons in the contiguous United States has been focused on the history and evolution of the Grand Canyon, starting with Powell (1875). Since then, the Grand Canyon has seen an abundance of creative geomorphic and geodynamic investigations. Some of this work includes dating of fill terraces through the canyon (e.g. Pederson et al., 2006), dating water interacting speleothems (e.g. Polyak, Hill, & Asmerom, 2008), significant work on understanding the structure of the crust and mantle beneath the canyon (e.g. K. E. Karlstrom et al., 2012; Moucha et al., 2009), and many other

techniques and studies summarized by Darling and Whipple (2015) and references therein. Despite this focus on the Grand Canyon, the deepest canyon carved by a river in North America is Hells Canyon (Figures 4.1 and 4.2). This canyon, located on the Oregon-Idaho border, is 600 m deeper than the Grand Canyon and has not received the same rigorous examination (Figure 4.3). In fact, the timing of incision of Hells Canyon is poorly constrained, as are the mechanisms which drove that incision. These outstanding questions drove the inquiry developed herein.

Recent work in northeastern Oregon and west-central Idaho has touched on the formation of Hells Canyon (Larimer et al., 2018; N. Mitchell & Yanites, 2019; M. C. Morriss & Wegmann, 2017). These studies indicate potential impact of lithospheric delamination involvement in the geomorphology of the region (Larimer et al., 2018). There is already ample evidence of the interplay between the Yellowstone Plume and regional geology through the eruption of the Columbia River Basalts (CRBG; ∼16.7–6 Ma; Kasbohm & Schoene, 2018; S. P. Reidel et al., 2013). These basalt flows significantly altered the geomorphology of the region, damming and rerouting rivers throughout their eruption (Fecht, Reidel, & Tallman, 1987; S. P. Reidel & Tolan, 2013b). Moreover, there was a large lake – Lake Idaho, in southern Idaho present from ∼11 Ma to perhaps as recently as ∼3 Ma (Figure 1; Wheeler & Cook, 1954; S. H. Wood & Clemens, 2002). Distinct fossil fauna within this lake are evidence that the Snake River lacked an integrated connection between the continental interior and the inland Pacific Northwest (Smith et al., 2017).

Hells Canyon sits between the Northern Rocky Mountains and the inland Pacific Northwest. The canyon is a key biological passageway for numerous aquatic fish species between low-elevation ocean draining rivers and those draining colder alpine regions of the continental interior (Smith et al., 2002, 2017). The canyon is also a geographic barrier for small mammals and amphibian species, potentially

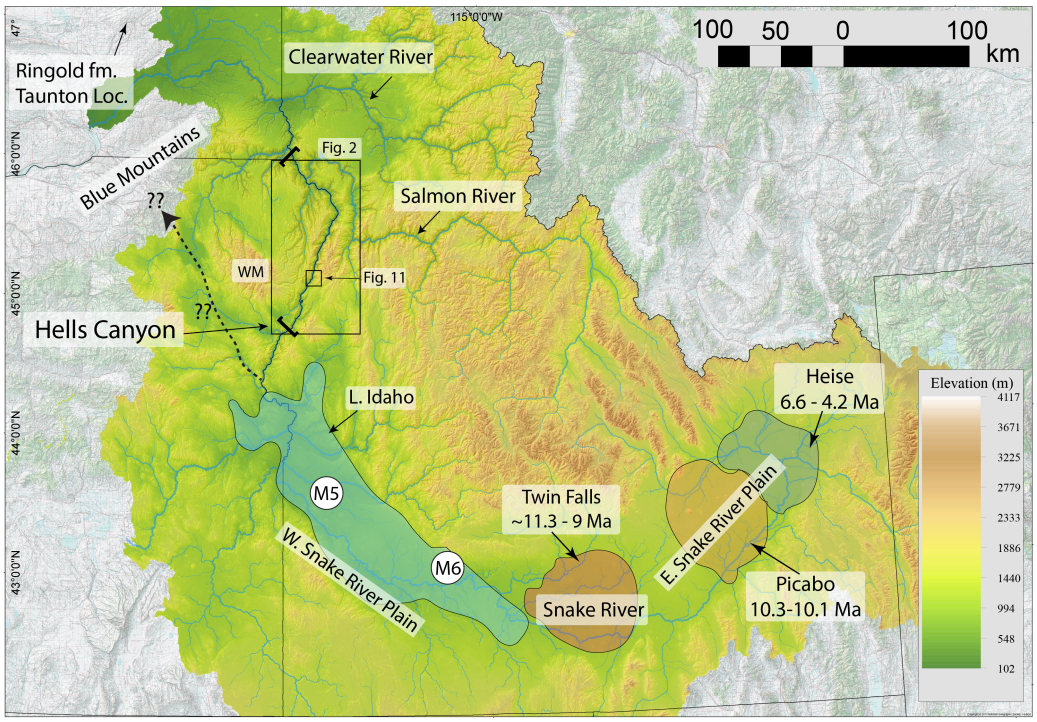

Figure 4.1. Map of Snake River catchment and major geographic features pertinent to this investigation. The geographic areas of the Western and Eastern Snake River Plain are highlighted. Major eruptive centers for the Yellowstone Hotspot are highlighted across the central and eastern Snake River Plain. The Twin Falls volcanic center (∼11.3-9 Ma); the Picabo volcanic field (10.3-10.1 Ma), and the Heise volcanic field (6.6-4.2 Ma; Ellis et al., 2010; Morgan & McIntosh, 2005). The approximate area for the Miocene-Pliocene Lake Idaho is shown in blue (Smith et al., 2017). The dashed line is a hypothesized path for the Snake River preceding the eruption of the Grande Ronde Basalts (S. P. Reidel & Tolan, 2013a). The Taunton fossil locality is where fossil evidence of an established fluvial connection between the western Snake River Plain and Columbia Basin was first discussed (Smith et al., 2002). WM is the Wallowa Mountains; Hells Canyon is located between the two bold brackets. Areas encompassed by Figure 4.2 and 4.11 are also highlighted.

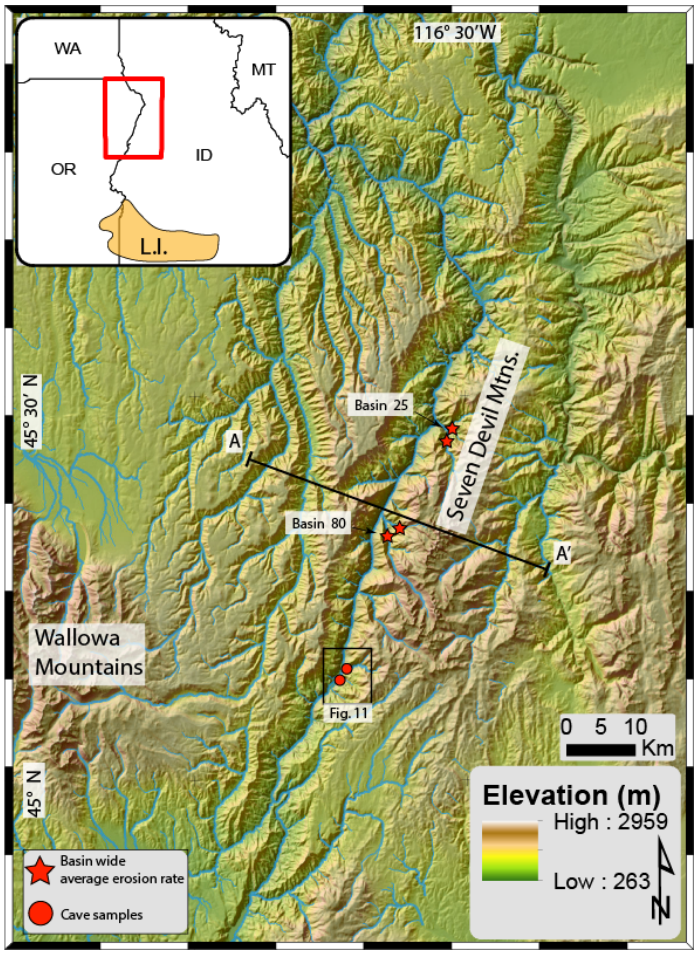

Figure 4.2. Topography in the greater Hells Canyon Region. The canyon is carved between two mountain ranges: the Wallowa Mountains (OR) and the Seven Devil Mountains (ID). The canyon corridor is quite narrow, ranging from 8 to 16 km wide. Inset. Map showing position of main figure and region in which Lake Idaho sediments are maps (Wood and Clemens, 2002). Cross-section **A-A'** is a swath-profile shown in Figure 3. Stars show sample locations for basin-wide average erosion rates collected by (Belmont, 2015). Circles are fluvial sediments collected from caves as part of this study for detrital zircon and cosmogenic burial dating.

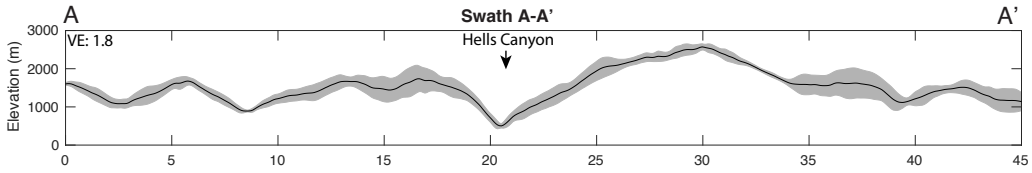

Figure 4.3. Swath profile across Hells Canyon for 10 km wide window. The canyon is asymmetric, with the east side being higher than the west side. In Chapter 2, I hypothesized that 0.5 km of this topographic asymmetry is due to anticlinal warping, which offsets the CRBG across the canyon.

driving genetic divergence across the region (Demboski & Sullivan, 2003; Nielson et al., 2006). Parsing the timing of when the paleo-Snake River integrated into the larger Columbia River network is key to understanding the evolution of anadromous fish species now common in the region and could help with models of biological diversification across the Rocky Mountain-Inland Northwest region (e.g. Spruell et al., 2003).

The dynamic geology and geomorphology surrounding Hells Canyon are key to understanding the canyon's history. Herein, we reveal a systematic geomorphic signal of the Snake River integration into the Columbia River system in the Hells Canyon landscape. Through a combination of cosmogenic basin-wide average erosion rates and cosmogenic burial dates, we provide estimates on the timing of Snake River incision in Hells Canyon. Finally, we test explicit models of stream capture and knickpoint generation, which further supports an observed pattern of knickpoints spread throughout tributaries to the Snake River. These knickpoints recreate a relict drainage network which preceded the modern canyon's formation.

4.3 Geologic Background

Hells Canyon is carved through 16.6-16.1 Ma basalt flows of the CRBG (Kasbohm & Schoene, 2018; Lewis et al., 2012; Walker & MacLeod, 1991). Beneath

the CRBG is a series of Triassic and Permian age accreted terranes (LaMaskin, Vervoort, Dorsey, & Wright, 2011; Vallier, 1977). These terranes docked with North America in the Jurassic and were stitched together by granitoid plutons (R. M. Gaschnig et al., 2017; Schwartz et al., 2014). By the Eocene, some of these granitoid bodies were exposed at the surface in the bottom of E-W oriented river channels transporting Proterozoic quartzite and Challis volcanic cobbles and boulders from the east (Allen, 1991; Cowan & Reiners, 2004). These deposits are now preserved as inverted topography in the Wallowa Mountains — beneath the oldest flows of the CRBG (Allen, 1991).

Thermochronometric evidence supports a period of slow exhumation ($\sim$0.02 mm yr$-$1) across the region throughout the post-Eocene Cenozoic (Fayon et al., 2017, Chapter 2). During this period, much of central Idaho may have been part of a large Altiplano-like feature, the Nevadaplano, created as a result of crustal thickening during the Sevier and Laramide orogenies (DeCelles, 2004; Fayon et al., 2017; Long, 2012). Portions of this high-elevation, low-relief landscape may persist to this day in central Idaho (Larimer et al., 2018; N. Mitchell & Yanites, 2019). Before the eruption of the CRBG, the western margin of this plateau developed canyons with $\sim$600-1200 m of relief, which drained to the west (Bond, 1963; Holden & Hooper, 1976). The Imnaha basalts ($\sim$16.6 Ma) partially filled these paleo-canyons, and the Grande Ronde Basalts (16.5-16.1 Ma) blanketed any remaining topographic relief (V. Camp, Reidel, et al., 2017; S. P. Reidel & Tolan, 2013a).

The exact course of the paleo-drainages across NE Oregon before the eruption of the Columbia River basalts is subject to some debate. S. P. Reidel and Tolan (2013b) argue that the pre-CRBG Snake River may have crossed Oregon in a more direct NW route. Meta-volcanic and meta-sedimentary clasts found in the Umatilla Basin of SE Washington which are similar to accreted terrane

rocks in northeastern Oregon and western Idaho were hypothesized to have been deposited by a pre-CRBG Snake River that cut more directly across NE Oregon (Figure 4.1; Tolan, Lindsey, & Beeson, 1996). This hypothesized route is coincident with a corridor of thicker CRBG flows that approximately follows this course from SW Idaho to SE Washington (S. P. Reidel & Tolan, 2013b). This route was likely cutoff by the eruption of the Grande Ronde Basalts (16.5-16.1 Ma; Kasbohm & Schoene, 2018) of the uplift of the Blue Mountains (Figure 4.1). There is some genetic evidence of a more north-westly route across NE Oregon preserved in the Mitochondrial DNA of Bull Trout distributed throughout the Columbia-Snake watershed. Mitochondrial DNA analysis of Bull Trout reveals close genetic ties between fish in the Snake River and those in central Oregon, located in exactly the region S. P. Reidel and Tolan (2013b) hypothesized the proto-Snake once flowed (Figure 14.1; Spruell et al., 2003).

4.3.1 Mio-Pliocene Lake Sedimentation

The area directly upstream of Hells Canyon contained the Lake Idaho lacustrine system throughout the Miocene (∼10 Ma), Pliocene, and perhaps into the earliest Pleistocene, making it a natural location to search for a sedimentological signal of drainage integration (Clemens & Wood, 1993). Geochronology on the youngest lacustrine units in the basin could provide a maximum age for the integration of the Snake River through Hells Canyon.

The beginning of sedimentation at ∼10 Ma in the western Snake River Plain did not coincide with the eruption of the Grande Ronde Basalts (S. H. Wood & Clemens, 2002). The lack of any extensive lake sediments between 16-10 Ma in this region indicates that if there was a paleo-Snake River at this time it may have flowed out to the Ocean, flowed east, or drained internally elsewhere. By 11 Ma,

normal faulting began in the western Snake River Plain, opening accommodation space for sediment deposition (Ekren, McIntyre, Bennett, & Marvin, 1982). Lake sedimentation in the western Snake River Plain began with the Chalk Hills formation between ∼10 and 9 Ma (Ekren et al., 1982; S. H. Wood & Clemens, 2002). Sedimentation continued as faulting and some folding disturbed the oldest beds of the Chalk Hills formation. By the middle Miocene, an erosional surface truncates the upper Chalk Hills formation. This indicates a decrease in lake level, exposing the Chalk Hills sediments to surface conditions (S. H. Wood & Clemens, 2002). Lake shrinkage was followed by a transgressive event in which lake level rose by ∼200 m. This period is recorded by the deposition of ooilitic sands along the lake margins and mud and clay in the mid-basin. Deposits from this time period are mapped as the Terteling Springs Formation, ranging in age from 10.7 ± 0.6 - ∼6 Ma (Beranek, Link, & Fanning, 2006; S. Wood & Burnham, 1987).

Lake Idaho reached its highest elevation between ∼11 and 6 Ma, ∼1100 m a.s.l., as measured from modern mapping of lake deposits (S. H. Wood & Clemens, 2002). Lake levels began to decline after ∼6 Ma. This period is recorded by the deposition of the 60 m thick sandstone of the Glenns Ferry Formation was deposited across the basin. This unit records rivers prograding into the basin which the lake had formerly occupied. One hypothesis for lake levels declining at this time is either the formation of a temporary outlet for Lake Idaho — perhaps into northern Nevada, or a shift in the continental divide to the east, robbing Lake Idaho of some of its primary drainage area (S. H. Wood & Clemens, 2002). The shift in headwaters of the paleo-Snake may coincide with the Heise Volcanic field in the eastern Snake River Plain (Figure 4.1). There is no evidence that the lake was draining through Hells Canyon at ca. 6 Ma, since deposits of this age in downstream basins do not contain detrital zircons from the western Snake

River Plain (Staisch et al., 2017, 2019). Moreover a persistent outlet through Hells Canyon would likely preclude another significant rise in lake level discussed below.

At ∼4.5 Ma the lake rose again and sediment was deposited on top of the Chalk Hill units exposed along the basin margins (S. H. Wood & Clemens, 2002). This increase in the size of the lake is thought to coincide with an increase in drainage area tied to an eastward migration of Yellowstone Hotspot (Figure 4.1; S. H. Wood & Clemens, 2002). The final major deposit found in the western Snake River Plain is the Tuana gravels, which are a cut and fill sequence of coarse sediment exposed in the south-central Snake River Plain (Beranek et al., 2006; Sadler & Link, 1996). These deposits have been interpreted as post-dating the draining of Lake Idaho and appear contemporaneous with the Tenmile Gravels exposed in the northwestern Snake River Plain (Othberg, 1994). Both units are believed to represent the renewed progradation of former lake draining river systems. Existing age control on the Tuana gravels is from detrital zircons which date to as young as ∼2.5 Ma (Beranek et al., 2006). Because this age is a maximum depositional age, the gravels themselves could be younger than 2.5 Ma. The Tuana gravels are found across the basin and extend to nearly the elevation of the modern Snake River. These gravels are one of the sedimentary units most likely to represent a time period after the integration of the Snake River through Hells Canyon (Othberg, 1994; S. H. Wood & Clemens, 2002).

4.3.2 Paleontological Evidence

Pliocene sedimentary units in the Pasco Basin area of central Washington contain a tantalizing species development story germane to the incision of Hells Canyon (Table 4.1). During Pliocene deposition of the White Bluffs section of the Ringold Formation, there are no paleontological commonalities between the

fish fossils found in central Washington and those in the Lake Idaho deposits from this time period (Smith et al., 2002). This section of the Ringold has been dated with U-Pb zircon dating from tephras and ranges in age from ∼9.5 – 6.7 Ma (Staisch et al., 2017). However, the younger Taunton locality, higher in the Ringold section, does contain fewer than a dozen bones and teeth from 3 species from the family Cyprinidae endemic to the western Snake River Plain which had never before been seen in the Columbia Basin (Figure 4.1; Smith et al., 2002). *Klamathella milleri,Acrocheilus alutaceus*, and *Lavinia hibbardi* were all abundant in the western Snake River Plain in the Miocene and Pliocene and only appear in the youngest Tauton sediments (Figure 4.1; Smith et al., 2002). New U-Pb zircon dating from a tephra within the Taunton section dates this unit as 3.48 ± 0.11 Ma (Staisch et al., 2017). However, the exact signal of capture and connection remains enigmatic because the detrital zircon record of the younger Ringold units do not contain zircons from the western Snake River Plain, but they do contain zircons from the eastern Snake River plain. This suggests, despite fossil evidence to the contrary, that there may not have been a direct fluvial connection between the western Snake River Plain and Washington through Hells Canyon at ca. 3.5 Ma (Staisch et al., 2019). It is also possible that more work may be needed to refine fossil identification or there was a short-lived alternate outlet from Lake Idaho (see Van Tassell et al., 2001).

4.4 Driving Question

A landscape with as much relief as Hells Canyon warrants thorough investigation and hypothesis testing (Figure 4.2 and 4.3). The available literature provides a clear model for canyon formation, which I herein set out to test.

Age (Ma)	Uncertainty (Ma)	Evidence	Maximum/Minimum	Up/Down	Location	Reference
3.48	0.11	Detrital zircon age in the Tauton section of Ringold formation. A section which is found to have similar fish to the WSRP, but no zircons from the western Snake River Plain	Maximum age	Downstream	Taunton, Washington	Staisch et al. (2017)
2.5		Age of the Tuana gravels which prograde into the basin formerly occupied by Lake Idaho. Interpretted to mark the end of the lake and beginning of a period of sedimentation across the basin.	Minimum Age	Upstream	Hagerman, Idaho	Beranek et al. (2006)
1.6	0.1	Age of the Tenmile Gravel in the northwestern Snake River Plain. From Ar/AR basalt flow of Pickles Butte that caps a terrace. The terrace had already been incised by this point, so this is a minimum age.	Minimum Age	Upstream	Marsing, Idaho	Othberg (1994)
3.4	0.6	AHe cooling age from in Hells Canyon, showing that rocks in that region of the canyon cooled below ~60 °C at this point in time	Potential age of canyon formation	In Hells Canyon	Pittsburgh Landing	Kahn (2018)
3.7 - 3.8		Fish fossil ages in Grand Ronde Valley	Minimum Age	Hells Canyon adjacent	Imbler, OR	Van Tassel et al. (2001)

Table 4.1. Constraints on Age of Hells Canyon

Moreover, the driving question: When did Hells Canyon form? is a key line of inquiry.

After the eruption of the CRBG, a north-northwest flowing river system developed in northern Idaho and SE Washington. This "Clearwater-Salmon" river-system incised into the CRBG and underlying rocks. During this time period an equivalent south-flowing river system would have become established, flowing into Lake Idaho (Figure 4.4A). These two former drainage networks were not integrated into to the Snake River catchment through Hells Canyon until the capture of Lake Idaho (Figure 4.4B). Capture was likely initiated by filling of the lake to the elevation of the drainage divide between the two catchments and its overtopping. This mode predicts an observable distribution of transient signals or knickpoints in the tributaries to Hells Canyon.

We hypothesize that a significant amount of the relief in Hells Canyon has been carved following the Pliocene or Pleistocene capture of Lake Idaho and that we will see a distinct pattern of knickpoints reflecting this drainage integration.

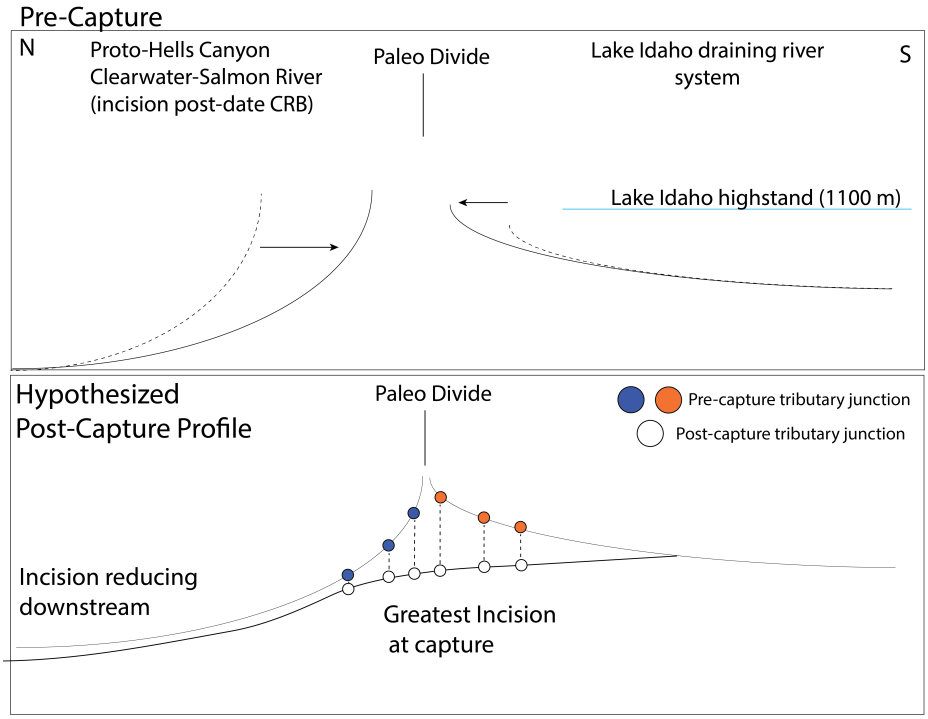

Figure 4.4. Conceptual model for **Pre-capture landscape**. A north-flowing Clearwater-Salmon river is connected to the Columbia River. A small drainage network develops flowing to the south and into Lake Idaho. These two networks incise into Miocene basalt plateau. **Post Capture**. The two river networks are integrated and have incised through the intervening divide. Tributaries formerly flowing into each separate network have incised to keep pace with the mainstem river.

Below, I setup to test this hypothesis. Evaluating this hypothesis involves: (1) numerical landscape evolution modeling; (2) observations of the geomorphology in the landscape; (3) detrital zircon provenance studies from cave sands, and (4) cosmogenic burial dating of cave-bound sediment.

4.5 Methods

4.5.1 Stream Power

Landscapes are formed by the balance between competing processes of erosion and uplift. Geomorphologists have developed a series of empirical and numerical based relationships that describe this competition on both hillslopes and in river channels. The past 25 years has seen rapid advancement in the field of fluvial tectonic geomorphology, with the use of numerical models of detachment-limited fluvial systems (Perron & Royden, 2013; Tucker & Whipple, 2002; Whipple & Tucker, 1999). These numerical models coupled with higher resolution topographic datasets allow for a robust understanding of tectonic and geomorphic phenomenon that affect that landscape over large areas. Hypothesis tests can now be calibrated with parameters such as normalized channel steepness (e.g. k_{sn} or slope in χ-z space). The system of detachment limited erosion models begins with a model referred to as the stream power based erosion model:

$$U - E = \frac{dz}{dt} = U - KA^m S^n. \tag{4.1}$$

This equates changing elevation through time $\frac{dZ}{dt}$ to rock uplift rate (U), m and n describe drainage area (A) and slope (S) dependencies, and K is erosional efficiency (Crosby & Whipple, 2006; Tucker & Whipple, 2002; Whipple, 2002; Whittaker, Attal, Cowie, Tucker, & Roberts, 2008). K incorporates many phenomenon, ranging from rock erodibility, climate, to erosional process (Whipple,

2004). At steady-state, erosion (E) and uplift (U) are balanced, allowing one to solve for slope:

$$\frac{dz}{dx} = S = \left(\frac{U}{K}\right)^{\frac{1}{n}} A^{\frac{-m}{n}} \tag{4.2}$$

(Flint, 1974; Hack, 1957; Howard & Kerby, 1983; Tucker & Whipple, 2002). $\frac{m}{n}$ is often replaced with θ or channel concavity, and $\frac{U}{K}^{\frac{1}{n}}$ is replaced with k_s or the channel steepness index:

$$k_s = SA^{\theta} = \left(\frac{E}{K}\right)^{\frac{1}{n}} \tag{4.3}$$

ks is a measure of river steepness normalized to drainage area. This index is easily derived from a digital elevation model (DEM). Equation 4.2 links the slope of a river to its uplift rate and drainage area, and equation 4.3 connects the DEM derived k_s term to measurable erosion rates (E). Empirical studies of ks and erosion rates note an observed scaling (Kirby & Whipple, 2012; Kirby, Whipple, Tang, & Chen, 2003). The scaling between k_s and erosion rates is often described as mildly non-linear relationship in fast eroding environments (e.g. eastern Tibet Ouimet, Whipple, & Granger, 2009), and potentially linear in slow eroding ones (e.g. the Appalachians S. R. Miller, Sak, Kirby, & Bierman, 2013). θ both through theory and many empirical observations has been shown not to vary with uplift or erosion (Kirby & Whipple, 2012; Roe, Montgomery, & Hallet, 2003; Whipple & Tucker, 1999).

Equation 4.3 has been a key driver of much geomorphological inquiry over the past 2 decades as it allows for metrics readily measurable from a DEM to be compared directly to erosion rates (Duvall, Kirby, & Burbank, 2004; Kirby et al., 2003; Whittaker, 2012; Whittaker et al., 2008; Wobus et al., 2006, and references therein). Additionally, the scaling between ks and erosion allow map-view patterns

in k_s to highlight tectonic gradients and even active faults (Kirby, Whipple, Kirby, Studies, & Barbara, 2001; Wobus et al., 2006). To allow for easy comparison between drainage basins, owing to the covariance between k_s and θ, a reference concavity or θ_{ref} is often used (Kirby & Whipple, 2012). Many studies choose a value of $\sim$0.45 for a θ_{ref}, which allows the author to measure normalized channel steepness or k_{sn}. This value can be calculated for segments along a river for easy visual comparison of channel steepness.

This numerical framework, and the ability to measure channel steepness from a DEM allows for the hypotheses in the Hells Canyon region enumerated above to be tested against the actual landscape. Another common prediction from the stream power model presented above is that changes in boundary conditions are transmitted upstream in the form of distinct changes in river channel slope, or knickpoints (Niemann, Gasparini, Tucker, & Bras, 2001; Rosenbloom & Anderson, 1994). In the context of the equations above, knickpoints may separate regions of higher k_{sn} and lower k_{sn}. This relationship also extends to erosion rates. Areas below a knickpoint, with higher ksn, are expected from eq. 4.3 to have higher rates of erosion than areas with lower ksn above the knickpoints (Kirby & Whipple, 2012; Wobus et al., 2006). One important caveat is if the knickpoint is a vertical step knickpoint, as classified in slope-area space. This class of knickpoints does not represent a break in the slope-area scaling for the catchment and therefore is less likely tied to boundary condition changes (see Kirby & Whipple, 2012, for more discussion on knickpoints).

One ongoing challenge with the stream power approach discussed above has been the use of the derivative slope with drainage area, which results in a loss of topographic information and introduction of noise. This issue was recently

simplified by the introduction of the χ metric developed by Harkins et al. (2007) and further explored by Royden and Perron (2013), developed below:

$$z(x) = z\left(x_b\right) + \left(\frac{U}{K}\right)^{\frac{1}{n}} \int_{x_b}^{x} \frac{dx}{A(x)^{m/n}} \tag{4.4}$$

In equation 4.4, z is elevation along a channel and x_b is baselevel for a particular stream. x is the distance upstream from the mouth of a particular stream. The integrand is replaced with the variable χ in equation 4.5, below:

$$z(x) = z\left(x_b\right) + \left(\frac{U}{K A_0^m}\right)^{\frac{1}{n}} \chi \tag{4.5}$$

A_o is introduced as a reference drainage area, and the equation now has the form of a line, plotting z – elevation – against χ. When A_o is assumed to be 1 m^2, the slope of this line is the same as k_{sn} as determined from slope-area data. The variable χ is also readily calculated from a DEM, and when $n = 1$, χ is a stand-in for the response time of a knickpoint to propagate upstream (Royden & Perron, 2013). Under steady-state conditions a river long profile should plot in $\chi - z$ space as a straight line. The steepness of a river profile examined in $\chi - z$ space (visa vis k_{sn}) is a proxy for uplift or erosion rate, if K is constant across the length of the profile (Perron & Royden, 2013). These equations become relevant for Hells Canyon as we aim to pick out knickpoints along the tributaries to Hells Canyon and evaluate any patterns within these knickpoints in the context of our end member models.

4.5.2 Numerical Modeling

In order to better understand how landscapes respond to a stream capture at their headwaters, we implemented a first-order upwind finite difference scheme model. This model incorporated nine streams converging on a trunk stream

to simulate the stream-power predicted solution to a drainage area integration (Figure 4.5). The mainstem of the modeled river network could be thought of as the north flowing Clearwater-Salmon river which is connected ultimately to the Columbia River (Figure 4.5). The drainage area addition takes place at the headwaters of this river system and the tributary streams evolve as predicted by the stream power model (eq. 4.3). Several different parameters of each model were adjusted in various model runs to evaluate how the network responds. Model parameters include a dx spacing of 50 m, and a dt time interval of 10 years. The model runtime is 5 x 10^6 years, with an output plot for evaluation generated every 1 x 10^6 years. First, the drainage area gain at the headwaters of the trunk stream alternated through 10^5 and 10^8 km^2. The model was run with the slope parameter n with values of 0.67, 1, and 1.5, and the area parameter m is taken as 0.5 * n. The erosional efficiency term K was evaluated with the following values: 4.76 * $10^{-6} m^{0.33}$ yr^{-1}, 1 * $10^{-6} yr^{-1}$, and 4.42 * $10^{-8} m^{-0.5} yr^{-1}$. Finally, the uplift rates for the model domain pre-capture and post-capture were modulated. In one set of simulations, models were run with a background uplift rate constant at 0.1 mm yr^{-1} across the pre-capture landscape and the post-capture landscape. In another slew of models, the uplift rate after capture accelerated to 0.5 mm yr^{-1}. These changes in parameter space provide 24 different models from which we can evaluate tributary response to drainage integration and baselevel lowering.

The drainage area for each model was created using Hack's Law (Hack, 1957):

$$A(\ell) = C\ell^h \tag{4.6}$$

where ℓ is the distance downstream, C is a coefficient [ℓ^{2-h}], and h is donated as the Hack exponent. C and h are taken to be 1 $m^{(2-h)}$ and 1.8. These

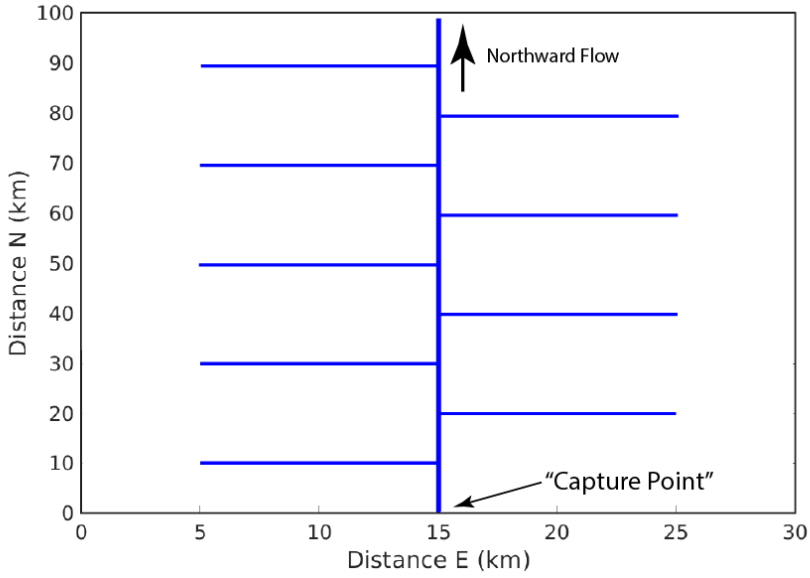

Figure 4.5. Mapview setup for upwind finite-difference model. One trunk stream with nine tributaries. The hypothesized capture point is located at the upstream most point of the trunk stream.

values fall within the literature established range for these variables (Whipple & Tucker, 1999). The critical drainage area for a stream to start incising was set to 0.1 km^2. This initial drainage area was subsequently modified by several orders of magnitude depending on which model parameters were evaluated, as described above.

4.5.3 Knickpoint Picking

In order to properly analyze the landscape of Hells Canyon, 97 tributaries to the Snake River through Hells Canyon were selected for detailed geomorphic analysis. This represents all of the streams large enough to pass the slope-area scaling threshold from landslide and debris-flow dominated space into fluvial transport space (Montgomery, 2001). The 10 m National Elevation Dataset was downloaded and clipped to the region of interest in NE Oregon. We then made

use of the Topographic Analysis Kit (TAK) which leverages TopoToolBox 2.0, both operated within the Matlab coding environment (Forte & Whipple, 2019; Schwanghart & Scherler, 2014). River long profiles were investigated in both distance-elevation space and $\chi - z$ space. Knickpoints were recognized as distinct slope changes in the river profile in $\chi - z$ space, which from theory should indicate a change in the pace of uplift, or erosion, experienced through the fluvial system (Kirby & Whipple, 2012; Royden & Perron, 2013). Knickpoints were manually picked using the tools built into TAK.

Knickpoint locations were then compared to regional and state geologic maps, any knickpoint located within $\sim$1 km of a geologic contact or mapped fault were removed (Lewis et al., 2012; Walker & MacLeod, 1991). We also attempted to identify the style of knickpoint, whether it was a sharp slope change in $\chi - z$ space or a rollover in slope, which could indicate whether the slope exponent n in equation 4.3 is greater than, equal to, or less than 1 (Tucker & Whipple, 2002). For subsequent plots and discussion, we exclusively discuss those knickpoints found on the trunk channels for each tributary with a relatively sharp transition in slope. Above and below each knickpoint, the k_{sn} for these segments was calculated using the ChiProfiler code operated in Matlab (Gallen & Wegmann, 2017). This allows for inter-basin comparison between the steepness of relict reaches to steeper reaches below knickpoints.

The river-mile distance along the Snake River for each tributary junction was measured. In subsequent figures, knickpoints are plotted and analyzed in reference to this distance along the Snake River. This provides an easy reference point to different locations within the canyon. Knickpoints were also identified by their host state (Oregon or Idaho), which is an easy way of differentiating tributaries draining the west side (Oregon) or the east side (Idaho) of the canyon.

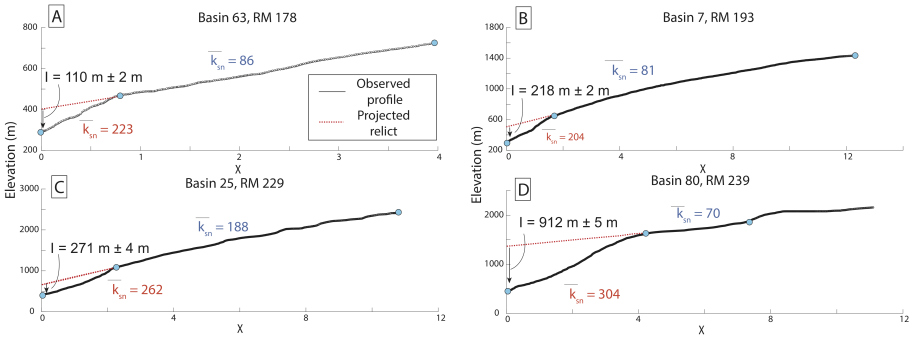

Figure 4.6. Stream profile projections from selected basins along Hells Canyon. Profiles are projected in $\chi - z$ space using the Topographic Analysis Kit (Forte & Whipple, 2019). Important stream metrics discussed below are measured here: stream steepness as measured on distinct segments (k_{sn}) and incision as measured from projected stream profiles (I).

4.5.4 Steam Projection

Channel segments with lower slope in $\chi - z$ space are coincident with lower slope and lower relief landscapes perched at higher elevations above knickpoints. These lower gradient or relict reaches can be projected to the tributary junction with the Snake River, providing insight into how much incision has taken place across the landscape (Figure 4.2; e.g. Harkins et al., 2007). Equation 4.2 can be solved for slope in its derivative form $\frac{dz}{dx}$. The scaling between drainage area and slope for the relict reach is then projected with distance, assuming the same increase in drainage area toward the junction with the Snake River as displayed by the modern tributary. This technique is easily visualized in $\chi - z$ space (Figure 4.6). We were able to successfully project the profiles of 41 relict reaches along the length of Hells Canyon. These streams covered the deepest reach of the canyon.

The projected tributary outlet elevations represent the former channel elevation before the incision event that created the knickpoints initiated. The difference between the projected elevations and the modern Snake River–tributary

junction is the amount of incision that has taken place since knickpoints entered the system.

4.5.5 Erosion Rate Modeling

Quantifying the rate of erosion above and below knickpoints would aid our understanding of how dynamic and potentially mobile these knickpoints are. There are already several basin-wide averaged erosion rate data available for several tributary basins within Hells Canyon (Figure 4.2; Table C.2; Belmont, 2015). Two basins in which erosion rates were measured also contain knickpoints on two different sub-tributaries. Erosion rate measurements were made from the mouth of each of these sub-tributaries, both of which contain knickpoints. Because the baselevel fall experienced by the main tributary is propagating upstream, the pace of landscape response should be equal below each knickpoint. This nested sampling within the basins allowed us to infer potential erosion rates within the basins above and below the knickpoints, assuming the linear relationship shown below:

$$E_{\text{total}} * A_{\text{total}} = (A_a * E_a) + (A_b * E_b) \tag{4.7}$$

Where E_{total} is the erosion rate measured on a tributary stream in a primary basin, A_{total} is the total area upstream of the point at which the sample was collected, and A is the drainage area above a knickpoint, denoted with subscript a, and the drainage area below the knickpoint denoted with b (Granger, Kirchner, & Finkel, 1996). E is the erosion rate above and below the knickpoint, denoted with the a and b subscripts, respectively. This equation was set up for the two tributary basins with erosion rate data. The theory driving this work is that as knickpoints migrate upstream from the confluence of the main tributary with the Snake River,

the erosion rate should be similar between the two branches of the main tributary above each knickpoint (Niemann et al., 2001).

The erosion rate measured at the outlet for each tributary branch is a combined signal that incorporates the erosion rate above the knickpoint and below. Here, we exploit the proximity of the two tributaries and their similar morphologic signatures to solve for E_a and assuming that these erosion rates estimated above and below the knickpoints are indistinguishable in each tributary. With two equations and two unknowns, we can then solve for the erosion rate above and below the knickpoint. This technique was implemented for Basin 25 and 80 (Figure 4.2; Table C.1). To fully describe the probability density function of possible values for the erosion rates above and below the knickpoints, we incorporated a Monte-Carlo sampling approach. We sampled the original E_{total} with its uncertainty 300,000 times to provide the full range of potential erosion rate for these basins.

However, a common assumption of basin-wide average erosion rates, that all sediment is derived equally from throughout the upstream basin, is violated by these particular basins as some portions of each was glaciated. This complicates the simple linear mixing model as areas at higher elevation may be skewed in the following ways: 1) glacially eroded material could be transported into the streams that were sampled, lowering the measured concentration of radionuclides and raising the calculated erosion rates. 2) Glacial lakes act as sediment sinks, shrinking the overall area contributing sediment in each catchment.

Modeling by Adams and Ehlers (2018) addresses the first concern. These authors showed that ∼5-10 kyr was enough time for a glaciated landscape to return to radionuclide isotopic equilibrium. This result is robust even for landscapes eroding as slow as 0.1 mm yr^{-1}; a faster eroding landscape would reach isotopic equilibrium more quickly (Adams & Ehlers, 2018). Erosion rates measured on

such a landscape, after this adjustment timescale, could then be interpreted as a non-glaciated landscape would be. To address the issue of glacial lakes in the headwaters of these catchments, we adopt the approach of Moon et al. (2011), clipping out the areas of these basins above the outlets to each lake. This ensures areas which are not contributing sediment are not incorporated into our estimates of erosion rates.

4.5.6 Cave sediments for estimating canyon incision history

In deep canyons, caves which interacted with the fluvial system at one point in time have the potential to record million-year timescale rates of incision (e.g. Granger, Kirchner, & Finkel, 1997). Fluvial deposits stranded in the back of a cavern are shielded from cosmogenic ray flux and can be dated with cosmogenic burial dating (Granger et al., 1997; Stock, Anderson, & Finkel, 2005). The exposure of the Triassic Martin Bridge Limestone along portions of Hells makes it a promising location for a similar exploration of caverns and these methods (Stanley, Jr. et al., 2008).

After exploration of ∼50 caverns in Hells Canyon over the 2017, 2018, and 2019 field seasons, 3 sites were identified which had promising morphology that indicated interaction with ground water, so called vadose caves (see Anthony & Granger, 2007, Figure 4.4). These caverns are named by local cavers: Roundhouse, Ashmead, and Red Fish Caves. They were located by the Gem State Grotto, and access to Red Fish Cavern was secured through negotiation with the U.S. Forest Service. These caverns are ∼375 m, ∼343 m, and ∼242 m above the pre-dam river thalweg, respectively. A detailed survey revealed fluvial sediments for Ashmead and Red Fish are viewable in Figure **??**and C.2; Roundhouse was excluded as we have yet to see results from these sediments. Care was taken to excavate fluvial deposits

to avoid contamination with other cave deposits and terrestrial sediment outside the caverns. All sediment was collected from locations deep enough in the cave to be shielded from any cosmogenic flux (Granger et al., 1997).

4.5.7 Cosmogenic Burial Age Sample Preparation and Analysis

The cave samples were then taken to the Indiana University Geomorphology and Landscape Evolution Laboratory for initial components of the cosmogenic analyses, following the procedure described in Kohl and Nishiizumi (1992). Samples were disaggregated with a jaw-crusher. Then ground still finer with a disc mill, prioritizing a grainsize of 2 mm. Samples were then wet-sieved to separate different grain sizes. The grain size most significant for our study is between 200 and 600 μm. These separates were then cleaned in an initial hot-bath of HCl for 12 hours. In some cases, due to the excess $CaCO_3$ clinging to the grains, two HCl cleanings were used. The cleaned sediment was then density separated using Lithium Metatungstate. This step separates sediment with a density greater than that of quartz. This density separate was then washed and placed into plastic 1 liter Nalgene containers for hydrofluoric etching.

The quartz etching step used 20 ml of 48% HF solution, 15 mL of 80% HNO_3, ~950 ml of water, and quartz separates. These Nalgene containers were then heated and rotated for a 24 hour period. After 24 hours, each sample was drained of its acid solution and the process repeated. ^{10}Be and ^{26}Al wet-chemistry and accelerated mass-spectrometer measurements will be done at PRIME Laboratory (Purdue University). As of August, 2020, these results have not been returned from PRIME lab.

Dating of the collected fluvial deposits is rooted in the concept of shielding. This sediment which was once in a river system, exposed to cosmogenic

radionuclide flux, is now buried. Two cosmogenic radionuclides within that sediment ^{26}Al and ^{10}Be form from spallation of O and Si with a minor component of fast muon interactions and negative muon capture (Lal, 1991). Once buried, ^{26}Al and ^{10}Be will begin to decay as they are shielded from further cosmic rays. If the sediment is shielded by more than ∼3 m of bedrock, then the muogenic production is reduced to a level at which the decay of ^{26}Al and ^{10}Be are unperturbed by the low rates of successful cosmic ray production.

Following the methods outlined by Stock et al. (2005), the steady-state, long-term concentration of radionuclides (Ni) at the surface is as follows:

$$N_i = \frac{P_n}{\left(\frac{1}{\tau_i} + \frac{\rho\varepsilon}{\Lambda_n}\right)} + \frac{P_\mu}{\left(\frac{1}{\tau_i} + \frac{\rho\varepsilon}{\Lambda_\mu}\right)} \tag{4.8}$$

In the above equation, P_n is the production rate via spallation, τ_i is the mean life of ^{26} Al (0.02 ± 0.04 My; Norris, Gancarz, Roico, & Thomas, 1983). ρ is the density of the local rock (assumed to be 2.7 g cm^{-3}); ϵ is the local rock erosion rate; Λ_n is the penetration length for nucleons. P_μ is the muogenic production rate, and Λ_u is the penetration length for muons. The production rate for both ^{26}Al and ^{10}Be varies with changes in the Earth's magnetic field, elevation of sample, and latitude of the sample (Lal, 1991; Stone, 2000). The ratio of production between ^{26}Al and ^{10}Be is always fixed at 6:1 (Nishiizumi et al., 1989). Upon burial, the decay of each radionuclide is governed by the following equation:

$$N_i = (N_{i_0})\, e^{-t}/\tau_i \tag{4.9}$$

In this equation, t is the elapsed time since sediment burial. Given the differences between decay rates for each radionuclide, the ratio of these two radionuclides decreases exponentially, following:

$$\frac{N_{26}}{N_{10}} = \left(\frac{N_{26}}{N_{10}}\right)_0 e^{-t\left(\frac{1}{\tau_{26}} - \frac{1}{\tau_{10}}\right)} \tag{4.10}$$

N_{26} and N_{10} are the ^{26}Al and ^{10}Be concentrations at any given point in time (t). $\frac{N_{26}}{N_{10}\,0}$ is the original, pre-burial, ratio of $\frac{^{26}Al}{^{26}Be}$. Using the methods outlined by Granger et al. (1997), equation 4.9 and 4.10 can be iteratively solved for ϵ, t, and $\frac{N_{26}}{N_{10}}$. The limits on this technique result from the radioactive decay of both nuclides. At least 0.3 Myr is needed to have elapsed since burial in order for a significant difference in the ratio between the two radionuclides to be measured. On the upper end, samples older than 5 Myr do not contain enough 26Al to provide a recoverable age.

4.5.8 Detrital Zircon Ages

In addition to samples being taken for cosmogenic burial dating, we also collected sediment from Ashmead and Red Fish Caves for detrital zircon analysis. This component of the work provides a better constraint of the provenance of the sediment in each cavern. We can test whether these sediments are tapping into southern Idaho or only being deposited by local streams in Hells Canyon, which will provide an enhanced regional context for cavern burial ages.

Two samples were sent to the Menlo Park USGS office where they underwent a standard mineral separation routine including crushing, sieving, magnetic separation, and density separation with heavy liquids. This process used standard mineral separation protocols. The samples were then sent to be analyzed at the USGS LA-ICP-MS laboratory in Denver Colorado.

For each sample, we dated ∼120 zircons using U-Pb LA-ICPMS (Laser Ablation Inductively Coupled Mass Spectrometry). Zircon was ablated with a Photon Machines Excite^{TM} 193 nm ArF excimer laser that was coupled to a Nu Instruments AttoM high-resolution magnetic-sector inductively coupled plasma mass spectrometer in spot mode (150 total bursts for zircon) with a repetition rate of 5 Hz, laser energy of ∼3 mJ, and an energy density of 4.11 J cm^{-2}. Pit depths are typically less than 20 μm. The rate of He carrier gas flow from the HelEx cell of the laser was ∼0.6 L min^{-1}. Make-up Ar gas (∼0.2 L min^{-1}) was added to the sample stream prior to its introduction into the plasma. Nitrogen with flow rate of 5.5 mL L min^{-1} was added to the sample stream to allow for significant reduction in ThO+/Th+ (<0.5%) and improved the ionization of refractory Th (Hu et al., 2008). The laser spot sizes for zircon were ∼25 μm. With the magnet parked at a constant mass, the flat tops of the isotope peaks of ^{202}Hg, ^{204}(Hg+Pb),^{206}Pb, ^{207}Pb, ^{208}Pb, ^{232}Th, ^{235}U, and ^{238}U were measured by rapidly deflecting the ion beam with a 30 s on-peak background measured prior to each 30s analysis. Raw data were reduced off-line using the Iolite^{TM} 2.5 program (Paton, Hellstrom, Paul, Woodhead, & Hergt, 2011) to subtract on-peak background signals, correct for U-Pb downhole fractionation, and normalize the instrumental mass bias using external mineral reference materials, the ages of which had previously been determined by ID-TIMS. Ages were corrected by standard sample bracketing with the primary zircon reference material Temora2 (ca. 417; L. P. Black et al., 2004) and/or secondary reference materials FC-1 (ca. 1099 Ma; Paces & Miller, 1999), Plešovice (ca. 337 Ma; Sláma et al., 2008) and Fish Canyon tuff (ca. 28 Ma Schmitz & Bowring, 2001). Reduced data were compiled into Wetherill concordia diagrams using Isoplot 4.15 (Ludwig, 2012). $^{206}Pb/^{238}U$ ages are reported for igneous zircon samples

less than ∼1300 Ma and $^{206}Pb/^{206}Pb$ ages are used for older ages following the recommendations of (Gehrels, 2012).

4.6 Results

4.6.1 Numerical Modeling

24 numerical simulations of drainage capture and integration were run using the finite-difference methods described above. Across all parameters evaluated, capture and integration of a larger drainage area results in incision along the trunk stream and knickpoint generation along each tributary. The highest knickpoints are on those tributaries located closer to the capture point (Figures 4.5 and 4.7). The uppermost knickpoint is at ∼600 m in the first recorded timestep. Knickpoint elevation decreases downstream, approaching the elevation of the tributary-trunk junction at the downstream-most knickpoint (Figure 4.7). The most downstream knickpoint is at ∼100 m in the first recorded timestep. In some models, notably C1, the knickpoints in the uppermost catchments have advected to the drainage divide over the course of the model run and disappear from Figure 4.7.

We also projected the modeled relict profile above each knickpoint out to the tributary-trunk junction using the same method described above for actual knickpoints in Hells Canyon. The difference between the projected outlet and outlet elevation in that timestep is a measure of incision resulting from the adjustment to changes in baselevel for each tributary (Figure 4.7). The trend in measured incision across parameter space is also consistent with the trend found in knickpoints: farther downstream from the capture point less incision has taken place. The uppermost tributary displays ∼500 m of incision. The lowermost tributary has ∼25 m of incision (Figure 4.7). This measure of incision is consistent across the examined parameter space. The reduction in incision and knickpoint elevation

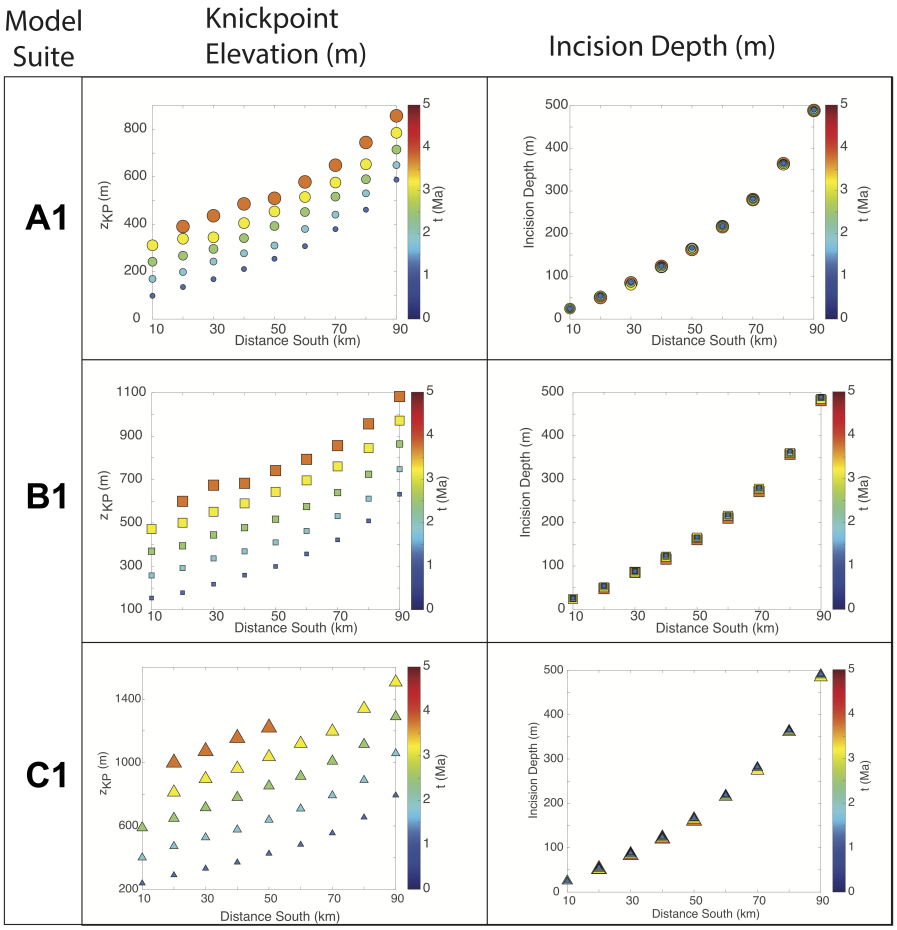

Figure 4.7. A select view of modeling results. Each row are the knickpoint elevation and calculated incision depths from a different suite of models. In all models, knickpoint elevations decrease downstream from the capture point. **A1.** This model was evaluated with $n = 0.67$, $K = 4.76$ x $10^{-6} m^{0.33} yr^{-1}$, an drainage area gain of 1.9 * $10^5 km^2$, and pre-capture uplift equivalent to post capture uplift. **B1.** This model was evaluated with $n = 1.0$, $K = 1.0x10^{-6} yr^{-1}$, an drainage area gain of $1.9x10^5$ km^2, and pre-capture uplift equivalent to post capture uplift. **C1.** This model was evaluated with $n = 1.5$, $K = 4.42x10^{-8} m^{-0.5} yr^{-1}$, a drainage area gain of 1.9 * $10^5 km^2$, and pre-capture uplift equivalent to post capture uplift. Models with variable uplift are included in the Supplement.

downstream is the result of the smaller and smaller proportion of the overall catchment drainage area which was increased as a result of the capture event. As erosion is tied closely to drainage area (eq. 4.1), the farther downstream one goes from the capture point the smaller the ratio of newly gained drainage area is as compared to the overall drainage area. The smaller the change in drainage area; the smaller the knickpoint and the less incision increases. This is consistent across parameter space. Our models reflect this intuitive framework with a robust numerical result. To review all 24 model scenarios see Supplemental Figures C.3, C.4, and C.5.

4.6.2 Knickpoints and Stream Orientation

Of the 97 tributary streams examined in this study, we located knickpoints along 54 (Figure 4.8A). Picked knickpoints are summarized in Table C.2. Starting from the North (left) side of Figure 4.8A, knickpoints climb in elevation in a nearly monotonic fashion from just above the modern river. These lowest knickpoints range in elevation from 300-500 m a.s.l. Moving upstream, knickpoints increase in elevation quickly (Figure 4.8A and 4.9A). The highest knickpoints found along tributaries to the Snake are ∼1600 m a.s.l (Figure 4.9A). These knickpoints are located nearly 1.5 km above the modern Snake River. Moving further south (upriver), the knickpoints decrease in elevation more gradually than the northern knickpoints increase in elevation. These knickpoints again move closer to the modern Snake River in elevation space (700-900 m a.s.l.).

The trend in knickpoint elevation and river plan-view profiles are superimposed in Figure 4.8B. When the river network is visualized in this manner, there is also a visible transition in the overall orientation of the stream network. Following the drainage divide between the Imnaha River and Pine Creek (Figure

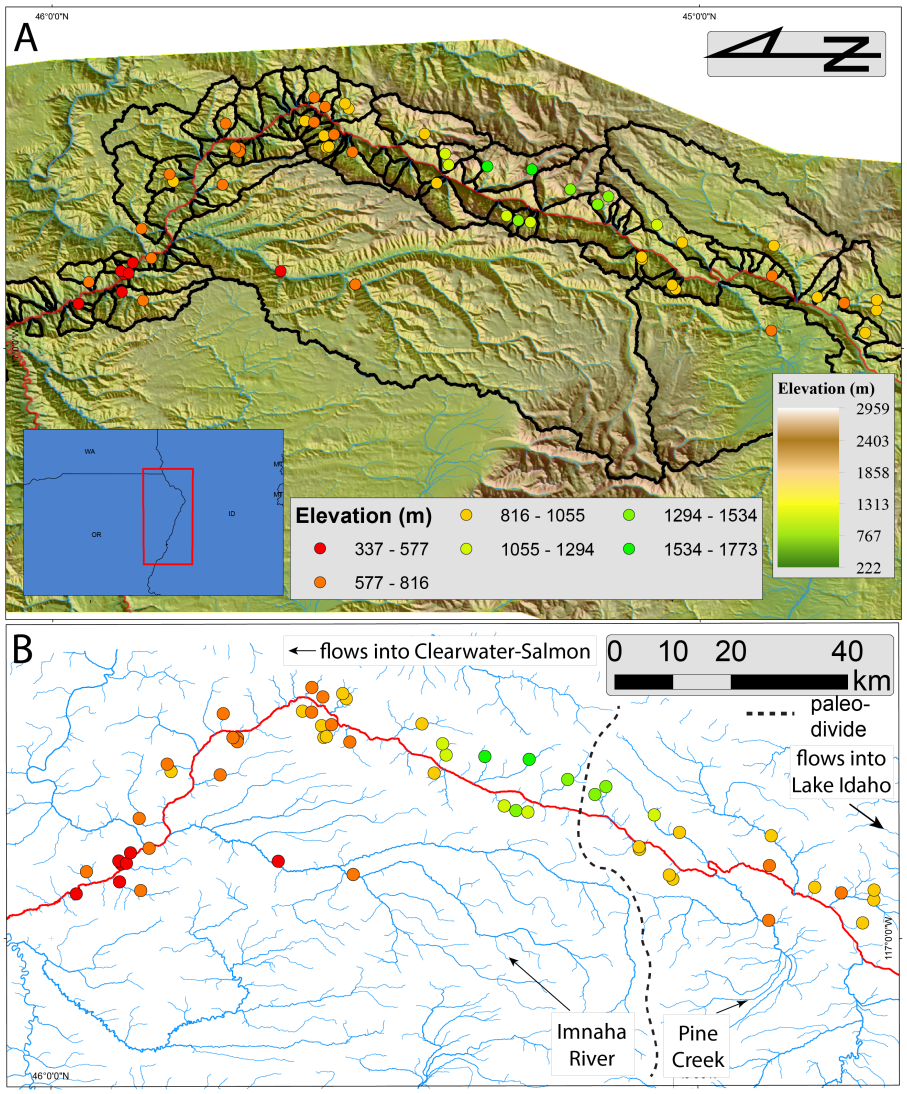

Figure 4.8. A. Elevation map Hells Canyon region with identified knickpoints colored by elevation. Note that from north-to-south, knickpoints climb in elevation and then decrease in elevation. **B.** The plan-form pattern of drainages in the same region. Looking at the drainage network from this perspective highlights an abrupt change in river orientation which is co-located with the highest elevation knickpoints. The inferred pre-capture drainages on either side of this paleo-drainage divide flowed into the Clearwater-Salmon River to the north, and Lake Idaho to the south.

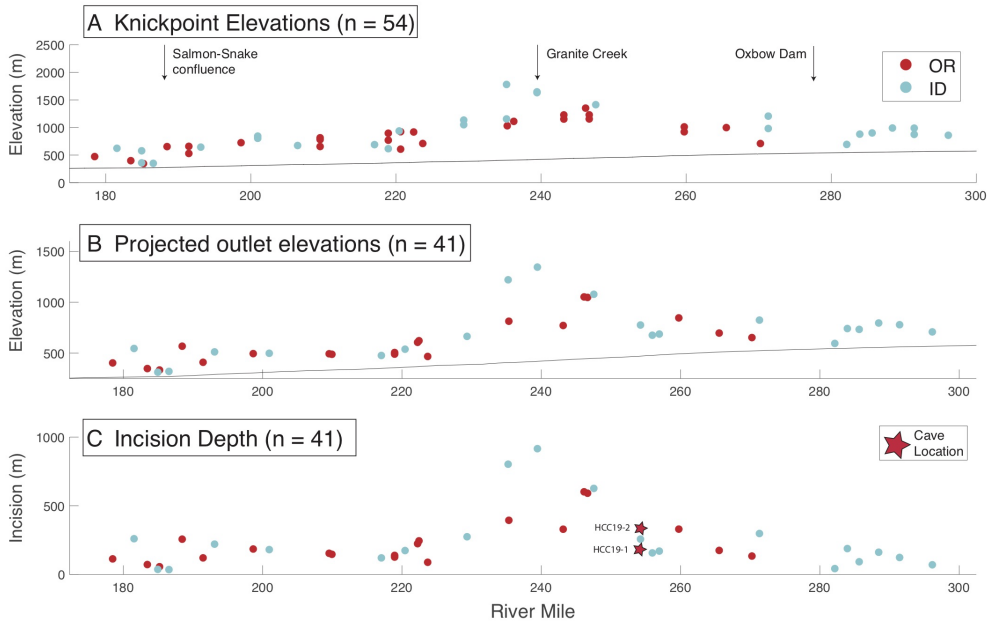

Figure 4.9. A. Elevations of picked knickpoints along Hells Canyon, colored by which state the tributary is draining. The knickpoints start very close to the river elevation near the Salmon-Snake confluence and climb to ∼2 km a.s.l. at RM 240. **B.** Projections of relict river profiles follow a similar shape. **C.** The difference between the modern river elevation at the modern tributary outlet and the projected stream outlet provides a measure of river incision. While the pattern is very similar to knickpoint elevations, it represents how much the Snake river has incised since knickpoint initiation.

4.8B), drainage basins on the left side of the divide are oriented north; meanwhile, basins on the right side of the divide are oriented south. This is despite the fact that the modern Snake River flows south-to-north (Figure 4.8B). The Imnaha-Pine Creek divide is inferred to be a paleo-divide between two former river networks, which may have drained in opposite directions: to the north and to the south.

4.6.3 Channel Steepness Analysis

Given the relationship between channel steepness and uplift and erosion rate (eq. 4.3), it is important to examine the stream steepness above each knickpoint. This allows us to parse whether the observed patterns in knickpoints are merely reflecting a warped uplift field. Segments of each tributary with an identified knickpoint were analyzed for their normalized channel steepness above and below the trunk knickpoint. Steepness values are distinctly different between areas of the tributaries above the knickpoints and those regions below the knickpoints. Steepness values above knickpoints range from ∼60 to ∼200 $m^{0.9}$, with a mean value of 111 $m^{0.9}$ (Figure 4.10). Values of channel steepness below knickpoints range from 115 to ∼400 $m^{0.9}$, with a mean steepness of 204 $m^{0.9}$ (Figure 4.10). The variability in k_{sn} is not unusual and has been observed in other studies and is likely due to changes in rock properties (N. Mitchell & Yanites, 2019). The overall pattern of k_{sn} above the knickpoints is consistent throughout the canyon, indicating that this region before knickpoint initiation experienced a steady uplift gradient. Importantly, these similar k_{sn} values are expressed across many different rock types.

4.6.4 Erosion Rate Modeling

Our 300,000 Monte-Carlo simulations were conducted in two basins: Granite and Sheep Creeks, Basins 25 and 80 — respectively (Figure 4.2). These sampling

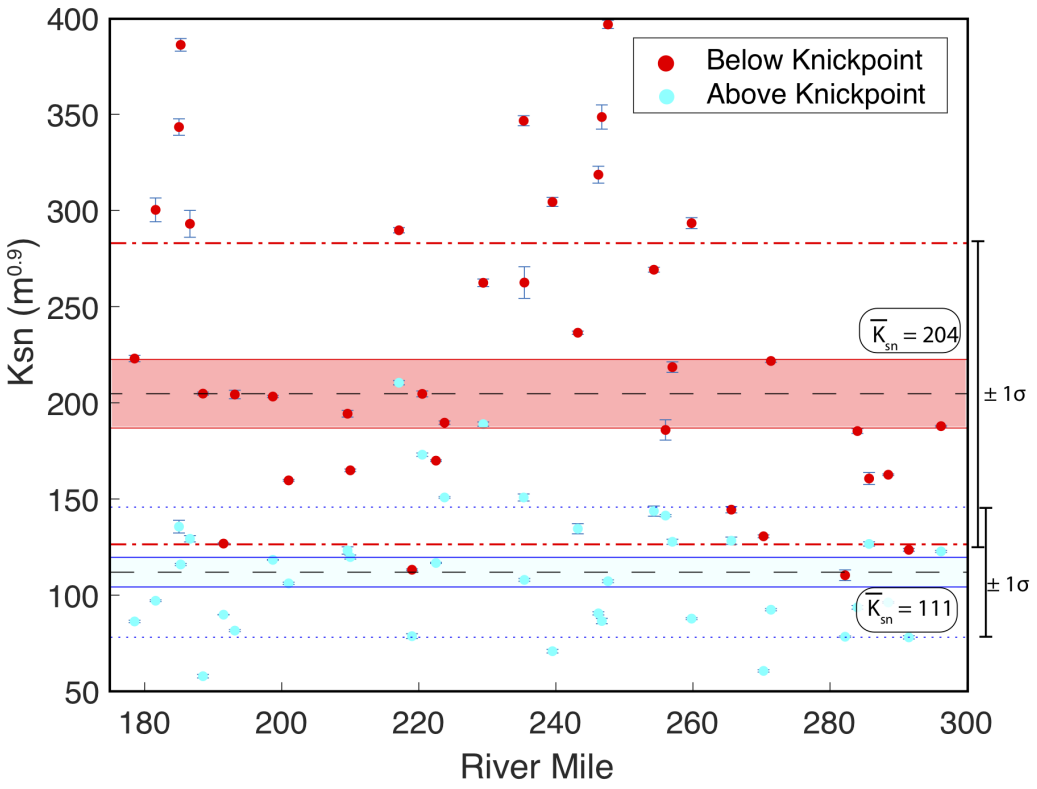

Figure 4.10. Normalized stream steepness (k_{sn}) for trunk tributary stream segments above and below knickpoints. Shaded regions are standard error envelops around mean ksn and dashed lines are 1-σ envelopes. Plot shows clustering of regions above knickpoints at low values of stream steepness, and very high values of steepness below knickpoints.

routines result in an estimate of the erosion rate above and below knickpoints in the two basins. We report the estimated rates as a mean of the sample distribution with a 1σ uncertainty (Table C.2). Granite Creek (Basin 80) has a relict erosion rate above the knickpoint of 0.04 ± 0.03 mm yr^{-1} and an adjusted rate below the knickpoint of 0.17 ± 0.02 mm yr^{-1}. Sheep Creek (Basin 25) provided a relict rate of 0.01 ± 0.01 mm yr^{-1} and an adjusted rate below the knickpoint of 0.27 ± 0.04 mm yr^{-1}. These rates are consistent with long-term low-temperature thermochronology data for the region (Chapter 3) and erosion rates collected in central Idaho above knickpoints in the Salmon River catchment (Larimer et al., 2018). Erosion rates below the knickpoints are consistent with incision rates calculated from dating of fluvial terraces on a proximal tributary to the Snake River (M. C. Morriss & Wegmann, 2017).

4.6.5 Stream Projections

41 tributary streams were successfully projected from their relict reach to their junction with the Snake River (Figure 4.9B; Table C.3). These outlets represent a reconstruction of the paleo-profile of the river networks that existed before the baselevel lowering event that generated these knickpoints took place. The overall trend in projected outlets mirrors the one seen in the knickpoint elevations. Projected outlets at RM 180 are ∼400-500 m a.s.l., quickly rising in elevation to ∼600 m a.s.l. by RM 220. The highest elevation projected outlet is ∼1340 m at RM 240 (Fig 4.9B). Continuing upstream, the projected outlets go back down in elevation to 600-700 m a.s.l. by RM 260.

To constrain the overall amount of incision that has taken place since knickpoint generation, we also subtracted the modern tributary-Snake junction elevation from the projected outlet elevations. (Figure 4.9C). On both the northern

Sample Number	Cave Name	Height above Snake River (m)
HCC19-2	Ashmead	343
HCC19-1	Red Fish	242

Table 4.2. Cave sample numbers, cave name, and elevation.

and southern ends of Hells Canyon there is as little as 60 m of incision (RM 180 and 290), rising to as much as ∼1 km in the middle of the canyon (RM 240; Figure 4.9C). This pattern of incision indicates that tributaries everywhere along the network have experienced at-least 60 m of baselevel lowering and as much as 1 km.

4.6.6 Provenance Analysis

Detrital zircon provenance analysis of Samples HCC19-1 and HCC19-2 reveal a striking pattern dissimilar from other detrital zircon datasets along the Snake River (Figure 4.2). Cave elevations are summarized in Table 4.2. Each cave is located slightly up a tributary to the Snake River (Figure 4.11). Similar to river terraces, caves formed proximal to a river system will young toward lower elevations (Granger et al., 1997; Stock et al., 2005). Channel profile projections (Figure 4.9C) place sample HCC19-2 above the projected outlet of the paleo-river; HCC19-1 is below the projected outlet, meaning this cave likely formed after the initiation of this knickpoint. We hypothesize that the lower cave, HCC19-1, would potentially contain zircons exotic to Hells Canyon if knickpoints initiated due to the capture of Lake Idaho.

Detrital zircon LA-ICPMS ages are returned as dates with a 1-σ uncertainty. For each sample, ∼100 zircons were successfully analyzed. Sample HCC19-2 contains zircons exclusively from the early Cretaceous (Fig 4.12A; Table C.4 and C.5). The mean grain-date from this sample is 123 ± 3.1 Ma. Given

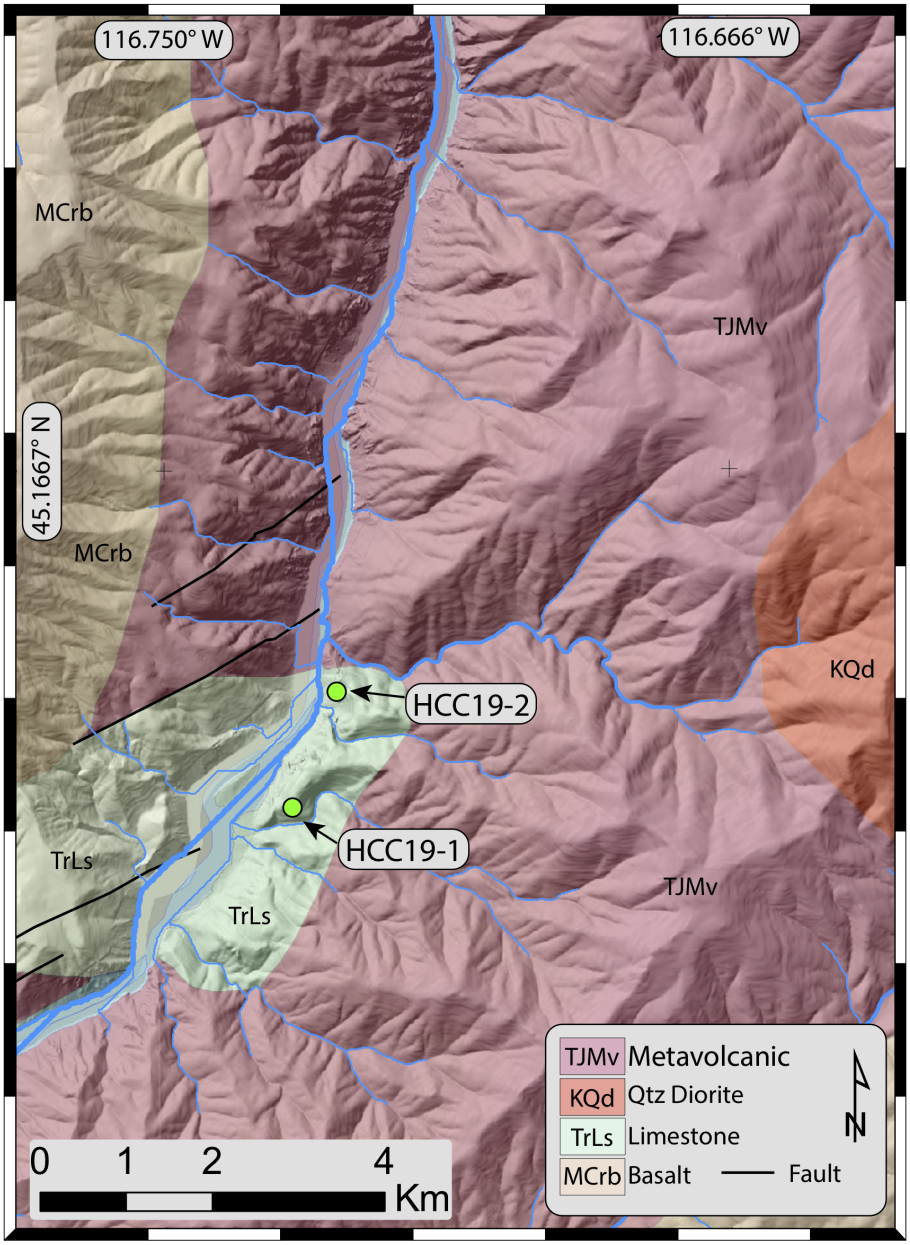

Figure 4.11. Location of sampled caverns and pertinent lithologies. Metavolcanic units are the Triassic and Jurassic Wild Sheep Creek formation (Vallier, 1977). The quartz diorite is an undated pluton likely from a suite of intrusive throughout the canyon that post-date terrain accretion and perhaps the resumption of subduction on the western margin of N.A. (Vallier, 1995). The limestones are the Triassic Martin Bridge Limestone (Stanley, Jr. et al., 2008), and the basalts are the Miocene Columbia River Basalts (S. P. Reidel & Tolan, 2013a)

the consistency in grain ages, it is likely that this sample taps a local source, potentially a plutonic body up a tributary from the cavern. Sample HCC19-1, the cave most likely to postdate incision, contains a similar early Cretaceous grain age population; however, it also contains ages ranging from 8 Ma to as old as ∼1.4 Ga (Figure 4.12B; Table C.4 and C.5). There is not an abundance of these extreme young and old ages. Only one grain is 8 Ma, followed by a 16 Ma grain; moreover, there is only a single grain at 1.4 GA (Figure 4.12B; Table C.4 and C.5). Out of all 101 grains which returned promising dates from this sample, only 7 were beyond the ∼120-130 Ma envelope identified in sampled HCC19-2.

Detrital zircon age spectra from both samples (Figure 4.13A and 4.13B) shows little to no similarity with known age populations representative of the eastern Snake River Plain (Figure 4.1 and 4.13C). The ∼125 Ma age peak may represent a plutonic body local to Hells Canyon (Figure 4.11). The 8 Ma peak appears to line up with the Yellowstone Hotspot age; however, one grain is not statistically significant in the context of 101 dated zircon grains. The outlier grain ages of 200-240 Ma slightly overlap in age with Triassic plutons dated to 228 ± 5 to 227 ± 6 Ma elsewhere in Hells Canyon (Kauffman, Schmidt, Lewis, Stewart, & Othberg, 2009); however, these plutons are mapped farther north than the sampled cave. Directly upstream from the sampled cavern is the Wild Sheep Creek formation (TJMv in Figure 4.11; Vallier, 1995). It is possible these units could be the source of these Triassic grains.

4.7 Discussion

4.7.1 Landscape Dynamics

We began this study by investigating how a landscape responds to drainage integration and capture, posing a hypothesis that such a process should leave a

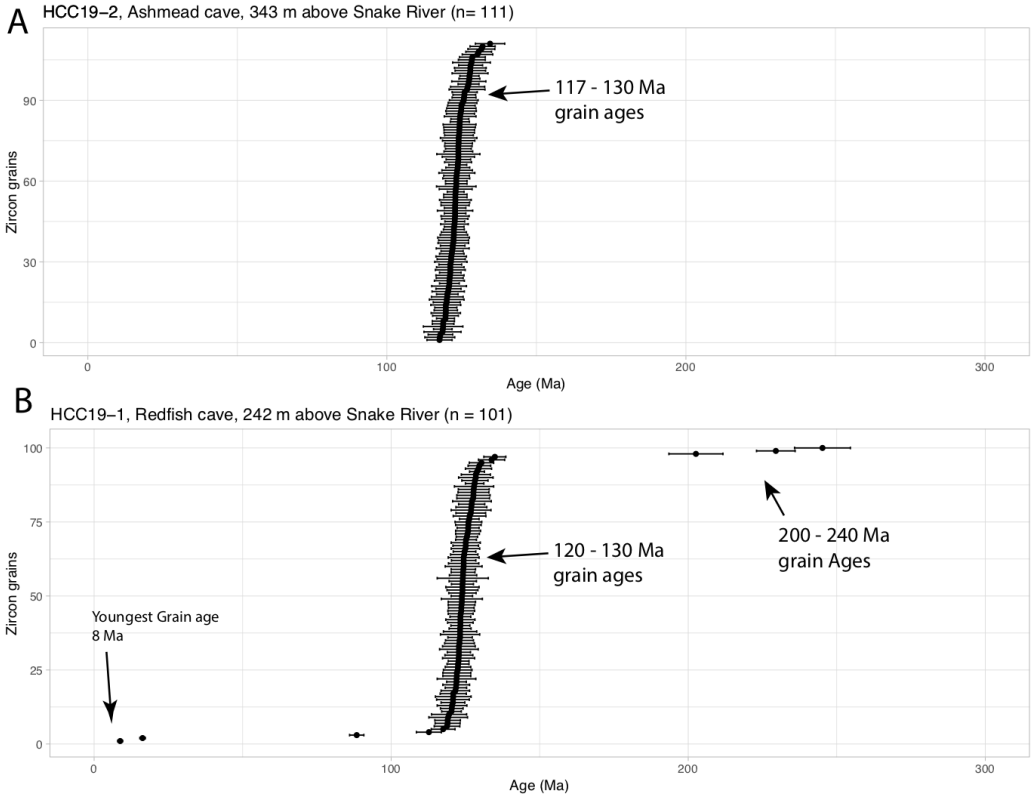

Figure 4.12. A. 111 zircon grain ages from USGS LA-ICPMS for sample HCC19-2. This sample collected in Ashmead cave ∼343 m above the Snake river shows only one population of zircon ages, ranging from 117-130 Ma. **B.** 101 zircon grains analyzed from sample HCC19-1. This sample was collected in Redfish Cave ∼242 m above the Snake River. This sample contains a collection of ages, ranging from 8 Ma, with a strong peak at 120-130; a few grains between 200 and 240 and a single 1.4 Ga grain.

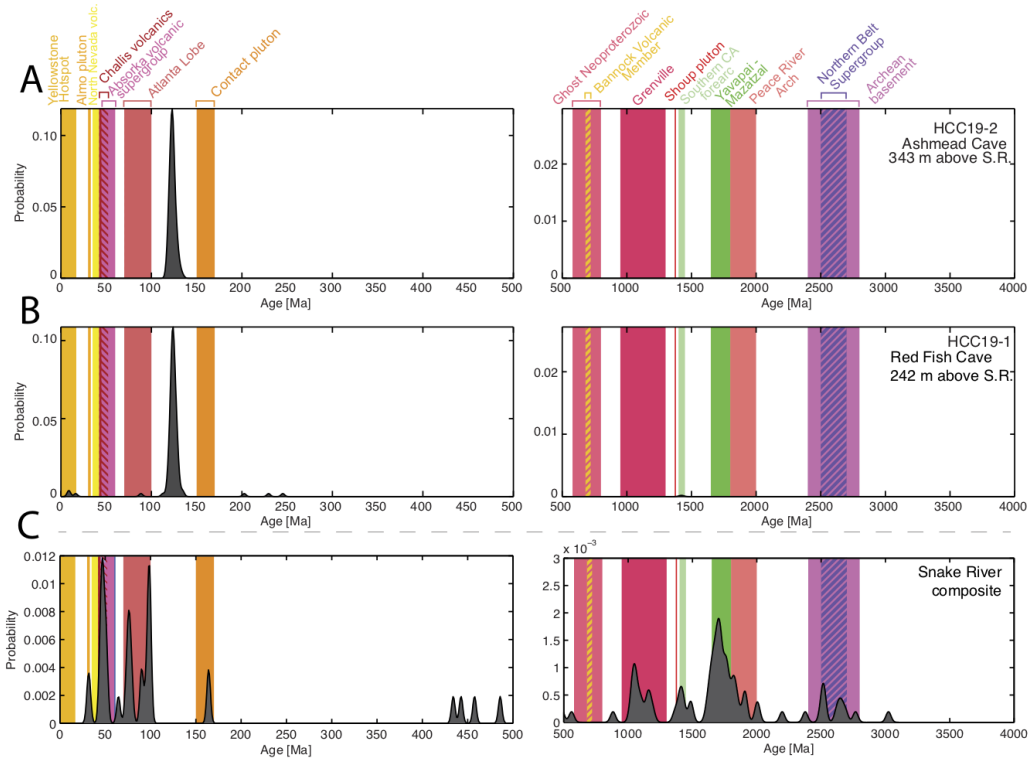

Figure 4.13. Detrital zircon spectra for both cave samples and Modern Snake River upstream of Hells Canyon. **A.** Age spectra for sample HCC19-2, collected ∼343 m above the Snake River. Spectra reveal a distinct age peak at ∼125 Ma, which is not consistent with any of the age populations represented by the eastern Snake River Plain. **B.** Age spectra for sample HCC19-1, collected ∼242 m above the Snake River. The same age peak of ∼125 Ma is shown as are the younger 8 Ma grain age and 200-250 grains. Only the 8 Ma age shares a commonality with any eastern Snake River Plain deposits. **C.** Age spectra for detrital zircons collected in the modern Snake River. Collected and published by (Beranek et al., 2006). Plotted samples are combination of samples M-5 and M6 collated by Staisch et al. (2017) (Figure 4.1). The modern Snake River shows many age peaks over 2.5 Ga of history, almost none of which overlap with samples HC19-2 and HCC19-1.

distinct signal on the landscape. Numerical experiments from a finite-difference model provide some of the first insights into what we should expect to find in the landscape. Across a series of 24 models, with various parameters, there is a consistent trend of knickpoints decreasing in elevation downstream from a simulated capture location (N. Mitchell & Yanites, 2019; Yanites, Ehlers, Becker, Schnellmann, & Heuberger, 2013). Moreover, the projected incision reflected in these knickpoints decreases downstream (Figure 4.7; see Figure C.3,C.4,C.5).

These model-derived predictions for the landscape are similar to the knickpoints and projected relict outlets along 41 tributaries to the Snake River through the Hells Canyon corridor (Figure 4.7 and 4.9). The trend of rising outlet projections in both the streams that are north of the inferred paleo-divide (Figure 4.14A) and those that are south of the paleo-divide appears robust (Figure 4.14B). Moreover, the presence of a distinct change in tributary orientation coincides with the point of the highest knickpoints (Figure 4.8B). This reflects an orientation developed during a previous pre-capture time period when two drainages developed separately — one draining north, the other south.

Taken together, the map-view stream orientations and the knickpoint pattern reinforced by our 1-D models, are strong evidence that Hells Canyon 1) initially evolved from two separate drainage systems – one flowing south into Lake Idaho, and the other north into the Columbia River, and 2) integration across the divide between these two systems produced the canyon observed today (Figure 4.3 and 4.14). An anachronism attributed to this pre-capture time period are the relict, low relief reaches at the upper portion of many tributary streams (Figure 4.6).

An ongoing and important consideration for these conclusions is the balance between erosion and uplift in these relict reaches. Indeed, our incision depth estimates can provide insight into whether the relict landscape has experienced

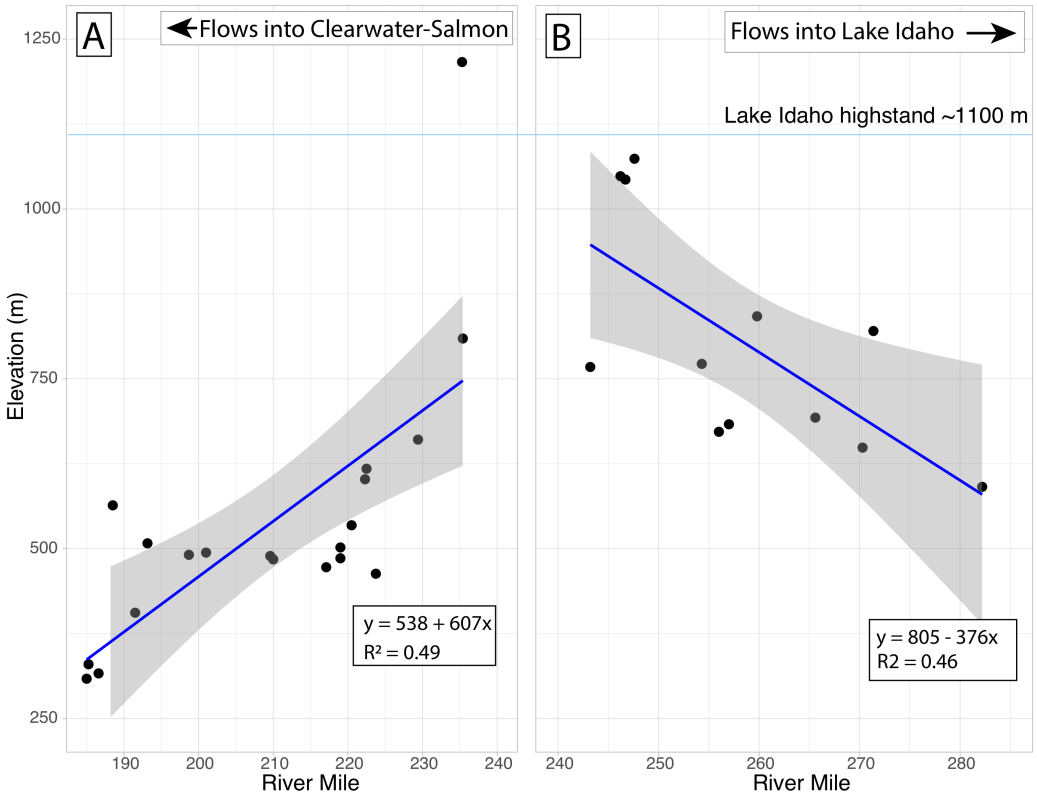

Figure 4.14. Linear regression of projected stream outlets. These regressions measure the relative slope of the outlets. **A.** Outlets downstream of the inferred paleo-divide (Figure 4.6B) have a steeper slope than outlets upstream of this divide. **B.** Projected outlets upstream of the inferred paleo-divide location. A steeper gradient stream pre-capture downstream of paleo-divide (**A**) would have been a robust driver of headward erosion for this catchment.

surface uplift (rock uplift minus erosion; England & Molnar, 1990). If erosion does not balance uplift when these drainages first initiated and since the knickpoints entered these catchments, their mean elevations could still be rising or falling relative to the geoid (England & Molnar, 1990). This becomes important when looking at the estimates of incision from our projected profiles (Figure 4.9C). The best estimates on long term uplift rates in the region come from thermochronology. These methods place the background exhumation rate over the last ∼40 Myr as consistently near ∼0.025-0.05 mm yr^{-1} (Chapter 2). This is similar to the estimates from basin wide average erosion rates in relict reaches of 0.01-0.04 mm yr^{-1}, indicating that there is a relatively consistent rate of erosion over a long period of time, which appears to be in balance with uplift rates (Belmont, 2015). Moreover, the consistent pattern of low k_{sn} (Figure 4.10) above knickpoints is evidence that these channels were not in any systematic disequilibrium with background forcing before knickpoints entered these tributaries. The visible range in k_{sn} could be due to paleotopography or the effects of variable lithology which can have an effect on k_{sn} (N. Mitchell & Yanites, 2019).

4.7.2 Cave Sediments

The data revealed from the cave burial dating have yet to be returned from PRIME lab; therefore, we are unable to directly calculate an incision rate from these cave locations. However, the youngest detrital zircon grain date provides one possible constraint on the depositional age of the sampled sediments. A single zircon grain date of 8.7 ± 1.3 Ma means deposition of sample HCC19-1 (Redfish Cave; Figure 4.12B) must be younger than this zircon grain. Given the lack statistically significant number of zircons of this age, we do not further discuss this grain herein.

Moreover, the lack of sediment from the Eastern Snake River Plain indicates that the caves from which samples HCC19-2 and HCC19-1 were collected from were not filled with Snake River sediment at the time of sampled sediment deposition (Figure 4.13 Beranek et al., 2006; Staisch et al., 2017). The broader array of ages returned from sample HCC19-1 could indicate a more diverse sediment source than HCC19-2 (Figure 4.11). However, the simplest scenario for the origin of these grains is that they came from the Permian-Triassic Seven Devils volcanics, composed of the Permian Hunsaker Creek and Triassic Wild Sheep Creek formations (Vallier, 1977). These units are the sub-aerial volcanic sequences associated with the oldest plutonic bodies in Hells Canyon and contain zircons and are located directly upstream from this sample site (Figure 4.11).

One conclusion we can draw from these sediments is they do not appear to post-date the capture of Lake Idaho and integration of the Snake River. However, this inference is challenged by the location of Sample HCC19-1 relative to the projected relict profile on a nearby tributary (Figure 4.9C). This projection indicates that this cave would have formed after the baselevel lowering event we hypothesize is the capture of Lake Idaho and should therefore record a tributary signal post-dating capture. This discrepancy could be because this cave is $\sim$1 km up a tributary from the main channel of the Snake River. In this scenario, the stream which the cave is open to is tied to the Snake River as its ultimate base level, but grains transported as suspended or bedload in the Snake are unlikely to have been directly deposited in this cave. This means the younger grains may have been from a tephra that blanketed the drainage basin upstream of the cave and the older grains could be from the metavolcanics Triassic Wild Sheep Creek formation exposed in the upper reaches of this catchment (Figures 4.11 Vallier, 1977). Under these circumstances, the projected stream profile still represents a meaningful signal

of baselevel lowering, but the detrital zircon grains are decoupled from the Snake River. Importantly, this means that the burial dating of these cave deposits could still provide incision rates relevant to Snake River carving of Hells Canyon.

4.7.3 Capture Timing and Style

The exact nature and timing of the integration of Lake Idaho and the Snake River into the Columbia River system remains uncertain. The evidence collected and discussed herein does not provide a single date which could be robustly interpreted as capture. However, the mirror image knickpoint pattern on either side of RM ∼240 provides some evidence for the style of capture (Figure 4.9). It is likely that the drainage divide between Lake Idaho and the Columbia River system was incised through at this location. This process of incision was likely aided by pre-existing fracture and faults in this region (Wheeler & Cook, 1954).

Based on the available evidence, incision through Hells Canyon must be younger than the ∼8 Ma age zircon grain collected 242 m above the Snake River with sample HCC19-1. Detrital zircon evidence in downstream basins indicates integration of the western Snake River Plain could not have occurred before 3.48 Ma (Staisch et al., 2017). The 2.5 Ma maximum depositional age for the Tenmile and Tuana gravels which prograde across the western Snake River Plain, provides a potential maximum incisional age constraint on canyon carving (Table 4.1 Beranek et al., 2006; Othberg, 1994). Meanwhile, the presence of a single 3.4 Ma low-temperature apatite U-Th/He sample in northern Hells Canyon provides a potential age for the integration and incision event tied to rapid exhumation (Kahn et al., 2020). However, this age is not consistent with the landscape metrics for incision tied to integration. Propagated relict profiles in the region around this sample (RM 215) suggest that only ∼200 m of incision has taken place since

knickpoint initiation (Figure 4.9B). With a partial retention temperature of ∼60 °C, the apatite U-Th/He system would require ∼2 km of exhumation with a 30 °C km^{-1} geotherm in order for a cooling signal to be detected. The detected signal could instead be cooling which predates capture, perhaps the initial incision signal through the CRBG tied to headward erosion by a tributary of the Columbia River. In this scenario, the 3.4 Ma age would represent a maximum age for drainage integration and incision.

We therefore estimate that the capture of Lake Idaho took place roughly between ∼3.4 Ma and potentially 2.5 Ma, or possibly younger. This time frame fits within the existing geologic literature and would just post-date the migration of the Yellowstone volcanic center from the Heise volcanic field to its present location (Figure 4.1 Ellis et al., 2010). This shift in volcanism may have coincided with an eastward shift in the continental divide, which provided greater drainage area to the Snake River and a potential increase in the surface water elevation of Lake Idaho (S. H. Wood & Clemens, 2002). This expansion of drainage area may also have been compounded by a late Pliocene increases in precipitation across the region (Bartoli et al., 2005).

We can further estimate the age of incision by combining the modeled erosion rates below knickpoints on tributaries along the canyon with the elevation of our caves above the Snake River. We treat the higher cavern as having formed before capture, and the lower cavern as having formed after the capture of Lake Idaho. The age for Ashmead, the cavern 343 m above the Snake River, is calculated as ranging from 2.0 ± 0.25 Ma to as young as 1.2 ± 0.18 Ma. We calculate Red Fish Cave as ranging from 1.4 ± 0.17 Ma to as young as 0.9 ± 0.11 Ma. These two age ranges bracket the age of Hells Canyon as falling between ∼2.0 and ∼0.9 Ma, both of which are younger than previous estimates discussed above.

Further constraints in the form of cosmogenic burial dates from cave deposits will be helpful in narrowing this range or estimates for the age of Hells Canyon. Additional timing constraints could also be provided in the form of a formal stream-profile inversion (*sensu* Goren, Fox, & Willett, 2014) . This process would use tributary river profiles as a geomorphic tape recorder (Whittaker & Boulton, 2012). Steepness trends along the length of each tributary would be interpreted as reflecting uplift or erosion rates through time. However, this type of inversion requires the assumption that $n = 1$. Data herein already show a non-linear relationship between steepness and erosion as k_{sn} doubles while erosion rates increase by between 4 and 27 fold (Figure 4.10). Moreover, data in the proximal Salmon River (Figure 4.1) indicate $n = 0.67$ (Larimer et al., 2018). There is also the potential that a detailed detrital zircon study of sediments cores from the Astoria fan would be able to detect the grains associated with the western Snake River Plain. There should be a distinct change in the zircon populations from before to after the capture of Lake Idaho and integration of western Idaho drainages. This is a promising area for future research in the Hells Canyon region and drainage reorganization in the inland Pacific Northwest more broadly.

4.8 Conclusions

Prior to this study, the landscape of Hells Canyon was enigmatic and hypotheses for its formation were built on peripheral geologic constraints – upstream and downstream. In this study, we provide the first geomorphic analysis of the canyon itself. We confirmed that a distinct transient signal is present on tributaries to the Snake River through the canyon corridor. The spatial pattern and relative height of these knickpoints constrain a paleo-drainage divide that existed before the capture and integration of Lake Idaho. This pattern was expected and

is supported by our 1-D stream profile forward models. Moreover, the map view drainage pattern in the region contains an inherited pattern related to its original form. Projected relict profiles provide key constraints for the amount of fluvial incision in the canyon to 1 km, decreasing to the north and south from the point of capture.

The timing of fluvial incision through Hells Canyon remains poorly constrained. Cosmogenic burial dating of cave sediments will provide the most robust measure of incision rate over million-year timescales, which we will use to bracket the age of the canyon. Based on a thorough literature review, we believe the canyon is younger than ∼3.5 Ma and potentially younger than ∼2.5 Ma. Our model-derived erosion rates bracket the cave ages as between ∼2.0 and ∼0.9 Ma, suggesting that modern canyon incision is younger than published estimates. Our caves will allow us to test and refine these estimates. As of this writing, it appears that the deepest canyon in North America has been carved in the past 1-3 Myr, which implies rapid rates of fluvial incision.

APPENDIX A

CHIEF JOSEPH DIKE SWARM SUPPLEMENTARY MATERIALS

All of the material presented below can be accessed through the Geological Society of America Data Repository for our paper. Which at the time of this writing was published with the Geological Society of America Journal *Geosphere*. In fact the supplementary Plates and tables should be referenced from M. Morriss et al. (2020)

What is presented below are the supplementary tables, figures, and plates for that paper and Chapter II.

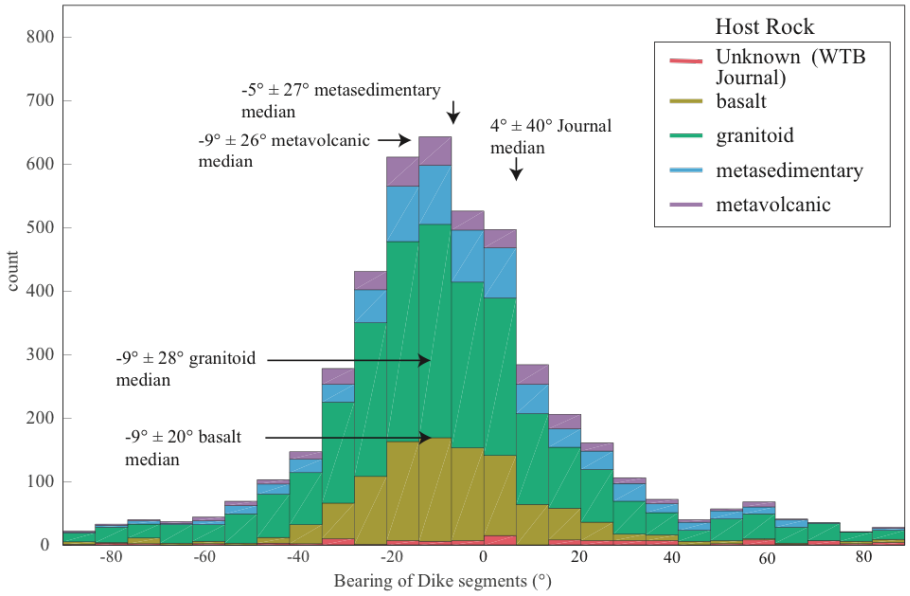

Figure A.1. Dike bearing, binned by host rock type. This plot shows the predominance of the NNW orientation and how these orientations are consistent across rock types.

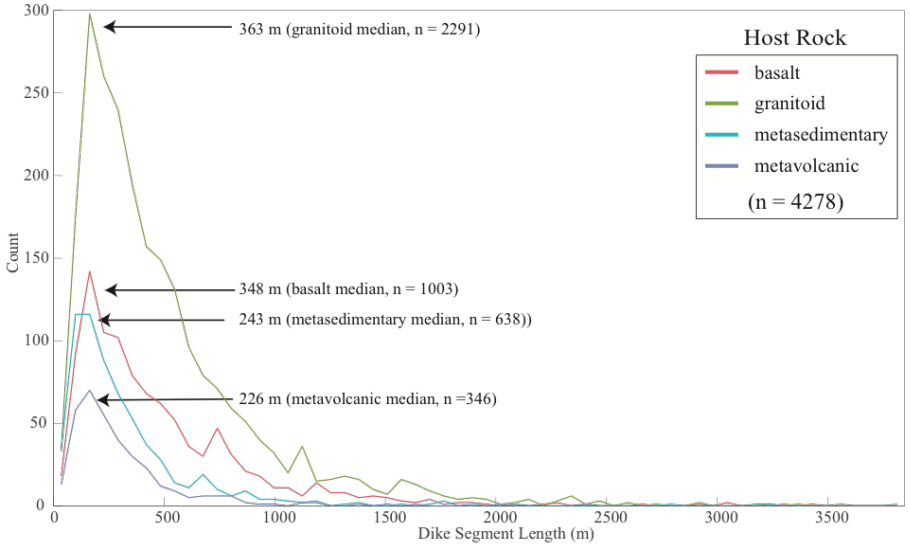

Figure A.2. Dike segment length, broken out by host rock type. Dike segments hosted within granitoids dominate.

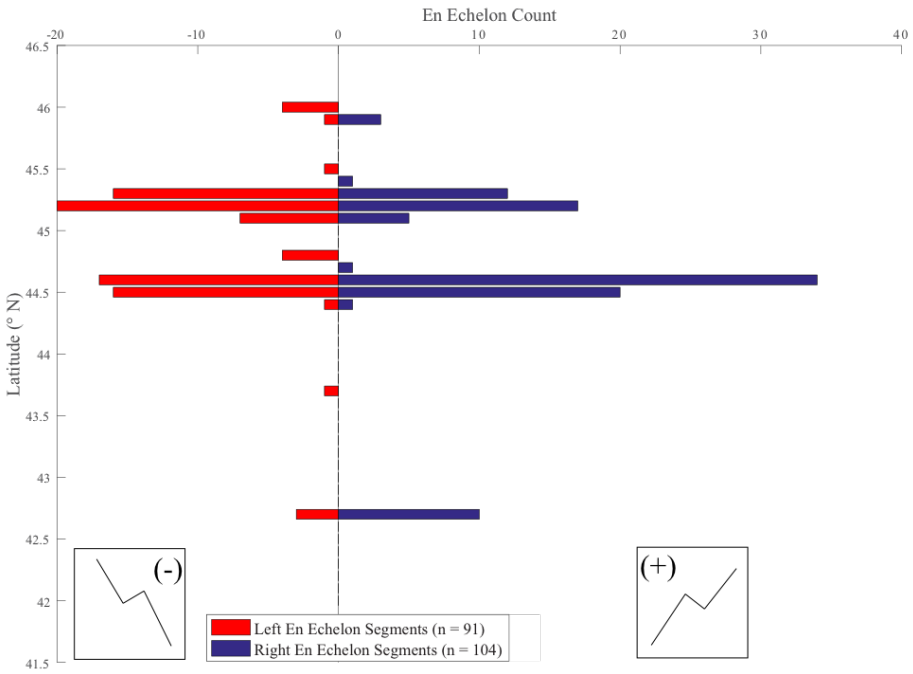

Figure A.3. En echelon or stepped offsets of dike segments were measured across the CJDS. Offsets were classified as "left-stepping" and "right-stepping" as indicated by inset figures. The hypotheses tested by this figure is the presence of a gradient or rotation in the orientation of principal horizontal stresses, which could drive a systematic shift in en echelon segmentation of dikes (Pollard et al., 1982)

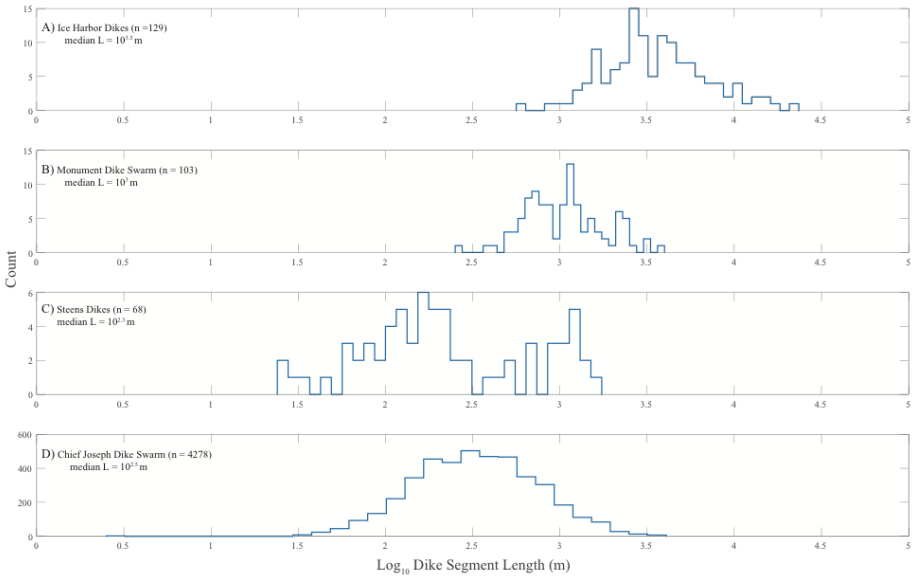

Figure A.4. Base 10 logarithm of dike segment length, broken out by different swarms and subswarms (Plate 1 in M. Morriss et al. (2020)). **A)** The Ice Harbor dikes. **B)** The Monument Dike Swarm dikes. **C)** The Steens dikes. **D)** Chief Joseph Dike Swarm dikes (note larger number than other swarms).

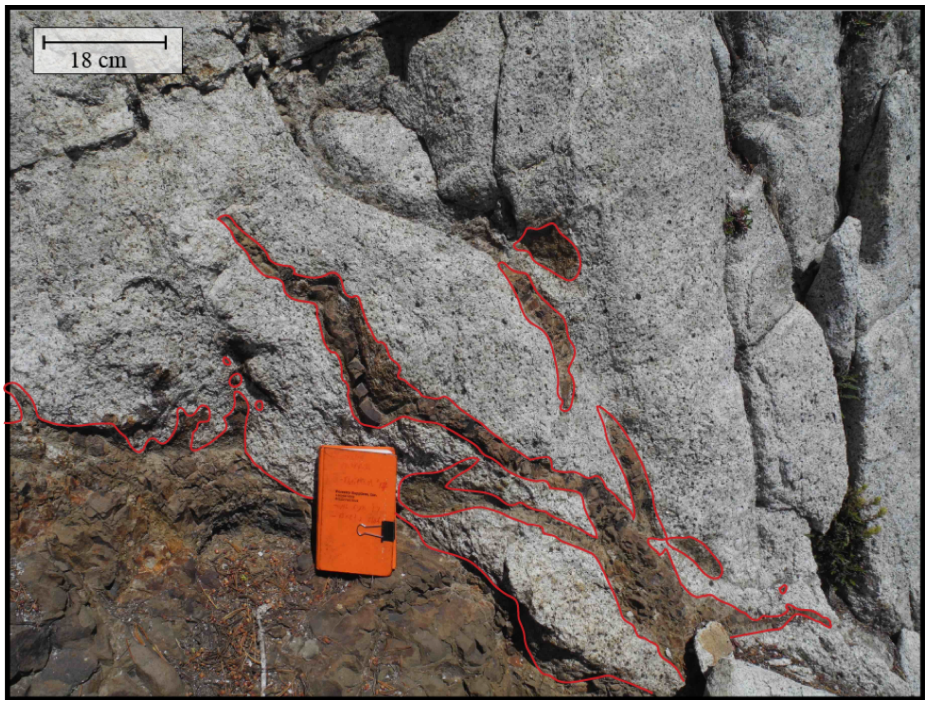

Figure A.5. An example of flame-like structure in a host-rock (granitoid) within the CJDS. This type of host-rock-dike interaction was only seen once in the 2016 and 2017 field seasons. The approximate location of this outcrop: 45.040663° N, 117.252655 ° W. Red lines are drawn around dike margins to highlight the degree of fragmentation.

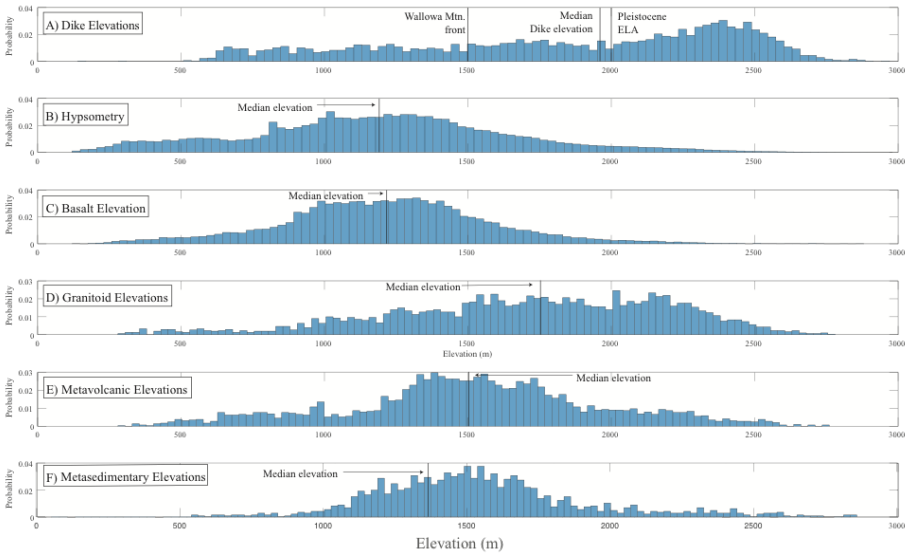

Figure A.6. Complete hypsometry of NE Oregon Dikes **(A)**; Topography **(B)**; and major rock types **(C-F)**.

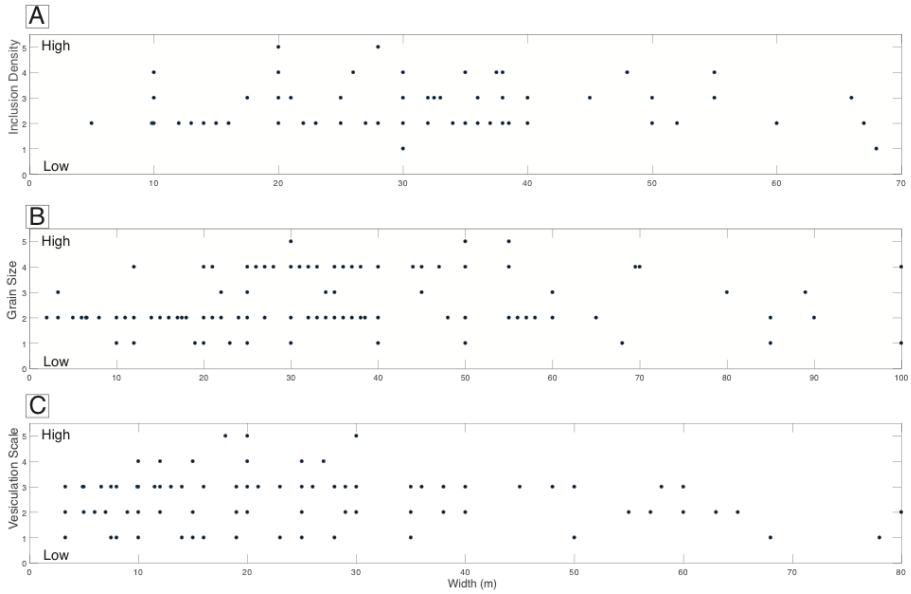

Figure A.7. WHT journal derived data regarding dike width versus inclusion scale, grain size, and vesiculation. **A.** Dike width versus a relative inclusion density. This relative scale for inclusions is described in the primary text. No discernable trend is visible nor was there a relationship that provided statistically significant. **B.** Dike width versus relative grain size. The dike grainsize scale originated in the WHT journal entries. No trend is visually apparent nor statistically significant. **C.** Dike width versus a relative vesicularity scale. No relationship was directly discernable from this data.

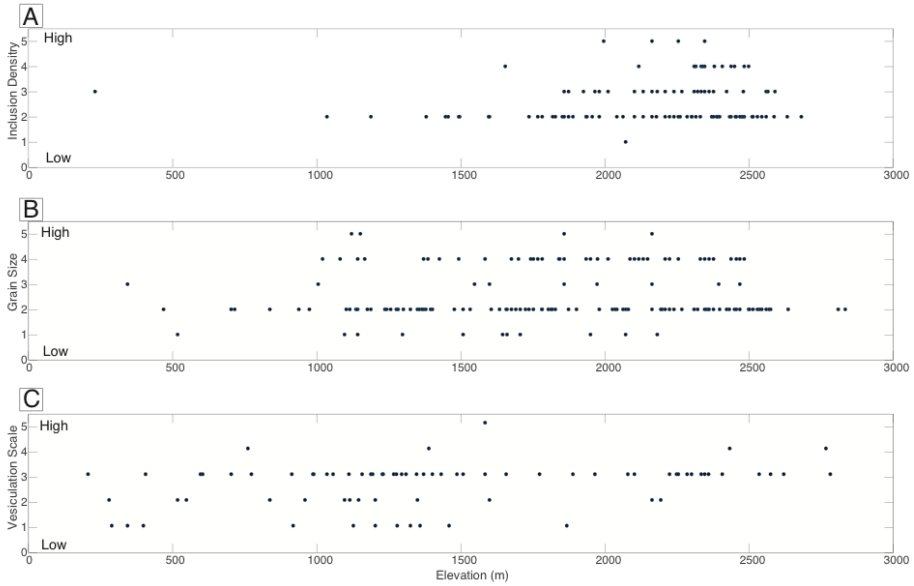

Figure A.8. Dike elevation versus inclusion scale, grain size, and vesicularity. All of these data are taken directly from the WHT journal collection. **A.** Dike elevation in meters versus a relative scale of inclusion density. While there is a left-skewed distribution, no statistically significant relationship could be discerned. **B.** Dike elevation versus dike grain size. There is no visually discernable relationship between these two variables, nor is there a statistically significant relationship. **C.** Dike elevation versus vesicularity. Here again, there is no discernable trend. Elevation can in certain areas of the CJDS be related to paleo-depth, so the lack of a greater vesicularity trend may have implications for degassing.

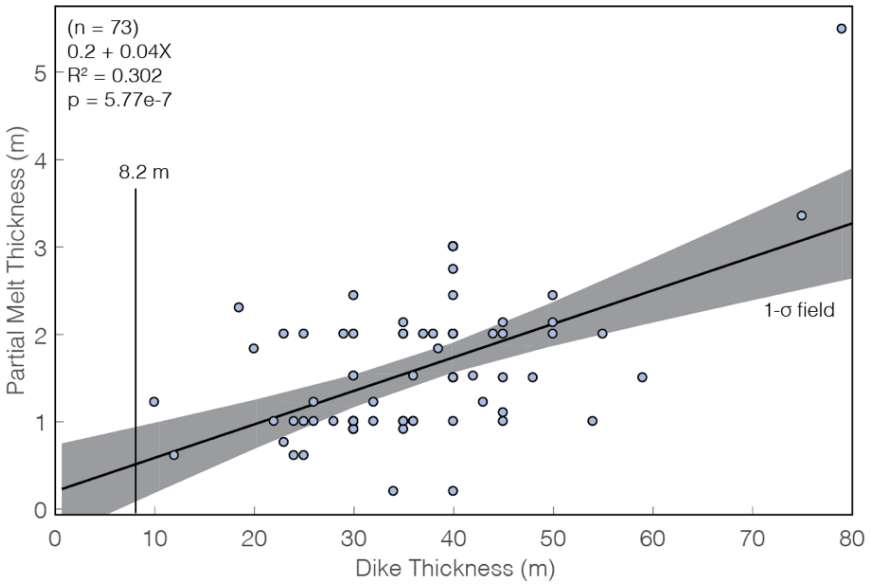

Figure A.9. Relationship between dike width and thickness of partial melt of host rock from WHT notebooks. Note that all of these dikes with partial melt are significantly thicker than the median dike width. This may imply that these dikes experienced multiple magma injections. The R2 of ∼0.3 indicates that 30% of the scatter in the plot above is explained well by the linear model above. The p-value for this model is 5.7 x 10^{-7}, indicating we can robustly say there is a positive relationship between dike thickness and the width of the partial melt zone.

APPENDIX B

HELLS CANYON EXHUMATION SUPPLEMENTARY MATERIALS

Herein are the supplementary tables and figures referenced in Chapter 4. This Appendix will be referenced within the main text and uploaded as part of our publication, submitted soon to *Earth and Planetary Science Letters*

B.1 Basalt Geochemistry

B.1.1 X-Ray Flourescence

Sample BRS 38 was sent to the Franklin and Marshall College X-Ray laboratory for Major and Trace element compositional analysis. This work took place in the spring of 2014. Below are the analytical methods used by that laboratory at the time.

B.1.2 Sample preparation for major element analysis

Sample analysis starts with a total volatile determination (% LOI) is made by weighing out ∼1 gram of sample to 4 decimal places, placing in a muffle furnace at 950 °C for 1.5 hours, removing and cooling to room temperature in a desiccator, and re-weighing and noting the weight change. A portion of this anhydrous sample powder (0.4000 ± 0.0001 grams) is mixed with lithium tetraborate (3.6000 ± 0.0002 grams), placed in a platinum crucible and heated with a meeker burner until molten. This molten material is swirled and mixed several time over 10-12 minutes and transferred to a platinum casting dish and quenched. This procedure produces a glass disk that is used for XRF analysis including SiO_2, TiO_2, Al_2O_3, Fe_2O_3 Total, MnO, MgO, CaO, Na_2O, K_2O, and P_2O_5, working curves for each element are determined by analyzing geochemical rock standards prepared exactly as described in the paragraph above. (See Abbey (1983) and Govindaraju (1994)

for chemical analyses of the rock standards). Between 50 and 60 data points are gathered for each working curve; various element interferences are also taken into account. Results are calculated and presented as percent oxide.

B.1.3 Ferrous iron titration and Loss on Ignition

The amount of ferrous Fe is determined by the titration using a modified Reichen and Fahey (1962) method. XRF determines total iron as Fe_2O_3. Loss on ignition is determined by heating an exact aliquot of the sample at 950 °C for 1.5 hours.

B.1.4 Preparation for XRF trace element analysis

Trace element analysis is accomplished by weighing out 7.0000 ± 0.0004 grams of whole rock powder and adding 1.4000 ± 0.0002 of high purity copolywax powder, mixing for 10 minutes, and pressing the powder into a briquette at 50,000 psi. Data are reported as parts per million (ppm) for Rb, Sr, Y, Zr, V, Ni, Cr, Nb, Ga, Cu, Zn, Co, Ba, U, Th, La, Ce, Sc, and Pb. Working curves for each element are determined by analyzing geochemical rock standards prepared exactly as outlined above, data for which has been synthesized in Abbey (1983) and Govindaraju (1994). Between 50 and 6 and a 4kW Rh super sharp X-ray tube. Zero data points are gathered for each working curve; various elemental interferences are also taken into considered. The Rh Compton peak is utilized for a mass absorption correction for region one elements.

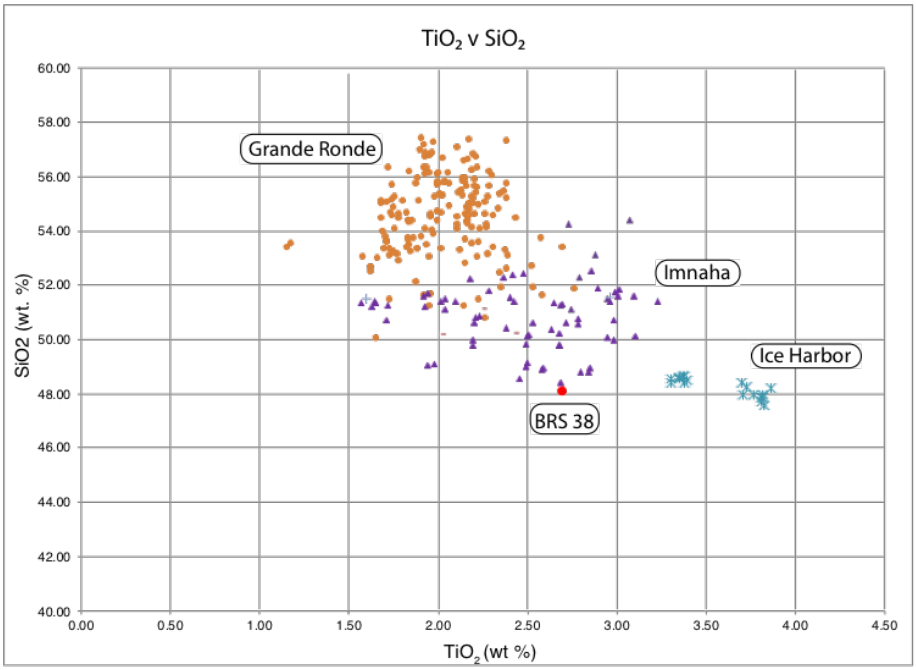

Figure B.1. TiO_2 v SiO_2 plot comparing BRS 38 to distribution of data for the Grande Ronde, Imnaha, and Ice Harbor units of the CRB. BRS 38 plots along the margin of the Imnaha distribution of points. All data were derived from Martin, Petcovic, and Reidel (2005).

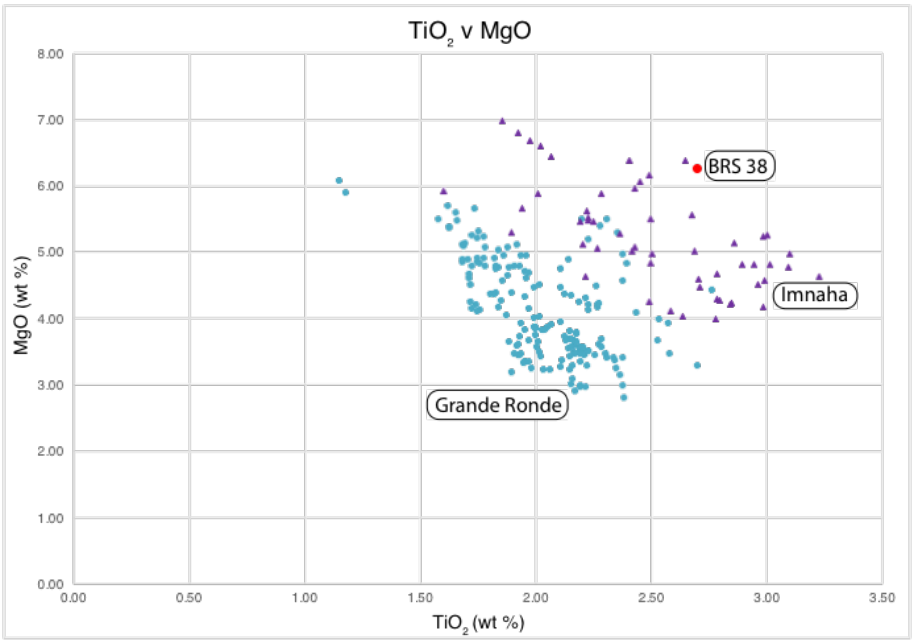

Figure B.2. TiO_2 v MgO plot, comparing BRS 38 to the distribution of Grande Ronde and Imnaha units from the CRB. Sample BRS 38 falls within the region defined by Imnaha samples. All data were derived from Martin et al. (2005).

B.2 Low-Temperature Thermochronology Analytical Methods

Noble Gas Thermochronology is rooted in a temperature dependent retention of daughter products of radiogenic decay in certain minerals. Both apatite and zircon are used in this study to infer a cooling, not crystallization, history of rocks along an elevation transect in Hells Canyon. These two minerals have unique temperature sensitivities due to different helium diffusivity through each mineral (Reiners & Brandon, 2006; Reiners et al., 2005). Broadly speaking apatite has a closure temperature of ∼70 °C, and zircon has a closure temperature of 180-200 °C (Reiners et al., 2005; Shuster, Flowers, & Farley, 2006). However, in both minerals, closure temperatures may be altered by the effect of collective radiation damage (R. M. Flowers et al., 2009; Guenthner et al., 2013). Shifts in the retentivity of helium in each grain can now be modeled with grain age and effective

uranium concentrations (eU). Effective uranium approximates the alpha production rate in the grain and is a stand-in for the amount of overall radiation damage. For both apatite and zircon there are now radiation damage models ZRDAAM (zircon) and RDAAM (apatite) that allow for a more holistic thermal history to be extracted from grains that contain information about their radiation damage (R. M. Flowers et al., 2009; Guenthner et al., 2013). These models represent the current standard for helium behavior in apatite and zircon. The inverse thermal modeling software, QTQT discussed below, also incorporates these radiation damage models (Gallagher, 2012).

B.2.1 Sample Preparation

The bulk of rock samples were sent to GeoSeps Services LLC in Moscow, Idaho for apatite and zircon separation (BRS39 – BRS50). Samples HS17-22 and 23 were processed by Zirchron LLC in Tucson, Arizona. Both mineral separation labs use standard routines for crushing, sieving, magnetic and heavy liquid separation. All apatite and zircon separates were sent to the CU Thermchronology Research and Instrumentation Laboratory (TRaIL) facility for processing/analysis outlined below.

B.2.2 Apatite and zircon (U-Th)/He Thermochronometry

Mineral grains were picked using a Leica M165 binocular microscope, with both transmitted and reflected polarized light, at the CU TRaIL facility in Boulder, Colorado. Priority was given to grains based on clarity, size, crystal form, and the lack of any visible inclusions. Grain dimensional measurements were made using a calibrated digital camera on the microscope in order to choose grains of similar size

to correct for alpha-ejection. After characterization and measurement, all grains were placed into Nb tubes, closed on both ends.

For helium analysis, grain packets were loaded into an ASI Alphachron He extraction and measurement line. Packets were placed in the UHC extraction line (∼3 x 10-8 torr) and heated with a 25W diode laser to ∼800-1100 °C for 5 to 10 minutes to extract radiogenic ^{4}He. The degassed ^{4}He was then spiked with approximately 13 ncc of pure ^{3}He, cleaned via interaction with two SAES getters, and analyzed on a Balzers PrismaPlus QME 220 quadrupole mass spectrometer. This procedure was repeated at least once to ensure complete mineral degassing. Degassed grains were then removed from the line, and taken to a Class 10 clean lab for dissolution.

Apatite grains, still enclosed in the Nb tubes, were placed in 1.5 mL Cetac vials, spiked with a ^{235}U - ^{230}Th - ^{145}Nd tracer in HNO_3, capped, and baked in a lab oven at 80 °C for 2 hours. Zircon, titanite, and other more refractory phases were dissolved using Parr large-capacity dissolution vessels in a multi-step acid-vapor dissolution process. Grains (including the Nb tube) were placed in Ludwig-style Savillex vials, spiked with a ^{235}U - ^{230}Th - ^{145}Nd tracer, and mixed with 200 μl of Optima grade HF. The vials were then capped, stacked in a 125 mL Teflon liner, placed in a Parr dissolution vessel, and baked at 220 °C for 72 hours. After cooling, the vials were uncapped and dried down on a 90 °C hot plate until dry. The vials then underwent a second round of acid-vapor dissolution, this time with 200 μl of 6N Optima grade HCl in each vial that was baked at 200 °C for 24 hours. Vials were then dried down a second time on a hot plate. Once dry, 200 μl of a 7:1 HNO_3:HF mixture was added to each vial, the vial was capped, and cooked on the hot plate at 90 °C for 4 hours.

Once the minerals were dissolved, regardless of the dissolution process, they were diluted with 1 to 3 mL of doubly-deionized water, and taken to the ICP-MS lab for analysis. Sample solutions, along with normal solutions and blanks, were analyzed for U, Th, and Sm content using an Agilent 7900 quadrupole ICP-MS. After the U, Th, and Sm contents were measured, He dates and all associated data were calculated on a custom spreadsheet using the methods described in (Ketcham, Gautheron, & Tassan-Got, 2011). The natural occurring 238U/235U ratio used in data reduction was 137.818 after (Hiess, Condon, McLean, & Noble, 2012). Every batch of samples includes standards run sporadically throughout the process to monitor procedures and maintain consistency from run to run. Long term averages of Fish Canyon Tuff zircons and Durango fluorapatites run in the CU TRaIL are 28.7 ± 1.8 Ma (n=150) and 31.1 ± 2.1 (n=85), respectively.

B.3 Supporting Information for Thermochronology Results

B.4 Supporting Information On Modeling Results

B.4.1 QTQt Inverse Model Parameters

Model constraints include a modern mean annual temperature for the uppermost sample of 0 ± 5 °C at ∼2500 m. We used an average environmental lapse rate of 6 ± 3 °C km^{-1} to approximate the temperature separation between each sample, knowing sampled modern elevation and inferred paleodepth. This lapse rate means the lowest sample should be ∼12 °C in the modern, which is very close to the annual average temperature in Riggins, Idaho the town closest in elevation to our deepest sample with a permanent weather station. We also chose a geothermal gradient of 15 ± 15 °C km^{-1}. This large range allows for a geotherm up to 30 °C which is likely realistic for this region but also allows for a much cooler geotherm. We make use of two different prior pieces of information about

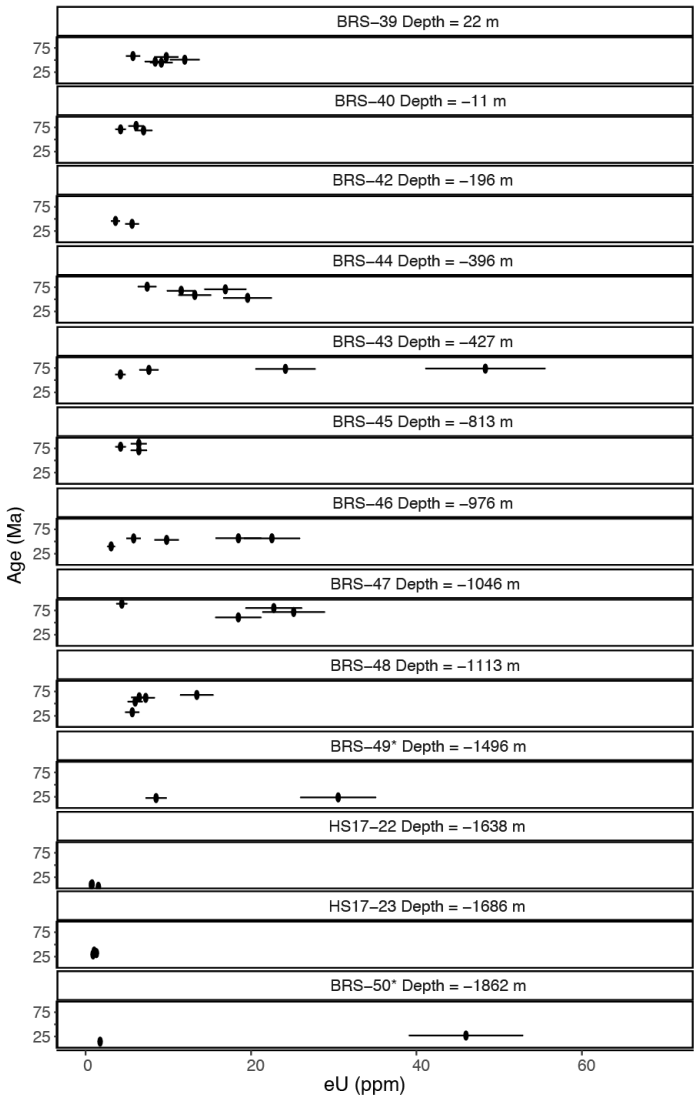

Figure B.3. Effective Uranium versus sample grain age, plotted by sample depth. Those samples with asterisks next to their number were treated as potentially reset by proximal CRB flows (BRS-39 and BRS-42) or hydrothermally altered (HS17-22).These plots can reveal the rate at which samples cooled through the partial retention zone (PRZ), no eU-Age trend could mean fast cooling. However, a visible eU-Age trend would indicate slow cooling through the PRZ. Several samples lower in the canyon (BRS-48 and BRS-50) appear to display such an eU-Age trend. The presence of this trend also provides motivation for using the R. M. Flowers et al. (2009) RDAAM radiation damage models for apatite in our thermal inverse modeling. BRS-49 and BRS-50 (marked with asterisk have single grains which plot beyond the limit of the x-axis, see supplementary table B.2 for more details)

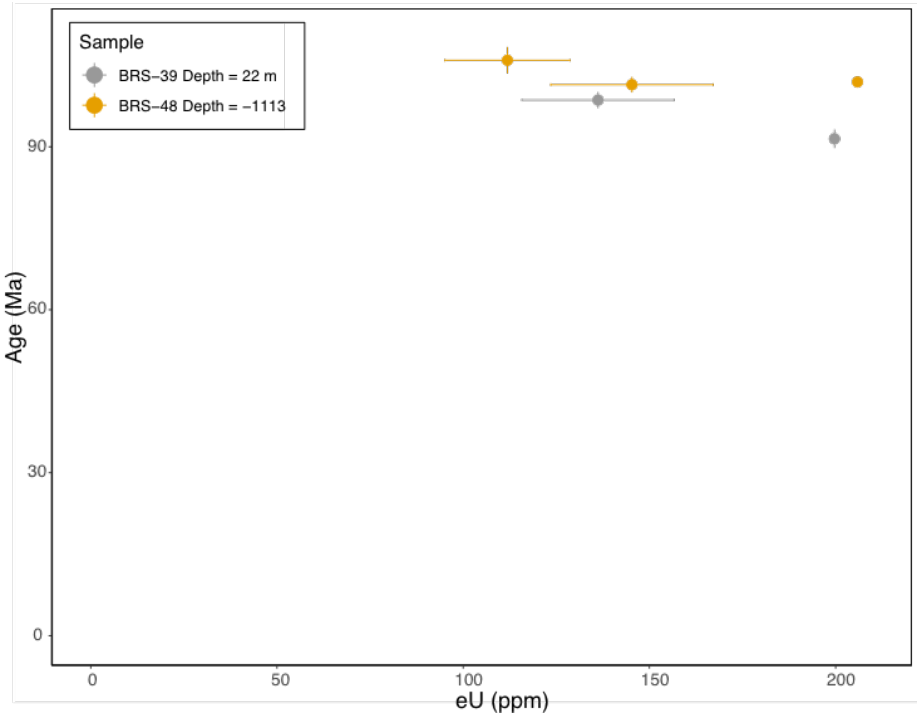

Figure B.4. Effective Uranium versus sample grain age for ZHe samples. Both sample BRS 39 and BRS-49 show a slightly negative eU-age trend, potentially indicative of radiation damage (Guenthner et al., 2013). Given these data, our inverse modeling for these zircon samples use the radiation damage model for zircons from Guenthner et al. (2013).

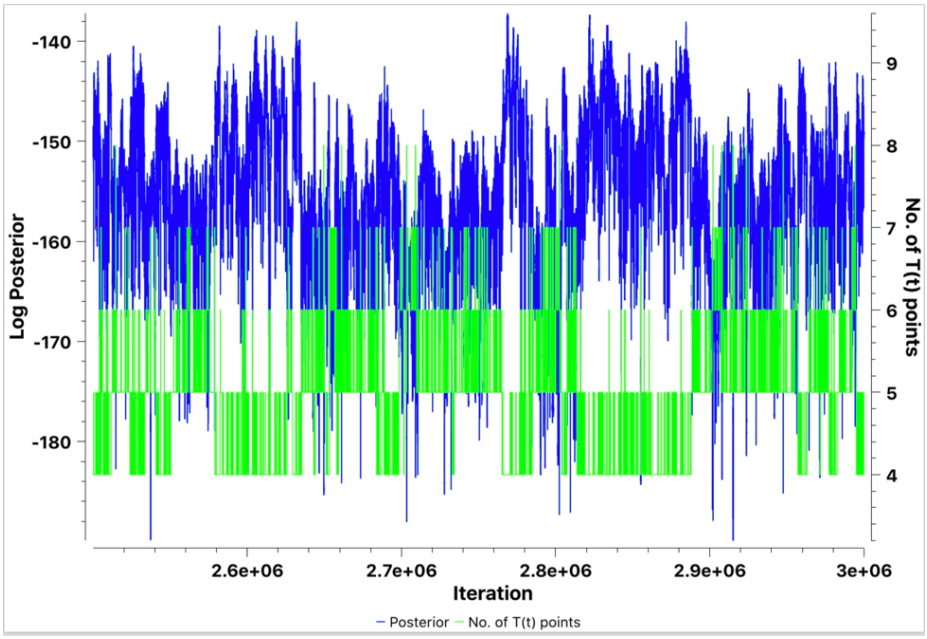

Figure B.5. Posterior chain performance. The log posterior as a function of post-burn-in sampling for our vertical transect (shown in blue with left axis). The number of time-temperature points are shown in green, on the right axis. This chain is developed after 2.5 * 10^6 burn-in iterations and shows reasonable convergence for this sample suite. Convergence is evaluated as the log posterior stabilizing around a mean, and the value changing with each model run.

the cooling of our sample profile. Vallier (1995) determined the age of this pluton as ∼115 ± 2.5 Ma, placing an initial temperature for the study transect cooling through ∼350 °C and 550 °C for biotite and hornblende, respectively. QTQt then incorporates these constraints into its best fitting model for all of the samples in our profile.

We ran QTQt for 2.5*10^6 burn-in iterations, followed by 500,000 iterations. Model efficacy was determined by comparing measured sample data with model produced results (Fig. 3.6). Model stability was assessed by examining the posterior chain (Fig. B.6). We used such a long burn-in period to ensure the model has exhausted its exploration of parameter space.

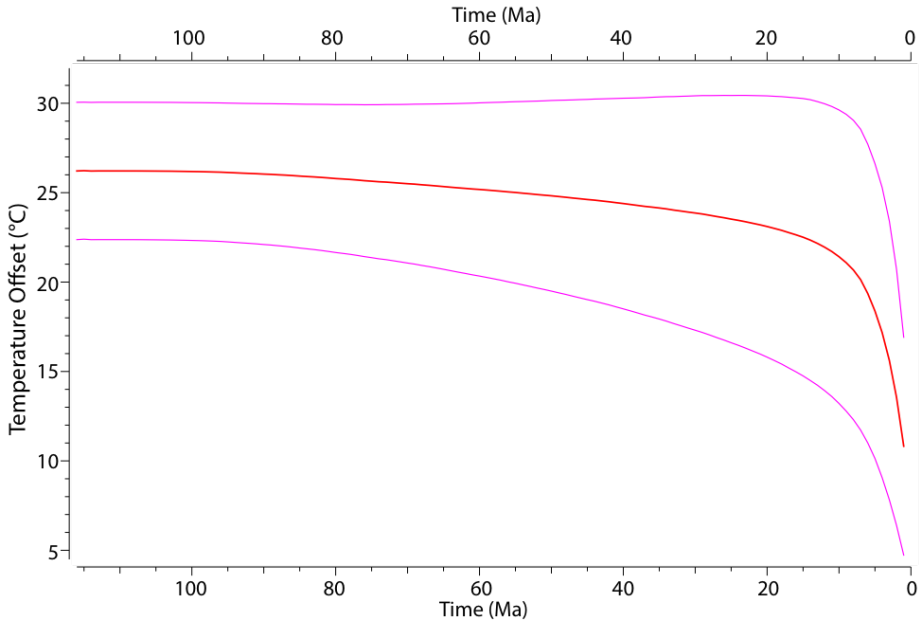

Figure B.6. Predicted thermal offset between shallowest (159 m) and deepest (-1258 m) samples from QTQt model. These results can easily be converted to a geotherm with the 1416 m of separation between the highest and lowest samples. The mean predicted geotherm from 110 Ma to ∼10 Ma is ∼18 °C km^{-1}, cooling significantly after ∼10 Ma to the present temperature offset seen in our elevation transect of 5 °C km^{-1}.

Supplementary Table 1. Major oxide and trace element geochemistry of sample BRS 38 collected 45.349175 °N, 116.573559 °W

Specimen	BRS38
SiO2	48.04
TiO2	2.70
Al2O3	14.96
Fe2O3	2.67
FeO	10.27
MnO	0.21
MgO	6.26
CaO	9.44
Na2O	2.78
K2O	0.67
P2O5	0.25
LOI	1.54
Total	**99.79**
Fe2O3T	14.08
Rb	14.5
Sr	385
Y	28.2
Zr	149
V	324
Ni	97
Cr	151
Nb	10.6
Ga	20.5
Cu	121
Zn	108
Co	53
Ba	288
La	10
Ce	16
U	<0.5
Th	0.6
Sc	21
Pb	<1

Table B.1. Major oxide and trace element geochemistry of sample BRS-38 collected 45.349175 °N, 116.573559 °W

Sample[a]	length[b] 1 (µm)	width[b] 1 (µm)	length[b] 2 (µm)	width[b] 2 (µm)	U (ppm)	Th (ppm)	Sm (ppm)	eU[c] (ppm)	1-σ[d]	He (nmol/g)	Raw date (Ma)	Corr date (Ma)	2-σ[e] (Ma)	Notes
BRS 39	45.333623° N, 116.575056° W, 2182.4 m			*granitoid*										
a1	117.9	86.9	119.2	66.6	6.4	11.6	34.9	9.2	1.4	1.4	27.9	44.7	3.2	
a2	133.6	82.0	131.3	62.3	5.4	12.8	35.4	8.4	1.3	1.4	28.6	46.7	2.9	
a3	136.7	60.6	138.9	50.6	7.7	8.6	38.0	9.8	1.5	1.7	30.8	56.2	3.9	
a4	131.1	70.8	130.5	58.2	4.6	4.7	12.1	5.7	0.9	1.1	34.4	58.2	6.4	
a5	147.3	88.8	148.0	67.2	9.2	12.1	39.9	12.0	1.8	2.2	32.8	50.7	2.2	
z1	155.9	66.4	158.1	64.8	64.8	64.8	64.8	136.2	20.4	52.8	71.5	98.6	3.0	
z2	133.4	61.4	129.2	52.0	52.0	52.0	52.0	199.7	30.0	67.4	62.2	91.5	3.4	
BRS 40	45.284205° N, 116.578051° W, 2499 m			*metavolcanic*										
a1	199.7	122.1	184.3	92.4	6.3	2.8	3.9	7.0	1.1	1.9	50.7	68.7	4.3	
a2	97.8	92.9	97.2	70.2	4.1	0.6	8.7	4.2	0.6	1.0	45.1	70.9	11.1	
a3	158.9	57.6	163.7	56.6	5.6	2.4	4.2	6.1	0.9	1.5	45.7	77.9	6.8	
BRS 42	45.273893° N, 116.574019° W, 2377 m			*metavolcanic*										
a1	*151.0*	*104.7*	*154.9*	*85.6*	*1.4*	*2.0*	*28.0*	*1.8*	*0.3*	*0.8*	*71.2*	*98.1*	*9.7*	rejected
a3	*133.7*	*80.4*	*124.3*	*69.3*	*1.2*	*2.2*	*28.7*	*1.7*	*0.3*	*0.7*	*67.2*	*101.5*	*23.9*	< 2 ppm eU with old ages, possible injection
a4	120.8	75.9	119.9	64.0	3.8	7.8	36.0	5.6	*0.8*	0.8	24.3	39.9	*4.3*	
a5	89.0	74.1	92.2	48.8	2.9	3.1	42.5	3.6	*0.5*	0.5	24.9	45.9	*10.0*	
BRS 43	45.283051° N, 116.594185° W, 2118 m			*granitoid*										
a1	159.4	117.6	163.4	96.5	3.0	5.3	12.2	4.2	0.6	1.1	45.1	61.8	3.6	
a2	114.9	79.7	121.6	58.5	16.1	137.3	37.0	48.3	7.2	10.9	41.2	73.6	1.4	
a4	111.4	78.5	110.2	64.1	7.6	70.4	20.6	24.2	3.6	5.6	42.6	73.2	2.2	
a5	131.8	84.0	121.8	60.8	5.4	9.8	22.1	7.7	1.1	1.8	43.0	71.0	4.8	
BRS 44	45.289354° N, 116.602215° W, 1828 m			*granitoid*										
a1	161.5	80.7	166.3	51.1	13.0	16.7	30.1	16.9	2.5	3.7	39.7	70.6	2.3	
a2	116.5	85.0	114.7	64.3	10.1	13.1	23.3	13.2	2.0	2.6	36.2	58.9	2.8	
a3	198.1	119.3	200.0	70.9	15.2	18.6	27.7	19.6	2.9	3.9	35.9	52.9	1.0	
a4	130.7	77.4	129.5	50.5	9.5	8.8	26.1	11.6	1.7	2.4	37.4	67.5	3.4	
a5	152.9	86.5	150.3	56.5	5.7	7.6	35.1	7.4	1.1	1.9	45.7	76.0	5.2	
BRS 45	45.295135° N, 116.60997° W, 1585 m			*granitoid*										
a1	242.9	158.4	231.1	91.1	5.2	5.2	31.6	6.4	1.0	2.3	64.1	84.5	2.2	
a2	136.3	92.9	134.2	74.8	3.4	3.4	27.4	4.2	0.6	1.3	52.8	78.2	6.4	
a3	104.3	62.1	110.9	46.3	5.7	3.3	39.6	6.4	1.0	1.4	36.9	70.9	8.0	
BRS 46	45.298845° N, 116.613251° W, 1402 m			*granitoid*										
a1	210.5	100.0	215.2	*57.8*	14.6	16.3	27.0	18.5	2.8	3.7	36.7	56.8	2.0	
a2	142.3	71.9	144.1	52.9	*7.8*	8.3	17.3	9.8	1.5	1.6	30.3	53.3	3.5	
a3	192.0	87.9	195.7	65.4	19.7	12.0	28.0	22.5	3.4	4.6	37.3	56.7	1.2	
a4	132.4	92.1	139.4	83.7	4.8	4.5	16.1	5.8	0.9	1.3	39.3	56.4	18.5	
a5	91.6	79.0	88.2	67.8	2.8	1.4	5.6	3.1	0.5	0.4	24.2	40.0	9.1	
BRS 47	45.301639° N, 116.625116° W, 1158 m			*granitoid*										
a1	136.2	67.7	140.3	46.3	3.5	3.7	26.1	4.4	0.7	1.2	46.4	88.8	10.7	
a2	144.7	88.2	155.4	54.5	19.6	23.8	40.3	25.2	3.8	5.6	40.8	71.8	1.7	
a3	174.7	65.6	168.3	51.6	19.9	12.3	34.4	22.8	3.4	5.7	45.4	79.8	2.3	
a4	*134.0*	*70.9*	*136.8*	*50.1*	*3.7*	*1.9*	*11.5*	*4.1*	0.6	*2.0*	*87.2*	*157.7*	17.6	rejected
a5	78.8	100.7	75.2	74.6	15.6	12.3	33.0	18.5	2.8	3.8	37.1	60.7	3.1	old age, low eU, potential injection
BRS 48	45.308693° N, 116.637963° W, 952 m			*granitoid*										
a1	159.3	73.9	146.0	68.9	5.3	2.9	33.6	6.0	0.9	1.2	35.6	54.1	2.5	
a2	141.7	87.2	143.0	53.9	11.0	10.5	57.8	13.4	2.0	3.1	41.3	67.8	2.6	
a3	132.9	78.2	133.9	60.9	5.9	6.0	32.9	7.3	1.1	1.6	38.1	61.8	3.2	
a4	132.2	79.0	133.3	75.9	4.9	6.9	28.3	6.5	1.0	1.5	41.2	62.9	4.5	
a5	137.0	74.7	134.4	48.8	5.4	1.0	12.9	5.6	0.8	0.5	17.4	32.3	5.0	
z1	293.4	147.7	302.9	118.2	105.6	26.9	30.5	111.9	16.8	55.3	90.8	105.9	4.9	
z2	350.9	125.3	351.7	137.7	196.6	39.4	0.0	205.9	30.9	98.3	88.0	101.9	1.7	
z3	278.9	108.1	283.4	84.9	137.7	32.6	0.0	145.3	21.8	65.2	82.7	101.4	2.9	
BRS 49	45.318724° N, 116.643612° W, 731 m			*metavolcanic*										
a1	134.0	71.8	137.9	51.8	113.0	97.2	10.7	135.8	20.4	4.2	5.7	10.2	0.3	
a2	105.1	89.5	95.8	64.2	26.7	16.4	11.1	30.5	4.6	2.4	14.5	23.9	1.2	
a3	79.9	65.5	79.9	57.0	8.2	1.6	3.3	8.5	1.3	0.6	12.6	22.5	4.1	
BRS 50	45.349123° N, 116.653378° W, 487 m			*metavolcanic*										
a1	95.9	97.2	89.4	62.8	1.7	0.3	0.1	1.8	0.3	0.1	8.7	14.5	3.3	
a2	94.4	85.2	94.4	62.7	95.3	53.9	45.8	108.0	16.2	10.1	17.2	29.1	0.7	
a3	108.7	64.6	108.7	59.8	24.7	90.7	31.4	46.0	6.9	3.8	15.2	27.1	1.0	
HS17 22	45.40837° N, 116.60178° W, 500 m			*metavolcanic*										
a1	130.0	80.0	140.0	80.0	0.5	1.4	17.0	0.8	0.1	0.0	7.2	10.4	2.6	
a2	140.0	110.0	140.0	120.0	1.0	2.5	23.1	1.5	0.2	0.0	3.9	5.3	1.0	
a3	130.0	160.0	124.0	120.0	0.5	0.9	12.5	0.7	0.1	0.0	7.0	9.2	2.2	
HS17 23	45.4037° N, 116.61022° W, 500 m			*metavolcanic*										
a1	100.0	69.0	100.0	50.0	0.9	1.9	14.2	1.3	0.2	0.1	17.5	32.2	6.1	
a2	100.0	100.0	100.0	80.0	0.7	0.9	13.3	0.9	0.1	0.1	19.9	29.5	4.9	
a3	100.0	70.0	90.0	80.0	0.7	1.6	19.5	1.0	0.2	0.2	23.6	35.5	4.0	
a4	*200.0*	*140.0*	*180.0*	*140.0*	*0.5*	*0.8*	*10.9*	*0.7*	0.1	*0.2*	*50.8*	*62.9*	3.9	rejected
														old age, low eU, potential injection

[a] a - apatite; z = zircon
[b] grain length and width, measured from two different angles
[c] eU - effective uranium concentration, weights U and Th for their alpha productivity, computed as [U] + 0.235 *
[d] estimated uncertainty in eU measurement. Approximately, 15% of original e
[e] Double analytical uncertainty based on uncertainties in U, Th, and He measurements

Table B.2. AHe and ZHe grain ages

Table S3, Mean Apatite and Zircon Ages.

Full Sample Name	Latitude (°N)	Longitude (°W)	Elevation (m)	Depth (m)	Mean Age (Ma)	1 σ (Ma)
			Apatite			
*BRS 39**	*45.333623*	*-116.575056*	*2182*	*-63*	*51.3*	*5.8*
BRS 40	45.284205	-116.578051	2499	159	72.5	4.8
*BRS 42**	*45.273893*	*-116.574019*	*2377*	*-49*	*42.9*	*4.2*
BRS 43	45.283051	-116.594185	2118	-102	69.9	5.5
BRS 44	45.283051	-116.594185	1829	-326	65.2	9.2
BRS 45	45.295135	-116.60997	1585	-517	77.9	6.8
BRS 46	45.298845	-116.613251	1402	-673	52.6	7.2
BRS 47	45.301639	-116.625116	1158	-812	75.3	12.0
BRS 48B	45.308693	-116.637963	952	-912	55.8	14.0
BRS 49	45.318724	-116.643612	732	-1094	18.9	7.5
BRS 50	45.349123	-116.653378	488	-1258	23.6	7.9
*HS 17 22**	*45.40837*	*-116.60178*	*500*	*-926*	*8.3*	*2.6*
HS 17 23	45.4037	-116.61022	500	-1017	32.4	3.0

* Sample treated as partially reset by CRBs or by hydrothermal alteration. These samples are not included in modeling or analsysis in this publication

			Zircon			
BRS 39	45.333623	-116.575056	2182	-63	95.0	5.0
BRS 48B	45.308693	-116.637963	952	-912	103.1	2.5

Table B.3. Mean Apatite and Zircon Ages

1. Thermochronologic data

Samples used in QTQT

AHe & ZHe Samples

Sample[a]	Depth	Length (μm)	Width (μm)	Thickness (μm)[b]	U (ppm)	Th (ppm)	Sm (ppm)	He (nmol/g)
BRS 39								
z1	-63	155.9	66.4	64.8	64.8	64.8	64.8	52.8
z2	-63	133.4	61.4	52.0	52.0	52.0	52.0	67.4
BRS 40								
a1	159	199.7	122.1	92.4	6.3	2.8	3.9	1.9
a2	159	97.8	92.9	70.2	4.1	0.6	8.7	1.0
a3	159	158.9	57.6	56.6	5.6	2.4	4.2	1.5
BRS 43								
a1	-102	159.4	117.6	96.5	3.0	5.3	12.2	1.1
a2	-102	114.9	79.7	58.5	16.1	137.3	37.0	10.9
a4	-102	111.4	78.5	64.1	7.6	70.4	20.6	5.6
a5	-102	131.8	84.0	60.8	5.4	9.8	22.1	1.8
BRS 44								
a1	-326	161.5	80.7	51.1	13.0	16.7	30.1	3.7
a2	-326	116.5	85.0	64.3	10.1	13.1	23.3	2.6
a3	-326	198.1	119.3	70.9	15.2	18.6	27.7	3.9
a4	-326	130.7	77.4	50.5	9.5	8.8	26.1	2.4
a5	-326	152.9	86.5	56.5	5.7	7.6	35.1	1.9
BRS 45								
a1	-517	242.9	158.4	91.1	5.2	5.2	31.6	2.3
a2	-517	136.3	92.9	74.8	3.4	3.4	27.4	1.3
a3	-517	104.3	62.1	46.3	5.7	3.3	39.6	1.4
BRS 46								
a1	-673	210.5	100.0	57.8	14.6	16.3	27.0	3.7
a2	-673	142.3	71.9	52.9	7.8	8.3	17.3	1.6
a3	-673	192.0	87.9	65.4	19.7	12.0	28.0	4.6
a4	-673	132.4	92.1	83.7	4.8	4.5	16.1	1.3
a5	-673	91.6	79.0	67.8	2.8	1.4	5.6	0.4
BRS 47								
a1	-812	136.2	67.7	46.3	3.5	3.7	26.1	1.2
a2	-812	144.7	88.2	54.5	19.6	23.8	40.3	5.6
a3	-812	174.7	65.6	51.6	19.9	12.3	34.4	5.7
a5	-812	78.8	100.7	74.6	15.6	12.3	33.0	3.8
BRS 48B								
a1	-912	159.3	73.9	68.9	5.3	2.9	33.6	1.2
a2	-912	141.7	87.2	53.9	11.0	10.5	57.8	3.1
a3	-912	132.9	78.2	60.9	5.9	6.0	32.9	1.6
a4	-912	132.2	79.0	75.9	4.9	6.9	28.3	1.5
a5	-912	137.0	74.7	48.8	5.4	1.0	12.9	0.5
z1	-912	293.4	147.7	118.2	105.6	26.9	30.5	55.3
z2	-912	350.9	125.3	137.7	196.6	39.4	0.0	98.3
z3	-912	278.9	108.1	84.9	137.7	32.6	0.0	65.2
BRS 49								
a1	-1094	134.0	71.8	51.8	113.0	97.2	10.7	4.2
a2	-1094	105.1	89.5	64.2	26.7	16.4	11.1	2.4
a3	-1094	79.9	65.5	57.0	8.2	1.6	3.3	0.6
BRS 50								
a1	-1258	95.9	97.2	62.8	1.7	0.3	0.1	0.1
a2	-1258	94.4	85.2	62.7	95.3	53.9	45.8	10.1
a3	-1258	108.7	64.6	59.8	24.7	90.7	31.4	3.8
HS17 23								
a1	-1017	100.0	69.0	50.0	0.9	1.9	14.2	0.1
a2	-1017	100.0	100.0	80.0	0.7	0.9	13.3	0.1
a3	-1017	100.0	70.0	80.0	0.7	1.6	19.5	0.2

[a] - Samples from Table S1 used in modeling, n.b. this is a subset of our total dataset

[b] - Second measure of width is used for thickness in QTQt

z1 = zircon sample

a1 = apatite sample

Table B.4. Inverse model sample ages

Prior Information*

K-Ar System[1]	Rock Type	Mineral	Apparent age (Ma)	Uncertainty (Ma)	Effective Closure Temp (°C)[2]	Uncertainty (°C)
V-3-86	Quartz Diorite	Biotite	115.5	2.5	348	25
V-3-86	Quartz Diorite	Hornblende	115.3	3.0	550	50

[1] - K-Ar data on sampled pluton from Vallier (1995)
[2] - Closure temperatures derived from Reiners and Brandon (2006)

* QTQt incorporates prior knowledge about the cooling history of the region. In this case, we can provide data from the K-Ar

Explanation and Data source

This prior knowledge regarding the cooling of the sampled pluton comes from Vallier (1995). A single sample was analyzed using the K-Ar dating system, in both Biotite and Horneblende.

Profile Temperature constraints

1)	M.A.T. of highest sample	0 ± 5 °C	This temperature range covers the annual average temperature at the closest USDA SNOTEL site at 2410 m on Mount Howard.
2)	Environmental lapse rate	6 ± 3 °C km^{-1}	The average environmental lapse rate for the Troposphere. This rate makes the M.A.T. for our lowest most sample ~12 °C, which is the M.A.T of the closest populated city: Riggins, ID at approximately the same elevation.
3)	Geotherm	15 ± 15 °C km^{-1}	This large range allows for a geotherm up to 30 °C which is likely realistic for this region.

3. System- and model-specific parameters

	System	Model	Citation
He kinetic model:	AHe	RDAAM	(Flowers et al., 2009)
	ZHe	ZRDAAM	(Guenthner et al (2013)
Reheating:	Allowed		
	Model	Citation	
Modeling code:	QTQt64R5.7.0k	(Gallagher, 2012)	
	Burn-in iterations	Main model iterations	
Model runs attempted:	2,500,000	500,000	

Table B.5. Inverse model Parameters

APPENDIX C

HELLS CANYON GEOMORPHOLOGY SUPPLEMENTARY MATERIALS

Herein are the supplementary tables and figures referenced in Chapter 4. This Appendix will be referenced within the main text.

Table 1 Raw Erosion Rates from Belmont (2015) and modeled erosion rates above and below knickpoints.

Sample Number	Basin Number	Basin Name	Drainage Area (km^2)	Erosion Rate (mm / yr)	Uncertainty
HC-2	80	Little Granite Creek	22.05	0.31	0.05
HC-3	80	Granite Creek	61.25	0.14	0.02
HC-7	25	Sheep Creek	56.91	0.14	0.01
HC-9	25	Sheep Creek – Clarks Fork	28.5	0.07	0.01

Tributary name	Basin Number	Relict Rate (mean ± 1σ)	Adjusted Rate (mean ± 1 σ)	Number of Monte-Carlo Simulations
Granite Creek	80	0.04 ± 0.03	0.17 ± 0.02	300000
Sheep Creek	25	0.01 ± 0.01	0.27 ± 0.04	300000

Table C.1. Raw Erosion rates and modeled erosion rates

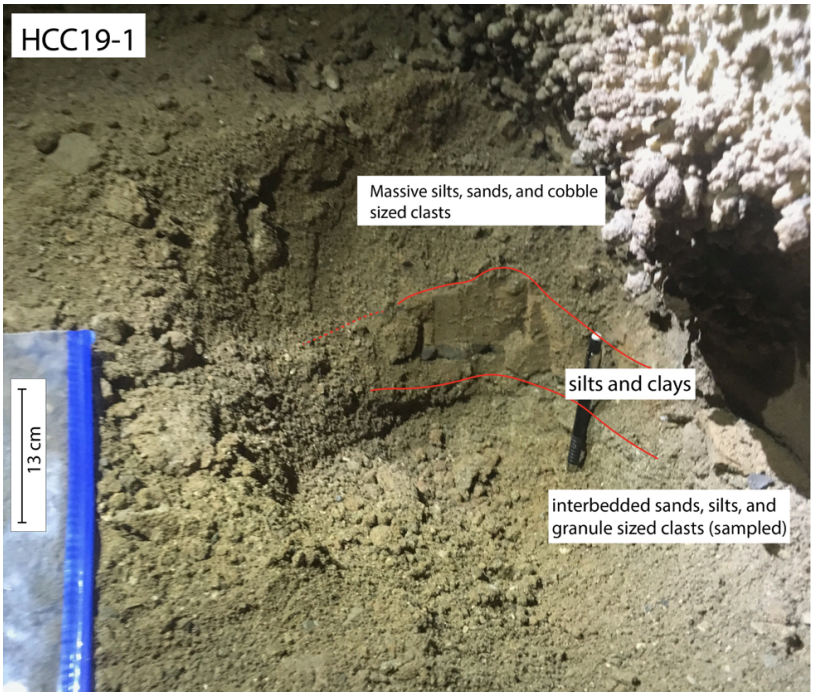

Figure C.1. Sample location for HCC19-1, collected in Red Fish Cave. The fluvial sediment was found under a cap of 20 cm of massive silts and sands which appeared to be native to the cave and another 7-8 cm of massive silt and clays. The sampled interval was composed of interbedded sands, silts and granule sized clasts. This sand and clasts were clearly allochthonous as quartz was common as were granule sized greenstone clasts.

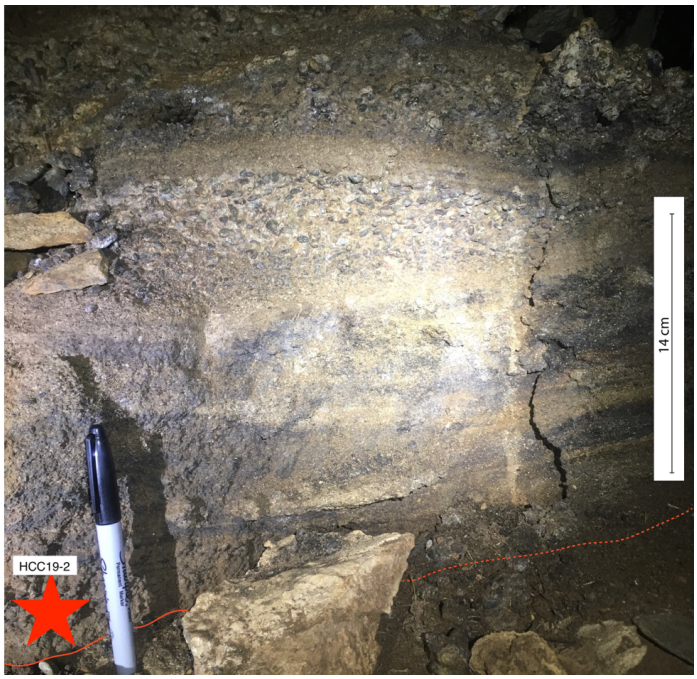

Figure C.2. Sample location for HCC19-2 in Ashmead Cave. This sample was collected at the bottom of this outcrop of sediment. The sediment covered a vertical distance of 1.5 m (mostly out of view). We sampled at the bottom of the outcrop. Most of the sediments could be characterized as sands to granule sized grains, well sorted and rounded. Small cobbles were located in beds toward the top of the section. Other than bedding few sedimentary structures were visible.

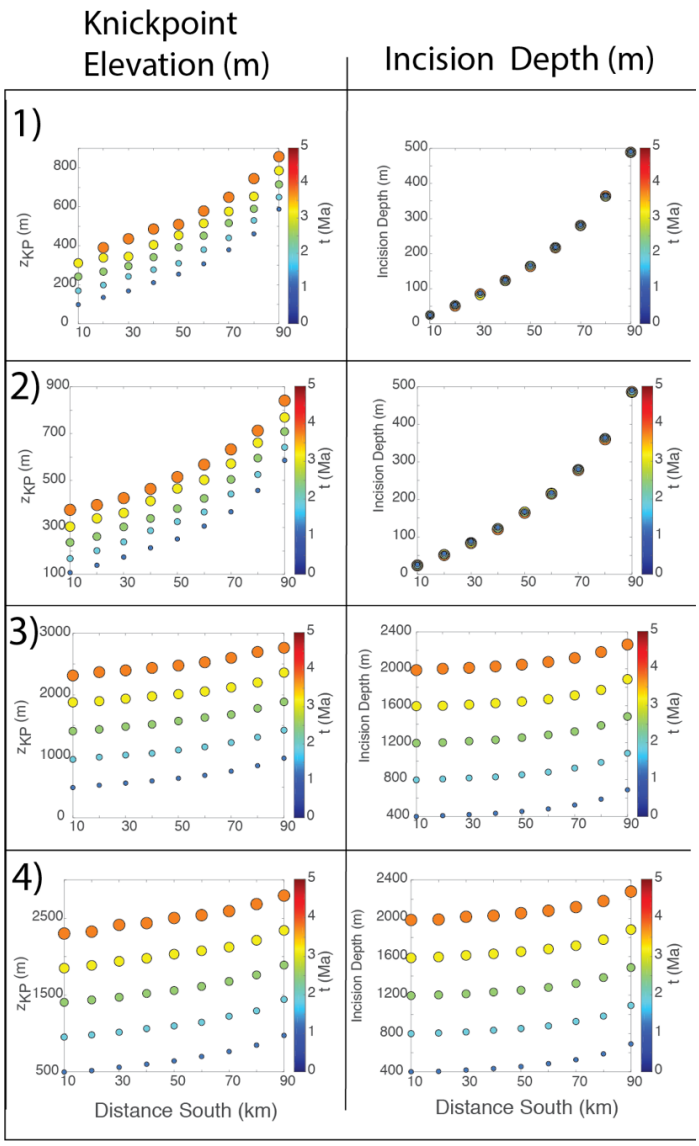

Figure C.3. First four models evaluated with 10 1-D stream profiles. Different parameters were changed within each model suite. However, for all four models, $n = 0.67$ and $K = 4.76$ x 10^{-6} $m^{0.33}$ yr^{-1}. The first column is the elevation of the knickpoints created by drainage capture and integration over time. The second column is the amount of incision measured by projecting the relict region out to the tributary-trunk junction. **1)** Area gain in this model is 1.9 x 10^5 km^2, and uplift before capture is equal to uplift after capture. **2)** Area gain in this model is 1.9 x 10^8 km^2, and uplift before capture is equal to uplift after capture. **3)** Area gain in this model is 1.9 x 10^5 km^2, and the uplift rate before capture is 0.1 mm yr^{-1} and the uplift rate after capture is 0.5 mm yr^{-1}. **4)** Area gain in this model is 1.9 x 10^5 km^2, and the uplift rate before capture is 0.1 mm yr^{-1} and the uplift rate after capture is 0.5 mm yr^{-1}.

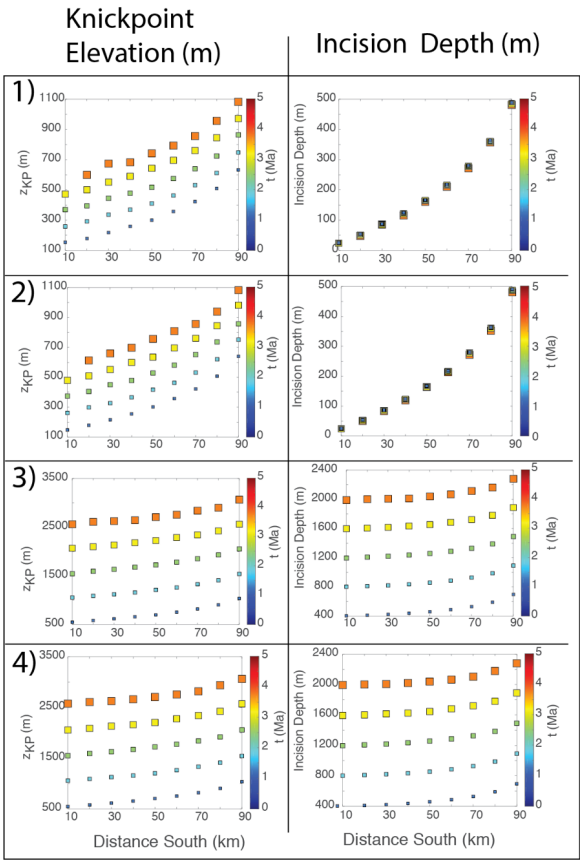

Figure C.4. Second four models evaluated with 10 1-D stream profiles. Different parameters were changed within each model suite. However, for all four models, n = 1 and K = 1.0 x 10^{-6} yr^{-1}. The first column is the elevation of the knickpoints created by drainage capture and integration over time. The second column is the amount of incision measured by projecting the relict region out to the tributary-trunk junction. **1)** Area gain in this model is $1.9x10^5$ km^2, and uplift before capture is equal to uplift after capture. **2)** Area gain in this model is $1.9x10^8$ km^2, and uplift before capture is equal to uplift after capture. **3)** Area gain in this model is $1.9x10^5$ km^2, and the uplift rate before capture is 0.1 mm yr^{-1} and the uplift rate after capture is 0.5 mm yr^{-1}. **4)** Area gain in this model is $1.9x10^5$ km^2, and the uplift rate before capture is 0.1 mm yr^{-1} and the uplift rate after capture is 0.5 mm yr^{-1}.

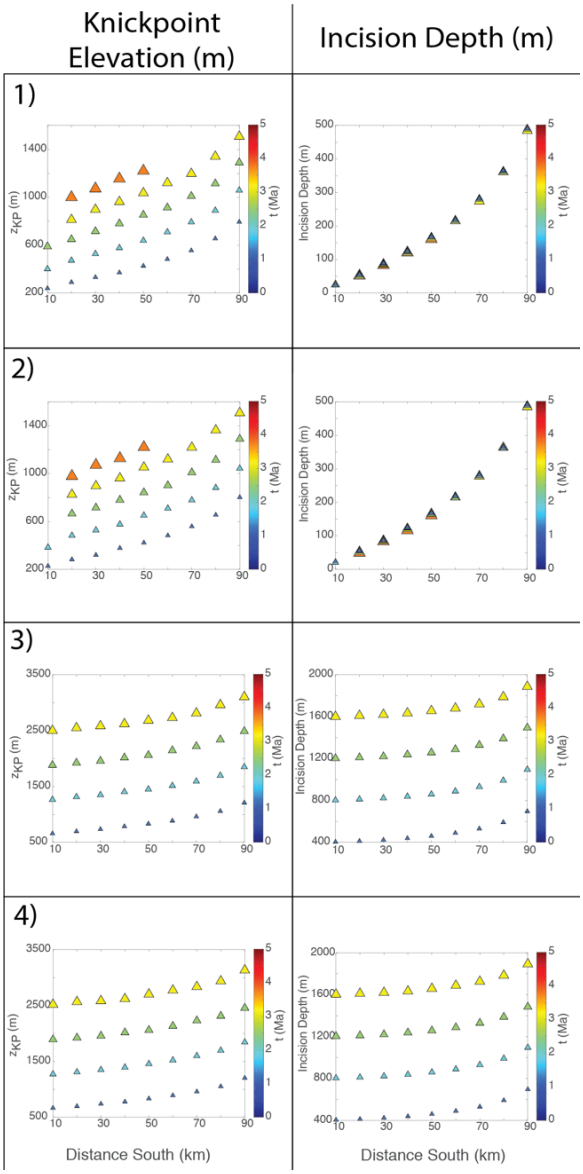

Figure C.5. Last four models evaluated with 10 1-D stream profiles. Different parameters were changed within each model suite. However, for all four models, $n = 1.5$ and $K = 4.42$ x 10^{-8} $m^{-0.5}$ yr^{-1}. The first column is the elevation of the knickpoints created by drainage capture and integration over time. The second column is the amount of incision measured by projecting the relict region out to the tributary-trunk junction. In some of the older models knickpoints have fluxed entirely through the system and no longer register in the model. **1)** Area gain in this model is 1.9 x 10^5 km^2, and uplift before capture is equal to uplift after capture. **2)** Area gain in this model is 1.9 x 10^8 km^2, and uplift before capture is equal to uplift after capture. **3)** Area gain in this model is 1.9 x 10^5 km^2, and the uplift rate before capture is 0.1 mm yr^{-1} and the uplift rate after capture is 0.5 mm yr^{-1}. **4)** Area gain in this model is 1.9 x 10^5 km^2, and the uplift rate before capture is 0.1 mm yr^{-1} and the uplift rate after capture is 0.5 mm yr^{-1}.

Easting (m)	Northing (m)	Latitude (°)	Longitude (°)	Elevation (m)	Upstream Distance (m)	Chi	Snake River Mileage	State
507651.823	5089778.25	45.962	-116.901	465.158	570.838	0.771	178.52	OR
511422.823	5088005.25	45.946	-116.853	615.156	1785.682	0.881	181.59	ID
508209.823	5078699.25	45.862	-116.894	669.609	6677.553	2.215	183.5	OR
509703.823	5082344.25	45.895	-116.875	391.095	2095.520	0.615	183.5	OR
512736.823	5082029.25	45.892	-116.836	351.260	224.735	0.188	185	ID
513258.823	5082479.25	45.896	-116.829	570.463	1017.484	0.863	185	ID
512889.823	5081156.25	45.884	-116.834	337.715	450.375	0.154	185.25	OR
514689.823	5080445.25	45.877	-116.811	342.669	167.912	0.165	186.6	ID
515481.823	5077268.25	45.849	-116.801	646.264	931.477	1.463	188.5	OR
510954.823	5042249.25	45.534	-116.860	650.734	43636.821	3.090	191.5	OR
513240.823	5055083.25	45.649	-116.830	521.917	26945.163	1.797	191.5	OR
510954.823	5042249.25	45.534	-116.860	650.734	43636.821	3.090	191.5	OR
520566.823	5078960.25	45.864	-116.735	636.164	5553.878	1.599	193.15	ID
528081.823	5065046.25	45.738	-116.639	717.324	6023.952	1.926	198.7	OR
528630.823	5073497.25	45.814	-116.631	836.500	5073.195	3.677	201	ID
529890.823	5074163.25	45.820	-116.615	796.515	5187.747	2.839	201	ID
538557.823	5064515.25	45.733	-116.504	665.684	3034.453	1.999	206.5	ID
534363.823	5062094.25	45.712	-116.559	647.688	2049.506	1.756	209.6	OR
533733.823	5062130.25	45.712	-116.567	806.645	2804.071	2.561	209.6	OR
534444.823	5062877.25	45.719	-116.557	773.514	2297.513	2.429	209.6	OR
543057.823	5049314.25	45.596	-116.448	681.976	2195.690	1.051	217.1	ID
541464.823	5047442.25	45.579	-116.469	607.979	1368.859	1.186	219	ID
539007.823	5050925.25	45.611	-116.500	888.539	3965.181	4.361	219	OR
538800.823	5049341.25	45.597	-116.503	761.887	2351.623	3.326	219	OR
541131.823	5043419.25	45.543	-116.473	930.019	4593.372	2.396	220.5	ID
542004.823	5044022.25	45.548	-116.462	896.536	4941.394	2.425	220.5	ID
536496.823	5047640.25	45.581	-116.532	916.014	3676.277	3.316	220.7	OR
536685.823	5045939.25	45.566	-116.530	599.550	1409.492	1.149	220.7	OR
534498.823	5047253.25	45.578	-116.558	910.950	4747.651	3.115	222.5	OR
534615.823	5046812.25	45.574	-116.556	905.846	4606.740	3.099	222.5	OR
533697.823	5042789.25	45.538	-116.568	702.398	4121.005	1.660	223.75	OR
536802.823	5030396.25	45.426	-116.530	1042.656	7200.193	2.143	229.4	ID
531483.823	5026274.25	45.389	-116.598	1165.459	2208.418	1.958	235.3	ID
533400.823	5026868.25	45.395	-116.573	1147.896	3903.086	2.267	235.3	ID
533940.823	5025473.25	45.382	-116.566	1773.604	5536.673	3.498	235.3	ID
528369.823	5028308.25	45.408	-116.637	1023.488	2111.336	2.118	235.4	OR
530718.823	5012000.25	45.261	-116.608	1639.580	11864.286	4.423	239.5	ID
531213.823	5019596.25	45.329	-116.602	1625.042	5819.136	3.050	239.5	ID
522744.823	5016293.25	45.300	-116.710	1220.852	3937.916	3.335	243.2	OR
521925.823	5014295.25	45.282	-116.720	1344.414	3730.012	3.258	246.2	OR
521664.823	5012207.25	45.263	-116.724	1222.239	2817.439	2.145	246.7	OR
527271.823	5005394.25	45.202	-116.653	1406.191	7526.377	2.505	247.6	ID
524679.823	5000705.25	45.159	-116.686	1382.353	4454.864	3.165	254.3	ID
526056.823	4998842.25	45.143	-116.669	1419.926	6094.892	3.979	254.3	ID
515301.823	4993082.25	45.091	-116.806	1004.394	1855.764	1.997	259.8	OR
515742.823	4993154.25	45.092	-116.800	914.050	1355.117	1.404	259.8	OR
510180.823	4987313.25	45.039	-116.871	990.960	3000.527	3.189	265.6	OR
510891.823	4987925.25	45.045	-116.862	1041.638	2770.255	3.267	265.6	OR
503079.823	4970888.25	44.891	-116.961	701.990	15852.958	1.662	270.3	OR
518181.823	4986188.25	45.029	-116.769	974.137	7974.787	2.075	271.38	ID
521187.823	4990508.25	45.068	-116.731	1198.941	15038.061	4.198	271.38	ID
512475.823	4970771.25	44.890	-116.842	685.665	1090.389	1.188	282.2	ID
517623.823	4970456.25	44.887	-116.777	871.965	13221.431	1.742	284	ID
508776.823	4962977.25	44.820	-116.889	893.859	1446.771	1.403	285.7	ID
506580.823	4952825.25	44.729	-116.917	983.370	7744.341	2.121	288.5	ID
507804.823	4958405.25	44.779	-116.901	805.233	1741.322	0.842	288.5	ID
508308.823	4952789.25	44.728	-116.895	1050.431	7812.348	2.564	288.5	ID
502665.823	4954760.25	44.746	-116.966	981.527	2916.439	2.339	291.5	ID
496293.823	4945571.25	44.663	-117.047	851.925	3453.195	1.151	296.2	ID

Table C.2. Picked Knickpoint Locations and Elevations

Basin Number	Easting	Northing	Modern Outlet Elevation (m)	Projected Outlet Elevation (m)	1-σ	Incision (m)	Snake River Mileage	State
63	507984.8227	5090084.251	289.0644531	399.5390504	1.788365154	110.4745972	178.52	OR
64	509955.8227	5087312.251	284.3284912	541.4762979	2.885460004	257.1478067	181.59	ID
1	510918.8227	5083559.251	274.8178711	344.1075994	2.079516457	69.28972832	183.5	OR
3	512646.8227	5081849.251	274.5624084	308.5670337	1.61044337	34.00462521	185	ID
4	512961.8227	5081534.251	276.3311157	329.8158288	1.480273667	53.48471306	185.25	OR
5	514572.8227	5080391.251	283.9133606	316.3962751	1.743487072	32.48291449	186.6	ID
6	516048.8227	5077691.251	309.8496399	563.750124	2.306764337	253.9004841	188.5	OR
68	518253.8227	5073713.251	287.84552	405.7027224	0.4244008	117.8572024	191.5	OR
7	520458.8227	5074793.251	289.9403076	507.8583925	2.277401212	217.9180849	193.15	ID
69	526848.8227	5069609.251	308.5906982	490.918541	0.718188221	182.3278428	198.7	OR
9	529575.8227	5069978.251	316.0725403	494.2102279	2.20588665	178.1376877	201	ID
71	535902.8227	5062085.251	338.269928	489.2311655	7.466419673	150.9612375	209.6	OR
14	536082.8227	5060006.251	340.442627	484.2064643	3.426228669	143.7638374	210	OR
18	541869.8227	5050340.251	354.8673096	472.6317565	2.459104297	117.7644469	217.1	ID
75	540249.8227	5048099.251	365.7316589	501.7525972	5.443540584	136.0209383	219	OR
74	541104.8227	5049080.251	362.2580261	485.8621501	3.896181525	123.604124	219	OR
20	539133.8227	5046245.251	363.3034973	534.4222955	4.524058156	171.1187982	220.5	ID
22	538935.8227	5046344.251	380.776001	602.1428668	2.259698272	221.3668658	222.3	OR
23	536811.8227	5044553.251	375.8076477	617.5994888	3.817736412	241.7918411	222.5	OR
24	536649.8227	5042987.251	377.2951355	463.1045171	1.781576514	85.80938156	223.75	OR
25	534849.8227	5035031.251	388.8176575	660.4810973	4.099588648	271.6634398	229.4	ID
28	530304.8227	5027633.251	416.6981201	1216.212579	6.648689151	799.5144586	235.3	ID
78	529638.8227	5026967.251	417.8840027	809.3304573	5.80269622	391.4464546	235.4	OR
80	527055.8227	5021693.251	428.0852356	1340.748143	5.712884075	912.6629076	239.5	ID
81	525471.8227	5017724.251	440.8938599	767.3848563	14.12046067	326.4909964	243.2	OR
82	524409.8227	5012558.251	449.3292542	1048.171709	4.30603238	598.8424546	246.2	OR
83	523797.8227	5011235.251	455.0095215	1043.227098	6.167833699	588.2175769	246.7	OR
84	523671.8227	5010218.251	450.3690796	1073.868721	6.883064531	623.4996412	247.6	ID
85	521556.8227	4999544.251	517.708313	771.9571211	15.25081946	254.2488081	254.3	ID
86	520467.8227	4997402.251	517.9731445	671.9834824	2.21607853	154.0103379	256	ID
87	519729.8227	4996241.251	515.8848877	683.1004531	3.231932492	167.2155654	257	ID
88	516876.8227	4993100.251	514.852478	841.960067	1.385225366	327.1075889	259.8	OR
90	512187.8227	4986143.251	520.7403564	692.8268714	12.81147004	172.086515	265.6	OR
91	511269.8227	4979798.251	517.6082153	648.6796212	0.432659012	131.0714059	270.3	OR
31	513573.8227	4981382.251	525.1295166	820.3131171	2.154357571	295.1836004	271.38	ID
93	512016.8227	4971320.251	551.2217407	591.0170898	2.759655876	39.79534908	282.2	ID
34	508128.8227	4966469.251	551.7407837	737.192547	1.51702256	185.4517633	284	ID
35	507687.8227	4963508.251	639.5814819	729.1097818	3.329205775	89.52829987	285.7	ID
36	506931.8227	4959242.251	632.7736816	791.7142586	1.270793994	158.9405769	288.5	ID
37	502269.8227	4956848.251	653.9750977	774.7169422	4.702813462	120.7418446	291.5	ID
39	494502.8227	4947776.251	636.6682739	704.3675824	1.894509498	67.69930845	296.2	ID

Table C.3. Projected Stream Outlets and incision

U-PB ZIRCON AGE RESULTS FOR SAMPLE HCC19-1

Aliquot	Ratios			Error	Age			Discordance		Concentration			Preferred Age
	207Pb/206Pb	207Pb/235U	206Pb/238U	Correlation	207Pb/235U (Ma)	206Pb/238U (Ma)	207Pb/206Pb (Ma)	206Pb/238U dates <1 Ga	U (ppm)	Th (ppm)	Pb (ppm)	(Ma)
HCC-19-1_088	0.0070 ± 0.0630	0.0060 ± 0.0100	0.001360 ± 0.000200	0.00100	6.00 ± 10.00	8.7 ± 1.30	-1300 ± 1800	31.0	-0.3	148.5	86.7	0.065	8.70 ± 1.30
HCC-19-1_020	-0.0040 ± 0.0270	0.0023 ± 0.0064	0.001360 ± 0.000130	0.32133	2.20 ± 6.50	8.77 ± 0.83	-1500 ± 1100	74.9	-1.0	220.7	190.1	0.122	8.77 ± 0.83
HCC-19-1_087	0.0405 ± 0.0099	0.0139 ± 0.0034	0.002530 ± 0.000140	0.00100	14.00 ± 3.40	16.31 ± 0.92	-210 ± 380	14.2	-0.7	486	415	0.525	16.31 ± 0.92
HCC-19-1_102	0.0459 ± 0.0022	0.0895 ± 0.0050	0.013810 ± 0.000380	0.45121	87.00 ± 4.60	88.4 ± 2.40	-10 ± 100	1.6	-0.3	795	159.7	1.156	88.40 ± 2.40
HCC-19-1_005	0.0528 ± 0.0076	0.1270 ± 0.0180	0.017640 ± 0.000660	0.15943	125.00 ± 15.00	112.7 ± 4.20	270 ± 290	-10.9	0.8	130.9	46.8	0.45	112.70 ± 4.20
HCC-19-1_003	0.0515 ± 0.0047	0.1290 ± 0.0100	0.018400 ± 0.000540	0.00100	123.00 ± 9.30	117.5 ± 4.00	240 ± 190	-4.7	0.6	235.6	98.4	1.017	117.50 ± 4.00
HCC-19-1_014	0.0483 ± 0.0056	0.1250 ± 0.0140	0.018600 ± 0.000670	0.04719	119.00 ± 13.00	118.8 ± 4.30	110 ± 220	-0.2	0.0	160.4	80.6	0.8	118.80 ± 4.30
HCC-19-1_046	0.0472 ± 0.0043	0.1230 ± 0.0120	0.018640 ± 0.000660	0.18070	117.00 ± 11.00	119 ± 4.20	80 ± 180	1.7	-0.2	233	98.4	1.01	119.00 ± 4.20
HCC-19-1_078	0.0495 ± 0.0037	0.1269 ± 0.0092	0.018630 ± 0.000690	0.11437	121.20 ± 8.30	119 ± 4.30	160 ± 150	-1.8	0.3	262	73.1	0.718	119.00 ± 4.30
HCC-19-1_066	0.0410 ± 0.0110	0.1050 ± 0.0280	0.018660 ± 0.001000	0.24811	100.00 ± 26.00	119.2 ± 6.50	-200 ± 420	16.1	-0.7	62.4	22.3	0.221	119.20 ± 6.50
HCC-19-1_103	0.0494 ± 0.0073	0.1280 ± 0.0180	0.018720 ± 0.000830	0.25397	121.00 ± 17.00	119.5 ± 5.90	150 ± 280	-1.3	0.1	99.8	44.22	0.481	119.50 ± 5.90
HCC-19-1_049	0.0480 ± 0.0053	0.1250 ± 0.0140	0.018840 ± 0.000520	0.14640	119.00 ± 13.00	120.3 ± 3.30	110 ± 210	1.1	-0.1	178.1	81.3	0.88	120.30 ± 3.30
HCC-19-1_024	0.0535 ± 0.0068	0.1400 ± 0.0200	0.018850 ± 0.000600	0.50171	133.00 ± 18.00	120.4 ± 3.80	360 ± 270	-10.5	0.7	143.8	43.4	0.463	120.40 ± 3.80
HCC-19-1_040	0.0486 ± 0.0065	0.1260 ± 0.0170	0.018870 ± 0.000800	0.34741	120.00 ± 15.00	120.5 ± 5.00	170 ± 260	0.4	0.0	128.1	36.6	0.382	120.50 ± 5.00
HCC-19-1_067	0.0479 ± 0.0023	0.1264 ± 0.0056	0.018920 ± 0.000640	0.30993	120.80 ± 5.10	120.8 ± 4.00	100 ± 100	0.0	0.0	528	197	2	120.80 ± 4.00
HCC-19-1_119	0.0565 ± 0.0086	0.1480 ± 0.0190	0.018920 ± 0.000670	0.00100	140.00 ± 17.00	120.8 ± 5.50	380 ± 310	-15.9	1.1	80	36.2	0.419	120.80 ± 5.50
HCC-19-1_117	0.0473 ± 0.0027	0.1265 ± 0.0095	0.018940 ± 0.000640	0.04034	120.80 ± 8.50	120.9 ± 6.00	70 ± 120	0.1	0.0	296	105	1.21	120.90 ± 6.00
HCC-19-1_031	0.0520 ± 0.0071	0.1310 ± 0.0200	0.018930 ± 0.000700	0.21597	125.00 ± 17.00	120.9 ± 4.40	230 ± 270	-3.4	0.2	126.2	40.2	0.479	120.90 ± 4.40
HCC-19-1_028	0.0440 ± 0.0110	0.1060 ± 0.0260	0.019050 ± 0.000770	0.19000	106.00 ± 26.00	121.6 ± 4.80	-70 ± 400	12.8	-0.6	99.1	43.4	0.371	121.60 ± 4.80
HCC-19-1_108	0.0481 ± 0.0040	0.1270 ± 0.0110	0.019080 ± 0.000560	0.00100	121.20 ± 10.00	121.8 ± 3.60	100 ± 160	0.5	-0.1	286	94.9	1.04	121.80 ± 3.60
HCC-19-1_086	0.0481 ± 0.0032	0.1289 ± 0.0096	0.019090 ± 0.000710	0.36393	122.90 ± 8.70	121.9 ± 4.50	140 ± 150	-0.8	0.1	260	150.6	1.49	121.90 ± 4.50
HCC-19-1_055	0.0475 ± 0.0047	0.1220 ± 0.0110	0.019110 ± 0.000520	0.00100	116.40 ± 9.90	122 ± 3.30	90 ± 190	4.6	-0.6	182.5	56.6	0.646	122.00 ± 3.30
HCC-19-1_090	0.0489 ± 0.0086	0.1310 ± 0.0240	0.019110 ± 0.001000	0.19945	124.00 ± 21.00	122 ± 6.50	110 ± 320	-1.6	0.1	117	62	0.608	122.00 ± 6.50
HCC-19-1_044	0.0455 ± 0.0054	0.1240 ± 0.0110	0.019120 ± 0.000740	0.00100	118.70 ± 9.70	122.1 ± 4.70	0 ± 220	2.8	-0.4	165	51.7	0.631	122.10 ± 4.70
HCC-19-1_105	0.0486 ± 0.0032	0.1304 ± 0.0074	0.019120 ± 0.000740	0.24169	124.40 ± 6.70	122.1 ± 4.70	130 ± 140	-1.9	0.3	304	160.3	1.75	122.10 ± 4.70
HCC-19-1_091	0.0509 ± 0.0031	0.1328 ± 0.0098	0.019170 ± 0.000760	0.31059	126.40 ± 8.80	122.4 ± 4.80	230 ± 130	-3.3	0.5	261.2	142.1	1.378	122.40 ± 4.80
HCC-19-1_065	0.0522 ± 0.0050	0.1410 ± 0.0150	0.019180 ± 0.000680	0.03164	134.00 ± 13.00	122.5 ± 4.30	320 ± 220	-9.4	0.9	130.9	54.6	0.636	122.50 ± 4.30
HCC-19-1_050	0.0542 ± 0.0053	0.1430 ± 0.0130	0.019190 ± 0.000590	0.07047	135.00 ± 12.00	122.5 ± 3.70	340 ± 210	-10.2	1.0	179.4	58.4	0.622	122.50 ± 3.70
HCC-19-1_077	0.0503 ± 0.0035	0.1348 ± 0.0087	0.019210 ± 0.000560	0.00100	128.30 ± 7.80	122.7 ± 3.50	200 ± 150	-4.6	0.7	247	109.5	1.1	122.70 ± 3.50
HCC-19-1_116	0.0526 ± 0.0044	0.1470 ± 0.0170	0.019210 ± 0.000850	0.33380	138.00 ± 15.00	122.7 ± 5.40	280 ± 170	-12.5	1.0	147	64	0.69	122.70 ± 5.40
HCC-19-1_053	0.0465 ± 0.0057	0.1200 ± 0.0140	0.019230 ± 0.000740	0.12239	115.00 ± 12.00	122.8 ± 4.70	90 ± 240	6.4	-0.7	106.2	45.4	0.477	122.80 ± 4.70
HCC-19-1_083	0.0481 ± 0.0033	0.1267 ± 0.0085	0.019230 ± 0.000620	0.22442	121.00 ± 7.60	122.8 ± 3.90	110 ± 140	1.5	-0.2	223	68.2	0.71	122.80 ± 3.90
HCC-19-1_027	0.0550 ± 0.0120	0.1420 ± 0.0310	0.019200 ± 0.001000	0.00746	133.00 ± 27.00	122.8 ± 6.50	280 ± 430	-8.3	0.4	69.8	32.3	0.318	122.80 ± 6.50
HCC-19-1_106	0.0538 ± 0.0067	0.1450 ± 0.0150	0.019240 ± 0.000870	0.08898	137.00 ± 13.00	122.8 ± 5.50	310 ± 250	-11.6	1.1	111.7	60.5	0.622	122.80 ± 5.50
HCC-19-1_010	0.0487 ± 0.0070	0.1260 ± 0.0190	0.019260 ± 0.000780	0.00100	120.00 ± 17.00	123 ± 5.00	130 ± 280	2.4	-0.2	88.2	38.6	0.41	123.00 ± 5.00
HCC-19-1_120	0.0520 ± 0.0038	0.1368 ± 0.0084	0.019280 ± 0.000740	0.00100	130.10 ± 7.50	123 ± 4.70	260 ± 150	-5.8	0.9	273	123.2	1.21	123.00 ± 4.70
HCC-19-1_036	0.0461 ± 0.0076	0.1200 ± 0.0190	0.019300 ± 0.000650	0.51467	115.00 ± 18.00	123.2 ± 4.10	150 ± 290	6.7	-0.5	114.9	52.1	0.524	123.20 ± 4.10
HCC-19-1_018	0.0463 ± 0.0083	0.1250 ± 0.0200	0.019300 ± 0.001000	0.00100	119.00 ± 18.00	123.2 ± 6.60	20 ± 320	3.4	-0.2	95.9	42.69	0.445	123.20 ± 6.60
HCC-19-1_114	0.0472 ± 0.0065	0.1280 ± 0.0160	0.019300 ± 0.000890	0.13125	122.00 ± 14.00	123.2 ± 5.60	70 ± 250	1.0	-0.1	107.1	45.2	0.456	123.20 ± 5.60
HCC-19-1_042	0.0510 ± 0.0060	0.1400 ± 0.0180	0.019290 ± 0.000590	0.18146	132.00 ± 16.00	123.2 ± 3.70	210 ± 230	-7.1	0.6	150.7	53.4	0.58	123.20 ± 3.70
HCC-19-1_029	0.0490 ± 0.0034	0.1263 ± 0.0089	0.019320 ± 0.000510	0.29859	120.70 ± 8.00	123.3 ± 3.20	140 ± 150	2.1	-0.3	240.2	73.7	0.763	123.30 ± 3.20
HCC-19-1_081	0.0468 ± 0.0048	0.1280 ± 0.0110	0.019300 ± 0.000680	0.03251	122.20 ± 9.80	123.3 ± 4.30	60 ± 190	0.9	-0.1	156.2	65.8	0.649	123.30 ± 4.30
HCC-19-1_002	0.0478 ± 0.0076	0.1320 ± 0.0210	0.019320 ± 0.000770	0.04326	125.00 ± 19.00	123.3 ± 4.90	140 ± 310	-1.4	0.1	122.6	71.1	0.679	123.30 ± 4.90
HCC-19-1_060	0.0525 ± 0.0044	0.1370 ± 0.0130	0.019320 ± 0.000550	0.19129	130.00 ± 12.00	123.3 ± 3.50	330 ± 200	-5.4	0.6	211	126.1	1.33	123.30 ± 3.50
HCC-19-1_095	0.0489 ± 0.0033	0.1306 ± 0.0086	0.019320 ± 0.000660	0.62337	124.50 ± 7.70	123.4 ± 4.20	140 ± 140	-0.9	0.1	272	103.8	1.03	123.40 ± 4.20
HCC-19-1_115	0.0471 ± 0.0040	0.1270 ± 0.0110	0.019360 ± 0.000720	0.96752	120.80 ± 9.90	123.6 ± 4.50	60 ± 170	2.3	-0.3	236	79.1	0.909	123.60 ± 4.50
HCC-19-1_093	0.0469 ± 0.0041	0.1273 ± 0.0090	0.019350 ± 0.000670	0.00100	121.50 ± 8.10	123.6 ± 4.30	60 ± 170	1.7	-0.3	359	158	1.655	123.60 ± 4.30
HCC-19-1_032	0.0521 ± 0.0043	0.1340 ± 0.0110	0.019380 ± 0.000720	0.37757	127.20 ± 9.50	123.7 ± 4.50	260 ± 170	-2.8	0.4	194	117	1.19	123.70 ± 4.50
HCC-19-1_038	0.0453 ± 0.0073	0.1210 ± 0.0190	0.019390 ± 0.000720	0.32076	115.00 ± 17.00	123.8 ± 4.60	-10 ± 290	7.1	-0.5	102.8	48.9	0.525	123.80 ± 4.60
HCC-19-1_039	0.0503 ± 0.0074	0.1330 ± 0.0200	0.019400 ± 0.001100	0.16117	126.00 ± 18.00	123.8 ± 6.90	180 ± 290	-1.8	0.1	95.4	48.4	0.55	123.80 ± 6.90
HCC-19-1_022	0.0504 ± 0.0052	0.1370 ± 0.0140	0.019390 ± 0.000580	0.24988	130.00 ± 13.00	123.8 ± 3.60	200 ± 210	-5.0	0.5	159.4	39.7	0.494	123.80 ± 3.60
HCC-19-1_056	0.0448 ± 0.0073	0.1200 ± 0.0210	0.019420 ± 0.000730	0.35526	114.00 ± 19.00	124 ± 4.60	-40 ± 280	8.1	-0.5	102	51.9	0.515	124.00 ± 4.60
HCC-19-1_062	0.0449 ± 0.0061	0.1320 ± 0.0170	0.019420 ± 0.000820	0.04400	125.00 ± 15.00	124 ± 5.20	120 ± 250	-0.8	0.1	103.2	67.3	0.734	124.00 ± 5.20
HCC-19-1_109	0.0495 ± 0.0038	0.1340 ± 0.0130	0.019420 ± 0.000880	0.63045	128.00 ± 11.00	124 ± 5.60	170 ± 160	-3.2	0.4	191.7	70.9	0.824	124.00 ± 5.60
HCC-19-1_054	0.0537 ± 0.0060	0.1400 ± 0.0150	0.019430 ± 0.000590	0.35787	133.00 ± 13.00	124 ± 3.70	320 ± 230	-7.3	0.7	138.4	48.64	0.53	124.00 ± 3.70
HCC-19-1_051	0.0521 ± 0.0095	0.1370 ± 0.0230	0.019450 ± 0.000730	0.00100	129.00 ± 21.00	124.1 ± 4.60	220 ± 330	-3.9	0.2	90.1	39.79	0.475	124.10 ± 4.60
HCC-19-1_016	0.0560 ± 0.0130	0.1440 ± 0.0280	0.019400 ± 0.001400	0.00100	135.00 ± 25.00	124.1 ± 8.60	290 ± 420	-8.8	0.4	57.5	24.1	0.252	124.10 ± 8.60
HCC-19-1_059	0.0489 ± 0.0048	0.1390 ± 0.0160	0.019460 ± 0.000730	0.10669	132.00 ± 14.00	124.2 ± 4.60	180 ± 210	-6.3	0.6	117.8	54.3	0.61	124.20 ± 4.60
HCC-19-1_045	0.0522 ± 0.0090	0.1870 ± 0.0900	0.019450 ± 0.000640	0.90713	164.00 ± 61.00	124.2 ± 4.00	250 ± 340	-32.0	0.7	101.8	43.11	0.484	124.20 ± 4.00
HCC-19-1_035	0.0495 ± 0.0076	0.1300 ± 0.0210	0.019470 ± 0.000650	0.26595	123.00 ± 19.00	124.3 ± 4.10	150 ± 300	1.0	-0.1	131.9	58.4	0.569	124.30 ± 4.10
HCC-19-1_113	0.0458 ± 0.0040	0.1230 ± 0.0120	0.019490 ± 0.000980	0.25041	118.00 ± 11.00	124.4 ± 6.20	20 ± 170	5.1	-0.6	127.7	54.7	0.585	124.40 ± 6.20
HCC-19-1_048	0.0493 ± 0.0049	0.1360 ± 0.0140	0.019480 ± 0.000800	0.26263	132.00 ± 12.00	124.4 ± 5.10	210 ± 220	-6.1	0.6	110.1	51.4	0.575	124.40 ± 5.10
HCC-19-1_079	0.0559 ± 0.0081	0.1500 ± 0.0210	0.019490 ± 0.000850	0.01668	141.00 ± 19.00	124.4 ± 4.10	370 ± 290	-13.3	0.9	85.5	44.05	0.52	124.40 ± 4.10
HCC-19-1_047	0.0547 ± 0.0068	0.1460 ± 0.0150	0.019490 ± 0.000820	0.00100	138.00 ± 13.00	124.4 ± 5.20	340 ± 260	-10.9	1.0	92.9	47.2	0.83	124.40 ± 5.20
HCC-19-1_098	0.0468 ± 0.0033	0.1272 ± 0.0093	0.019520 ± 0.000730	0.09529	121.40 ± 8.40	124.6 ± 4.60	50 ± 140	2.6	-0.4	381	183	1.89	124.60 ± 4.60
HCC-19-1_009	0.0530 ± 0.0042	0.1410 ± 0.0120	0.019530 ± 0.000600	0.34981	134.00 ± 11.00	124.7 ± 3.80	350 ± 180	-7.5	0.8	285	191	2.14	124.70 ± 3.80
HCC-19-1_070	0.0480 ± 0.0100	0.1290 ± 0.0260	0.019580 ± 0.000750	0.00100	122.00 ± 23.00	125 ± 4.80	50 ± 360	2.4	-0.1	110.5	69.1	0.773	125.00 ± 4.80
HCC-19-1_052	0.0507 ± 0.0060	0.1320 ± 0.0130	0.019600 ± 0.000690	0.00100	126.00 ± 12.00	125.1 ± 4.30	210 ± 240	-0.7	0.1	147.8	50.12	0.503	125.10 ± 4.30
HCC-19-1_100	0.0533 ± 0.0065	0.1430 ± 0.0160	0.019600 ± 0.000770	0.00100	135.00 ± 14.00	125.1 ± 4.90	290 ± 240	-7.9	0.7	109.7	48.6	0.514	125.10 ± 4.90
HCC-19-1_026	0.0483 ± 0.0027	0.1287 ± 0.0080	0.019610 ± 0.000550	0.57200	122.80 ± 7.20	125.2 ± 3.50	116 ± 120	1.9	-0.3	245.9	98	0.944	125.20 ± 3.50
HCC-19-1_107	0.0478 ± 0.0030	0.1320 ± 0.0077	0.019670 ± 0.000580	0.00100	125.80 ± 6.90	125.5 ± 3.60	130 ± 140	-0.2	0.0	431	238	2.5	125.50 ± 3.60
HCC-19-1_111	0.0455 ± 0.0034	0.1229 ± 0.0090	0.019690 ± 0.000630	0.24109	117.50 ± 8.20	125.7 ± 4.00	0 ± 140	6.5	-1.0	268	110.5	1.23	125.70 ± 4.00
HCC-19-1_099	0.0469 ± 0.0051	0.1280 ± 0.0130	0.019720 ± 0.000660	0.01103	122.00 ± 12.00	125.9 ± 4.20	60 ± 210	3.1	-0.3	180	55.8	0.66	125.90 ± 4.20
HCC-19-1_007	0.0611 ± 0.0096	0.1620 ± 0.0280	0.019730 ± 0.000590	0.47309	151.00 ± 24.00	125.9 ± 3.70	530 ± 300	-19.9	1.0	178	79.5	0.819	125.90 ± 3.70
HCC-19-1_034	0.0444 ± 0.0059	0.1220 ± 0.0170	0.019730 ± 0.000680	0.09462	116.00 ± 15.00	126 ± 4.30	-50 ± 230	7.9	-0.7	126.1	62.1	0.677	126.00 ± 4.30
HCC-19-1_033	0.0494 ± 0.0060	0.1290 ± 0.0160	0.019730 ± 0.000710	0.15380	123.00 ± 14.00	126 ± 4.50	140 ± 230	2.4	-0.2	130.3	67.5	0.686	126.00 ± 4.50
HCC-19-1_037	0.0447 ± 0.0064	0.1210 ± 0.0170	0.019780 ± 0.000530	0.39166	115.00 ± 16.00	126.3 ± 3.30	30 ± 270	8.9	-0.7	129.8	52.5	0.543	126.30 ± 3.30
HCC-19-1_082	0.0452 ± 0.0084	0.1290 ± 0.0180	0.019800 ± 0.000880	0.11218	123.00 ± 16.00	126.4 ± 5.50	50 ± 270	2.7	-0.2	95.4	46	0.462	126.40 ± 5.50
HCC-19-1_018	0.0420 ± 0.0048	0.1200 ± 0.0120	0.019860 ± 0.000790	0.00100	115.00 ± 11.00	126.8 ± 5.00	-90 ± 210	9.3	-1.1	162.2	89.1	0.938	126.80 ± 5.00
HCC-19-1_071	0.0498 ± 0.0099	0.1360 ± 0.0280	0.019880 ± 0.001100	0.04609	128.00 ± 25.00	126.9 ± 6.70	130 ± 360	-0.9	0.0	74.7	43.9	0.448	126.90 ± 6.70
HCC-19-1_057	0.0524 ± 0.0069	0.1420 ± 0.0180	0.019900 ± 0.000820	0.00100	135.00 ± 16.00	127 ± 5.20	320 ± 280	-6.3	0.5	161.9	66.3	0.719	127.00 ± 5.20
HCC-19-1_076	0.0545 ± 0.0057	0.1510 ± 0.0160	0.019910 ± 0.000700	0.33540	142.00 ± 14.00	127.1 ± 4.40	350 ± 220	-11.7	1.1	123.1	83.4	0.892	127.10 ± 4.40
HCC-19-1_110	0.0480 ± 0.0100	0.1230 ± 0.0340	0.019920 ± 0.001000	0.13416	126.00 ± 26.00	127.2 ± 6.50	90 ± 390	0.9	0.0	77.2	33.2	0.342	127.20 ± 6.50
HCC-19-1_097	0.0532 ± 0.0067	0.1490 ± 0.0190	0.019990 ± 0.000680	0.00100	140.00 ± 17.00	127.6 ± 5.50	280 ± 240	-9.7	0.7	108.1	46.9	0.55	127.60 ± 5.50
HCC-19-1_075	0.0500 ± 0.0040	0.1390 ± 0.0120	0.020000 ± 0.000890	0.00100	132.00 ± 11.00	127.7 ± 5.60	230 ± 180	-3.4	0.4	136.9	58.8	0.992	127.70 ± 5.60
HCC-19-1_063	0.0503 ± 0.0041	0.1400 ± 0.0120	0.020010 ± 0.000820	0.16427	133.00 ± 11.00	127.7 ± 5.20	230 ± 170	-4.2	0.5	149.8	55.1	0.588	127.70 ± 5.20
HCC-19-1_013	0.0467 ± 0.0057	0.1340 ± 0.0150	0.020020 ± 0.000820	0.00100	128.00 ± 11.00	127.8 ± 5.20	0 ± 220	7.7	-0.9	134.4	56.5	0.599	127.80 ± 5.20
HCC-19-1_025	0.0460 ± 0.0100	0.1240 ± 0.0260	0.020000 ± 0.001000	0.00100	117.00 ± 24.00	127.9 ± 6.60	20 ± 400	8.5	-0.5	91.1	39.7	0.403	127.90 ± 6.60
HCC-19-1_015	0.0513 ± 0.0043	0.1400 ± 0.0110	0.019920 ± 0.000570	0.32736	133.30 ± 9.70	128.1 ± 3.10	240 ± 180	-4.1	0.5	141.7	46	0.496	128.10 ± 3.10
HCC-19-1_021	0.0532 ± 0.0056	0.1480 ± 0.0140	0.020080 ± 0.000700	0.24686	140.00 ± 13.00	128.2 ± 4.40	310 ± 220	-9.2	0.9	137.5	60.8	0.775	128.20 ± 4.40
HCC-19-1_008	0.0486 ± 0.0054	0.1250 ± 0.0160	0.020140 ± 0.000910	0.22311	124.00 ± 12.00	128.5 ± 5.80	120 ± 200	3.5	-0.4	93.8	38.64	0.397	128.50 ± 5.80
HCC-19-1_084	0.0558 ± 0.0058	0.1490 ± 0.0130	0.020130 ± 0.000780	0.08040	141.00 ± 12.00	128.5 ± 4.90	400 ± 210	-9.7	1.0	157.5	66.1	0.651	128.50 ± 4.90
HCC-19-1_023	0.0471 ± 0.0023	0.1301 ± 0.0062	0.020190 ± 0.000400	0.57383	124.20 ± 5.50	128.9 ± 2.50	61 ± 100	3.6	-0.9	569	217	2.31	128.90 ± 2.50
HCC-19-1_073	0.0497 ± 0.0040	0.1382 ± 0.0097	0.020280 ± 0.000700	0.00100	131.30 ± 8.70	129.4 ± 4.40	170 ± 160	-1.5	0.2	327.1	126.8	1.45	129.40 ± 4.40
HCC-19-1_068	0.0471 ± 0.0027	0.1331 ± 0.0079	0.020330 ± 0.000600	0.20464	126.80 ± 7.10	129.7 ± 3.80	60 ± 120	2.2	-0.4	306.6	128.3	1.38	129.70 ± 3.80
HCC-19-1_001	0.0480 ± 0.0073	0.1320 ± 0.0180	0.020430 ± 0.000650	0.17158	125.00 ± 17.00	130.4 ± 4.10	100 ± 280	4.1	-0.3	156.9	98	1.05	130.40 ± 4.10
HCC-19-1_085	0.0481 ± 0.0032	0.1399 ± 0.0091	0.020970 ± 0.000690	0.23821	132.90 ± 8.10	133.8 ± 4.40	110 ± 130	0.7	-0.1	640	257	3.23	133.80 ± 4.40
HCC-19-1_064	0.0514 ± 0.0032	0.1464 ± 0.0082	0.021150 ± 0.000580	0.24407	140.40 ± 7.30	134.9 ± 3.70	240 ± 130	-4.1	0.8	223.6	90.7	1.189	134.90 ± 3.70
HCC-19-1_041	0.0516 ± 0.0028	0.2300 ± 0.0160	0.031900 ± 0.001500	0.68473	210.00 ± 13.00	202.6 ± 9.10	250 ± 120	-3.7	0.6	318	147.3	2.54	202.60 ± 9.10
HCC-19-1_094	0.0517 ± 0.0025	0.2576 ± 0.0110	0.036250 ± 0.001000	0.00337	232.60 ± 9.10	229.5 ± 6.50	265 ± 110	-1.4	0.3	387.5	85.6	1.71	229.50 ± 6.50
HCC-19-1_118	0.0533 ± 0.0038	0.2960 ± 0.0230	0.038800 ± 0.001500	0.13762	263.00 ± 18.00	245.2 ± 9.40	320 ± 150	-7.3	1.0	113	24	0.594	245.20 ± 9.40
HCC-19-1_043	0.0899 ± 0.0032	3.0720 ± 0.1000	0.245400 ± 0.005700	0.69009	1425.00 ± 26.00	1414 ± 29.00	1422 ± 69	-0.8	0.4	190.7	61.1	7.75	1422.00 ± 69.00

Table C.4. Detrital Zircon Data sample HCC19-1

U-PB ZIRCON AGE RESULTS FOR SAMPLE HCC19-3

Aliquot	Ratios			Error	Age			Discordance		Concentration			Preferred Age
	207Pb/206Pb	207Pb/235U	206Pb/238U	Correlation	207Pb/235U (Ma)	206Pb/238U (Ma)	207Pb/206Pb (Ma)	206Pb/238U dates <1 Ga	U (ppm)	Th (ppm)	Pb (ppm)	(Ma)
HCC-19-3_005	0.0538 ± 0.0061	0.1380 ± 0.0170	0.018410 ± 0.000670	0.00100	131.00 ± 15.00	117.6 ± 4.20	320 ± 240	-11.4	0.9	126.6	41.7	0.479	117.60 ± 4.20
HCC-19-3_024	0.0600 ± 0.0120	0.1540 ± 0.0300	0.018430 ± 0.000780	0.00100	144.00 ± 27.00	117.7 ± 5.00	440 ± 410	-22.3	1.0	68	27.4	0.256	117.70 ± 5.00
HCC-19-3_072	0.0518 ± 0.0049	0.1320 ± 0.0130	0.018450 ± 0.000650	0.06387	126.00 ± 12.00	117.9 ± 4.10	260 ± 200	-6.9	0.7	121.2	50.2	0.528	117.90 ± 4.10
HCC-19-3_029	0.0518 ± 0.0100	0.1460 ± 0.0240	0.018580 ± 0.000980	0.00100	138.00 ± 21.00	118.6 ± 6.20	400 ± 350	-16.4	0.9	66.9	30.6	0.29	118.60 ± 6.20
HCC-19-3_037	0.0507 ± 0.0051	0.1300 ± 0.0140	0.018580 ± 0.000490	0.15724	124.00 ± 13.00	118.7 ± 3.10	250 ± 220	-4.5	0.4	207	71.9	0.76	118.70 ± 3.10
HCC-19-3_089	0.0513 ± 0.0099	0.1360 ± 0.0260	0.018600 ± 0.001000	0.00100	128.00 ± 23.00	118.8 ± 6.60	190 ± 360	-7.7	0.4	77.4	38.8	0.38	118.80 ± 6.60
HCC-19-3_106	0.0495 ± 0.0018	0.1279 ± 0.0065	0.018610 ± 0.000570	0.09034	122.10 ± 5.80	118.8 ± 3.60	167 ± 79	-2.8	0.6	675	252	1.97	118.80 ± 3.60
HCC-19-3_041	0.0560 ± 0.0110	0.1440 ± 0.0300	0.018620 ± 0.000580	0.00100	135.00 ± 27.00	118.9 ± 3.70	330 ± 390	-13.5	0.6	77.6	40.6	0.44	118.90 ± 3.70
HCC-19-3_018	0.0482 ± 0.0029	0.1297 ± 0.0089	0.018730 ± 0.000480	0.08997	125.20 ± 7.00	119.6 ± 3.00	110 ± 130	-4.7	0.8	461	206	2.12	119.60 ± 3.00
HCC-19-3_048	0.0559 ± 0.0067	0.1430 ± 0.0200	0.018720 ± 0.000680	0.55731	135.00 ± 17.00	119.6 ± 4.30	390 ± 230	-12.9	0.9	251	96	1.09	119.60 ± 4.30
HCC-19-3_067	0.0496 ± 0.0054	0.1230 ± 0.0160	0.018750 ± 0.000770	0.22111	117.00 ± 15.00	119.7 ± 4.90	70 ± 240	2.3	-0.2	114.2	48.4	0.539	119.70 ± 4.90
HCC-19-3_039	0.0513 ± 0.0096	0.1330 ± 0.0250	0.018740 ± 0.000610	0.00100	126.00 ± 22.00	119.7 ± 3.90	280 ± 380	-5.3	0.3	80.6	40.11	0.445	119.70 ± 3.90
HCC-19-3_013	0.0506 ± 0.0054	0.1340 ± 0.0140	0.018740 ± 0.000590	0.00100	127.00 ± 12.00	119.7 ± 3.70	200 ± 210	-6.1	0.6	119.1	48.9	0.474	119.70 ± 3.70
HCC-19-3_025	0.0550 ± 0.0100	0.1450 ± 0.0270	0.018750 ± 0.000790	0.04710	136.00 ± 24.00	119.7 ± 5.00	390 ± 370	-13.6	0.7	74.1	38.3	0.355	119.70 ± 5.00
HCC-19-3_006	0.0447 ± 0.0048	0.1200 ± 0.0140	0.018790 ± 0.000720	0.18971	115.00 ± 13.00	120 ± 4.50	-20 ± 200	4.2	-0.4	189	76.3	0.839	120.00 ± 4.50
HCC-19-3_004	0.0468 ± 0.0098	0.1220 ± 0.0260	0.018790 ± 0.000920	0.00220	116.00 ± 23.00	120 ± 5.80	110 ± 380	3.3	-0.2	58.1	28.2	0.304	120.00 ± 5.80
HCC-19-3_096	0.0452 ± 0.0063	0.1210 ± 0.0190	0.018820 ± 0.000830	0.38473	115.00 ± 17.00	120.2 ± 5.30	-10 ± 250	4.3	-0.3	88.2	47.8	0.447	120.20 ± 5.30
HCC-19-3_023	0.0490 ± 0.0043	0.1330 ± 0.0130	0.018820 ± 0.000580	0.00100	126.70 ± 12.00	120.2 ± 3.60	150 ± 180	-5.4	0.5	140.3	57.1	0.635	120.20 ± 3.60
HCC-19-3_046	0.0523 ± 0.0071	0.1360 ± 0.0200	0.018870 ± 0.000850	0.01125	131.00 ± 18.00	120.5 ± 5.40	250 ± 260	-8.7	0.6	127.8	45.1	0.458	120.50 ± 5.40
HCC-19-3_112	0.0490 ± 0.0042	0.1300 ± 0.0120	0.018890 ± 0.000660	0.02275	123.80 ± 11.00	120.6 ± 4.20	140 ± 170	-2.7	0.3	242	166	1.247	120.60 ± 4.20
HCC-19-3_094	0.0477 ± 0.0055	0.1250 ± 0.0130	0.018920 ± 0.000920	0.00100	120.00 ± 12.00	120.8 ± 5.80	150 ± 240	0.7	-0.1	106.4	54.3	0.516	120.80 ± 5.80
HCC-19-3_086	0.0475 ± 0.0028	0.1228 ± 0.0082	0.018920 ± 0.000520	0.37561	117.50 ± 7.40	120.9 ± 3.30	80 ± 120	2.8	-0.5	318	110	1.05	120.90 ± 3.30
HCC-19-3_074	0.0530 ± 0.0051	0.1390 ± 0.0130	0.018930 ± 0.000780	0.00100	132.00 ± 12.00	120.9 ± 5.00	300 ± 200	-9.2	0.9	110.5	49.6	0.538	120.90 ± 5.00
HCC-19-3_040	0.0481 ± 0.0038	0.1300 ± 0.0140	0.018960 ± 0.000710	0.65608	123.00 ± 13.00	121 ± 4.50	150 ± 180	-1.7	0.2	151	90.6	0.87	121.00 ± 4.50
HCC-19-3_044	0.0503 ± 0.0069	0.1260 ± 0.0170	0.018970 ± 0.000740	0.17735	124.00 ± 17.00	121.1 ± 4.70	230 ± 270	-2.4	0.2	97.1	41.9	0.38	121.10 ± 4.70
HCC-19-3_059	0.0439 ± 0.0067	0.1150 ± 0.0180	0.018970 ± 0.000580	0.35847	110.00 ± 17.00	121.2 ± 3.60	-70 ± 260	9.2	-0.7	89.6	39.6	0.461	121.20 ± 3.60
HCC-19-3_047	0.0529 ± 0.0073	0.1380 ± 0.0210	0.018810 ± 0.000730	0.18909	131.00 ± 16.00	121.2 ± 5.00	280 ± 280	-8.1	0.5	106.7	44.4	0.485	121.20 ± 5.00
HCC-19-3_053	0.0500 ± 0.0047	0.1337 ± 0.0110	0.018980 ± 0.000730	0.00100	127.30 ± 9.50	121.2 ± 4.60	230 ± 200	-5.0	0.6	121.4	51.4	0.498	121.20 ± 4.60
HCC-19-3_113	0.0512 ± 0.0028	0.1335 ± 0.0085	0.018980 ± 0.000600	0.00618	127.10 ± 7.60	121.2 ± 3.80	240 ± 120	-4.9	0.8	231.6	88.4	0.659	121.20 ± 3.80
HCC-19-3_104	0.0465 ± 0.0081	0.1270 ± 0.0250	0.019010 ± 0.000850	0.02541	120.00 ± 23.00	121.4 ± 5.40	120 ± 270	1.2	-0.1	78.3	43.8	0.392	121.40 ± 5.40
HCC-19-3_011	0.0506 ± 0.0093	0.1300 ± 0.0240	0.019030 ± 0.000750	0.02391	123.00 ± 21.00	121.5 ± 4.70	160 ± 340	-1.2	0.1	78.1	37.1	0.492	121.50 ± 4.70
HCC-19-3_105	0.0489 ± 0.0072	0.1300 ± 0.0180	0.019030 ± 0.000800	0.00100	128.00 ± 15.00	121.5 ± 5.10	190 ± 290	-5.3	0.4	98.3	78.5	0.678	121.50 ± 5.10
HCC-19-3_082	0.0461 ± 0.0035	0.1174 ± 0.0110	0.019060 ± 0.000650	0.42079	112.50 ± 9.80	121.7 ± 4.10	-10 ± 150	7.6	-0.9	138.2	83.2	0.851	121.70 ± 4.10
HCC-19-3_070	0.0496 ± 0.0073	0.1280 ± 0.0190	0.019070 ± 0.000580	0.00100	122.00 ± 17.00	121.8 ± 3.70	150 ± 280	-0.2	0.0	121	43.2	0.447	121.80 ± 3.70
HCC-19-3_016	0.0467 ± 0.0086	0.1190 ± 0.0200	0.019100 ± 0.000870	0.00100	119.00 ± 21.00	122 ± 5.50	120 ± 360	2.5	-0.1	97.3	52.4	0.574	122.00 ± 5.50
HCC-19-3_098	0.0507 ± 0.0052	0.1370 ± 0.0150	0.019110 ± 0.000650	0.38840	130.00 ± 14.00	122 ± 4.10	220 ± 210	-6.6	0.6	103.9	62.5	0.56	122.00 ± 4.10
HCC-19-3_027	0.0457 ± 0.0096	0.1200 ± 0.0240	0.019130 ± 0.000810	0.13048	114.00 ± 23.00	122.2 ± 5.10	0 ± 370	6.7	-0.4	89.1	40.9	0.454	122.20 ± 5.10
HCC-19-3_107	0.0479 ± 0.0063	0.1250 ± 0.0160	0.019150 ± 0.000790	0.23391	119.00 ± 15.00	122.3 ± 5.00	100 ± 250	2.7	-0.2	95	59.8	0.34	122.30 ± 5.00
HCC-19-3_100	0.0507 ± 0.0092	0.1340 ± 0.0240	0.019160 ± 0.000840	0.00100	127.00 ± 22.00	122.3 ± 5.30	200 ± 360	-3.8	0.2	93.7	52.4	0.443	122.30 ± 5.30
HCC-19-3_114	0.0465 ± 0.0047	0.1200 ± 0.0150	0.019160 ± 0.000730	0.26260	115.00 ± 14.00	122.4 ± 4.60	40 ± 190	6.0	-0.5	110	75.2	0.591	122.40 ± 4.60
HCC-19-3_043	0.0518 ± 0.0057	0.1320 ± 0.0150	0.019180 ± 0.000670	0.00100	125.00 ± 14.00	122.4 ± 4.20	300 ± 210	-2.1	0.2	111	55.8	0.587	122.40 ± 4.20
HCC-19-3_092	0.0489 ± 0.0032	0.1304 ± 0.0100	0.019170 ± 0.000550	0.20967	124.30 ± 9.00	122.4 ± 3.50	140 ± 140	-1.6	0.2	285	124	1.3	122.40 ± 3.50
HCC-19-3_017	0.0476 ± 0.0064	0.1290 ± 0.0170	0.019190 ± 0.000520	0.00100	127.00 ± 14.00	122.5 ± 3.30	80 ± 250	-3.7	0.3	105.2	55.1	0.632	122.50 ± 3.30
HCC-19-3_035	0.0444 ± 0.0073	0.1170 ± 0.0190	0.019200 ± 0.000730	0.00100	112.00 ± 17.00	122.6 ± 4.60	-50 ± 280	8.6	-0.6	107	45	0.457	122.60 ± 4.60
HCC-19-3_061	0.0473 ± 0.0040	0.1240 ± 0.0120	0.019220 ± 0.000510	0.00440	118.00 ± 11.00	122.7 ± 3.30	40 ± 170	3.8	-0.4	157.8	58.7	0.605	122.70 ± 3.30
HCC-19-3_090	0.0482 ± 0.0032	0.1265 ± 0.0094	0.019210 ± 0.000700	0.09606	120.90 ± 8.50	122.7 ± 4.40	110 ± 140	1.5	-0.2	189.5	66.4	0.716	122.70 ± 4.40
HCC-19-3_014	0.0480 ± 0.0064	0.1330 ± 0.0200	0.019230 ± 0.000740	0.35062	126.00 ± 18.00	122.8 ± 4.70	90 ± 250	-2.6	0.2	92.5	37.5	0.404	122.80 ± 4.70
HCC-19-3_073	0.0500 ± 0.0046	0.1330 ± 0.0130	0.019230 ± 0.000570	0.16132	126.00 ± 12.00	122.8 ± 3.60	190 ± 190	-2.6	0.3	190.6	74.9	0.784	122.80 ± 3.60
HCC-19-3_036	0.0527 ± 0.0073	0.1390 ± 0.0210	0.019030 ± 0.000870	0.09086	131.00 ± 18.00	122.8 ± 5.90	270 ± 280	-6.7	0.5	95.8	66.3	0.671	122.80 ± 5.90
HCC-19-3_050	0.0503 ± 0.0034	0.1341 ± 0.0110	0.019240 ± 0.000570	0.18374	127.70 ± 10.00	122.8 ± 3.60	240 ± 170	-4.0	0.5	196	66.5	0.669	122.80 ± 3.60
HCC-19-3_060	0.0510 ± 0.0040	0.1350 ± 0.0130	0.019230 ± 0.000750	0.36273	128.30 ± 11.00	122.8 ± 4.70	260 ± 170	-4.5	0.5	160.9	51.9	0.416	122.80 ± 4.70
HCC-19-3_118	0.0435 ± 0.0083	0.1170 ± 0.0190	0.019240 ± 0.000750	0.33341	112.00 ± 17.00	122.9 ± 4.80	-80 ± 250	8.9	-0.6	101.8	67.5	0.517	122.90 ± 4.80
HCC-19-3_031	0.0475 ± 0.0076	0.1280 ± 0.0220	0.019250 ± 0.000830	0.00100	121.00 ± 20.00	122.9 ± 5.30	70 ± 290	1.5	-0.1	70.4	41.2	0.418	122.90 ± 5.30
HCC-19-3_064	0.0500 ± 0.0095	0.1310 ± 0.0230	0.019250 ± 0.000610	0.00100	124.00 ± 21.00	122.9 ± 3.90	140 ± 340	-0.9	0.1	98.3	43.4	0.452	122.90 ± 3.90
HCC-19-3_030	0.0486 ± 0.0065	0.1300 ± 0.0160	0.019250 ± 0.000610	0.00100	124.00 ± 15.00	122.9 ± 3.90	180 ± 270	-0.9	0.1	143.5	44.2	0.41	122.90 ± 3.90
HCC-19-3_020	0.0474 ± 0.0031	0.1288 ± 0.0110	0.019260 ± 0.000440	0.27424	122.90 ± 9.60	123 ± 2.80	80 ± 140	0.1	0.0	284	146	1.55	123.00 ± 2.80
HCC-19-3_081	0.0535 ± 0.0072	0.1460 ± 0.0160	0.019260 ± 0.000860	0.00100	138.00 ± 14.00	123 ± 5.50	310 ± 280	-12.2	1.1	71.4	30.7	0.346	123.00 ± 5.50
HCC-19-3_103	0.0455 ± 0.0059	0.1260 ± 0.0190	0.019290 ± 0.001000	0.07541	120.00 ± 17.00	123.2 ± 6.60	0 ± 230	2.6	-0.2	96.1	44.4	0.276	123.20 ± 6.60
HCC-19-3_038	0.0485 ± 0.0035	0.1300 ± 0.0110	0.019300 ± 0.000580	0.00100	124.00 ± 9.90	123.2 ± 3.60	170 ± 170	-0.6	0.1	280	109.6	1.09	123.20 ± 3.60
HCC-19-3_069	0.0524 ± 0.0072	0.1330 ± 0.0170	0.019300 ± 0.000570	0.00100	130.00 ± 14.00	123.2 ± 3.60	250 ± 270	-5.5	0.5	113	57.9	0.578	123.20 ± 3.60
HCC-19-3_042	0.0528 ± 0.0065	0.1410 ± 0.0170	0.019300 ± 0.000710	0.02450	133.00 ± 15.00	123.2 ± 4.50	280 ± 250	-8.0	0.7	112.9	66.8	0.684	123.20 ± 4.50
HCC-19-3_077	0.0481 ± 0.0045	0.1270 ± 0.0120	0.019310 ± 0.000690	0.06376	121.00 ± 11.00	123.3 ± 4.30	140 ± 190	1.9	-0.2	142.7	49.6	0.55	123.30 ± 4.30
HCC-19-3_097	0.0501 ± 0.0094	0.1420 ± 0.0270	0.019320 ± 0.000950	0.14282	133.00 ± 24.00	123.4 ± 6.00	220 ± 350	-7.8	0.4	93.1	53.8	0.45	123.40 ± 6.00
HCC-19-3_108	0.0436 ± 0.0077	0.1180 ± 0.0200	0.019350 ± 0.000810	0.00100	113.00 ± 18.00	123.5 ± 5.10	-70 ± 300	8.5	-0.6	85.6	65.2	0.49	123.50 ± 5.10
HCC-19-3_022	0.0522 ± 0.0086	0.1360 ± 0.0180	0.019370 ± 0.000640	0.16935	129.00 ± 16.00	123.7 ± 4.00	260 ± 250	-4.3	0.3	113	50.6	0.514	123.70 ± 4.00
HCC-19-3_117	0.0487 ± 0.0012	0.1318 ± 0.0054	0.019380 ± 0.000470	0.19994	125.70 ± 4.90	123.7 ± 3.00	131 ± 56	-1.6	0.4	1267	921	7.32	123.70 ± 3.00
HCC-19-3_062	0.0496 ± 0.0043	0.1300 ± 0.0120	0.019390 ± 0.000720	0.39795	124.00 ± 11.00	123.8 ± 4.50	160 ± 180	-0.2	0.0	153	63.6	0.646	123.80 ± 4.50
HCC-19-3_078	0.0460 ± 0.0065	0.1230 ± 0.0180	0.019410 ± 0.000650	0.19350	117.00 ± 16.00	123.9 ± 4.10	20 ± 260	5.6	-0.4	102.2	41.52	0.482	123.90 ± 4.10
HCC-19-3_115	0.0480 ± 0.0050	0.1280 ± 0.0160	0.019400 ± 0.000860	0.35956	122.00 ± 14.00	123.9 ± 5.40	90 ± 200	1.5	-0.1	113	65	0.526	123.90 ± 5.40
HCC-19-3_015	0.0480 ± 0.0110	0.1320 ± 0.0270	0.019400 ± 0.001100	0.00100	125.00 ± 24.00	123.9 ± 7.20	50 ± 370	-0.9	0.0	89.3	36.6	0.473	123.90 ± 7.20
HCC-19-3_056	0.0505 ± 0.0092	0.1340 ± 0.0240	0.019410 ± 0.000760	0.74988	127.00 ± 21.00	123.9 ± 4.80	160 ± 340	-2.5	0.1	95.8	57.3	0.639	123.90 ± 4.80
HCC-19-3_010	0.0498 ± 0.0068	0.1360 ± 0.0200	0.019410 ± 0.000690	0.47385	129.00 ± 18.00	123.9 ± 4.30	150 ± 250	-4.1	0.3	120.1	47.7	0.542	123.90 ± 4.30
HCC-19-3_033	0.0531 ± 0.0098	0.1420 ± 0.0270	0.019410 ± 0.000730	0.00100	133.00 ± 24.00	123.9 ± 4.60	270 ± 360	-7.3	0.4	79.6	41.7	0.445	123.90 ± 4.60
HCC-19-3_093	0.0460 ± 0.0047	0.1270 ± 0.0160	0.019420 ± 0.000720	0.21689	121.00 ± 14.00	124 ± 4.60	20 ± 190	2.4	-0.2	127.6	54.5	0.501	124.00 ± 4.60
HCC-19-3_079	0.0502 ± 0.0079	0.1310 ± 0.0210	0.019430 ± 0.000860	0.07949	125.00 ± 19.00	124 ± 5.40	160 ± 300	-0.8	0.1	115.5	48.1	0.46	124.00 ± 5.40
HCC-19-3_087	0.0507 ± 0.0044	0.1370 ± 0.0130	0.019420 ± 0.000660	0.29681	130.00 ± 12.00	124 ± 6.10	210 ± 170	-4.8	0.5	99.7	33.76	0.38	124.00 ± 6.10
HCC-19-3_051	0.0570 ± 0.0099	0.1530 ± 0.0290	0.019440 ± 0.000760	0.19227	143.00 ± 25.00	124.1 ± 4.80	380 ± 340	-15.2	0.8	87.3	37.1	0.348	124.10 ± 4.80
HCC-19-3_066	0.0456 ± 0.0086	0.1220 ± 0.0230	0.019450 ± 0.000800	0.00100	116.00 ± 21.00	124.2 ± 5.10	10 ± 340	6.6	-0.4	71.6	34.6	0.417	124.20 ± 5.10
HCC-19-3_034	0.0502 ± 0.0094	0.1350 ± 0.0240	0.019460 ± 0.000810	0.00100	128.00 ± 21.00	124.2 ± 5.10	140 ± 330	-3.1	0.2	89.2	39.9	0.444	124.20 ± 5.10
HCC-19-3_099	0.0476 ± 0.0033	0.1260 ± 0.0120	0.019470 ± 0.000840	0.14849	120.00 ± 11.00	124.3 ± 5.30	90 ± 140	3.5	-0.4	130.9	59.5	0.527	124.30 ± 5.30
HCC-19-3_065	0.0467 ± 0.0087	0.1280 ± 0.0250	0.019480 ± 0.000870	0.00100	121.00 ± 22.00	124.3 ± 5.50	40 ± 330	2.7	-0.2	68.8	33.31	0.32	124.30 ± 5.50
HCC-19-3_058	0.0475 ± 0.0047	0.1280 ± 0.0150	0.019480 ± 0.000500	0.33004	122.00 ± 13.00	124.4 ± 3.20	70 ± 190	1.9	-0.2	162	61.8	0.58	124.40 ± 3.20
HCC-19-3_008	0.0482 ± 0.0032	0.1346 ± 0.0110	0.019480 ± 0.000480	0.00100	128.10 ± 10.00	124.4 ± 3.00	100 ± 140	-3.0	0.4	487	50.87	0.496	124.40 ± 3.00
HCC-19-3_001	0.0438 ± 0.0080	0.1230 ± 0.0230	0.019500 ± 0.000830	0.00100	117.00 ± 21.00	124.5 ± 5.30	30 ± 350	6.0	-0.4	77.2	33.6	0.36	124.50 ± 5.30
HCC-19-3_076	0.0451 ± 0.0057	0.1250 ± 0.0170	0.019510 ± 0.000740	0.15527	119.00 ± 15.00	124.6 ± 4.70	40 ± 240	4.5	-0.4	108.8	48.2	0.475	124.60 ± 4.70
HCC-19-3_068	0.0483 ± 0.0069	0.1290 ± 0.0180	0.019560 ± 0.000800	0.00100	123.00 ± 16.00	124.8 ± 5.10	100 ± 270	1.4	-0.1	84.9	38.5	0.408	124.80 ± 5.10
HCC-19-3_116	0.0467 ± 0.0056	0.1190 ± 0.0150	0.019560 ± 0.000770	0.18209	120.00 ± 13.00	124.9 ± 4.90	10 ± 220	3.9	-0.4	85.1	54.2	0.469	124.90 ± 4.90
HCC-19-3_091	0.0500 ± 0.0037	0.1420 ± 0.0130	0.019560 ± 0.000730	0.24401	135.00 ± 12.00	124.9 ± 4.60	190 ± 160	-8.1	0.8	110	50.6	0.456	124.90 ± 4.60
HCC-19-3_026	0.0490 ± 0.0100	0.1360 ± 0.0310	0.019620 ± 0.000760	0.00100	127.00 ± 27.00	125.3 ± 4.80	110 ± 380	-1.4	0.1	76.5	37.6	0.377	125.30 ± 4.80
HCC-19-3_085	0.0448 ± 0.0095	0.1200 ± 0.0240	0.019690 ± 0.000760	0.00100	114.00 ± 22.00	125.7 ± 4.80	40 ± 380	9.3	-0.5	85	41	0.482	125.70 ± 4.80
HCC-19-3_021	0.0445 ± 0.0060	0.1220 ± 0.0180	0.019710 ± 0.000640	0.38569	117.00 ± 16.00	125.8 ± 4.00	-40 ± 240	7.0	-0.6	95.1	32.5	0.33	125.80 ± 4.00
HCC-19-3_075	0.0473 ± 0.0086	0.1210 ± 0.0220	0.019730 ± 0.000610	0.02333	115.00 ± 20.00	125.9 ± 3.80	130 ± 300	8.7	-0.5	92.4	56.5	0.558	125.90 ± 3.80
HCC-19-3_088	0.0494 ± 0.0029	0.1368 ± 0.0110	0.019740 ± 0.000680	0.32955	130.00 ± 9.90	126 ± 4.20	160 ± 120	-3.2	0.4	261	124	1.32	126.00 ± 4.20
HCC-19-3_109	0.0474 ± 0.0056	0.1300 ± 0.0200	0.019870 ± 0.000950	0.10803	127.00 ± 17.00	126.8 ± 6.00	140 ± 240	-0.2	0.0	94.9	55.9	0.383	126.80 ± 6.00
HCC-19-3_120	0.0517 ± 0.0048	0.1440 ± 0.0140	0.019890 ± 0.000900	0.18676	136.00 ± 13.00	127 ± 5.70	260 ± 190	-7.1	0.7	103.3	57.8	0.458	127.00 ± 5.70
HCC-19-3_095	0.0462 ± 0.0052	0.1256 ± 0.0090	0.019950 ± 0.000550	0.21788	122.00 ± 9.00	127.3 ± 3.50	30 ± 130	4.2	-0.6	296	158	1.38	127.30 ± 3.50
HCC-19-3_002	0.0522 ± 0.0079	0.1450 ± 0.0210	0.019970 ± 0.000910	0.00100	137.00 ± 19.00	127.4 ± 5.70	220 ± 280	-7.5	0.5	86.5	32.5	0.428	127.40 ± 5.70
HCC-19-3_119	0.0468 ± 0.0094	0.1286 ± 0.0084	0.020000 ± 0.000580	0.05587	122.80 ± 7.60	127.6 ± 3.50	50 ± 120	3.8	-0.6	231	94.6	0.774	127.60 ± 3.50
HCC-19-3_019	0.0458 ± 0.0039	0.1300 ± 0.0130	0.020000 ± 0.000510	0.00100	124.10 ± 11.00	127.6 ± 3.20	20 ± 160	2.7	-0.3	223	74	0.9	127.60 ± 3.20
HCC-19-3_083	0.0510 ± 0.0083	0.1410 ± 0.0240	0.020020 ± 0.000960	0.16138	133.00 ± 22.00	127.8 ± 6.00	190 ± 310	-4.1	0.2	81.3	37.5	0.405	127.80 ± 6.00
HCC-19-3_003	0.0442 ± 0.0099	0.1210 ± 0.0270	0.020040 ± 0.000810	0.00100	115.00 ± 25.00	127.9 ± 5.10	-60 ± 380	10.1	-0.5	81.4	40.2	0.477	127.90 ± 5.10
HCC-19-3_007	0.0553 ± 0.0081	0.1520 ± 0.0240	0.020040 ± 0.000840	0.15524	143.00 ± 21.00	127.9 ± 5.30	350 ± 290	-11.8	0.7	79.3	34	0.399	127.90 ± 5.30
HCC-19-3_009	0.0500 ± 0.0053	0.1460 ± 0.0140	0.020050 ± 0.000630	0.01279	138.00 ± 13.00	128 ± 4.00	250 ± 190	-7.8	0.8	116.3	35.8	0.45	128.00 ± 4.00
HCC-19-3_111	0.0513 ± 0.0081	0.1320 ± 0.0250	0.020110 ± 0.001000	0.01407	131.00 ± 19.00	128.3 ± 6.30	210 ± 310	-2.1	0.1	84.7	49.1	0.425	128.30 ± 6.30
HCC-19-3_049	0.0510 ± 0.0053	0.1400 ± 0.0170	0.020120 ± 0.000710	0.44997	133.00 ± 15.00	128.4 ± 4.50	220 ± 210	-3.6	0.3	103.8	52.3	0.491	128.40 ± 4.50
HCC-19-3_063	0.0458 ± 0.0044	0.1280 ± 0.0120	0.020140 ± 0.000690	0.04954	122.50 ± 10.00	128.6 ± 4.30	10 ± 180	4.7	-0.6	233	73.7	0.685	128.60 ± 4.30
HCC-19-3_101	0.0527 ± 0.0047	0.1530 ± 0.0150	0.020410 ± 0.000800	0.00100	144.00 ± 13.00	130.3 ± 5.10	330 ± 200	-10.5	1.1	131.5	51.7	0.416	130.30 ± 5.10
HCC-19-3_071	0.0445 ± 0.0036	0.1260 ± 0.0120	0.020480 ± 0.000670	0.28062	120.30 ± 11.00	130.7 ± 4.30	-40 ± 150	8.0	-0.9	190	126	1.45	130.70 ± 4.30
HCC-19-3_055	0.0488 ± 0.0071	0.1300 ± 0.0180	0.020620 ± 0.000710	0.00100	124.00 ± 16.00	131.6 ± 4.50	120 ± 270	5.8	-0.5	90.7	42.7	0.463	131.60 ± 4.50
HCC-19-3_012	0.0497 ± 0.0023	0.1456 ± 0.0096	0.020700 ± 0.000660	0.68555	137.90 ± 8.50	132 ± 4.20	177 ± 100	-4.5	0.7	611	297	3.51	132.00 ± 4.20
HCC-19-3_028	0.0509 ± 0.0042	0.1484 ± 0.0130	0.021080 ± 0.000780	0.37855	140.30 ± 11.00	134.5 ± 4.90	250 ± 180	-4.3	0.5	181.8	74.9	0.911	134.50 ± 4.90

Table C.5.

REFERENCES CITED

Abbey, S. (1983). *Studies in "Standard Samples" of silicate rocks and minerals 1969-1982* (Tech. Rep.). Ottawa, CA: Geological Survey of Canada.

Adams, B. A., & Ehlers, T. A. (2018). Tectonic controls of Holocene erosion in a glaciated orogen. *Earth Surface Dynamics*, *6*(3), 595–610. doi: 10.5194/esurf-6-595-2018

Adams, B. A., Hodges, K. V., Whipple, K. X., Ehlers, T. A., Van Soest, M. C., & Wartho, J. (2015). Constraints on the tectonic and landscape evolution of the Bhutan Himalaya from thermochronometry. *Tectonics*, *34*(6), 1329–1347. doi: 10.1002/2015TC003853

Allen, J. (1991). The case of the inverted auriferous paleotorrent – exotic quartzite gravels on Wallowa Mountain peaks. *Oregon Geology*, *53*(5), 104–107.

Anderson, E. (1942). *The Dynamics of Faulting and Dyke Formation with Application to Britain*. Edinburgh: Oliver and Boyd.

Anthony, D., & Granger, D. (2007). A new chronology for the age of the Appalachian erosional surfaces determined by cosmogenic nuclides in cave sediments. *Earth Surface Processes and Landforms*, *32*(November 2006), 874–887. Retrieved from `http://www3.interscience.wiley.com/journal/121517813/abstract` doi: 10.1002/esp

Arundel, S. T., Phillips, L. A., Lowe, A. J., Bobinmyer, J., Mantey, K. S., Dunn, C. A., ... Usery, E. L. (2015). Preparing the National Map for the 3D Elevation Program-products, process and research. *Cartography and Geographic Information Science*, *42*(1), 40–53. Retrieved from `http://dx.doi.org/10.1080/15230406.2015.1057229` doi: 10.1080/15230406.2015.1057229

Babiker, M., & Gudmundsson, A. (2004). Geometry, structure and emplacement of mafic dykes in the Red Sea Hills, Sudan. *Journal of African Earth Sciences*, *38*(3), 279–292. doi: 10.1016/j.jafrearsci.2004.01.003

Bailey, M. (1989). Evidence for magma recharge and assimilation in the Picture Gorge Basalt subgroup, Columbia River Basalt Group. In Reidel, Stephen P & P. Hooper (Eds.), *Volcanism and tectonism in the columbia river flood-basalt province* (pp. 343–355). Boulder, Colorado: Geological Society of America Special Paper 239.

Barry, T. L., Kelley, S. P., Camp, V., Self, S., Jarboe, N., & Duncan, R. (2013). Eruption chronology of the Columbia River Basalt Group. *Geological Society of America Special Papers*, *2497*(02), 45–66. doi: 10.1130/2013.2497(02).

Bartoli, G., Sarnthein, M., Weinelt, M., Erlenkeuser, H., Garbe-Schönberg, D., & Lea, D. W. (2005). Final closure of Panama and the onset of northern hemisphere glaciation. *Earth and Planetary Science Letters*, *237*(1-2), 33–44. doi: 10.1016/j.epsl.2005.06.020

Belmont, P. (2015). *Measuring long-term erosion rates and dating fluvial terraces in Hells Canyon , Idaho and Oregon* (Tech. Rep.). Logan, Utah: Utah State University.

Beranek, L., Link, P., & Fanning, C. (2006). Miocene to Holocene landscape evolution of the western Snake River Plain region, Idaho: Using the SHRIMP detrital zircon provenance record to track eastward migration of the Yellowstone hotspot. *Bulletin of the Geological Society of America*, *118*(9-10), 1027–1050. doi: 10.1130/B25896.1

Black, B. A., & Manga, M. (2017). Volatiles and the tempo of flood basalt magmatism. *Earth and Planetary Science Letters*, *458*, 130–140. Retrieved from `http://dx.doi.org/10.1016/j.epsl.2016.09.035` doi: 10.1016/j.epsl.2016.09.035

Black, L. P., Kamo, S. L., Allen, C. M., Davis, D. W., Aleinikoff, J. N., Valley, J. W., ... Foudoulis, C. (2004). Improved 206Pb/238U microprobe geochronology by the monitoring of a trace-element-related matrix effect; SHRIMP, ID-TIMS, ELA-ICP-MS and oxygen isotope documentation for a series of zircon standards. *Chemical Geology*, *205*(1-2), 115–140. doi: 10.1016/j.chemgeo.2004.01.003

Blakely, R. J., Sherrod, B. L., Weaver, C. S., Wells, R. E., & Rohay, A. C. (2014). The Wallula fault and tectonic framework of south-central Washington, as interpreted from magnetic and gravity anomalies. *Tectonophysics*, *624-625*, 32–45. Retrieved from `http://dx.doi.org/10.1016/j.tecto.2013.11.006` doi: 10.1016/j.tecto.2013.11.006

Bohrson, W. A., & Spera, F. J. (2003). Energy-constrained open-system magmatic processes IV: Geochemical, thermal and mass consequences of energyconstrained recharge, assimilation and fractional crystallization (EC-RAFC). *Geochemistry, Geophysics, Geosystems*, *4*(2). doi: 10.1029/2002GC000316

Bond, J. (1963). *Geology of the Clearwater embayment:* (Tech. Rep.). Boise, Idaho: Idaho Bureau of Mines and Geology.

Bond, J., Kauffman, J., Miller, D., & Venkatakrishnan, R. (1978). *Geologic map of Idaho* (Tech. Rep.). Moscow, Idaho: Moscow, Idaho, Idaho Bureau of Mines and Geology, with contributions from U.S. Geological Survey.

Braun, J. (2003). Pecube: A new finite-element code to solve the 3D heat transport equation including the effects of a time-varying, finite amplitude surface topography. *Computers and Geosciences*, *29*(6), 787–794. doi: 10.1016/S0098-3004(03)00052-9

Braun, J., van der Beek, P., Valla, P., Robert, X., Herman, F., Glotzbach, C., ... Prigent, C. (2012). Quantifying rates of landscape evolution and tectonic processes by thermochronology and numerical modeling of crustal heat transport using PECUBE. *Tectonophysics*, *524-525*, 1–28. Retrieved from `http://dx.doi.org/10.1016/j.tecto.2011.12.035` doi: 10.1016/j.tecto.2011.12.035

Brown, C., & Thayer, T. (1966). *Geologic map of the Canyon City quadrangle, northeastern Oregon* (Tech. Rep.). Denver, Colorado: U.S. Geological Survey.

Bunger, A. P., Menand, T., Cruden, A., Zhang, X., & Halls, H. (2013). Analytical predictions for a natural spacing within dyke swarms. *Earth and Planetary Science Letters*, *375*, 270–279. Retrieved from `http://dx.doi.org/10.1016/j.epsl.2013.05.044` doi: 10.1016/j.epsl.2013.05.044

Burgess, S. D., Muirhead, J. D., & Bowring, S. A. (2017). Initial pulse of Siberian Traps sills as the trigger of the end-Permian mass extinction. *Nature Communications*, *8*(1), 1–4. Retrieved from `http://dx.doi.org/10.1038/s41467-017-00083-9` doi: 10.1038/s41467-017-00083-9

Burov, E., Guillou-Frottier, L., D'Acremont, E., Le Pourhiet, L., & Cloetingh, S. (2007). Plume head-lithosphere interactions near intra-continental plate boundaries. *Tectonophysics*, *434*(1-4), 15–38. doi: 10.1016/j.tecto.2007.01.002

Cahoon, E. B., Streck, M. J., Koppers, A. A. P., & Miggins, D. P. (2020). Reshuffling Columbia River Basalt Chronology - Picture Gorge Basalt , the Earliest and Longest Reshuffling Columbia River Basalt Chronology – Picture Gorge Basalt , the Earliest and Longest Erupting Formation. *Geology*, *In press*.

Camp, V., Reidel, S., Ross, M., Brown, R., & Self, S. (2017). Field-Trip Guide to the Vents, Dikes, Stratigraphy, and Structure of the Columbia River Basalt Group Eastern Oregon and Southeastern Washington. *Scientific Investigations Report 5022*, 88 p.

Camp, V., Ross, M., Duncan, R. A., & Kimbrough, D. (2017). Uplift, rupture, and rollback of the Farallon slab reflected in volcanic perturbations along the Yellowstone adakite hot spot track. *Journal of Geophysical Research: Earth Surface*(122), 1–24. doi: 10.1002/2016JB013451

Camp, V. E. (2013). Origin of Columbia River Basalt: Passive rise of shallow mantle, or active upwelling of a deep-mantle plume? *The Geological Society of America Special Paper*, *497*(07), 181–199. doi: 10.1130/2013.2497(07).

Camp, V. E., & Hanan, B. B. (2008). A plume-triggered delamination origin for the Columbia River Basalt Group. *Geosphere*, *4*(3), 480–495. doi: 10.1130/GES00175.1

Camp, V. E., Pierce, K. L., & Morgan, L. A. (2015). Yellowstone plume trigger for Basin and Range extension, and coeval emplacement of the Nevada-Columbia Basin magmatic belt. *Geosphere*, *11*(2), 203–225. doi: 10.1130/GES01051.1

Camp, V. E., & Ross, M. E. (2004). Mantle dynamics and genesis of mafic magmatism in the intermontane Pacific Northwest. *Journal of Geophysical Research: Solid Earth*, *109*(8), 1–14. doi: 10.1029/2003JB002838

Cardozo, N., & Allmendinger, R. W. (2013). Spherical projections with OSXStereonet. *Computers and Geosciences*, *51*, 193–205. Retrieved from `http://dx.doi.org/10.1016/j.cageo.2012.07.021` doi: 10.1016/j.cageo.2012.07.021

Castelltort, S., Goren, L., Willett, S. D., Champagnac, J. D., Herman, F., & Braun, J. (2012). River drainage patterns in the New Zealand Alps primarily controlled by plate tectonic strain. *Nature Geoscience*, *5*(10), 744–748. Retrieved from `http://dx.doi.org/10.1038/ngeo1582` doi: 10.1038/ngeo1582

Catchings, R. D., & Mooney, W. D. (1988). Crustal structure of the Columbia Plateau: evidence for continental rifting. *Journal of Geophysical Research*, *93*(B1), 459–474. doi: 10.1029/JB093iB01p00459

Clemens, D., & Wood, S. (1993). Radiometric datring, volcanic stratigraphy, and sedimentation in the Boise foothills, northeastern margin of the western Snake River Plain, Ada County, Idaho. *Isochron/West*, *59*, 3–10.

Cloetingh, S., Burov, E., & Francois, T. (2013). Thermo-mechanical controls on intra-plate deformation and the role of plume-folding interactions in continental topography. *Gondwana Research*, *24*(3-4), 815–837. Retrieved from `http://dx.doi.org/10.1016/j.gr.2012.11.012` doi: 10.1016/j.gr.2012.11.012

Colgan, J. P. (2013). Reappraisal of the relationship between the northern Nevada rift and Miocene extension in the northern Basin and Range Province. *Geology*, *41*(2), 211–214. doi: 10.1130/G33512.1

Colón, D. P., Bindeman, I. N., & Gerya, T. V. (2018). Thermomechanical Modeling of the Formation of a Multilevel, Crustal-Scale Magmatic System by the Yellowstone Plume. *Geophysical Research Letters*, *45*(9), 3873–3879. doi: 10.1029/2018GL077090

Corti, G., Cioni, R., Franceschini, Z., Sani, F., Scaillet, S., Molin, P., ... Glerum, A. (2019). Aborted propagation of the Ethiopian rift caused by linkage with the Kenyan rift. *Nature Communications*, *10*(1), 1–11. Retrieved from `http://dx.doi.org/10.1038/s41467-019-09335-2` doi: 10.1038/s41467-019-09335-2

Cowan, D., & Reiners, P. W. (2004). Age and provenance of lower Tertiary fluvial strata, Elkhorn Mountains, E. Oregon. *Geological Society of America Abstracts with Programs*, *4*, 34.

Crisp. (1984). Rates of magma emplacement and volcanic output. *Journal of Volcanology and Geothermal Research*, *20*(3-4), 177–211.

Crosby, B. T., & Whipple, K. X. (2006). Knickpoint initiation and distribution within fluvial networks: 236 waterfalls in the Waipaoa River, North Island, New Zealand. *Geomorphology*, *82*(1-2), 16–38. doi: 10.1016/j.geomorph.2005.08.023

Darling, A., & Whipple, K. (2015). Geomorphic constraints on the age of the western grand canyon. *Geosphere*, *11*(4), 958–976. doi: 10.1130/GES01131.1

Darold, A., & Humphreys, E. (2013). Upper mantle seismic structure beneath the Pacific Northwest: A plume-triggered delamination origin for the Columbia River flood basalt eruptions. *Earth and Planetary Science Letters*, *365*, 232–242. doi: 10.1016/j.epsl.2013.01.024

Davenport, K., Hole, J., Tikoff, B., Russo, R., & Harder, S. (2017). A strong contrast in crustal architecture from accreted terranes to craton, constrained by controlled-source seismic data in Idaho and eastern Oregon. *Lithosphere*, *9*(2), 325–340. Retrieved from `http://lithosphere.gsapubs.org/lookup/doi/10.1130/L553.1` doi: 10.1130/L553.1

Davis, K. N., Wolff, J. A., Rowe, M. C., & Neill, O. K. (2017). Sulfur release from main-phase Columbia River Basalt eruptions. *Geology*, *45*(11), 1043–1046. doi: 10.1130/G39371.1

DeCelles, P. G. (2004). LATE JURASSIC TO EOCENE EVOLUTION OF THE CORDILLERAN THRUST BELT AND FORELAND BASIN SYSTEM, WESTERN U.S.A. *American Journal of Science*, *304*(February), 105–168. Retrieved from `http://ajsonline.org/cgi/content/abstract/304/2/105` doi: 10.2475/ajs.304.2.105

Delaney, P., Pollard, D. D., Ziony, J., & McKee, E. (1986). Field relations between dikes and joints: Emplacement processes and paleostress analysis. *Journal of Geophysical Research*, *91*(B5), 4920. doi: 10.1029/JB091iB05p04920

Delaney, P. T., & Gartner, A. E. (1997). Physical processes of shallow mafic dike emplacement near the San Rafael Swell, Utah. *Bulletin of the Geological Society of America*, *109*(9), 1177–1192. doi: 10.1130/0016-7606(1997)109⟨1177:PPOSMD⟩2.3.CO;2

Demboski, J. R., & Sullivan, J. (2003). Extensive mtDNA variation within the yellow-pine chipmunk, Tamias amoenus (Rodentia: Sciuridae), and phylogeographic inferences for northwest North America. *Molecular Phylogenetics and Evolution*, *26*(3), 389–408. doi: 10.1016/S1055-7903(02)00363-9

Dickinson, W. R. (1979). Mesozoic forearc basin in central Oregon. *Geology*, *7*(4), 166–170. doi: 10.1130/0091-7613(1979)7⟨166:MFBICO⟩2.0.CO;2

Dorsey, R. J., & LaMaskin, T. A. (2007). Stratigraphic record of Triassic-Jurassic collisional tectonics in the Blue Mountains province, northern Oregon. *American Journal of Science*, *307*(10), 1167–1193. doi: 10.2475/10.2007.03

Dorsey, R. J., & LaMaskin, T. A. (2008). Mesozoic collision and accretion of oceanic terranes in the Blue Mountains province of northeastern Oregon: New insights from the stratigraphic record. *Arizona Geological Society Digest*, *22*(1), 325–332.

Duvall, A., Kirby, E., & Burbank, D. W. (2004). Tectonic and lithologic controls on bedrock channel profiles and processes in coastal California. *Journal of Geophysical Research*, *109*(F3), F03002. Retrieved from `http://doi.wiley.com/10.1029/2003JF000086` doi: 10.1029/2003JF000086

Ekren, E., McIntyre, D., Bennett, E., & Marvin, R. (1982). Cenozoic stratigraphy of western Owyhee County, Idaho. In *Cenozoic geology of idaho: Idaho bureau of mines and geology bulletin 26* (pp. 215–236). Moscow, Idaho: Idaho Bureau of Mines and Geology.

Ellis, B. S., Barry, T., Branney, M. J., Wolff, J. A., Bindeman, I., Wilson, R., & Bonnichsen, B. (2010). Petrologic constraints on the development of a large-volume, high temperature, silicic magma system: The Twin Falls eruptive centre, central Snake River Plain. *Lithos*, *120*(3-4), 475–489. Retrieved from `http://dx.doi.org/10.1016/j.lithos.2010.09.008` doi: 10.1016/j.lithos.2010.09.008

England, P., & Molnar, P. (1990). Surface uplift, uplift of rocks, and exhumation of rocks. *Geology*, *18*(12), 1173–1177. doi: 10.1130/0091-7613(1990)018⟨1173:SUUORA⟩2.3.CO;2

Ernst, R. E., & Baragar, W. R. A. (1992). Evidence from magnetic fabric for the flow pattern of magma in the Mackenzie giant radiating dyke swarm. *Nature*, *356*(6369), 511–513. doi: 10.1038/356511a0

Ernst, R. E., & Buchan, K. L. (1997). Giant Radiating Dyke Swarms: Their Use in Identifying Pre-Mesozoic Large Igneous Provinces and Mantle Plumes. *Geophysical Monograph*, *100*, 297–333. Retrieved from http://doi.wiley.com/10.1029/GM100p0297 doi: 10.1029/GM100p0297

Farley, K. A. (2000). Helium diffusion from apatite: General behavior as illustrated by Durango fluorapatite. *Journal of Geophysical Research: Solid Earth*, *105*(B2), 2903–2914. doi: 10.1029/1999jb900348

Fayon, A., Tikoff, B., Kahn, M., & Gaschnig, R. (2017). Cooling and exhumation of the southern Idaho batholith. *Lithosphere*, *9*(2), 299–314. Retrieved from http://lithosphere.gsapubs.org/lookup/doi/10.1130/L565.1 doi: 10.1130/L565.1

Fecht, K., Reidel, S., & Tallman, A. (1987). Paleodrainage of the Columbia River system on the Columbia Plateau of Washington State: A summary. *Washington Division of Geology and Earth Resources Bulletin*, *77*, 219–248. Retrieved from http://www.osti.gov/energycitations/product.biblio.jsp?osti{_}id=5940458

Fialko, Y., & Rubin, A. (1999). Thermal and mechanical aspects of magma emplacementin giant dikes warms. *Journal of Geophysical Research*, *104*(B10), 23033–23049.

Finnegan, N. J., Hallet, B., Montgomery, D. R., Zeitler, P. K., Stone, J. O., Anders, A. M., & Yuping, L. (2008). Coupling of rock uplift and river incision in the Namche Barwa-Gyala Peri massif, Tibet. *Bulletin of the Geological Society of America*, *120*(1-2), 142–155. doi: 10.1130/B26224.1

Fisher, R. (1992). *Statistical Methods for Research Workers*. New York City: Spinger.

Flint, J. J. (1974). Stream gradient as a function of order, magnitude, and discharge. *Water Resources Research*, *10*(5), 969–973. doi: 10.1029/WR010i005p00969

Flowers, R., & Farley, K. (2012). Evidence for an Ancient Grand Canyon. *Science*, *338*(December), 1616–1619.

Flowers, R. M., Ketcham, R. A., Shuster, D. L., & Farley, K. A. (2009). Apatite (U-Th)/He thermochronometry using a radiation damage accumulation and annealing model. *Geochimica et Cosmochimica Acta*, *73*(8), 2347–2365. Retrieved from http://dx.doi.org/10.1016/j.gca.2009.01.015 doi: 10.1016/j.gca.2009.01.015

Forte, A. M., & Whipple, K. X. (2019). Short Communication: The Topographic Analysis Kit (TAK) for TopoToolbox. *Earth Surface Dynamics*, *7*, 87–95.

Fruchter, J. S., & Baldwin, S. F. (1975). Correlations between Dikes of the Monument Swarm, Central Oregon, and Picture Gorge Basalt Flows. *Bulletin of the Geological Society of America*, *86*(4), 514–516. doi: 10.1130/0016-7606(1975)86⟨514:CBDOTM⟩2.0.CO;2

Gallagher, K. (2012). Transdimensional inverse thermal history modeling for quantitative thermochronology. *Journal of Geophysical Research: Solid Earth*, *117*(2), 1–16. doi: 10.1029/2011JB008825

Gallen, S. F., & Wegmann, K. W. (2017). River profile response to normal fault growth and linkage: An example from the Hellenic forearc of south-central Crete, Greece. *Earth Surface Dynamics*, *5*(1), 161–186. doi: 10.5194/esurf-5-161-2017

Gaschnig, R., Vervoort, J., Tikoff, B., & Lewis, R. (2016). Construction and preservation of batholiths in the northern U.S. Cordillera. *Lithosphere*, *9*(2), 315–324. doi: 10.1130/l497.1

Gaschnig, R. M., Macho, A. S., Fayon, A., Schmitz, M., Ware, B. D., Vervoort, J. D., ... Tikoff, B. (2017). Intrusive and depositional constraints on the Cretaceous tectonic history of the southern Blue Mountains, eastern Oregon. *Lithosphere*, *9*(2), 265–282. doi: 10.1130/L554.1

Gaschnig, R. M., Vervoort, J. D., Lewis, R. S., & McClelland, W. C. (2010). Migrating magmatism in the northern US Cordillera: In situ U-Pb geochronology of the Idaho batholith. *Contributions to Mineralogy and Petrology*, *159*(6), 863–883. doi: 10.1007/s00410-009-0459-5

Gaschnig, R. M., Vervoort, J. D., Lewis, R. S., & Tikoff, B. (2011). Isotopic evolution of the idaho batholith and Challis intrusive province, Northern US Cordillera. *Journal of Petrology*, *52*(12), 2397–2429. doi: 10.1093/petrology/egr050

Gehrels, G. E. (2012). Detrital zircon U-Pb geochronology: current methods and new opportunites. In C. J. Busby & A. Azor (Eds.), *Tectonics of sedimentary basins* (Vol. 253, pp. 47–63). Chichester, UK: Blackwell Publishing Ltd. doi: 10.1130/SPE253-p57

Geshi, N., Kusumoto, S., & Gudmundsson, A. (2010). Geometric difference between non-feeder and feeder dikes. *Geology*, *38*(3), 195–198. doi: 10.1130/G30350.1

Getty, S. R., Selverstone, J., Wernicke, B. P., Jacobsen, S. B., Aliberti, E., & Lux, D. R. (1993). Sm-Nd dating of multiple garnet growth events in an arc-continent collision zone, northwestern U.S. Cordillera. *Contributions to Mineralogy and Petrology*, *115*, 45–57.

Ghiorso, M. M. S., & Sack, R. O. R. (1995). Chemical mass transfer in magmatic processes IV. A revised and internally consistent thermodynamic model for the interpolation and extrapolation of liquid-solid. *Contributions to Mineralogy and Petrology*, *119*(2-3), 197–212. Retrieved from `http://link.springer.com/article/10.1007/BF00307281{%}5Cnhttp://link.springer.com/10.1007/BF00307281` doi: 10.1007/BF00307281

Giorgis, S., McClelland, W., Fayon, A., Singer, B. S., & Tikoff, B. (2008). Timing of deformation and exhumation in the western Idaho shear zone, McCall, Idaho. *Bulletin of the Geological Society of America*, *120*(9-10), 1119–1133. doi: 10.1130/B26291.1

Glen, J. M. G., & Ponce, D. A. (2002). Large-scale fractures related to inception of the Yellowstone hotspot. *Geology*, *30*(7), 647–650. doi: 10.1130/0091-7613(2002)030⟨0647:LSFRTI⟩2.0.CO;2

Goren, L., Fox, M., & Willett, S. D. (2014). Tectonics from fluvial topography using formal linear inversion: Theory and applications to the Inyo Mountains, California. *Journal of Geophysical Research F: Earth Surface*, *119*(8), 1651–1681. doi: 10.1002/2014JF003079

Govindaraju, K. (1994). Compilation of Working Values and Sample Description for 383 Geochemical standards. *Geostandards Newsletters*, *18*(Special Issue), pp. 1–58.

Granger, D. E., Kirchner, J. W., & Finkel, R. (1996). Spatially Averaged Long-Term Erosion Rates Measured from in Situ-Produced Cosmogenic Nuclides in Alluvial Sediment. *The Journal of Geology*, *104*(3), 249–257.

Granger, D. E., Kirchner, J. W., & Finkel, R. C. (1997). Quaternary downcutting rate of the New River, Virginia, measured from differential decay of cosmogenic 26Al and 10Be in cave-deposited alluvium. *Geology*, *25*(2), 107–110. doi: 10.1130/0091-7613(1997)025⟨0107:QDROTN⟩2.3.CO;2

Gray, K. D., Isakson, V., Schwartz, D., & Vervoort, J. D. (2020). Orogenic link 41 N-46 N: Collisional mountain building and basin closure in the Cordillera of western North America. *Geosphere*, *16*(1), 136–181. doi: 10.1130/GES02074.1

Gray, K. D., & Oldow, J. S. (2005). *Contrasting structural histories of the Salmon River belt and Wallowa terrane: Implications for terrane accretion in northeastern Oregon and west-central Idaho* (Vol. 117) (No. 5-6). doi: 10.1130/B25411.1

Gudmundsson, A. (1990). Emplacement of dykes, sill and crustal magma chambers at divergent plate boundaries. *Tectonophysics*, *176*, 257–275.

Gudmundsson, A. (1995). Infrastructure and mechnics of volcanic system in Iceland. *Journal of Volcanology and Geothermal Research*, *64*(94), 1–22.

Guenthner, W. R., Reiners, P. W., Ketcham, R. A., Nasdala, L., & Giester, G. (2013). Helium diffusion in natural zircon: radiation damage, anisotropy, and the interpretation of zircon (U-TH)/He thermochronology. *American Journal of Science*, *313*(3), 145–198. doi: 10.2475/03.2013.01

Guillou-Frottier, L., Burov, E., Nehlig, P., & Wyns, R. (2007). Deciphering plume-lithosphere interactions beneath Europe from topographic signatures. *Global and Planetary Change*, *58*(1-4), 119–140. doi: 10.1016/j.gloplacha.2006.10.003

Hack, J. (1957). Studies of longitudinal stream profiles in Virginia and Maryland. *U.S. Geological Survey Professional Paper*, *249B*.

Hales, T. C., Abt, D. L., Humphreys, E. D., & Roering, J. J. (2005). A lithospheric instability origin for Columbia River flood basalts and Wallowa Mountains uplift in northeast Oregon. *Nature*, *438*(7069), 842–845. doi: 10.1038/nature04313

Hallet, B., & Molnar, P. (2001). Distorted drainage basins as markers of crustal strain east of the Himalaya. *Journal of Geophysical Research: Solid Earth*, *106*(B7), 13697–13709. doi: 10.1029/2000jb900335

Hamilton, W. (1963). Metamorphism in the Riggins region, Western Idaho. *U.S. Geological Survey Professional Paper*, *436*, 95 p. includes reconnaissance Geologic Map of the.

Harkins, N., Kirby, E., Heimsath, A., Robinson, R., & Reiser, U. (2007). Transient fluvial incision in the headwaters of the Yellow River, northeastern Tibet, China. *Journal of Geophysical Research: Earth Surface*, *112*(3), 1–21. doi: 10.1029/2006JF000570

Hiess, J., Condon, D. J., McLean, N., & Noble, S. R. (2012). 238U/235U systematics in terrestrial uranium-bearing minerals. *Science*, *335*(6076), 1610–1614. doi: 10.1126/science.1215507

Hoek, J. D. (1991). A classification of dyke-fracture geometry with examples from Precambrian dyke swarms in the Vestfold Hills, Antarctica. *Geologische Rundschau*, *80*(2), 233–248. doi: 10.1007/BF01829363

Holden, G. S., & Hooper, P. R. (1976). Petrology and chemistry of a Columbia River basalt section, Rocky Canyon, west-central Idaho. *Bulletin of the Geological Society of America*, *87*(2), 215–225. doi: 10.1130/0016-7606(1976)87⟨215:PACOAC⟩2.0.CO;2

Hooper, P. R. (2000). Chemical discrimination of Columbia River basalt flows. *Geochemistry, Geophysics, Geosystems*, *1*(6). doi: 10.1029/2000GC000040

Hooper, P. R., Binger, G. B., & Lees, K. R. (2002). Ages of the Steens and Columbia River flood basalts and their relationship to extension-related calc-alkalic volcanism in eastern Oregon. *Bulletin of the Geological Society of America*, *114*(1), 43–50. doi: 10.1130/0016-7606(2002)114⟨0043:AOTSAC⟩2.0.CO;2

Hooper, P. R., Kleck, W. D., Knowles, C. R., Reidel, S. P., & Thiessen, R. L. (1984). Imnaha basalt, Columbia river basalt group. *Journal of Petrology*, *25*(2), 473–500. doi: 10.1093/petrology/25.2.473

Hoshi, H., & Takahashi, M. (1999). Miocene counterclockwise rotation of Northeast Japan: a review and new model. *Bulletin of the Geological Survey of Japan*, *50*(1), 3–16. Retrieved from `http://ci.nii.ac.jp/naid/40002358367/en/`

Howard, A. D., & Kerby, G. (1983). Channel changes in badlands. *Geological Society of America Bulletin*, *94*(6), 739–752. doi: 10.1130/0016-7606(1983)94⟨739:CCIB⟩2.0.CO;2

Hu, Z., Gao, S., Liu, Y., Hu, S., Chen, H., & Yuan, H. (2008). Signal enhancement in laser ablation ICP-MS by addition of nitrogen in the central channel gas. *Journal of Analytical Atomic Spectrometry*, *23*(8), 1093–1101. doi: 10.1039/b804760j

Huntting, M. T., Bennett, W. A. G., Livingston, V. E. J., & Moen, W. S. (1961). *Geologic Map of Washington* (Tech. Rep.). Olympia, Washington: Washington Division of Mines and Geology.

Hutter, I. (1997). *The Wallula Fault Zone: A Study of the Structure and Tectonic History of a Portion of the Olympic-Wallowa Lineament* (M.S. Thesis). Western Washington University.

Irving, E. (1979). Paleopoles and paleolatitudes of North America and speculations about displaced terrains. *Canadian Journal of Earth Sciences*, *16*(3), 669–694. Retrieved from `http://dx.doi.org/10.1139/e79-065` doi: 10.1139/e79-065

Isola, I., Mazzarini, F., Bonini, M., & Corti, G. (2014). Spatial variability of volcanic features in early-stage rift settings: The case of the Tanzania Divergence, East African rift system. *Terra Nova*, *26*(6), 461–468. doi: 10.1111/ter.12121

Jarboe, N. A., Coe, R. S., Renne, P. R., Glen, J. M., & Mankinen, E. A. (2008). Quickly erupted volcanic sections of the Steens Basalt, Columbia River Basalt Group: Secular variation, tectonic rotation, and the Steens Mountain reversal. *Geochemistry, Geophysics, Geosystems*, *9*(11). doi: 10.1029/2008GC002067

John, D. a., Wallace, A. R., Ponce, D. a., Fleck, R. B., & Conrad, J. E. (2000). New Perspectives on the Geology and Origin of the Northern Nevada Rift. *U. S. Geological Survey - Geology and Ore Deposits 2000: The Great Basin and Beyond: Geological Society of Nevada Symposium Proceedings, Reno/Sparks, May 15-18, 2000*, *1*, 127–154.

Johnson, D., Hooper, P. R., & Conrey, R. (1999). XRF Analysis of Rocks and Minerals for Major and Trace Elements on a Single Low Dilution Li-tetraborate Fused Bead. *Advances in X-Ray Analysis*, *41*, 843–867.

Johnson, K., Schwartz, J. J., Wooden, J. L., O'Driscoll, L., & Jeffcoat, R. (2011). The Wallowa batholith: New Pb/U (SHRIMP–RG) ages place constraints on arc magmatism and crustal thickening in the Blue Mountains Province, NE Oregon. In *Geological society of america abstracts with programs* (p. 5).

Jolly, R., & Sanderson, D. (1997). A Mohr circle construction for the opening of a pre-existing fracture. *Journal of Structural Geology*, *19*(6), 887–892. Retrieved from `http://linkinghub.elsevier.com/retrieve/pii/S019181419700014X` doi: 10.1016/S0191-8141(97)00014-X

Jolly, R. J. H., & Sanderson, D. J. (1995). Variation in the form and distribution of dykes in the Mull swarm, Scotland. *Journal of Structural Geology*, *17*(11), 1543–1557. doi: 10.1016/0191-8141(95)00046-G

Kahn, M. (2018). *Exhumation across the Idaho-Oregon border: implications for the arc-continent suture and Hells Canyon extensional province* (M.Sc.). University of Wisconsin – Madison.

Kahn, M., Fayon, A. K., & Tikoff, B. (2020). Constraints on the post-orogenic tectonic history along the Salmon River suture zone from low-temperature thermochronology , western Idaho and eastern Oregon. *Rocky Mountain Geology*, *55*(1), 27–54. doi: 10.24872/rmgjournal.55.1.27

Karlstrom, K. E., Coblentz, D., Dueker, K., Ouimet, W., Kirby, E., Van Wijk, J., ... Donahue, M. S. (2012). Mantle-driven dynamic uplift of the Rocky Mountains and Colorado Plateau and its surface response: Toward a unified hypothesis. *Lithosphere*, *4*(1), 3–22. Retrieved from `https://pubs.geoscienceworld.org/lithosphere/article/4/1/3-22/145610` doi: 10.1130/L150.1

Karlstrom, L., Dufek, J., & Manga, M. (2009). Organization of volcanic plumbing through magmatic lensing by magma chambers and volcanic loads. *Journal of Geophysical Research: Solid Earth*, *114*(10), 1–16. doi: 10.1029/2009JB006339

Karlstrom, L., Murray, K. E., & Reiners, P. W. (2019). Bayesian Markov-Chain Monte Carlo Inversion of Low-Temperature Thermochronology Around Two 8 - 10 m Wide Columbia River Flood Basalt Dikes. *Frontiers in Earth Science*, *7*(May). Retrieved from `https://www.frontiersin.org/article/10.3389/feart.2019.00090/full` doi: 10.3389/feart.2019.00090

Karlstrom, L., Paterson, S. R., & Jellinek, A. M. (2017). A reverse energy cascade for crustal magma transport. *Nature Geoscience*, *10*(8), 604–608. Retrieved from `http://www.nature.com/doifinder/10.1038/ngeo2982` doi: 10.1038/ngeo2982

Karlstrom, L., & Richards, M. (2011). On the evolution of large ultramafic magma chambers and timescales for flood basalt eruptions. *Journal of Geophysical Research: Solid Earth*, *116*(8), 1–13. doi: 10.1029/2010JB008159

Karlstrom, L., Wright, H. M., & Bacon, C. R. (2015). The effect of pressurized magma chamber growth on melt migration and pre-caldera vent locations through time at Mount Mazama, Crater Lake, Oregon. *Earth and Planetary Science Letters*, *412*, 209–219. Retrieved from `http://dx.doi.org/10.1016/j.epsl.2014.12.001` doi: 10.1016/j.epsl.2014.12.001

Kasbohm, J., & Schoene, B. (2018). Rapid eruption of the Columbia River flood basalt and correlation with the mid-Miocene climate optimum. *Science Advances*, *4*(9), 1–8. doi: 10.1126/sciadv.aat8223

Kauffman, J., Schmidt, K., Lewis, R., Stewart, D. E., Othberg, K. L., & Garwood, D. L. (2014). *Geologic Map of the Idaho Part of the Grangeville 30 x 60 Minute Quadrangle, and Adjoining Areas of Washington and Oregon* (Tech. Rep.). Moscow, Idaho: Idaho Geological Survey.

Kauffman, J., Schmidt, K., Lewis, R. S., Stewart, D. E., & Othberg, K. L. (2009). Geologic Map of the Idaho Parts of the Orofino and Clarkston 20 x 60 Minute Quadrangle, Idaho. *Idaho Geological Survey Geologic Map 48*, scale 1:100,000.

Ketcham, R. A. (2005). Forward and inverse modeling of low-temperature thermochronometry data. *Reviews in Mineralogy and Geochemistry*, *58*(1), 275–314.

Ketcham, R. A., Gautheron, C., & Tassan-Got, L. (2011). Accounting for long alpha-particle stopping distances in (U-Th-Sm)/He geochronology: Refinement of the baseline case. *Geochimica et Cosmochimica Acta*, *75*(24), 7779–7791. Retrieved from `http://dx.doi.org/10.1016/j.gca.2011.10.011` doi: 10.1016/j.gca.2011.10.011

Kirby, E., Whipple, K., Kirby, E., Studies, C., & Barbara, S. (2001). Quantifying differential rock-uplift rates via stream profile analysis. *Geology*, *29*(5), 415–418. doi: 10.1130/0091-7613(2001)029⟨0415:QDRURV⟩2.0.CO;2

Kirby, E., & Whipple, K. X. (2012). *Expression of active tectonics in erosional landscapes* (Vol. 44). Elsevier Ltd. Retrieved from `http://dx.doi.org/10.1016/j.jsg.2012.07.009` doi: 10.1016/j.jsg.2012.07.009

Kirby, E., Whipple, K. X., Tang, W., & Chen, Z. (2003). Distribution of active rock uplift along the eastern margin of the Tibetan Plateau: Inferences from bedrock channel longitudinal profiles. *Journal of Geophysical Research*, *108*, 2217. doi: 10.1029/2001JB000861

Kneissl, T., Van Gasselt, S., Wendt, L., Gross, C., & Neukum, G. (2011). Layering and degradation of the Rupes Tenuis unit, Mars – a structural analysis south of Chasma Boreale. *Geological Society, London, Special Publications*, *356*(1), 257–279. Retrieved from `http://sp.lyellcollection.org/lookup/doi/10.1144/SP356.13` doi: 10.1144/SP356.13

Kohl, C. P., & Nishiizumi, K. (1992). Chemical isolation of quartz for measurement of in-situ-produced cosmogenic nuclides. *Geochemica et Cosmochimica Acta*, *56*, 3583–3587.

Krumbholz, M., Hieronymus, C. F., Burchardt, S., Troll, V. R., Tanner, D. C., & Friese, N. (2014). Weibull-distributed dyke thickness reflects probabilistic character of host-rock strength. *Nature communications*, *5*, 3272. Retrieved from `http://www.pubmedcentral.nih.gov/articlerender.fcgi?artid=3926007{&}tool=pmcentrez{&}rendertype=abstract` doi: 10.1038/ncomms4272

Kurz, G. A., Schmitz, M. D., Northrup, C. J., & Vallier, T. L. (2017). Isotopic compositions of intrusive rocks from the Wallowa and Olds Ferry arc terranes of northeastern Oregon and western Idaho: Implications for Cordilleran evolution, lithospheric structure, and Miocene magmatism. *Lithosphere*, *9*(2), 235–264. doi: 10.1130/L550.1

Lal, D. (1991). Cosmic ray labeling of erosion surface: in situ nuclide production rates and erosion models. *Earth and Planetary Science Letters*, *104*, 424–439.

LaMaskin, T. A., Dorsey, R. J., Vervoort, J. D., Schmitz, M. D., Tumpane, K. P., & Moore, N. O. (2015). Westward growth of laurentia by pre–late jurassic terrane accretion, Eastern Oregon and Western Idaho, United States. *Journal of Geology*, *123*(3), 233–267. doi: 10.1086/681724

LaMaskin, T. A., Vervoort, J. D., Dorsey, R. J., & Wright, J. E. (2011). Early Mesozoic paleogeography and tectonic evolution of the western United States: Insights from detrital zircon U-Pb geochronology, Blue Mountains Province, northeastern Oregon. *Geological Society of America Bulletin*, *123*(9-10), 1939–1965. doi: 10.1130/B30260.1

Larimer, J. E., Yanites, B. J., Phillips, W., & Mittelstaedt, E. (2018). Late Miocene rejuvenation of central Idaho landscape evolution: A case for surface processes driven by plume-lithosphere interaction. *Lithosphere*, *11*(1), 59–72. doi: 10.1130/l746.1

Lewis, R. S., Link, P. K., Stanford, L., & Long, S. (2012). *Geologic Map of Idaho* (Tech. Rep.). Moscow: Idaho Geological Survey Map 9, scale 1:750,000.

Lindgren, W. (1901). *The gold belt of the Blue Mountains of Oregon*.

Lister, J. R., & Kerr, R. C. (1991). Fluid-mechanical models of crack propagation and their application to magma transport in dykes. *Journal of Geophysical Research*, *96*(B6), 10049. Retrieved from `http://doi.wiley.com/10.1029/91JB00600` doi: 10.1029/91JB00600

Liu, L., & Stegman, D. R. (2011). Segmentation of the Farallon slab. *Earth and Planetary Science Letters*, *311*(1-2), 1–10. Retrieved from `http://dx.doi.org/10.1016/j.epsl.2011.09.027` doi: 10.1016/j.epsl.2011.09.027

Long, S. P. (2012). Magnitudes and spatial patterns of erosional exhumation in the Sevier hinterland, eastern Nevada and western Utah, USA: Insights from a Paleogene paleogeologic map. *Geosphere*, *8*(4), 881–901. doi: 10.1130/GES00783.1

Ludwig, K. (2012). *User's Manual for isopolot 3.75-4.15* (Tech. Rep.). Berkeley, Ca: Berkeley Geochronology Center.

Lustrino, M. (2005). How the delamination and detachment of lower crust can influence basaltic magmatism. *Earth-Science Reviews*, *72*(1-2), 21–38. doi: 10.1016/j.earscirev.2005.03.004

Manduca, C. A., Kuntz, M. A., & Silver, L. T. (1993). Emplacement and deformation history of the western margin of the Idaho batholith near McCall, Idaho: influence of a major terrane boundary. *Geological Society of America Bulletin*, *105*(6), 749–765. doi: 10.1130/0016-7606(1993)105⟨0749:EADHOT⟩2.3.CO;2

Mann, G. M., & Meyer, C. E. (1993). Late Cenozoic structure and correlations to seismicity along the Olympic-Wallowa Lineament, northwest United States. *Geological Society of America Bulletin*, *105*(7), 853–871. doi: 10.1130/0016-7606(1993)105⟨0853:LCSACT⟩2.3.CO;2

Martin, B. S., Petcovic, H. L., & Reidel, S. P. (2005). *Goldschmidt Conference 2005: Field Trip Guide to the Columbia River Basalt Group* (Tech. Rep. No. May). Portland, Oregon: Goldschmidt Conference.

Mathieu, L., van Wyk de Vries, B., Holohan, E. P., & Troll, V. R. (2008). Dykes, cups, saucers and sills: Analogue experiments on magma intrusion into brittle rocks. *Earth and Planetary Science Letters*, *271*(1-4), 1–13. doi: 10.1016/j.epsl.2008.02.020

McCaffrey, R., King, R. W., Payne, S. J., & Lancaster, M. (2013). Active tectonics of northwestern U.S. inferred from GPS-derived surface velocities. *Journal of Geophysical Research: Solid Earth*, *118*(2), 709–723. doi: 10.1029/2012JB009473

McClaughry, J. D., Ferns, M. L., Streck, M. J., Patridge, K., & Gordon, C. L. (2009). Paleogene calderas of central and eastern Oregon: Eruptive sources of widespread tuffs in the John Day and Clarno Formations. In J. O'connor, R. J. Dorsey, & I. P. Madin (Eds.), *Volcanoes and vineyards, geologic field trips through the dynamic landscape of the pacific northwest* (Vol. 15, pp. 407–434). Geological Society of America Field Guide. Retrieved from `http://books.google.com/books?hl=en{&}lr={&}id=Cy9ErSxZFhQC{&}oi=fnd{&}pg=PA237{&}dq=Cataclysms+and+controversy+\OT1\textemdash+Aspects+of+the+geomorphology+of+the+Columbia+River+Gorge{&}ots=rA4EzUMRD5{&}sig=pq4qnSqi8rsQ5nRevRstHcap7RE` doi: 10.1130/2009.fl

McQuarrie, N., & Wernicke, B. P. (2005). An animated tectonic reconstruction of southwestern north america since 36 Ma. *Geosphere*, *1*(3), 147–172. doi: 10.1130/GES00016.1

Mège, D., & Korme, T. (2004). Dyke swarm emplacement in the Ethiopian Large Igneous Province: Not only a matter of stress. *Journal of Volcanology and Geothermal Research*, *132*(4), 283–310. doi: 10.1016/S0377-0273(03)00318-4

Menand, T., Daniels, K. A., & Benghiat, P. (2010). Dyke propagation and sill formation in a compressive tectonic environment. *Journal of Geophysical Research: Solid Earth*, *115*(8), 1–12. doi: 10.1029/2009JB006791

Meyer, G. A., Fawcett, P. J., & Locke, W. W. (2004). Late-Pleistocene Equilibrium-Line Altitudes, Atmospheric Circulation, and Timing of Mountain Glacier Advances in the Interior Northwestern United States. *Geological Field Trips in Southern Idaho, Eastern Oregon, and Northern Nevada, Open-File Report 2004-1222*, 63–68. Retrieved from `https://pubs.usgs.gov/of/2004/1222/chapters/Ch4.pdf`

Michaels, Z. D., Davenport, K., & Hole, J. A. (2017). Exploring the western Idaho shear zone using the StraboSpot data system. In R. Haugerud & H. M. Kelsey (Eds.), *From the puget lowland to east of the cascade range: Geologic excursions in the pacific northwest. geolgoical society of america field guide.* (Vol. 49, pp. 229–254). doi: 10.1130/2017.0049(10).

Michel, L., Ehlers, T. A., Glotzbach, C., Adams, B. A., & Stübner, K. (2018). Tectonic and glacial contributions to focused exhumation in the Olympic Mountains, Washington, USA. *Geology*, *46*(6), 491–494. doi: 10.1130/G39881.1

Miller, J. M. L., Nelson, E. P., Hitzman, M., Muccilli, P., & Hall, W. D. (2007). Orthorhombic fault-fracture patterns and non-plane strain in a synthetic transfer zone during rifting: Lennard shelf, Canning basin, Western Australia. *Journal of Structural Geology*, *29*(6), 1002–1021. doi: 10.1016/j.jsg.2007.01.004

Miller, S. R., Sak, P. B., Kirby, E., & Bierman, P. R. (2013). Neogene rejuvenation of central Appalachian topography: Evidence for differential rock uplift from stream profiles and erosion rates. *Earth and Planetary Science Letters*, *369-370*, 1–12. Retrieved from `http://dx.doi.org/10.1016/j.epsl.2013.04.007` doi: 10.1016/j.epsl.2013.04.007

Mitchell, N., & Yanites, B. (2019). Spatially variable increase in rock uplift in the northern U.S. Cordillera recorded in the distribution of river knickpoints and incision depths. *Journal of Geophysical Research: Earth Surface*, *124*, 1238–1260. Retrieved from `https://doi.org/10.1029/2018JF004880` doi: 10.1029/2018JF004880

Mitchell, S., & Reiners, P. W. (2003). Influence of wildfires on apatite and zircon (U-Th)/He ages. *Geology*(12), 1025–1028. Retrieved from `http://dialnet.unirioja.es/servlet/articulo?codigo=780854` doi: 10.1130/G19758.1

Montgomery, D. R. (2001). Slope distributions, threshold hillslopes, and steady-state topography. *American Journal of Science*, *301*(4-5), 432–454. doi: 10.2475/ajs.301.4-5.432

Moon, S., Page Chamberlain, C., Blisniuk, K., Levine, N., Rood, D. H., & Hilley, G. E. (2011). Climatic control of denudation in the deglaciated landscape of the Washington Cascades. *Nature Geoscience*, *4*(7), 469–473. Retrieved from `http://dx.doi.org/10.1038/ngeo1159` doi: 10.1038/ngeo1159

Moore, N. E., Grunder, A. L., & Bohrson, W. A. (2018). The three-stage petrochemical evolution of the Steens Basalt (southeast Oregon, USA) compared to large igneous provinces and layered mafic intrusions. *Geosphere*, *14*(6), 2505–2532. doi: 10.1130/GES01665.1

Morgan, L. A., & McIntosh, W. C. (2005). Timing and development of the Heise volcanic field, Snake River Plain, Idaho, western USA. *Bulletin of the Geological Society of America*, *117*(3-4), 288–306. doi: 10.1130/B25519.1

Morriss, M., Karlstrom, L., Nasholds, M. W., & Wolff, J. A. (2020). The Chief Joseph Dike Swarm of the Columbia River Flood Basalts, and the Legacy Dataset of William H. Taubeneck. *Geosphere*, *16*(X), In Press. doi: 10.1130/GES02173.1/5019688/ges02173.pdf

Morriss, M. C., & Wegmann, K. W. (2017). Geomorphology of the Burnt River, eastern Oregon, USA: Topographic adjustments to tectonic and dynamic deformation. *Geomorphology*, *278*, 43–59. doi: 10.1016/j.geomorph.2016.09.015

Moucha, R., Forte, A. M., Rowley, D. B., Mitrovica, J. X., Simmons, N. A., & Grand, S. P. (2009). Deep mantle forces and the uplift of the Colorado Plateau. *Geophysical Research Letters*, *36*(19), 1–6. doi: 10.1029/2009GL039778

Muller, O. H. (1986). Changing stresses during emplacement of the radial dike swarm at Spanish Peaks, Colorado, (USA). *Geology*, *14*(2), 157–159. doi: 10.1130/0091-7613(1986)14⟨157:CSDEOT⟩2.0.CO;2

Muller, O. H., & Pollard, D. D. (1977). The stress state near Spanish Peaks, colorado determined from a dike pattern. *Pure and Applied Geophysics PAGEOPH*, *115*(1-2), 69–86. doi: 10.1007/BF01637098

Munro, M. A., & Blenkinsop, T. G. (2012). MARD-A moving average rose diagram application for the geosciences. *Computers and Geosciences*, *49*, 112–120. Retrieved from `http://dx.doi.org/10.1016/j.cageo.2012.07.012` doi: 10.1016/j.cageo.2012.07.012

Murray, K. E., Braun, J., & Reiners, P. W. (2018). Toward Robust Interpretation of Low-Temperature Thermochronometers in Magmatic Terranes. *Geochemistry, Geophysics, Geosystems*, *19*(10), 3739–3763. doi: 10.1029/2018GC007595

Nielson, M., Lohman, K., Daugherty, C. H., Allendorf, F. W., Knudsen, K. L., Sullivan, J., ... Belan, I. (2006). Allozyme and Mitochondrial Dna Variation in the Tailed Frog (Anura: Ascaphus): the Influence of Geography and Gene Flow. *Herpetologica*, *62*(3), 235–258. doi: 10.1655/0018-0831(2006)62[235:aamdvi]2.0.co;2

Niemann, J. D., Gasparini, N. M., Tucker, G. E., & Bras, R. L. (2001). A quantitative evaluation of playfair's law and its use in testing long-term stream erosion models. *Earth Surface Processes and Landforms*, *26*(12), 1317–1332. doi: 10.1002/esp.272

Nishiizumi, K., Winterer, E., Kohl, C., Klein, J., Middleton, R., Lal, D., & Arnold, J. R. (1989). Cosmic ray production rates of 10Be and 26Al in quartz from glacially polished rocks. *Journal of Geophysical Research*, *94*(B12), 17907–17915. doi: 10.1029/jb094ib12p17907

Norris, T. L., Gancarz, A. J., Roico, D. J., & Thomas, K. W. (1983). Half-Life of 26A1: Proceedings of the Fourteenth Lunar and Planetary Science Conference, Part I. *Journal of Geophysical Research*, *88*, 331–333.

Othberg, K. L. (1994). Geology and geomorphology of the Boise Valley and adjoining areas, western Snake River Plain, Idaho. *Idaho Geological Survey Bulletin*, *29*, 54 p.

Ouimet, W. B., Whipple, K. X., & Granger, D. E. (2009). Beyond threshold hillslopes: Channel adjustment to base-level fall in tectonically active mountain ranges. *Geology*, *37*(7), 579–582. doi: 10.1130/G30013A.1

Paces, J., & Miller, J. D. J. (1999). Precise U-Pb Ages of Duluth Complex and related mafic intrusions, Northeastern Minnesota: Geochronological Insights to Physical, Petrogenetic, and Paleomagnetic, and Tectonomagmatci Processes Associated with the 1.1 Ga Midcontinent Rift System. *Journal of Geophysical Research*, *98*(93), 13997–14013.

Paquet, F., Dauteuil, O., Hallot, E., & Moreau, F. (2007). Tectonics and magma dynamics coupling in a dyke swarm of Iceland. *Journal of Structural Geology*, *29*(9), 1477–1493. doi: 10.1016/j.jsg.2007.06.001

Parfitt, E. A., & Wilson, L. (1994). The 1983-86 Pu'u 'O'o eruption of Kilauea Volcano, Hawaii: a study of dike geometry and eruption mechanisms for a long-lived eruption. *Journal of Volcanology and Geothermal Research*, *59*(3), 179–205. doi: 10.1016/0377-0273(94)90090-6

Passarelli, L., Rivalta, E., & Shuler, A. (2014). Dike intrusion during rifting episodes obey scaling relationships similar to earthquakes. *Scientific Reports*, *4*, 7 p. doi: 10.1038/srep03886

Paton, C., Hellstrom, J., Paul, B., Woodhead, J., & Hergt, J. (2011). Iolite: Freeware for the visualisation and processing of mass spectrometric data. *Journal of Analytical Atomic Spectrometry*, *26*(12), 2508–2518. doi: 10.1039/c1ja10172b

Pederson, J. L., Anders, M. D., Rittenhour, T. M., Sharp, W. D., Gosse, J. C., & Karlstrom, K. E. (2006). Using fill terraces to understand incision rates and evolution of the Colorado River in eastern Grand Canyon, Arizona. *Journal of Geophysical Research: Earth Surface*, *111*(2), 1–10. doi: 10.1029/2004JF000201

Perron, J. T., & Royden, L. (2013). An integral approach to bedrock river profile analysis. *Earth Surface Processes and Landforms*, *38*(6), 570–576. doi: 10.1002/esp.3302

Perry-houts, J., & Karlstrom, L. (2019). Anisotropic viscosity and time-evolving lithospheric instabilities due to aligned igneous intrusions. *Geophysical Journal International*, *216*, 794–802. doi: 10.1093/gji/ggy466

Petcovic, H., & Grunder, A. (2003). Textural and Thermal History of Partial Melting in Tonalitic Wallrock at the Margin of a Basalt Dike, Wallowa Mountains, Oregon. *Journal of Petrology*, *44*(12), 2287–2312. doi: 10.1093/petrology/egg078

Petcovic, H. L., & Dufek, J. D. (2005). Modeling magma flow and cooling in dikes: Implications for emplacement of Columbia River flood basalts. *Journal of Geophysical Research: Solid Earth*, *110*(10), 1–15. doi: 10.1029/2004JB003432

Petford, N., Kerr, R. C., & Lister, J. R. (1993). Dike transport of granitoid magmas. *Geology*, *21*(9), 845–848.

Pierce, K. L., & Morgan, L. A. (2009). Is the track of the Yellowstone hotspot driven by a deep mantle plume ? — Review of volcanism , faulting , and uplift in light of new data. *Journal of Volcanology and Geothermal Research*, *188*(1-3), 1–25. Retrieved from `http://dx.doi.org/10.1016/j.jvolgeores.2009.07.009` doi: 10.1016/j.jvolgeores.2009.07.009

Pinel, V., Carrara, A., Maccaferri, F., Rivalta, E., & Corbi, F. (2017). A two-step model for dynamical dike propagation in two dimensions: Application to the July 2001 Etna eruption. *Journal of Geophysical Research: Solid Earth*, *122*(2), 1107–1125. doi: 10.1002/2016JB013630

Pollard, D. D., Segall, P., & Delaney, P. T. (1982). Formation and interpretation of dilatant echelon cracks. *Geological Society of America Bulletin*, *93*(12), 1291–1303. doi: 10.1130/0016-7606(1982)93⟨1291:FAIODE⟩2.0.CO

Polyak, V., Hill, C., & Asmerom, Y. (2008). Age and Evolution of the Grand Canyon Revealed by U-Pb Dating of Water Table–Type Speleothems. *Science*, *319*(7), 1377–1380.

Powell, J. (1875). *Exploration of the Colorado River of the West and its Tributaries: Explored in 1869, 1870, 1871, and 1872* (U. G. P. Office, Ed.). Washington, D.C..

Reches, Z. (1978). Analysis of faulting in three-dimensional strain field. *Tectonophysics*, *47*(1-2), 109–129. doi: 10.1016/0040-1951(78)90154-3

Reches, Z. (1983). Faulting of Rocks in Three-Dimensional Strain Fields Ii. Theoretical Analysis. *Tectonophysics*, *95*, 133–156. Retrieved from http://www.sciencedirect.com/science/article/pii/0040195183902640 doi: 10.1016/0040-1951(83)90264-0

Reichen, L., & Fahey, J. (1962). An Improved Method for the Determination of FeO in Rocks and Minerals Including Garnet. *U.S. Geologic Survey Bulletin*, *1144B*, pp. 1–5.

Reidel, S. (1982). Stratigraphy of the Grande Ronde Basalt , Columbia River Basalt Group , From the Lower Salmon River and Northern Hells Canyon Area, Idaho, Oregon and Washington. *Cenozoic Geology of Idaho: Idaho Bureau of Mines and Geology Bulletin*, *26*, 77–101. Retrieved from http://geology.isu.edu/Digital{_}Geology{_}Idaho/papers/B-26ch2-2.pdf

Reidel, S. P., Camp, V. E., Martin, B. S., Tolan, T. L., & Wolff, J. A. (2016). The Columbia River Basalt Group of western Idaho and eastern Washington—Dikes, vents, flows, and tectonics along the eastern margin of the flood basalt province. In R. S. Lewis & K. L. Schmidt (Eds.), *Exploring the geology of the inland northwest* (Field Guid ed., pp. 127–150). Boulder, Colorado: The Geological Society of America. doi: 10.1130/2016.0041(04)

Reidel, S. P., Camp, V. E., Tolan, T. L., & Martin, B. S. (2013). The Columbia River flood basalt province: Stratigraphy, areal extent, volume, and physical volcanology. *Geological Society of America Special Papers*, *497*(01), 1–43. doi: 10.1130/2013.2497(01).

Reidel, S. P., & Tolan, T. L. (2013a). The Grande Ronde Basalt , Columbia River Basalt Group. *Geological Society of America Special Papers*, *497*(05), 117–153. doi: 10.1130/2013.2497(05).For

Reidel, S. P., & Tolan, T. L. (2013b). The late Cenozoic evolution of the Columbia River system in the Columbia River flood basalt province. In S. P. Reidel, V. E. Camp, M. E. Ross, J. Wolff, T. Tolan, & R. E. Wells (Eds.), *The columbia river flood basalt province* (pp. 201–230). Geological Society of America Special Paper 497. doi: 10.1130/2013.2497(08)

Reiners, P. W. (2005). Zircon (U-Th)/He Thermochronometry. *Reviews in Mineralogy and Geochemistry*, *58*(1), 151–179. Retrieved from http://rimg.geoscienceworld.org/cgi/doi/10.2138/rmg.2005.58.6 doi: 10.2138/rmg.2005.58.6

Reiners, P. W., & Brandon, M. T. (2006). Using Thermochronology To Understand Orogenic Erosion. *Annual Review of Earth and Planetary Sciences*, *34*(1), 419–466. Retrieved from http://www.annualreviews.org/doi/10.1146/annurev.earth.34.031405.125202 doi: 10.1146/annurev.earth.34.031405.125202

Reiners, P. W., Campbell, I. H., Nicolescu, S., Allen, C. M., Hourigan, J. K., Garver, J. I., ... Cowan, D. S. (2005). (U-Th)/(He-Pb) double dating of detrital zircons. *American Journal of Science*, *305*(4), 259–311. doi: 10.2475/ajs.305.4.259

Ridley, V. A., & Richards, M. A. (2010). Deep crustal structure beneath large igneous provinces and the petrologic evolution of flood basalts. *Geochemistry, Geophysics, Geosystems*, *11*(9), 1–21. doi: 10.1029/2009GC002935

Rivalta, E., Taisne, B., Bunger, A. P., & Katz, R. F. (2015). A review of mechanical models of dike propagation: Schools of thought, results and future directions. *Tectonophysics*, *638*(C), 1–42. Retrieved from `http://dx.doi.org/10.1016/j.tecto.2014.10.003` doi: 10.1016/j.tecto.2014.10.003

Robl, J., Hergarten, S., & Stüwe, K. (2008). Morphological analysis of the drainage system in the Eastern Alps. *Tectonophysics*, *460*(1-4), 263–277. Retrieved from `http://dx.doi.org/10.1016/j.tecto.2008.08.024` doi: 10.1016/j.tecto.2008.08.024

Rodriguez, S., & Sen, G. (2013). Eruption of the Grande Ronde Basalt lavas, Columbia River Basalt Group: Results of numerical modeling. In S. P. Reidel et al. (Eds.), *The columbia river flood basalt province* (Vol. 497, pp. 259–272). Geological Society of America Special Paper 497. doi: 10.1130/2013.2497(10)

Roe, G. H., Montgomery, D. R., & Hallet, B. (2003). Orographic precipitation and the relief of mountain ranges. *Journal of Geophysical Research: Solid Earth*, *108*(B6). doi: 10.1029/2001jb001521

Rohrmann, A., Schwanghart, W., & Kirby, E. (2018). Yangtze upstream-river network expansion reveals potential top-down incision. In *American geophysical union* (pp. abstract #EP53A–03). Washington, D.C..

Rosenbloom, N. A., & Anderson, R. S. (1994). Hillslope and channel evolution in a marine terraced landscape, Santa Cruz, California. *Journal of Geophysical Research: Solid Earth*, *99*(B7), 14013–14029. Retrieved from `http://doi.wiley.com/10.1029/94JB00048` doi: 10.1029/94JB00048

Royden, L., & Perron, T. (2013). Solutions of the stream power equation and application to the evolution of river longitudinal profiles. *Journal of Geophysical Research: Earth Surface*, *118*(2), 497–518. doi: 10.1002/jgrf.20031

Rubin, A. M. (1995). Propagation of Magma Filled Cracks. *Annual Review of Earth and Planetary Sciences*, *23*, 287–336.

Sadler, J., & Link, P. (1996). The Tuana Gravel: Early Pleistocene response to longitudinal drainage of a late-stage rift basin, western Snake River Plain, Idaho. *Northwest Geology*, *26*, 46–62.

Schildgen, T. F., Hodges, K. V., Whipple, P. W., Reiners, P. W., & Pringle, M. S. (2007). Uplift of the western margin of the Andean plateau revealed from canyon incision history, southern Peru. *Geology*, *35*(6), 523–526. doi: 10.1130/G23532A.1

Schmitz, M. D., & Bowring, S. A. (2001). U-Pb zircon and titanite systematics of the Fish Canyon Tuff: An assessment of high-precision U-Pb geochronology and its application to young volcanic rocks. *Geochimica et Cosmochimica Acta*, *65*(15), 2571–2587. doi: 10.1016/S0016-7037(01)00616-0

Schoettle-Greene, P., & Duvall, A. (2016). Mantle plumes and lithospheric foundering:Determining the timing and amplitude of post-Miocene uplift in the Wallowa mountains, north-east Oregon with low-temperature thermochronometry. *AGU Fall Meeting T33B-3031*.

Schuster, E. (2005). *Geologic Map of Washington* (Tech. Rep.). Olympia Washington: Washington State Department of Natural Resources, Division of Geology and Earth Resources.

Schwanghart, W., & Scherler, D. (2014). Short Communication: TopoToolbox 2 - MATLAB-based software for topographic analysis and modeling in Earth surface sciences. *Earth Surface Dynamics*, *2*(1), 1–7. doi: 10.5194/esurf-2-1-2014

Schwartz, J. J., Johnson, K., Mueller, P., Valley, J., Strickland, A., & Wooden, J. L. (2014). Time scales and processes of Cordilleran batholith construction and high-Sr/Y magmatic pulses: Evidence from the Bald Mountain batholith, northeastern Oregon. *Geosphere*, *10*(6), 1456–1481. doi: 10.1130/GES01033.1

Self, S. (2006). The effects and consequences of very large explosive volcanic eruptions. *Philosophical Transactions of the Royal Society A: Mathematical, Physical and Engineering Sciences*, *364*(1845), 2073–2097. doi: 10.1098/rsta.2006.1814

Seligman, A. N., Bindeman, I. N., McClaughry, J., Stern, R. a., & Fisher, C. (2014). The earliest low and high δ18O caldera-forming eruptions of the Yellowstone plume: implications for the 30-40 Ma Oregon calderas and speculations on plume-triggered delaminations. *Frontiers in Earth Science*, *2*(November), 1–9. Retrieved from `http://journal.frontiersin.org/article/10.3389/feart.2014.00034/abstract` doi: 10.3389/feart.2014.00034

Shaw, H. (1980). The fracture mechanisms of magma transport from the mantle to the surface. In R. Hargraves (Ed.), *Physics of magmatic processes* (pp. 201–264). Princeton, N.J.: Princeton Univ. Press.

Shuster, D. L., Flowers, R. M., & Farley, K. A. (2006). The influence of natural radiation damage on helium diffusion kinetics in apatite. *Earth and Planetary Science Letters*, *249*(3-4), 148–161. doi: 10.1016/j.epsl.2006.07.028

Silverman, B. (1986). *Density Estimation for Statistics and Data Analysis*. New York: Chapman and Hall.

Sláma, J., Košler, J., Condon, D. J., Crowley, J. L., Gerdes, A., Hanchar, J. M., ... Whitehouse, M. J. (2008). Plešovice zircon - A new natural reference material for U-Pb and Hf isotopic microanalysis. *Chemical Geology*, *249*(1-2), 1–35. doi: 10.1016/j.chemgeo.2007.11.005

Sleep, N. H. (2008). Channeling at the base of the lithosphere during the lateral flow of plume material beneath flow line hot spots. *Geochemistry, Geophysics, Geosystems*, *9*(8). doi: 10.1029/2008GC002090

Smith, G., Morgan, N., & Gustafson, E. (2002). Fishes of the Mio-Pliocene Ringold Formation, Washington: Pliocene capture of the Snake River by the Columbia River. *University of Michigan Museum Paleontology Papers*, *32*, 1–47. doi: 10.1007/s13398-014-0173-7.2

Smith, G., Unmack, P., Markle, D., Chow, J., & Dowling, T. (2017). Fishes of the Mio-Pliocene Western Snake River Plain and Vicinity. *University of Michigan Museum Paleontology Papers*, *204*(2), 1–46. Retrieved from `https://deepblue.lib.umich.edu/handle/2027.42/136783`

Snavely, P., MacLeod, N., & Wagner, L. S. (1968). Tholeiitic and alkalic basalts of the Eocene Siletz River volcanics, Oregon Coast Range. *American Journal of Science*, *266*, 454–481.

Sneddon, I., & Lowengrub, M. (1969). *Crack Problems in the Classical Theory of Elasticity*. New York: Wiley.

Snee, L. W., Lund, K., Sutter, J. F., Balcer, D. E., & Evans, K. V. (1995). An (40) Ar/ (39) Ar chronicle of the tectonic development of the Salmon River suture zone, western Idaho. *USGS Professional Paper*, *1438*, 359–414.

Sparks, R. S. J., Huppert, H. E., Turner, J. S., Sakuyama, M., & O'Hara, M. J. (1984). The Fluid Dynamics of Evolving Magma Chambers. *Philosophical Transactions of the Royal Society A: Mathematical, Physical and Engineering Sciences*, *310*(1514), 511–534. Retrieved from `http://rsta.royalsocietypublishing.org/cgi/doi/10.1098/rsta.1984.0006` doi: 10.1098/rsta.1984.0006

Spruell, P., Hemmingsen, A. R., Howell, P. J., Kanda, N., & Allendorf, F. W. (2003). Conservation genetics of bull trout: Geographic distribution of variation at microsatellite loci. *Conservation Genetics*, *4*(1), 17–29. doi: 10.1023/A:1021841000262

Staisch, L., Blakely, R., Kelsey, H., Styron, R., & Sherrod, B. (2018). Crustal Structure and Quaternary Acceleration of Deformation Rates in Central Washington Revealed by Stream Profile Inversion, Potential Field Geophysics, and Structural Geology of the Yakima Folds. *Tectonics*, *37*(6), 1750–1770. doi: 10.1029/2017TC004916

Staisch, L., Kelsey, H., Sherrod, B., Möller, A., Paces, J., Blakely, R., & Styron, R. (2017). Miocene-Pleistocene deformation of the Saddle Mountains: Implications for seismic hazard in central Washington, USA. *Bulletin of the Geological Society of America*, *130*(3-4), 411–437. doi: 10.1130/B31783.1

Staisch, L., O'Connor, J., Holm-Denoma, C., Lasher, J. P., & Alexander, J. (2019). RINGOLD FORMATION SEDIMENTOLOGY, PALEONTOLOGY, AND PROVENANCE: IMPLICATIONS FOR THE ANCESTRAL RIVERS OF THE PACIFIC NORTHWEST. *Geological Society of America Abstracts Programs*, *51*(4).

Stanley, Jr., G. D., McRoberts, C. a., & Whalen, M. T. (2008). Stratigraphy of the Triassic Martin Bridge Formation , Wallowa terrane : Stratigraphy and depositional setting. In R. Blodgett & G. Stanley (Eds.), *The terrane puzzle: New perspectives on paleontology and stratigraphy from the north american cordillera* (Vol. 442, pp. 227–250). Boulder, Colorado: Geological Society of America Special Paper 442. doi: 10.1130/2008.442(12).

Stock, G. M., Anderson, R. S., & Finkel, R. C. (2005). Rates of erosion and topographic evolution of the Sierra Nevada, California, inferred from cosmogenic 26Al and 10Be concentrations. *Earth Surface Processes and Landforms*, *30*(8), 985–1006. doi: 10.1002/esp.1258

Stockli, D. F., Dumitru, T. A., Mcwilliams, M. O., & Farley, K. A. (2003). Cenozoic tectonic evolution of the White Mountains, California and Nevada. *GSA Bulletin*, *115*(4), 788–816. doi: 10.1130/0016-7606(2003)115⟨0788:CTEOTW⟩2.0.CO;2

Stone, J. O. (2000). Air pressure and cosmogenic isotope production. *Journal of Geophysical Research,*, *105*(1), 753–759.

Stüwe, K. (2007). *Geodynamics of the Lithosphere* (2nd ed.). Heidelberg: Springer-Verlag.

Svensen, H., Planke, S., Polozov, A. G., Schmidbauer, N., Corfu, F., Podladchikov, Y. Y., & Jamtveit, B. (2009). Siberian gas venting and the end-Permian environmental crisis. *Earth and Planetary Science Letters*, *277*(3-4), 490–500. Retrieved from http://dx.doi.org/10.1016/j.epsl.2008.11.015 doi: 10.1016/j.epsl.2008.11.015

Swanson, D., Wright, T. L., Camp, V. E., Gardner, J., Helz, R., Price, S., ... Ross, M. E. (1980). *Reconnaissance geologic map of the Columbia River Basalt Group, Pullman and Walla Walla Quadrangles, southeast Washington and adjacent Idaho* (Tech. Rep.). Vancouver, Wa: U.S. Geological Survey.

Swanson, D. A., Wright, T. L., & Helz, R. T. (1975). *Linear vent systems and estimated rates of magma production and eruption for the Yakima Basalt on the Columbia Plateau* (Vol. 275). doi: 10.2475/ajs.275.8.877

Swanson, D. A., Wright, T. L., Hooper, P. R., & Bentley, R. D. (1979). Revisions in Stratigraphic Nomenclature of the Columbia River Basalt Group. *U.S. Geologic Survey Bulletin*, *1457-G*, 59 p.

Taubeneck, W. H. (1970). Dikes of the Columbia River Basalt in Northeastern Oregon, Western Idaho, and Southeastern Washington. In E. Gilmour & D. Stradling (Eds.), *Proceedings of the 2nd columbia river basalt symposium* (pp. 73–96). Cheney, Washington: Eastern Washington State Press.

Taubeneck, W. H. (1990). Significant discoveries during 1989 involving dikes of Columbia River Basalt in pre-Tertiary rocks in eastern Oregon (OR) and western Idaho (ID). *Geological Society of America Abstracts with Programs*, *22*(3), 88.

Taubeneck, W. H. (1997). Preferential occurrence of eruptive axes of dikes of the Columbia River Basalt Group in unmetamorphosed Mesozoic granitic intrusives, with 40Ar/39Ar dates for four dikes and two of the earliest flows of basalt northeast Oregon and western Idaho. *Geological Society of America Abstracts Programs*, *29*, p. 48.

Thiede, R. C., & Ehlers, T. A. (2013). Large spatial and temporal variations in Himalayan denudation. *Earth and Planetary Science Letters*, *371-372*(October), 278–293. Retrieved from http://dx.doi.org/10.1016/j.epsl.2013.03.004 doi: 10.1016/j.epsl.2013.03.004

Thordarson, T., & Self, S. (2003). Atmospheric and environmental effects of the 1783–1784 Laki eruption: A review and reassessment. *Journal of Geophysical Research*, *108*(D1), 4011. Retrieved from http://doi.wiley.com/10.1029/2001JD002042 doi: 10.1029/2001JD002042

Tikoff, B., Kelso, P., Manduca, C. A., Markley, M., & Gillaspy, J. (2001). Lithospheric and crustal reactivation of an ancient plate boundary: the assembly and disassembly of the Salmon River suture zone, Idaho, USA. In R. Holdsworth, R. Strachan, J. Magloughlin, & R. Knipe (Eds.), *The nature and tectonic significance of fault zone weakening* (Vol. 186, pp. 213–231). The geological society of London. doi: 10.1016/j.avsg.2015.06.050

Tolan, T. L., Lindsey, K., & Beeson, M. (1996). Neogene paleodrainage implications of exotic clast lithologies in the Chenoweth (Dalles) formation, Oregon – Rediscovery of old truths about the Dalles Formation. *Geological Society of America Abstracts with Programs1*, *27*(5), 118.

Tolan, T. L., Reidel, S. P., Beeson, M., Anderson, J., Fecht, K., & Swanson, D. (1989). Revisions to the esimates of the areal extent and volume of the Columbia River Basalt Group. In S. P. Reidel & P. R. Hooper (Eds.), *Volcanism and tectonism in the columbia river flood-basalt province* (Vol. 239). Boulder, Colorado.

Townsend, M. R., Pollard, D. D., & Smith, R. P. (2017). Mechanical models for dikes: A third school of thought. *Tectonophysics*, *703-704*, 98–118. Retrieved from `http://dx.doi.org/10.1016/j.tecto.2017.03.008` doi: 10.1016/j.tecto.2017.03.008

Tucker, G. E., & Whipple, K. X. (2002). Topographic outcomes predicted by stream erosion models: Sensitivity analysis and intermodel comparison. *Journal of Geophysical Research: Solid Earth*, *107*(B9), ETG 1–1–ETG 1–16. Retrieved from `http://doi.wiley.com/10.1029/2001JB000162` doi: 10.1029/2001JB000162

Umpleby, J. B. (1912). An Old Erosion Surface in Idaho: Its Age and Value as a Datum Plane. *The Journal of Geology*, *20*(2), 139–147. doi: 10.1086/621941

Vallier, T. L. (1974). *Preliminary report on the geology of the Snake River Canyon* (Tech. Rep.). Portland, Oregon: Oregon Department of Geology and Mineral Industries.

Vallier, T. L. (1977). *The Permian and Triassic Seven Devils Group, Western Idaho and Northeastern Oregon* (Vol. 1437).

Vallier, T. L. (1995). Petrology of pre-Tertiary igneous rocks in the Blue Mountains region of Oregon, Idaho, and Washington; implications for the geologic evolution of a complex island arc. In T. L. Vallier & H. Brooks (Eds.), *Geology of the blue mountains region of oregon, idaho, and washington: petrology and tectonic evolution of pre-tertiary rocks of the blue mountains region* (pp. 125–209). U.S. Geological Survey Professional paper 1438.

Vallier, T. L., Schmidt, K. L., & Lamaskin, T. A. (2016). Geology of the Wallowa Terrane, Blue Mountains Province, in the northern part of Hells Canyon, Idaho, Washignton, and Oregon. In R. S. Lewis & K. L. Schmidt (Eds.), *Exploring the geology of the inland northwest* (Vol. 41, pp. 211–249). The Geological Society of America. doi: 10.1130/2016.0041(07).

Van Tassell, J., Ferns, M., McConnell, V., & Smith, G. (2001). The mid-Pliocene Imbler fish fossils , Grande Ronde Valley , Union County , Oregon , and the connection between Lake Idaho and the Columbia River. *Oregon Geology*, *63*(3), 77–96.

Wadge, G. (1980). Output rate of magma from active central volcanoes. *Nature*, *288*(5788), 253–255. doi: 10.1038/288253a0

Walker, G., & MacLeod. (1991). Geologic map of Oregon. *U.S. Geologic Survey*, scale 1:500,000.

Wallace, R., & Calkins, J. (1956). *Reconnaissance geologic map of the Izee and Logdell quadrangles, Oregon* (Tech. Rep.). Denver, Colorado: U.S. Geological Survey.

Wells, R., Bukry, D., Friedman, R., Pyle, D., Duncan, R., Haeussler, P., & Wooden, J. (2014). Geologic history of Siletzia, a large igneous province in the Oregon and Washington Coast Range: Correlation to the geomagnetic polarity time scale and implications for a long-lived Yellowstone hotspot. *Geosphere*, *10*(4), 692–719. doi: 10.1130/GES01018.1

Wheeler, H. E., & Cook, E. F. (1954). Structural and Stratigraphic Significance of the Snake River Capture, Idaho-Oregon. *The Journal of Geology*, *62*(6), 525–536. doi: 10.1086/626205

Whipple, K. X. (2002). Implications of sediment-flux-dependent river incision models for landscape evolution. *Journal of Geophysical Research*, *107*(B2), 2039. Retrieved from `http://doi.wiley.com/10.1029/2000JB000044` doi: 10.1029/2000JB000044

Whipple, K. X. (2004). Bedrock Rivers and the Geomorphology of Active Orogens. *Annual Review of Earth and Planetary Sciences*, *32*(1), 151–185. Retrieved from `http://www.annualreviews.org/doi/10.1146/annurev.earth.32.101802.120356` doi: 10.1146/annurev.earth.32.101802.120356

Whipple, K. X., & Tucker, G. E. (1999). Dynamics of the stream-power river incision model: Implications for height limits of mountain ranges, landscape response timescales, and research needs. *Journal of Geophysical Research: Solid Earth*, *104*(B8), 17661–17674. Retrieved from `http://doi.wiley.com/10.1029/1999JB900120` doi: 10.1029/1999JB900120

White, D., & Vallier, T. L. (1994). Geologic evolution of the Pittsburgh Landing Area, Snake River Canyon, Oregon and Idaho. In T. L. Vallier & H. Brooks (Eds.), *Stratigraphy, physiography, and mineral resources of the blue mountains region* (pp. 55–74). Reston, Virginia: U.S. Geological Survey Professional paper 1439.

White, J. D., White, D. L., Vallier, T., Stanley, G. D., & Ash, S. R. (1992). Middle Jurassic strata link Wallowa, Olds Ferry, and Izee terranes in the accreted Blue Mountains island arc, northeastern Oregon. *Geology*, *20*(8), 729–732. doi: 10.1130/0091-7613(1992)020⟨0729:MJSLWO⟩2.3.CO;2

White, S. M., Crisp, J. A., & Spera, F. J. (2006). Long-term volumetric eruption rates and magma budgets. *Geochemistry, Geophysics, Geosystems*, *7*(3). doi: 10.1029/2005GC001002

Whittaker, A. C. (2012). How do landscapes record tectonics and climate? *Lithosphere*, *4*(2), 160–164. Retrieved from `https://pubs.geoscienceworld.org/lithosphere/article/4/2/160-164/145621` doi: 10.1130/RF.L003.1

Whittaker, A. C., Attal, M., Cowie, P. A., Tucker, G. E., & Roberts, G. (2008). Decoding temporal and spatial patterns of fault uplift using transient river long profiles. *Geomorphology*, *100*(3-4), 506–526. doi: 10.1016/j.geomorph.2008.01.018

Whittaker, A. C., & Boulton, S. J. (2012). Tectonic and climatic controls on knickpoint retreat rates and landscape response times. *Journal of Geophysical Research: Earth Surface*, *117*(2), 1–19. doi: 10.1029/2011JF002157

Wobus, C., Whipple, K. X., Kirby, E., Snyder, N., Johnson, J., Spyropolou, K., ... Sheehan, D. (2006). Tectonics from topography: procedurses, promise, and pitfalls. *Geological Society of America Special Paper*, *398*(04), 55–74. doi: 10.1130/2006.2398(04).

Wolff, J. A., & Ramos, F. C. (2013). Source materials for the main phase of the Columbia River Basalt Group: Geochemical evidence and implications for magma storage and transport. In S. P. Reidel et al. (Eds.), *The columbia river flood basalt province* (pp. 273–291). Boulder, Colorado: Geological Society of America Special Paper 497. doi: 10.1130/2013.2497(11)E-mail

Wolff, J. A., Ramos, F. C., Hart, G. L., Patterson, J. D., & Brandon, A. D. (2008). Columbia River flood basalts from a centralized crustal magmatic system. *Nature Geoscience*, *1*(3), 177–180. Retrieved from `http://www.nature.com/doifinder/10.1038/ngeo124` doi: 10.1038/ngeo124

Wood, S., & Burnham, W. (1987). Geologic framework of the Boise Warm Springs geothermal area, Idaho. In S. Buess (Ed.), *Geological society of america centennial field guide rocky mountain section* (pp. 117–122). Boulder: Geological Society of America.

Wood, S. H., & Clemens, D. M. (2002). Geologic and Tectonic History of the Western Snake River Plain, Idaho. *Idaho Geological Survey Bulletin*, *30*(January), 69–103.

Woods, A. W., Bokhove, O., de Boer, A., & Hill, B. E. (2006). Compressible magma flow in a two-dimensional elastic-walled dike. *Earth and Planetary Science Letters*, *246*(3-4), 241–250. doi: 10.1016/j.epsl.2005.11.065

Wylie, J. J., Helfrich, K. R., Dade, B., Lister, J. R., & Salzig, J. F. (1999). Flow localization in fissure eruptions. *Bulletin of Volcanology*, *60*(6), 432–440. doi: 10.1007/s004450050243

Yanites, B. J., Ehlers, T. A., Becker, J. K., Schnellmann, M., & Heuberger, S. (2013). High magnitude and rapid incision from river capture: Rhine River, Switzerland. *Journal of Geophysical Research: Earth Surface*, *118*(2), 1060–1084. doi: 10.1002/jgrf.20056

Zak, J., Verner, K., Johnson, K., & Schwartz, J. J. (2012). Magma emplacement process zone preserved in the roof of a large Cordilleran batholith , Wallowa Mountains, northeastern Oregon. *Journal of Volcanology and Geothermal Research*, *228*, 61–75. doi: 10.1016/j.jvolgeores.2012.03.001

Zar, J. H. (2010). *Biostatistical Analysis* (5th ed.). USA: Prentice-Hall, Inc.

Zeitler, P. K., Meltzer, A. S., Koons, P. O., Craw, D., Hallet, B., Chamberlain, C. P., ... Shroder, J. (2001). Erosion, Himalayan geodynamics, and the geomorphology of metamorphism. *GSA Today*, *11*(1), 4–9. doi: 10.1130/1052-5173(2001)011⟨0004:EHGATG⟩2.0.CO;2

Zollweg, J., & Wood, S. (1993). *Faulting relationships, seismicity, design earthquakes, and peak ground acceleration at hydroelectric facilities in Hells Canyon of the Snake River, Idaho-Oregon* (Tech. Rep.). Boise, Idaho: Idaho Power.